University of Glasgow

Carvalhal Calhau de Menezes, Pedro Duarte (2025) *Fabrication, integration and simulation: a complete design cycle of polystyrene microfluidic systems using LCD 3D printing and injection moulding.* PhD thesis.

https://theses.gla.ac.uk/85313/

Copyright and moral rights for this work are retained by the author

A copy can be downloaded for personal non-commercial research or study, without prior permission or charge

This work cannot be reproduced or quoted extensively from without first obtaining permission from the author

The content must not be changed in any way or sold commercially in any format or medium without the formal permission of the author

When referring to this work, full bibliographic details including the author, title, awarding institution and date of the thesis must be given

Enlighten: Theses
https://theses.gla.ac.uk/
research-enlighten@glasgow.ac.uk

Fabrication, Integration and Simulation:
A Complete Design Cycle of Polystyrene Microfluidic Systems using LCD 3D Printing and Injection Moulding

By Pedro Duarte Carvalhal Calhau de Menezes

Submitted in fulfilment of the requirements for the degree of Doctor of Philosophy in Biomedical Engineering. January 2025

James Watt School of Engineering
College of Science and Engineering
University of Glasgow, UK

University of Glasgow

Abstract

Microfluidics is a rapidly evolving field of science with high potential and growing applications across life science research and industry. By controlling fluidics at the microscale, it achieves faster reaction times, lower sample volumes, and greater analytical power to that of classical techniques. For the past two decades, microfluidic research has relied upon, and thrived with, polydimethylsiloxane (PDMS) as the standard material for device fabrication. However, despite its many advantages, replica moulding techniques using PDMS are limited in throughput and automation, which currently encourages the field to transition to more scalable materials, such as thermoplastics. This thesis sets out to develop a novel design cycle for polystyrene-based microfluidic devices, encompassing scalable fabrication, integration and simulation.

A new fabrication protocol was established, using liquid crystals display (LCD) three-dimensional (3D) printing and injection moulding as the two overarching technologies in the development of rapid tooling for polystyrene (PS) microfluidic devices. The dominant process parameters impacting the compatibility, quality, and scalability of the respective procedure were identified and optimized. This way, a protocol was defined, capable of delivering sub 50 µm feature resolution, high optical transparency, and scalable production (≈ 500 parts) of microfluidic devices. Importantly, it also provided a turnaround time from computer-aided design (CAD) to a fully functional device of only ≈ 2 h 30 min, and from CAD to 500 replicas of ≈ 8 h, this way providing unique potential to rapid prototyping and scalable manufacturing.

The functionalization of the respective devices began by exploring different bonding strategies. Thermal fusion was seen as the most promising technique, providing reliable, high-quality seals, for channels and polystyrene membranes, with little to no deformation. Ultrasonic welding was instead seen as extremely efficient in bonding and stretching polyester membranes. Fluidic interfacing was then explored, from which the integration of an injection moulded well plate layer established a standardized interface for both pressure- and gravity-driven fluidics. A protocol for the development of elastic membranes for plug-and-play microvalving was also established by exploring elastomer prepolymer resins using single-layer masked exposure with ultra-violet (UV) light and spin coating. Not only were the physical and mechanical properties of membranes characterized, but also their performance for fluidic switching and dynamic control over concentration gradient generation.

To enhance microfluidic design, in particular with porous membranes, a finite element method (FEM) model was established to study the kinetics of flow and transport as a function of membrane, channel geometry, fluidic and diffusion parameters. By doing so, a comprehensive study was conducted, discretizing the influence of each individual parameter and hierarchizing their impact on fluid flow, shear stress, transient transport and molecular concentration. Based on the

provided guidelines, the dominant influence of flow over permeability properties in determining porous transport was found to be especially critical for microfluidic and organ-on-chip (OOC) applications. *On chip* experiments were performed to validate the respective numerical data by studying the transport of fluorescein and evaluating the effect of Cytochalasin D on cultured cells, as a function of flow and permeability. By doing so, the experimental relevance of the provided numerical data was demonstrated. This was further reiterated by extending the model to investigate the unique kinetics of transport in convection-driven devices with recirculating flow.

Ultimately, this thesis provides a framework for the scalable production of microfluidic and OOC devices, with compatible solutions for microfluidic integration and extensive characterization of microenvironments with porous barriers, in regard to fluid dynamics and transport kinetics.

Acknowledgements

If during my MSc Degree I learnt the value of empathy in connecting people beyond distance, during my PhD, I was fortunate enough to realise those bonds, nourish them, and make true, meaningful relationships.

To Professor Nikolaj Gadegaard - who would have thought? - knocking on your office door during a warm afternoon in spring, with hopes of staying in Glasgow over summer to compete at the Henley Royal Regatta, I would leave that same office with hopes and dreams of so much more. Thank you for the world of opportunities you have extended me and for being the precursor to my career in research. I look back to my years in your lab with nothing but deep gratitude, pride and joy.

To the BIG family, firstly Sören and Iliyana, who have been with me since day one, and then Alysha, Maia, Nghia, Euan, Badri, Rakshit, Rui and Nicholas as well, for the many hours we have shared in the lab, the many frustrations and successes, 3D printing failures and achievements, days in the injection moulding room, keeping the machine running by the sheer power of music, the many chats, discussions and events together, and the countless lunches, always accompanied by many, perhaps too many, even though many are never enough, bowls of chips. It was an epic 4-year journey, making, testing and eating chips, always together.

To the team at HTH, in Oslo, particularly Mathias, Ludi, Sergei and Stefan, for the warm welcome I have received the first instance I came into contact with the group, for the incredible hosting every time I was in Oslo, and for all your help, support, and all the exciting opportunities you have provided me with. I enjoyed every moment I have shared with you, and your friendship is one of the things I esteem the most from my PhD.

To all my friends. Those in Porto, especially Mesquita, PP, Ana, Tomás, Ricardo and Diogo, with whom I am so fortunate to maintain close friendships with, despite the distance, and still share so many exciting moments, or just the casual chat, as we watch ourselves grow together. And those in Glasgow, particularly Chris, Rory, Seumas, Ethan and Josh, with whom I have shared so many crazy adventures

with, from the start of my Erasmus to the end of my PhD, so many hours in boats and damp regattas, so many moments in the flat and ceilidh parties, so many potlucks and camping trips together, so many miles on the road and on the trails, as we ran, cycled and hiked, enjoying the neighbouring views of the city or the desolate, awe-inspiring scene of the highlands. I am so happy to have met you all, and even though life moves on to many unknown destinations, I am sure what started in Glasgow, will remain beyond it.

To my family, for your unconditional love and support, and for overcoming distance with heart-warming messages, motivational support, weekly update chats, and wholesome adventures together, be it on top of two motorized wheels as we ride through Portugal, or on top of two metabolically driven feet, walking through high hills, deep snowy valleys and half marathons in Scotland. I feel so fortunate to be able to share all these moments with you and, despite the self-imposed distance, have you so close and present in my life.

And to Nina, my ultimate adventure partner, and my partner in life. If I have got someone to thank for empathy and the fortune of joining paths with, it is you. Winding back the days until the very start of this PhD, it is almost as if going back to the origins of our relationship, and seeing everything unfold. From long months apart and exhilarating days together - rowing across lakes and eating pastries, backpacking through mountains and cycling across countries - to finding in Glasgow our first wee nest. And I have got only you to thank for this. For your all your hope and sacrifice in moving, to finally bring our lives together. For your unconditional support and motivation, helping me see this thesis through with nothing but deep pride and fulfilment. And for all your love. Our lives have been nothing short of adventures, and I cannot wait for the one coming up just next!

"The mayhem of Glasgow is buried deep in my blood […]
No' the best place but there's diamonds in the mud."

Gerry Cinnamon

Author's Declaration

I hereby declare that the contents of this thesis are original and my own. The methods in 4.4.1.1, 4.4.1.2 and 4.4.1.3, and the data collection in 4.4.2 and 4.4.3 were performed by Rui Zhang, MSc Student, under my supervision. All the references made to the work of others are cited and included in the bibliography.

The data in Chapter 2 and 4 has been published in peer reviewed journals. The details of the respective publications are present below.

Duarte Menezes, 2025

Publications

Menezes et al, A membrane's blueprint: In silico investigation of fluid flow and molecular transport as a function of membrane design parameters in organ-on-a-chip. *Chemical Engineering Journal*, **2024**, 481.

Menezes et al, Scalable, Transparent, and Micro: 3D-Printed Rapid Tooling for Injection Moulded Microfluidics. *Advanced Engineering Materials*, **2024**, 26.

Aizenshtadt et al, Pump-Less, Recirculating Organ-on-Chip (rOoC) Platform to Model the Metabolic Crosstalk between Islets and Liver. Advanced Healthcare Materials, **2024**, 13.

Poster Presentations

Menezes et al, Rapid Tooling for Injection Moulding with 3D Printing. Oral presentation at: Micro and Nano Engineering (MNE) 2024 Conference, Berlin, Germany, September **2023.**

Menezes et al, Plug-and-Play Elastomeric Membranes for Valving in Microfluidics. Oral presentation at: BioMedEng 2024 Conference, London, United Kingdom, September **2024.**

Table of Contents

Table of Figures

List of Tables

Nomenclature

2D	Two Dimensional
3D	Three Dimensional
ADME	Absorption, Distribution, Metabolism and Excretion
AM	Additive Manufacturing
ANOVA	Analysis of Variance
AW	Anycubic White
bCAII	Bovine Carbonic Anhydrous II
BeWo	Human Placental Choriocarcinoma Cell Line
CAD	Computer-Aided Design
CC	Cell Channel
CFD	Computational Fluid Dynamics
COC	Cyclic Olefin Copolymer
CNC	Computer Numerical Control
ES	Electrospun
FB	Flyback Diodes
FC	Flow Channel
FEM	Finite Element Method
FDM	Fused Deposition Modelling
FEP	Fluorinated Ethylene Propylene
FF63A	Formfutura Flex 63A
FF82A	FF82A Formfutura Flex 82A
HSD	Honestly Significant DIfference
HUVEC	Human Umbilical Vein Endothelial Cells
IPA	Isopropyl Alcohol
I/O	Inlet and Outlet
LCD	Liquid Crystals Display

LEX	Liquid Elastomer-X
LOC	Lab-on-Chip
MDCK	Madin-Darby Canine Kidney
MC	Monoprice Clear
MEMS	Microelectromechanical Systems
MOSFETS	Semiconductor Field-Effect Transistors
MV	Membrane Valve
NP	Non-Polished
OOC	Organ-on-Chip
P	Polished
P_{air}	Air Pump
PAA	Poly (acrylic acid)
PBS	Phosphate-Buffered Saline
PDEs	Partial Differential Equations
PEEK	Polyether Ether Ketone
PET	Cyclic Poly (ethylene terephthalate)
PETE	Polyester
PFA	Perfluoroalkoxy Alkane
PM	Porous Membrane
PMMA	Poly (methyl methacrylate)
PP	Parallel Perfusion
PP_{OD}	Parallel Perfusion, with Opposite Direction Flow
PP_{SD}	Parallel Perfusion, with Same Direction Flow
PS	Polystyrene
PTFE	Polytetrafluoroethylene
PV	Pneumatic Valve
Q	MOSFETS
R	Current-Regulating Resistors

R&D	Research and Development
rOOC	Recirculating Organ-on-Chip
RP	Rapid Prototyping
RT	Rapid Tooling
S	Pressure Sensor
SA	Surface Area
SCP	Single Channel Perfusion
SCP_R	Single Channel Perfusion, Cell Channel as a Reservoir
SCP_O	Single Channel Perfusion, Cell Channel as an Outlet
sc	Stem-Cell
SEM	Scanning Electron Microscopy
SLA	Stereolithography
T_{air}	Air Tank
TE	Track-Etched
TPU	Thermoplastic Polyurethane
UV	Ultra-Violet

Symbols

BP_{air}	Bursting Pressure [mbar]
BS	Bore Size [mm]
C	Molecular Concentration [mol/m^3]
C_{in}	Inlet Molecular Concentration [mol/m^3]
C_n	Normalized Molecular Concentration []
C_{nCC}	Normalized Molecular Concentration in the Cell Channel []
C_{nCC}	Normalized Molecular Concentration in the Flow Channel []
D	Diffusion Coefficient [m^2/s]
D_{eff}	Effective Diffusion Coefficient Rate [m^2/s]
E_{USW}	Welding Energy [Ws]
$\mathbf{F}$	Volume Forces per Unit Mass of Fluid [N/kg]
H	Height of channels [µm]
H_{CC}	Cell Channel Height [µm]
H_{FC}	Flow Channel Height [µm]
$\mathbf{I}$	Identity Matrix
K	Permeability [m^2]
K_m	Membrane Permeability [m^2]
K_{tb}	Tissue Barrier Permeability [m^2]
L	Pore Length [m]
L_M	Membrane Length [mm]
LP_{air}	Limit Pressure [mbar]
P	Porosity []
P_0	Atmospheric Pressure [Pa]
P_{TF}	Thermal Fusion Pressure [bar]
P_{USW}	Welding Pressure [bar]
P_{air}	Pneumatic Pressure [mbar]

P_c	Cylinder Pressure [bar]
Pe	Péclet Number []
Pe_{CC}	Péclet Number in the Cell Channel []
Pe_{FC}	Péclet Number in the Flow Channel []
Q	Flow Rate [µL/h]
Q^A_n	Average Value for the Normalized Flow Rate []
Q^A_{nCC}	Average Value for the Normalized Flow Rate in the Cell Channel []
Q^A_{nFC}	Average Value for the Normalized Flow Rate in the Flow Channel []
Q_{BL}	Flow Rate in the Bottom Loop [µL/h]
Q_{CC}	Flow Rate in the Cell Channel [µL/h]
Q_{FC}	Flow Rate in the Flow Channel [µL/h]
Q_{TL}	Flow Rate in the Top Loop [µL/h]
Q_{in}	Inlet Flow Rate [µL/h]
Q_n	Normalized Flow Rate []
Q_{nCC}	Normalized Flow Rate in the Cell Channel []
Q_{nFC}	Normalized Flow Rate in the Flow Channel []
Ra	Surface Roughness [µm]
Re	Reynolds Number []
Re_{CC}	Reynolds Number in the Cell Channel []
Re_{FC}	Reynolds Number in the Flow Channel []
R_p	Flow Resistance [Pa.s/m^3]
SA	Surface Area [mm^2]
T_{TF}	Thermal Fusion Temperature [°C]
T_g	Glass Temperature [°C]
V_{USW}	Velocity of Approach []
W	Width of channels [µm]
WSS	Wall Shear Stress [Pa]
WSS^A_n	Average Value for the Normalized Wall Shear Stress []

WSS^{A}_{nCC}	Average Value for the Normalized Wall Shear Stress in the Cell Channel []
WSS^{A}_{nFC}	Average Value for the Normalized Wall Shear Stress in the Flow Channel []
WSS_{MCC}	Wall Shear Stress, in the Membrane Surface of the Cell Channel [Pa]
WSS_{MFC}	Wall Shear Stress, in the Membrane Surface of the Flow Channel [Pa]
WSS_{UCC}	Wall Shear Stress, in the Upper Surface of the Cell Channel [Pa]
WSS_{n}	Normalized Wall Shear Stress []
g	Gravity Constant [m^2/s]
h	Water Column Height [m]
p	Fluid Pressure [Pa]
r	Pore Radius [m]
s	Source/Sink of Diluted Species [$mol/(m^2s)$]
sf	Safety Factor []
ssC_{n}	Steady State Normalized Molecular Concentration []
ssC_{nCC}	Steady State Normalized Molecular Concentration in the Cell Channel []
ssC_{nFC}	Steady State Normalized Molecular Concentration in the Flow Channel []
st	Settling Time [s]
st_{CC}	Settling Time in the Cell Channel [s]
st_{FC}	Settling Time in the Flow Channel [s]
t	Time [s]
t_{M}	Membrane Thickness [μm]
t_{SC}	Spin Time [s]
t_{TF}	Thermal Fusion Process Time [s]
t_{UV}	UV Exposure Time [s]
t_{USW}	Welding Time [ms]
$\mathbf{u}$	Velocity Vector [m/s]

V	Flow Velocity [m/s]
V_n	Normalized Flow Velocity []

Greek Symbols

α_{3DR}	Pitch [°]
δ_M	Membrane Deflection [mm]
δ_{Mmax}	Maximum Membrane Deflection [mm]
ε	Strain []
σ	Stress [Pa]
τ	Tortuosity []
γ	Shear Rate [s^{-1}]
μ	Fluid Dynamic Viscosity [Pa.s]
ρ	Fluid Density [kg/m3]
ω_{3DR}	Revolutions per Minute [rpm]
ω_{SC}	Spin Rate [rpm]

Chapter 1

1 Introduction

1.1 Microfluidics

Engineering fluidics at the microscale is today a dynamic field of science with vast potential and growing application in life science research and industry. Microfluidics, as the field came to be known since 1993 [1], evolved from an eclectic background of influences, converging concepts of physics, chemistry, biology, material science, fluid dynamics and most importantly, microelectronics [2]. It is defined as the science and technology of systems manipulating minute (10^{-9} to 10^{-18} L) amounts of fluid using micro-sized channels (0.1 to 100 μm) [3]. It is exactly by exploring its characteristic small scale, that microfluidics has been demonstrated to outperform classical analytical techniques.

The advantages for the bio-chemical sector are numerous. Some are more obviously related to the length scale involved. Microfluidic devices require small sample volumes, leading to a reduction of costs in reagents while maximizing the information these provide. A smaller sample size also means that reaction times are quicker, contributing to faster analysis. A single microfluidic chip is also capable of running several operations in parallel, enabling batch sample processing and widely increasing screening throughput. Additionally, depending on material selection and manufacturing procedure, devices can be manufactured in high volumes, cheap and disposable [4]. Other advantages are more discretely associated with the behaviour of fluids in submillimetre channels. At the microscale, the relative influence of forces is measurably different than at the macroscale [5]. More meaningfully, the relative effect of gravity is significantly reduced at the microscale. Instead, it is surface tension and capillary forces that exert the most dominant roles. This shift in paradigm has several implications, most of which microfluidics harnesses to its own benefit. The reduced effect of inertia and growing influence of shear forces establish highly streamlined fluidics, known as laminar regime, with highly predictable spatial-temporal kinetics [6]. Surface tension enables the formation of monodisperse droplets in multi-phase media, effectively mass-producing microreactors with incredible precision and screening power. Passively driven fluidics, an extremely popular approach amongst commercial applications, is a result of precise handling of capillary action.

Amidst this development potential, researchers from various fields of science converged into microfluidics and, over the past three decades, contributed to defining what is now a well-established field and an extremely powerful tool. As of 2023, the global estimated size of the microfluidic market was of USD 32.15 billion [7]. The dominant driving force in this market is the medical segment, with a market share of 83.8%, and the leading application is lab-on-chip (LOC), at 37.8% [8]. The concept behind LOC devices is the incorporation of multiple, miniaturized lab functions in a single microfluidic chip. It encompasses devices such as point-of-care, DNA sequencing and, perhaps more notably, organ-on-chip (OOC). OOC is often referred to as the 'killer application' for microfluidics, with a potential transformative impact in the pharmaceutical market. The precise modelling of fluidics coupled with advanced cell culturing techniques establishes more relevant models of human physiology, aiming to suppress animal testing during drug trials by bridging the gap between *in vitro* and *in vivo* studies [6].

This section will explore the field of microfluidics and examine its various characteristics. From a brief history of the field to a more detailed understanding of the physics involved at the microscale. The traditional material and microfabrication techniques will also be explored, followed by a deeper characterization of the OOC field. Finally, a key challenge permeating the development of microfluidic systems will be identified and serve as an introduction to the research ambitions and contributions of this thesis.

1.1.1 Birth of the Field

'There is plenty of room at the bottom' were the words of Richard Feynman in 1959 [9] during a thought-provoking speech which sparkled the scientific community and launched the beginning of micro- and nanotechnology. Just five years later, at Texas Instrument, Jack Kilby was employing photolithography to effectively manufacture in silicon the first ever integrated circuit [10]. This development brought about the "silicon age" and perhaps the most enabling technology of the century: microelectronics [4]. Similarly enabled by photolithography, the seventies also saw the development of microelectromechanical systems (MEMS). Containing both electronic and moving mechanical parts, MEMS allowed, for the first time, to not only observe but also operate on the microscale, and with incredible precision [6]. The growing interest

from industry [11, 12] accelerated the production of MEMS and enhanced the development of photolithography and etching techniques, which ultimately, set the foundations for microfluidics.

The first silicon-based microfluidic device emerged in 1979, at the hands of Terry et al [13]. This work described a microscale gas chromatography system, illustrated in Figure 1.1, consisting of an injection valve and a 1.5 m long separating capillary coil, etched on a silicon wafer. These were further attached to a thermal conductivity sensor, batch fabricated using standard integrated circuit processing techniques. This seminal work demonstrated three fundamental points. First, that the reduction of the capillary cross-sectional area led to an increase of analytical performance and sensitivity. Second, that using a low volume injection valve reduced reagent consumption without compromising performance. And third, that a device manufactured on a 5 cm silicon wafer had

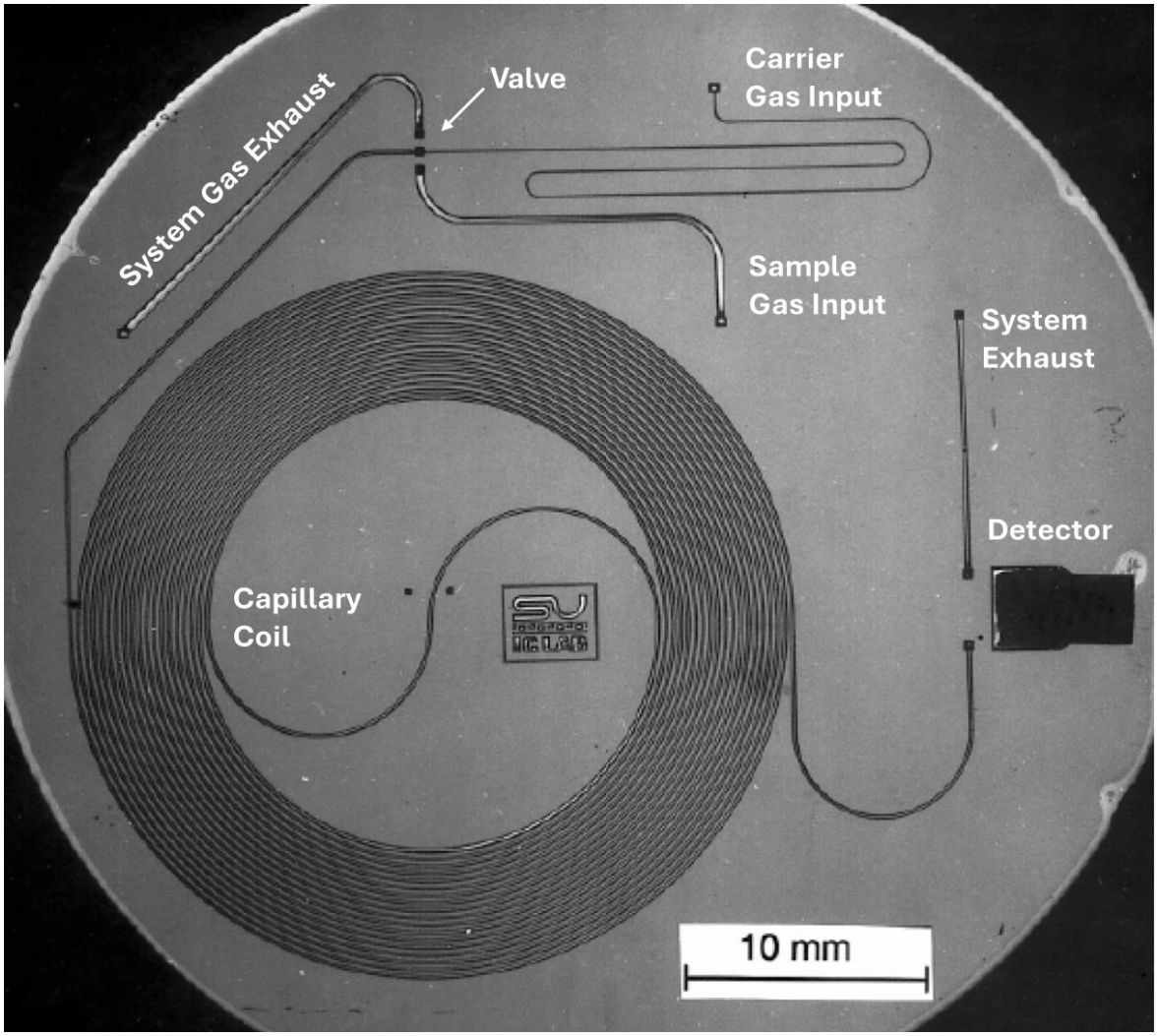

Figure 1.1: The first silicon-based microfluidic system, consisting of a miniaturized gas chromatography system integrating a separating capillary coil, valve and detection system, all in a 5 cm silicon wafer. This device is regarded today as the first lab-on-a-chip. Reprinted with permission of IEEE.

similar performance to more traditional and bulkier systems [14]. Terry's gas chromatography system is now regarded as the first LOC device. However, the respective technological leap remained isolated at the time, and it was only later, in 1992, that the advantages of miniaturization came into a wider spotlight [6]. A. Manz et al. reported the manufacture of the first electrokinetic separation microsystem [15], and with it, he coined two important aspects. First, that with miniaturization comes low-cost, high-performance and extreme efficiency. And second, the introduction of the acronym μTAS, for Micro Total Analysis Systems, a term which aggregated a community and launched the start of the microfluidic field.

1.1.2 Physics at the Microscale

The surface-to-volume ratio in microfluidic systems is characteristically high [16]. This phenomenon has far-reaching implications, which set fluid mechanics at the microscale apart from those at the macro scale. One of which is revealed by the Reynolds, *Re*, a dimensionless number describing the ratio between inertial and viscous forces. At the critical value of *Re* = 4000, a threshold between the turbulent and laminar regime is found. At the macroscale, fluid dynamics follow a turbulent regime, which is characterized by highly stochastic behaviour. However, by downsizing systems to the microscale, typically *Re* < 10, viscous forces become dominant over inertial, forcing flow to follow highly predictable, laminar paths, with little to no lateral mixing [17]. This is better illustrated by Figure 1.2, an example provided by Albert Folch [18] depicting the effects of the laminar regime. On the other hand, the Péclet number, *Pe*, evaluates the ratio between advective and diffusive transport. An analysis to *Pe* indicates that, at the microscale, transport is almost entirely dominated by diffusion. Ultimately, both the laminar regime and the diffusive behaviour of transport makes it notably easy to mathematically model microfluidic systems.

Another important aspect of the microscale is that volume forces, such as gravity, become negligible, and conversely, surface tension and capillary action take the dominant lead. Both these phenomena result from the interplay between cohesive and adhesive forces. Cohesive forces are those responsible for the bulk properties of liquids and bonding molecules of the same substance together. Adhesive forces are those that, instead, attract molecules of different substances towards one

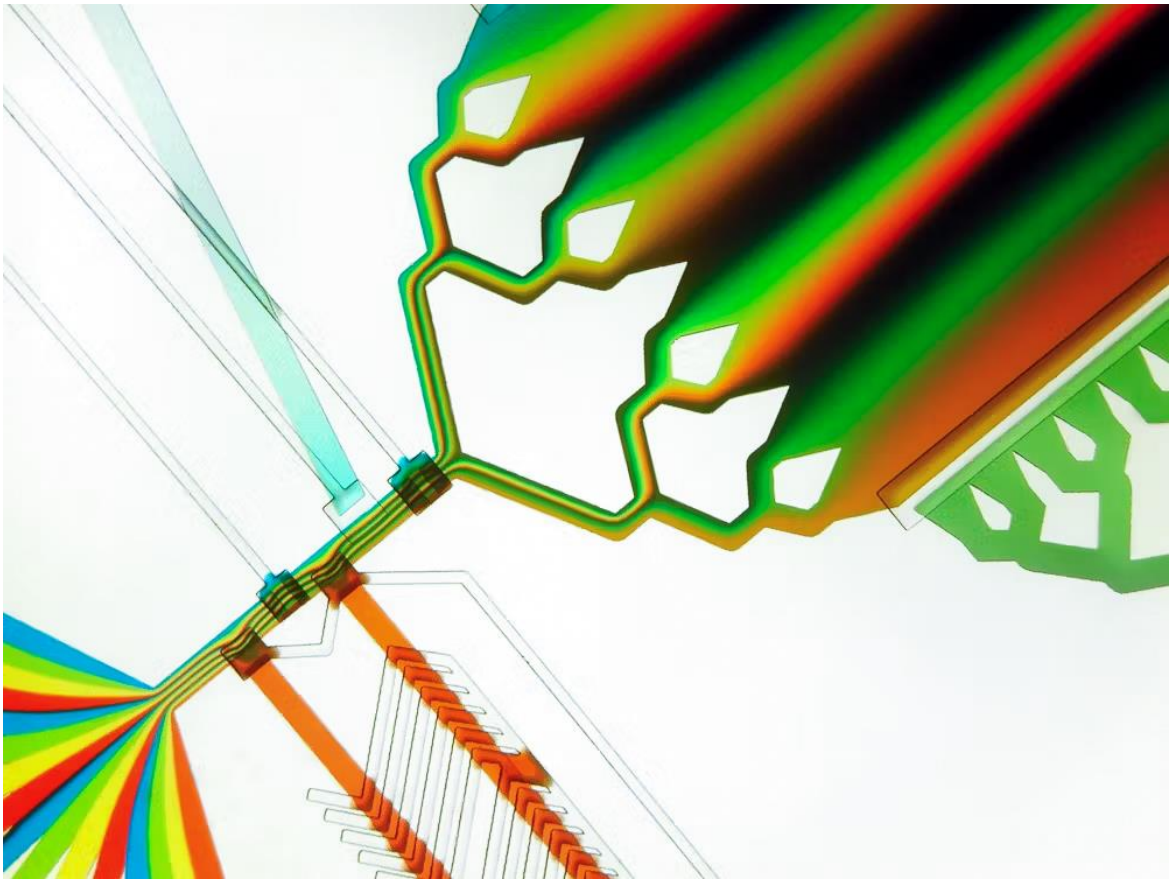

Figure 1.2: Visual representation of the laminar regime and its implications to flow and molecular transport. It is observed that the multiple, different-coloured streams of flow travel through the microfluidic channels with little to no lateral mixing, as a result of low *Re*. Image reproduced with permission of Albert Folch and *The Conversation* journal [18].

another. A result of this interaction is surface tension, where the dominance of cohesive over adhesive forces pull the body of liquid inwards, causing its surface to contract and achieve a minimum energy state. Control over this phenomenon has been explored in droplet microfluidics [19], protein and cell sorting [20], medical diagnosis and detection [21], syntheses of nanoparticles [22], and even in valving systems [23]. On the other hand, when adhesive forces exceed the cohesive, a concave meniscus is formed due to surface tension and the liquid is propelled forward. This is known as capillary action, an important phenomena which gave rise to passively driven microfluidic devices. Pregnancy tests [24], portable blood glucose meters [25], Covid-19 antigen tests [26] and paper analytical devices [27] are just some of its applications.

1.1.3 Microfabrication Techniques and Material Selection

The advent of photolithography launched the semiconductor industry, but it also set the foundations for both MEMS and microfluidics. The ability to realise features down to the micro- and nanoscale was key in attracting early microfluidic

researchers to explore the protocols already developed for the semiconductor industry. Since then, photolithography went on to become a fundamental piece in the field of microfluidics. However, if for the semiconductor industry silicon started and remained up until today the backbone material of the technology, for microfluidics, the material used in the development of devices has undergone large changes over the years [5].

1.1.3.1 Photolithography – Silicon and Glass

In photolithography, a geometric pattern is transferred from a photomask to a light-sensitive photoresists using ultra-violet (UV) exposure [28]. The protocol consists of spin coating a photoactive compound, known as a resist, onto a silicon wafer, and pre-baking it to remove any solvents or built-in stresses. UV light is then irradiated through a photomask, transferring its pattern to the exposed resist layer. During development, the unpolymerized resin is dissolved and the relief pattern is revealed. For positive tone resists, the dissolved material corresponds to the non-irradiated areas, whereas for negative tone ones, the opposite occurs. The pattern of the resist is then transferred to the silicon wafer via etching, and the resist is removed using a stripping solution [29]. An optimization to this protocol came later with the development of the SU-8 negative-tone resist. Greater mechanical and chemical stability [30], and the ability to deposit thicker layers, meant device fabrication with SU-8 could be done without etching [31].

Fabrication with silicon provided several benefits for early microfluidic research. Thermal and chemical stability, semiconducting properties, design flexibility and wide compatibility with surface treatments, made silicon a dominant material for decades [32-35]. However, historically, silicon was only chosen out of convenience [36]. It was only later, when microfluidics turned to biological detection, that its disadvantages, most critically its opacity to light, became constraining. Glass appeared then as a suitable alternative, with excellent optical properties as well as compatibility with microfabrication techniques [14]. Beyond that, glass is chemically inert [32], thermostable [37], electrically insulating [38], compatible with several surface treatments [37] and biocompatible [39]. Importantly as well, years of biology and chemistry research had been performed on a glass substrate. Adopting glass as the primary substrate meant microfluidics could, therefore, access this knowledge base. Glass came to be one of the most popular materials

for microfluidics [39]. However, both glass and silicon share similar disadvantages. Both are brittle, require non-trivial bonding strategies to seal microfluidic channels, and depend upon expensive, labour intensive and often inaccessible microfabrication techniques. Ultimately, despite their foundational role, both materials limit the growth of microfluidics [5]. The field turned instead to cheaper and more accessible techniques, and found in polydimethylsiloxane (PDMS) an exceptional solution [40].

1.1.3.2 Soft Lithography - PDMS

The fabrication of microfluidic devices with PDMS was pioneered by George Whitesides and his group at Harvard in the late 20th century [41]. Their work was truly transformative, and PDMS quickly became the leading material for microfluidics. Among its vast qualities, PDMS is non-toxic, biocompatible, insulating and optically clear [42]. It also provides tuneable stiffness by controlling the ratio between its base and cross-link agent. Importantly, not only does this enable the creation of compliant devices, but also, it enabled the first mass-integration of fluidic valves into a single microfluidic chip [43]. PDMS can also be easily bonded to itself or another material, such as glass. By establishing conformal contact, it creates a seal capable of withstanding moderate fluidic pressures [44]. However, PDMS can also be irreversibly bonded given the appropriate surface treatment, such as through plasma, and this way achieve a seal capable of withstanding high fluidic pressures [45]. And most importantly, fabrication with PDMS can be achieved without a cleanroom or specialized skills, being simple, cheap and extremely important in the democratization of the technology [6].

Beyond pioneering the material, the Whitesides group also revolutionized its fabrication, developing a set of techniques, designated as Soft Lithography, comprising of simple patterning methods in the development of a PDMS mould [46]. Of those, replica moulding is perhaps the simplest and most practised of the techniques. Initially, a positive relief known as a master mould is manufactured, either through advanced microfabrication techniques, such as photolithography, or rapid prototyping (RP), via injection moulding, hot embossing, or micromachining. Afterwards, a mixture of liquid PDMS prepolymer and cross-linking agent, typically in the ratio of 10:1, is casted onto the master. Its low

surface energy means that the liquid mixture easily flows into small features, ultimately enabling high-resolution feature replication, sub 0.1 μm [47]. The liquid mixture is then cured, after which a negative replica of the master mould is obtained in PDMS. Finally, the replica is peeled off from the mould which, depending on the material and surface functionalization employed, can be reused multiple times [48]. The channels contained on the negative replica can then be sealed through simple conformal contact or enhanced via oxygen plasma, respectively obtaining a reversible or irreversible sealing.

1.1.4 Organ-on-Chip

The pharmaceutical research and development (R&D) sector is facing currently a productivity crisis [49]. Despite increasing investment in R&D, the approval rates have been in constant decline [50]. Since 1950, the number of approved drugs per billion US dollar has approximately halved every 9 years [51]. This tendency is described by the "Eroom's Law", a model which implies the existence of countervailing forces outweighing those generated by technological progress. The reliance on 2D cell cultures and animal models is appointed as one of these counteracting forces. Their poor physiological relevance contributes to the low success rate in preclinical and human (phase I) trials [52], these being the most costly and time-consuming stages in the R&D pipeline [53]. There is, this way, a necessity to transition to models of greater physiological accuracy.

OOC aims to recapitulate organ level function *in vitro*, by culturing cells in microfluidic channels precisely engineered to mimic the appropriate physiological conditions [54, 55]. Their laminar nature enables the integration of crucial environmental cues, such as shear stress and concentration gradients, with known influence on cell expression [56], differentiation [57], morphology [58] and migration patterns [59]. More so, advanced microfabrication techniques allow the incorporation of more complex extracellular stimulus. Porous membranes enable the culture of connective multicellular constructs [60]. Material selection and pneumatic action allow mechanical stretching [61] and compression [62]. And integrated electrodes enable the stimulation of electrically active tissue, such as neural, skeletal muscle and cardiac [63]. Finally, OOC enables the integration of a wide range of advanced, real-time, non-invasive monitoring techniques [64]. The latent potential of OOC technology quickly captured the attention of the

scientific community. Huh et al. 2010 pioneered the concept of a “lung-on-a-chip” device, Figure 1.3, a biomimetic microsystem capable of delivering cyclic mechanical strain to a porous alveolar-capillary interface [65]. Since then, a variety of other tissues have been emulated on OOC platforms, from muscle [66] to bone [67], fat [68], liver [69], heart [70], brain [71], gut [72], blood vessels [73], and more. The integration of multiple organ tissues into a single, interconnected “human-on-chip” model is also a popular concept, aiming to provide a better representation of the absorption, distribution, metabolism and excretion (ADME) processes [74].

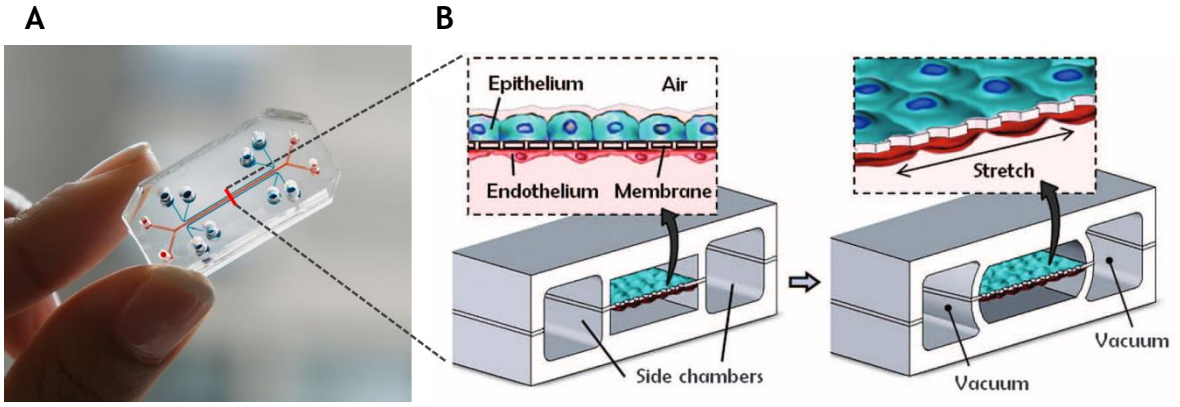

Figure 1.3: The pioneer “lung-on-a-chip” model. A, “Lung-on-a-chip” device made from PDMS. B, Working principle behind the “lung-on-a-chip” model. It consists of three layers of PDMS, forming compartmentalized microchannels separated by a thin, elastic, porous membrane, to mimic the alveolar-capillary barrier and replicate physiological breathing movement through the cyclic mechanical stretching of the membrane by applying vacuum. Images reproduced with permission of the Wyss Institute and Huh et al [65].

1.1.5 Moving beyond PDMS

PDMS has been the harbinger for microfluidic and OOC research over the past 20 years, fostering the best part of applications in the fields. However, it is not without drawbacks. PDMS is prone to absorbing small, hydrophobic molecules, making it extremely unsuitable for most cell-signalling and drug screening assays [75], as well as inadequate for the pharmaceutical industry and OOC applications. Evaporation, too, is a problem that critically affects biological studies on PDMS-based microfluidic devices, compromising any accurate predictions over concentration of solutions [76]. Its hydrophobicity can only be temporarily modified, given the transient effect of surface treatments on PDMS [77], which represents as well a significant limitation. Problems with uncured polymer leaching into the analyte are similarly impactful [78]. Flow-induced channel deformation, driven by the material’s elasticity, further compromises any

accurate calculation of flow rate and shear stress [79]. And finally, fabrication with PDMS and soft lithography is largely incompatible with automation and high-volume manufacturing. Not only does this significantly limit the dissemination and impact of microfluidics in society [80, 81], but also, by extension, it reduces the cost-efficiency of OOC technology and restrains its viability for the pharmaceutical R&D pipeline. These factors combined currently lead microfluidic research away from PDMS and into materials that may provide more suitable properties as well as enhanced potential for scalability.

1.2 Contribution of this Thesis

The overarching goal of this thesis lies exactly in researching and establishing new pathways for the development of scalable and cost-efficient microfluidic devices. It is based on exploring polystyrene as an alternative to PDMS, given its compatibility with high-volume manufacturing procedures and more suitable properties, avoiding problems such as absorption, evaporation and deformability. This thesis encompasses the integration of the respective devices as well, towards defining versatile platforms which are easily sealed, connectable with external fluidic elements, and compatible with higher order mechanical actuators. It also involves the study of fluid and molecular transport kinetics, towards providing greater control over design parameters and defining platforms of greater fluidic accuracy and physiological relevance.

These contributions are observed as playing a critical role in accelerating the transition away from PDMS and into thermoplastic substrates which, in turn, are expected to greatly contribute to the dissemination and impact of microfluidic technology in present society.

1.2.1 Research Aims

This leads to the three primary goals of this thesis, that are defined as follows:

1. Explore three-dimensional (3D) printing and injection moulding towards defining a protocol capable of fabricating polystyrene-based microfluidic devices of high optical quality and feature resolution, with high cost-efficiency, short lead production times and high scalability.

2. Investigate and optimize bonding strategies to define scalable, high-quality seals for microfluidic channels and porous membranes. Develop easy-to-use fluidic interfacing approaches, compatible with scalable manufacturing and different modes of fluidic perfusion. Develop dynamic fluidic valving technology, capable of seamless integration into rigid, polystyrene-based microfluidic substrates, and with proven performance.

3. Use finite element method (FEM) software to simulate and characterize the kinetics of flow and transport across porous membranes in microfluidic bilayer devices, and highlight the experimental relevance of the developed numerical model in the context of microfluidic and OOC applications.

1.2.2 Structure of this Thesis

In alignment with the respective research aims, this thesis is structured as follows:

- Chapter 1: Provides an initial introduction to microfluidic technology and current challenges associated with material selection, as well as contextualize the value and contributions of this thesis in providing a solution to the respective challenge.

- Chapter 2: Describes the current state-of-the-art associated with the three main research topics of this thesis. Provides a literature review over scalable manufacturing procedures and different polymers, highlighting the fabrication with injection moulding and polystyrene, with 3D printing, and ultimately introducing the concept of rapid tooling (RT). Describes the current state-of-the-art on back-end processes for thermoplastic microfluidic systems, focusing on substrate bonding, fluidic interfacing and valving integration. Describes present approaches to the simulation of microfluidic systems using FEM, as well as its benefits to describe fluid and transport kinetics and current challenges.

- Chapter 3: Identifies the main challenges with current RT methods for injection moulded microfluidics, and investigates 3D printing in the development of microfluidic tooling. Develops a novel RT protocol and characterizes the relevant process parameters determining the

compatibility, feature resolution, optical quality and scalability of the produced microfluidic devices. Applies the respective procedure to develop relevant, proof-of-concept, microfluidic devices, and highlights the unique ability of the developed procedure to enable both rapid prototyping and scalable manufacture.

- Chapter 4: Identifies the main challenges and technologies involved in microfluidic integration with thermoplastic substrates. Investigates different bonding strategies and optimizes their protocols to ensure a scalable and high-quality seal between microchannel layers and porous membranes. Explores different approaches to rapid fluidic interfacing, and addresses both pressure- and gravity-driven modes for fluidic perfusion. Defines a new strategy to plug-and-play dynamic valving with 3D printed soft components and elastic membranes, characterizes the respective fabrication protocol and investigates valving performance.

- Chapter 6: Establishes a FEM parametric model simulating the fluidic and mass transport kinetics of bilayer microfluidic devices with integrated porous membranes. Validates the respective model with examples present in literature. Provides a comprehensive study, systematically characterizing the effect of membrane parameters, channel geometry, fluidic architecture, and diffusion properties, to flow rate, shear stress, transport settling time and steady state molecular concentration. Validates the respective model with examples present in literatures. Validates the obtained numerical data and highlights its relevance for microfluidic and OOC applications by performing *on chip* permeability experiments with and without cells. Employs the model to investigate the transport kinetics associated with recirculating, pulsatile fluidic profiles, characteristic to gravity-driven microfluidic platforms using 3D rocking for fluidic perfusion.

- Chapter 7: Provides a summary of the research findings and evaluates the success of this thesis in meeting its own research objectives. Describes the limitations of the present body of work and, accordingly, suggests relevant directions for future work.

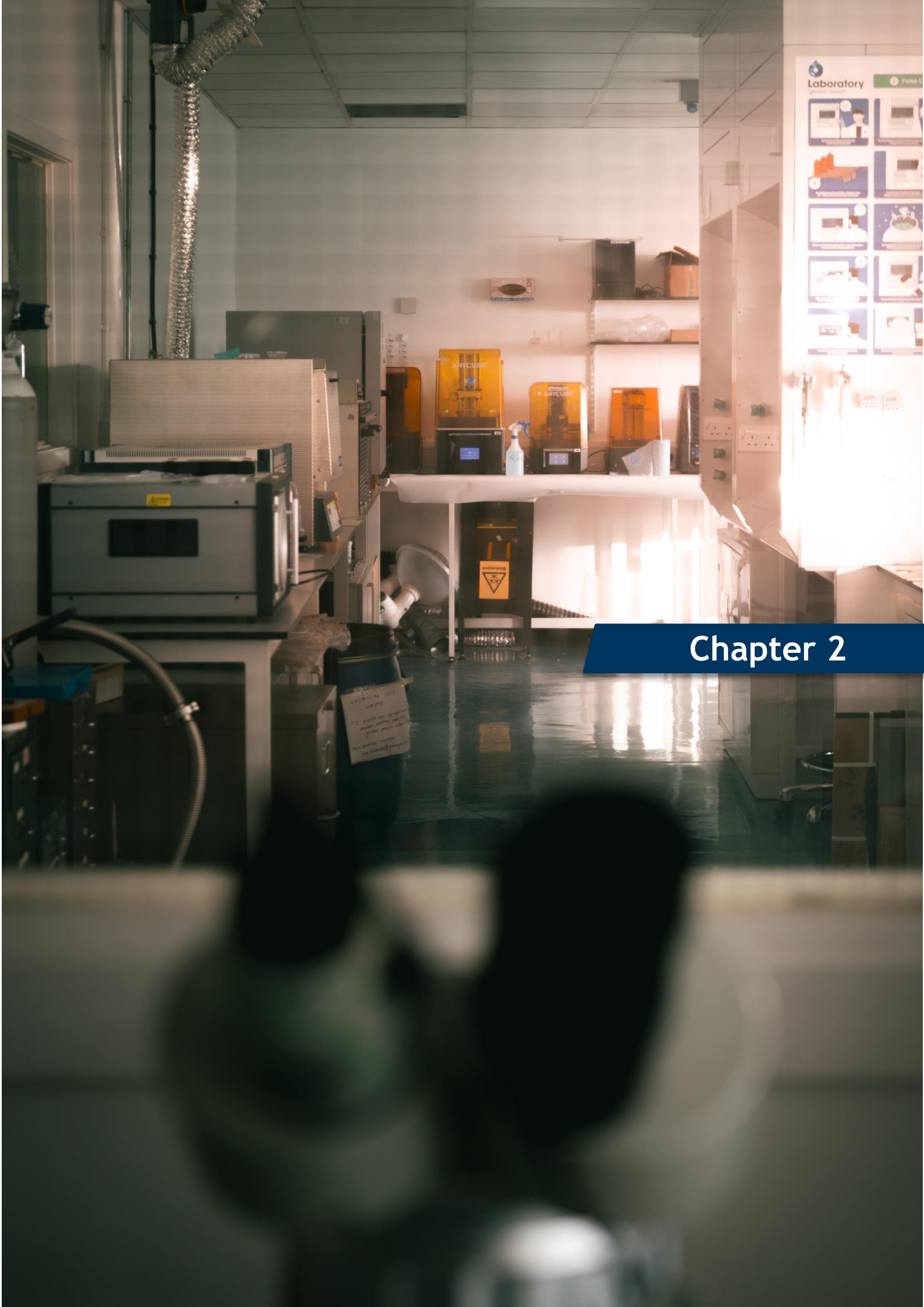

Chapter 2

2 State-of-the-Art Review

2.1 Polymers and Scalable Microfabrication Techniques

PDMS belongs to a class of polymers known as elastomers. These present a characteristically high viscoelasticity and weak intermolecular forces, enabling them to undergo large deformations and recover its original shape upon the release of stress. But the polymer family is wide and diverse, with many suitable candidates for microfluidic applications [82]. Thermoplastics are another class of polymers whose chains are branched together via weak forces, called Van der Waals forces. These forces weaken significantly with increasing temperature - a reversible process that allows the material to become pliable and mouldable, and then solidify again upon cooling [82]. For this reason, thermoplastics have been widely used in industry and refined for mass production, accessing high-volume manufacturing procedures based on high temperatures for plastic moulding. From the various procedures available, injection moulding remains as the golden standard for scalability, with proven micro- to nanofeature replication [83]. Contrary to thermoplastics, thermosets are characterized by strongly cross-linked polymeric chains. Cross-linking is an irreversible process, achieved chemically or via suitable radiation or heat, which turns a soft prepolymer into a hardened thermoset, of high thermal and chemical stability. A key advantage of thermosets is that they allow true 3D microfabrication via additive manufacturing (AM) [38], otherwise known as 3D printing. Not only is this technology extremely accessible and affordable today, but it also enables the quick manufacturing of complex, high-resolution structures, with minimal labour and skill [84].

In this section, the working principles behind injection moulding and 3D printing will be explored, as well as their complementary approach into rapid tooling. The discussion will address the relevant control parameters and material selection with an aim towards microfluidic applications. A brief review on the state-of-the-art of injection moulding, 3D printing, and rapid tooling for microfluidics will be provided.

2.1.1 Injection Moulding

Injection moulding is a process where molten polymer is injected at high temperature and pressure into the mould cavity, allowing the polymer to cool and shape before being ejected, for another cycle to begin. This method is, today, one of the most productive and cost-efficient ways of manufacturing scalable and high-quality products [85].

The first injection moulding machine was pioneered by the Hyatt brothers in 1872 [86]. But it was only later, with the break of the World War II and the demands it generated for cheap, mass-produced equipment, that the technology truly expanded. It culminated with the development of the first screw driven injection moulding machine, by James Watson Hendry in 1946 [87]. This technological step enabled the precise control over the delivery rate and volume of injected polymer, hence resulting in better quality products and greater reproducibility. In the years that followed, injection moulding continued to expand, establishing itself as a dominant technology in industry, with a market size estimated at 5.90 million tons in 2024 [88]. Injection moulding provides two key advantages over its competing technologies in thermoplastic fabrication. One, is that the heating of the polymer and the cooling of the part are kept separate [89]. This way, the polymer does not need to be heated and cooled for every cycle, unlike thermoforming and hot embossing, which drastically reduces the cycle time and increases the throughput. And second, the phenomena of shear thinning, common to most thermoplastics, yielding lower viscosity for higher shear [90], promotes the flow and filling of the polymer into the mould cavity. Ultimately, it facilitates the replication of smaller features, down to the nanoscale [91], where injection moulding has inclusively well-developed markets, more commonly associated with the production of CDs and Blu-rays.

2.1.1.1 Injection Moulding Process

The typical injection moulding machine is composed by four major parts, as shown in Figure 2.1. The computer control unit, Figure 2.1 element 1, where the process is monitored and controlled. The machine base, Figure 2.1 element 2, housing the driving systems. The injection unit, Figure 2.1 element 3, where the polymer pallets are inserted into and plasticized to the processing temperature. And the

clamping unit, Figure 2.1 element 4, housing both sides of the mould tool and providing enough force to maintain them together during the injection of the molten polymer [89]. Importantly, the clamping and injection units are kept separate, ensuring that the mould and plasticising areas can operate at different temperatures. In the plasticising barrel, the temperature is maintained well above the glass temperature, *Tg*, of the polymer, so that the latter may flow easily when injected into the tool. The mould, on the other hand, is usually kept below *Tg*, to solidify the polymer and enhance mould release.

The injection moulding process can be subdivided into four different stages. First, plasticization, consisting of feeding the polymer pellets from the hopper, Figure 2.1 element a, to the barrel, Figure 2.1 element b, heating them above their melt temperature and driving them towards the mould cavity. The function of the reciprocating screw is not only to drive the polymer flow, but also to mix and homogenize the melt, before entering the mould cavity. Second is mould filling, where the injection unit delivers a set dosage of polymer to the mould cavity, defined by the spacing between the fixed and moving plate, Figure 2.1 elements c and d respectively. Filling dynamics are of great importance, as they control factors such as warpage, surface finish properties, and the residual stress of the final product. They are similarly critical to ensure the reproducibility between shots, as slight parameter changes may result in wide variations. The third stage is part packing and solidification, where the mould is filled with extra melt to compensate for the decreasing volume and resulting shrinkage of the solidifying polymer, as it cools down to the mould temperature. Control of this stage is critical to ensure the dimensions of the part are within design tolerances and free of residual stresses. The last stage is ejection, where the mould is opened, by releasing the clamping force, and the part is pushed outwards using ejector pins, Figure 2.1 element e. As the mould begins to close after ejection, there is already plasticised polymer ready for a new injection cycle. The whole process is fully automatic.

2.1.1.2 Part Fabrication with Polystyrene

Thermoplastic injection moulding remains almost exclusive in industry, with thermoset resins being less prominent [92]. The spectrum of thermoplastics is, nonetheless, extremely wide and diverse, due to the shear versatility of polymeric

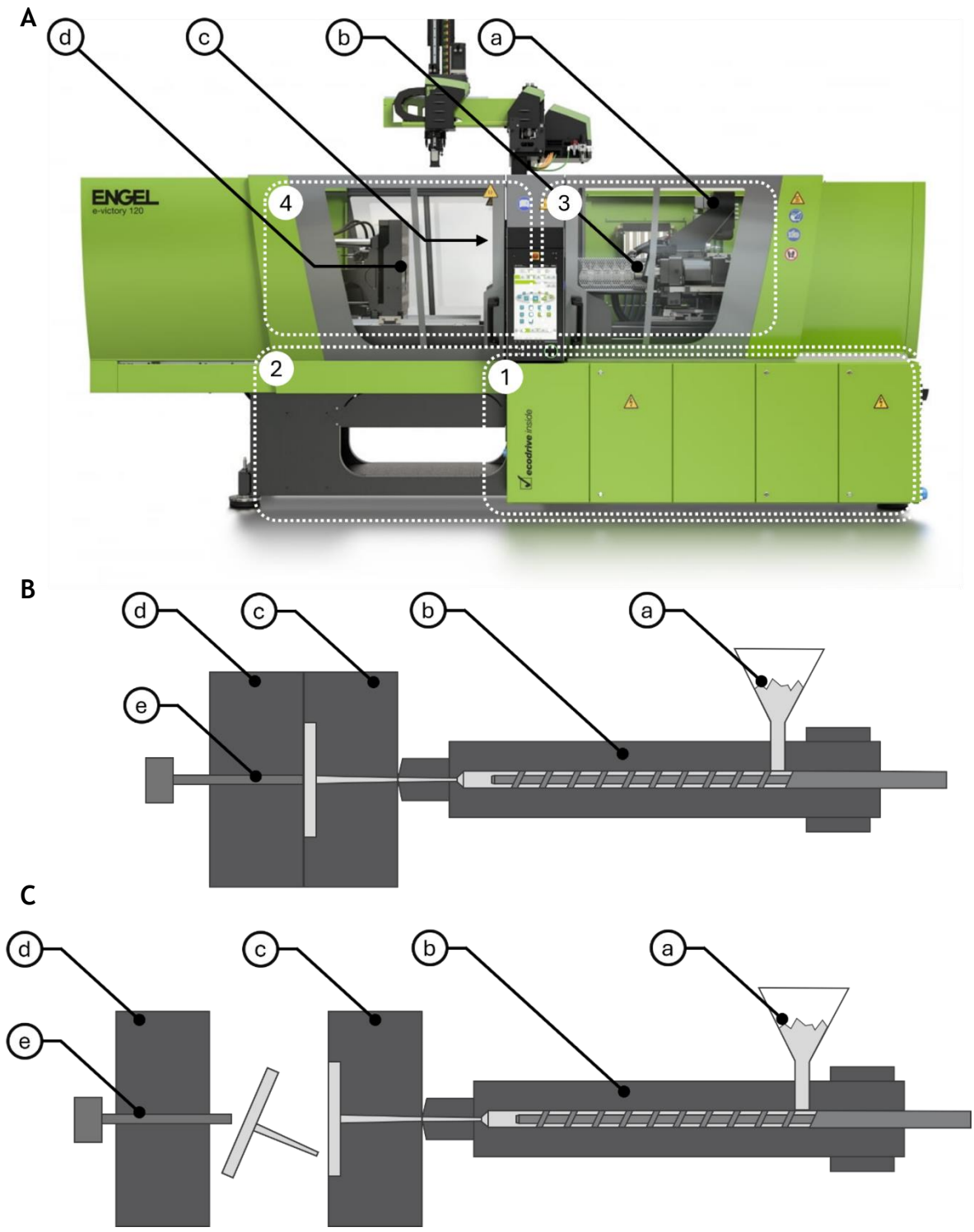

Figure 2.1: Injection moulding machine and process. A, Typical injection moulding machine, highlighting, 1, the computer unit, 2, machine base, 3, injection unit, and 4, clamping unit. The components, a, hopper, b, barrel, c, fixed plate, and d, moving plate, are also displayed. B, Mould filling stage, where the polymer melt is injected to the mould cavity. C, Ejection stage, where the cooled polymer is pushed outwards using, e, ejector pins. Image in A reproduced with permission of Engel (Engel, New Zealand) [93]. Images in B and C adapted with permission of Goodship [89].

compositions available. In the context of microfluidics, some of the most common thermoplastics include poly(methyl methacrylate) (PMMA), polycarbonate (PC) and polystyrene (PS), all biocompatible but with a different range of properties [94]. Data suggests, however, that the polymer gathering more traction within the microfluidic community is PS [95].

When it comes to microfluidic applications particularly in the context of OOC, PS is perhaps the most attractive material within the thermoplastics. This is because most of in vitro cell culture research data has been collected over the years from a PS surface, it being the standard material for life sciences and biological equipment, such as well plates, petri dishes and culture flasks [96, 97]. This way, the manufacture of microfluidic and OOC devices with PS means accessing and progressing this vast library of knowledge on cell culture, which from the perspective of a biologist, represents a far more attractive solution. When compared to PDMS, PS presents several advantages as well. For one, it is stiffer, displaying a Young's Modulus of 3 - 3.5 GPa [98] in comparison to 1.3 – 3.0 MPa of PDMS [99]. Greater stiffness translates into better channel stability under high fluidic pressure, and therefore more accurate delivery of flow and shear. PS also presents lower molecule absorption [75], making it a more suitable candidate material for drug-screening platforms then PDMS. Hydrophilization processes, such as oxygen plasma, are also more stable for PS [100] than for PDMS [101], meaning devices are more suitable for long-term studies and can be stored for longer, without any changes to their hydrophilicity. Other qualities of PS are its good chemical resistance with important solvents for sterilization of microfluidics systems, such as ethanol, isopropyl alcohol (IPA) and acetone [98], and its high optical transparency.

2.1.1.3 Mould Design and Fabrication

Mould design and material are two critical factors in injection moulding. They will directly influence the length of the production run, the quality of the product, the homogeneity across replicas, and the cost to benefit ratio of a production run. Therefore, careful consideration must be taken when designing and fabricating a mould for injection moulding [102].

During injection moulding, the mould is subject to a variety of forces. The injection pressure of the plastic inside the mould cavity generates expansion stresses. The clamping force delivered as the mould closes exerts compressive stresses. And the cyclic heat exchange between the melt and the mould causes thermal stresses. Therefore, the mould material should be considered across a variety of different mechanical properties, including yield strength, modulus of elasticity, toughness, wear resistance, thermal conductivity and thermal expansion. In industry, steel is typically the material of choice for mould manufacture. In the context of microfluidics too, steel has been used in the fabrication of moulds, traditionally using Computer Numerical Control (CNC) milling adapted to produce features on the microscale [103-105]. However, not only does CNC milling produce high surface roughness, but also significantly limit feature resolution, factors which compromise its suitability for microfluidics. Therefore, research has been exploring alternative methods to produce tooling for injection moulding microfluidics. Some of these methods and materials used in production today include the LIGA (Lithographie, Galvanoformung, Abformung, German for Lithography, Electroplating, Moulding) process [106], polytetrafluoroethylene (PTFE) backed nickel [107], SU-8 photoresist on nickel [108], SU-8 on polyamide sheets [109], etched silicon [110], etched quartz [111] and UV curable polyurethane resins [112]. Despite corresponding to an improvement in tooling quality for injection moulded microfluidics, the cost of each respective method is generally high and does not justify short production runs. For that reason, injection moulding is generally incompatible with rapid prototyping, which in itself, is a fundamental part of developmental microfluidics in both academia and industry.

2.1.2 3D Printing

Recent years have witnessed overwhelming growth in 3D printing. From public anonymity at its inception, 3D printing has reached today almost every sphere of industry and research, continuing to evolve its hardware and range of applications at an accelerated pace [113]. Part of this success is due to its accessibility, affordability and versatility in product development, truly expanding the concept of digital manufacturing to the consumer market [114].

The technology behind 3D printing dates back to 1986, when Chuck Hull pioneered the first stereolithography (SLA) apparatus, using laser scanning to selectively cure a liquid photopolymer into a 3D object, a process designated as vat polymerization [115]. What started as a technology for big industries, such as automotive and aerospace, rapidly expanded to the consumer market, with the Maker movement bringing 3D printing to the individual developer [116]. The ability to produce components based on a single digital file, with minimal labour, supervision and skill, meant the technology could be easily disseminated and democratized. Today, driven largely by consumer need, 3D printers have become smaller, cheaper and more accessible. Beyond vat polymerization, material extrusion techniques, such as fused deposition modelling (FDM), have been widely popularized. FDM is the most accessible and inexpensive 3D printing technology [117]. However, it is limited by low feature resolution and inferior surface finishes. Two-photon polymerization is the leading AM technology when it comes to feature resolution [118]. It relies on strongly focused femtosecond lasers to achieve a photochemical reaction by two-photon absorption [119]. This way, it enables feature resolution down to 100 nm, even if at the expense of print volume, throughput, and cost of equipment. Perhaps providing a middle ground between high printing quality and accessibility, liquid crystals display (LCD) 3D printing is a rapidly evolving technique within the spectrum of SLA. A typical LCD-based 3D printer is illustrated in Figure 2.2. By using an LCD screen (Figure 2.2, element a) to mask the UV light, a more compact setup is achieved, capable of shorter printing cycles and higher feature resolution [120].

2.1.2.1 Stereolithography Process

The basic elements of an SLA system are illustrated in Figure 2.2 A. They consist of a light source (Figure 2.2 b), optics (Figure 2.2 c), a resin vat (Figure 2.2 d) and a build plate (Figure 2.2 e). SLA can be described as upright or inverted, depending on printing orientation. Inverted SLA, illustrated in Figure 2.2, positions the light source below the resin vat and prints upside down. This method has proved the most successful technique over the years [121]. Not only does it provide a more efficient usage of resin, but it also enables the print size to significantly exceed the volume of the vat, despite a more compact, desktop-friendly setup.

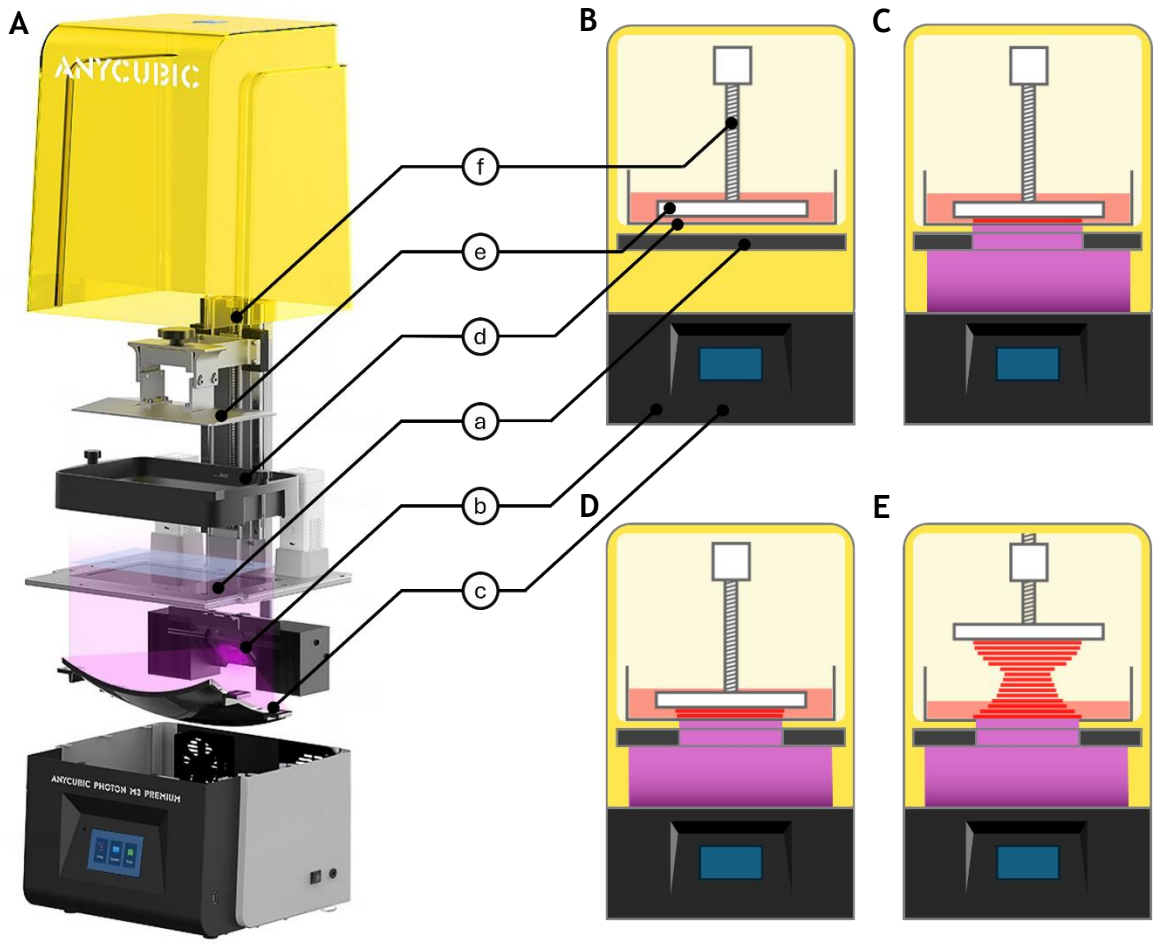

Figure 2.2: LCD 3D printer components and process. A, Exploded view of an LCD 3D printer, highlighting the, a, LCD screen, b, UV light source, c, optical collimator, d, resin vat, e, build plate, and f, lead screw. B, Beginning of the 3D printing process, with the build plate forming a film of resin against the vat, with a depth equivalent to the determined layer height. C and D, First and second layers, respectively, of the 3D component are cured, first against the build plate, and afterwards against the cured polymer. E, Last layer exposure and completion of the 3D printed component. Image in A reproduced with permission of Anycubic (Anycubic, China) [122]. Images from B to E adapted with permission of To Buy a 3D Printer [123].

The process begins by creating a 3D computer-aided design (CAD) model of the desired part, which is later converted into a stereolithography (STL) file and sliced into 2D layers, using a slicing software. After uploading the resulting file into the printer, the vat is filled with the prepolymer resin from which the 3D printed object will be created, layer by layer through photopolymerization, as illustrated in Figure 2.2 B-E. In this process, UV light (generally with a wavelength of 355 – 405 nm) provides the necessary energy dosage for polymerization to occur, selectively hardening the layer of resin corresponding to each of the planar sections of the 3D component. In a typical SLA system, controlled galvanometric mirrors direct a UV-laser beam along the predefined XY planar path [124]. Here, XY resolution is limited by the size of the laser spot. Instead, in an LCD system, a light source (Figure 2.2 b) produces UV light, which is then collimated using a curved optical mirror, designated as collimator (Figure 2.2 c), and finally masked

using an LCD screen, as illustrated in Figure 2.2 C-E. XY resolution is, this way, determined by the pixel resolution of the screen, and the resulting size of a single 3D printed voxel. During the printing process, the build plate moves vertically at the completion of each layer, as observed from Figure 2.2 B to D. This is done according to a fixed distance, designated as layer height, which allows each following layer to be cured and incorporated into the previous one. Vertical resolution is not only limited by the minimal step size achieved by the driving unit (composed by the printer's motor, motor drive and lead screw (Figure 2.2 f)), but also by the light penetration properties of the resin [125]. When all layers are completed (Figure 2.2 E), the build plate is removed, and the print is detached using a scraper.

When printing with an SLA system, there are, this way, a wide variety of control parameters to consider. One of the most important is, naturally, the energy dosage provided to the prepolymer, at each layer step, for photopolymerization to occur. This will not only determine the structural integrity of the print, but also its ability to accurately reproduce the parent CAD file. In typical laser-based SLA system, this aspect is controlled by parameters such as the fill exposure [mJ/cm^2], which regulate the energy density of the laser beam and, therefore, the amount of energy transferred for photopolymerization. In LCD systems, energy dosage is controlled instead via layer exposure. By defining the duration of UV exposure for each individual layer, it regulates the total amount of energy transferred to the prepolymer. The nature of inverted SLA setups further requires that the print remains attached to the surface of the build plate during the entire printing process. For this reason, UV exposure must be further, and separately considered for the first set of layers. This way, parameters such as early layer exposure, or bottom layer exposure, are employed in inverted SLA setups, typically meant to enhance the transfer of energy for the first set of layer, increasing photopolymerization and ultimately ensuring a secure attachment between print and build plate. Another important parameter, as it has been described already, is the layer height. This parameter defines the vertical height between each printed layer, and its implications are numerous. First, by controlling the vertical resolution, it regulates both the surface finish of side walls and the printing lead time. And second, by defining layer height, it modifies the required level of light penetration, which may come at the expense of layer exposure and ultimately

printing quality. Beyond these parameters, a multitude of others, such as the lifting speed of the build plate, lift distance, anti-alias, off-time, to name a few, are known to provide distinctive effects which should also be considered.

Once printing is finished, the printed component is known to be in a green state [126], and therefore two additional post-processing steps are required before the print is deemed functional. The first one consists of washing the print using an organic solvent, usually isopropyl alcohol (IPA), to remove any unpolymerized resin. The second consists of exposing the print to UV exposure and, additionally, thermal radiation. This final step completes polymerization and typically results on the improvement of mechanical properties [127].

2.1.2.2 3D Printed Microfluidics

Attempts to scale more conventional microfabrication techniques, particularly with PDMS, are leading to a "manufacturability roadblock" [128]. Many believe the solution lies in the integration of 3D printing, whose application in microfluidics has been steadily growing in the last decade [129]. 3D printing provides unparallel potential for rapid prototyping, with growing resolution and reproducibility. Particularly in the realization of complex geometric features, 3D printing is unmatched by more conventional techniques [130-132]. It also allows for multi-material printing, and hence a much richer range of design possibilities [133]. Finally, it is highly automated, low cost and extremely accessible, enhancing the dissemination of microfluidics [134]. 3D printing was first applied to microfluidics in the fabrication of a static micromixer [135]. The achieved degree of geometric complexity and fluidic mixing demonstrated an application otherwise not possible with more conventional methods. Further advances in two-photon polymerization allowed, 10 years later, the development of hollow 250 µm polymeric microneedles, with an inner bore diameter of 30 µm [136], Figure 2.3 A. This work further evidenced the unmatched potential of 3D printing for microfabrication. Today, there is a myriad of 3D printed microfluidic devices, as the field continues to expand. From droplet generators [137] (Figure 2.3 B) to micro-valving devices [138], gradient generators [139] (Figure 2.3 C), to systems for cell sorting [140], immunomagnetic separation of bacteria [141], DNA assembly [142] and OOC [143].

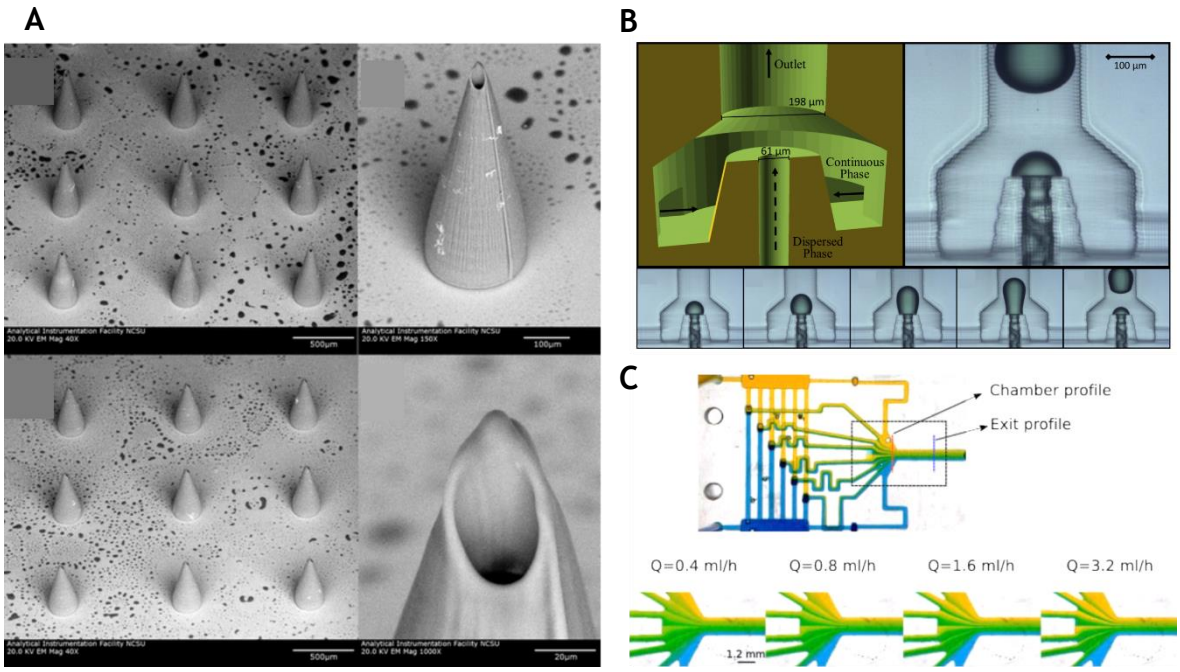

Figure 2.3: The potential of 3D printed microfluidics. A, Hollow polymeric microneedles, produced via two-photon polymerization, with a base diameter of 250 µm and an inner bore diameter of 30 µm. B, Annular, channel-in-channel, microfluidic droplet generator, featuring a 61 µm channel for the dispersed phase, produced via 3D printing. C, Flowrate-independent gradient generator device, highlighting laminar flow as a function of flow rate inside the 3D printed microchambers. Images in A reproduced with permission of Gittard et al [136]. Images in B reproduced with permission of Warr et al [137]. Images in C reproduced with permission of Cabaleiro [139].

There are, however, various factors limiting 3D printing in microfluidics. First, processes are far from being standardized. The selection of an appropriate printer, resin and processing parameters is both a challenging and time-consuming process, still object of much research [143]. Microchannel drainage remains a key challenge [134, 144] with the removal of uncured resin depending on channel geometry and non-trivial post-processing techniques. The biocompatibility of resins is as well a recurring issue, in part due to unclear guidance and lack of standardization in biocompatibility certification [145]. Finally, despite improving on more conventional techniques, 3D printing remains limited to a low throughput of approximately one chip per 1.5 hours, with post-processing considered [146]. With a scalability far from reaching industry standards and competing with processes such as injection moulding, the solution may not be to replace, but rather to combine 3D printing with injection moulding [128].

2.1.3 Rapid Tooling

The development of 3D printing introduced a new generation of tool-making techniques, often referred to as RT, or soft tooling. Such techniques enable the rapid fabrication of cost-efficient injection moulding tooling [147]. By reducing

the expenses associated with traditional mould-manufacturing processes, RT bridges the gap between injection moulding and prototyping. In this context, SLA presents perhaps the most promising and compatible 3D printing technology, providing high quality printing at an affordable cost and with thermally stable materials, given the thermoset nature of the resins employed. A general setup for the integration of rapid tooling inside an injection moulding machine can be observed in Figure 2.4, highlighting the clamping unit where a 3D printed mould is inserted in one of the metallic plates.

The compatibility of SLA for RT has long been under research [148], with an increasing number of applications surging over the years as the mechanical properties of resins also improved [149]. Nevertheless, the mechanical properties of SLA-based RT still present several drawbacks that need consideration. For one, tool life is significantly affected, with RT only being capable of sustaining small batch productions (< 10 000 cycles [147]) and often presenting significant mould and feature damage before 100 cycles [150]. Several factors contribute to the inferior tool durability, including a lower yield strength, tensile strength, and modulus of elasticity, when compared to more traditional injection moulding tooling. Second, the low thermal conductivity inherent to AM resins means SLA-based RT essentially act as insulators, reducing the ability to transfer heat and substantially increasing cycle time. Not only does the slower cooling rate compromise scalability [151], but it also contributes to higher part shrinkage, due to an increased level of polymer crystallinity [152]. These factors combined yield a reduction of process parameters when injection moulding with SLA-based RT. Lower injection speed and pressure, as well as decreased mould temperature and longer cooling time are critical parameters in ensuring extended tool life and successful moulding [151]. Nonetheless, the mechanical properties of parts moulded from an SLA-based tool or a metal mould have been investigated to suffer no significant changes [153]. The true value of transitioning to SLA-based RT lies, however, in the optimization of production costs and lead time [154]. A much lower investment in tooling translates in a wide decrease of production costs, up to 80 - 90% when compared to more traditional mould-manufacturing techniques [147]. Similarly, the lead time for tool fabrication is greatly reduced [155]. This

way, product development is highly streamlined, due to the increased prototyping capacity enabled by AM techniques.

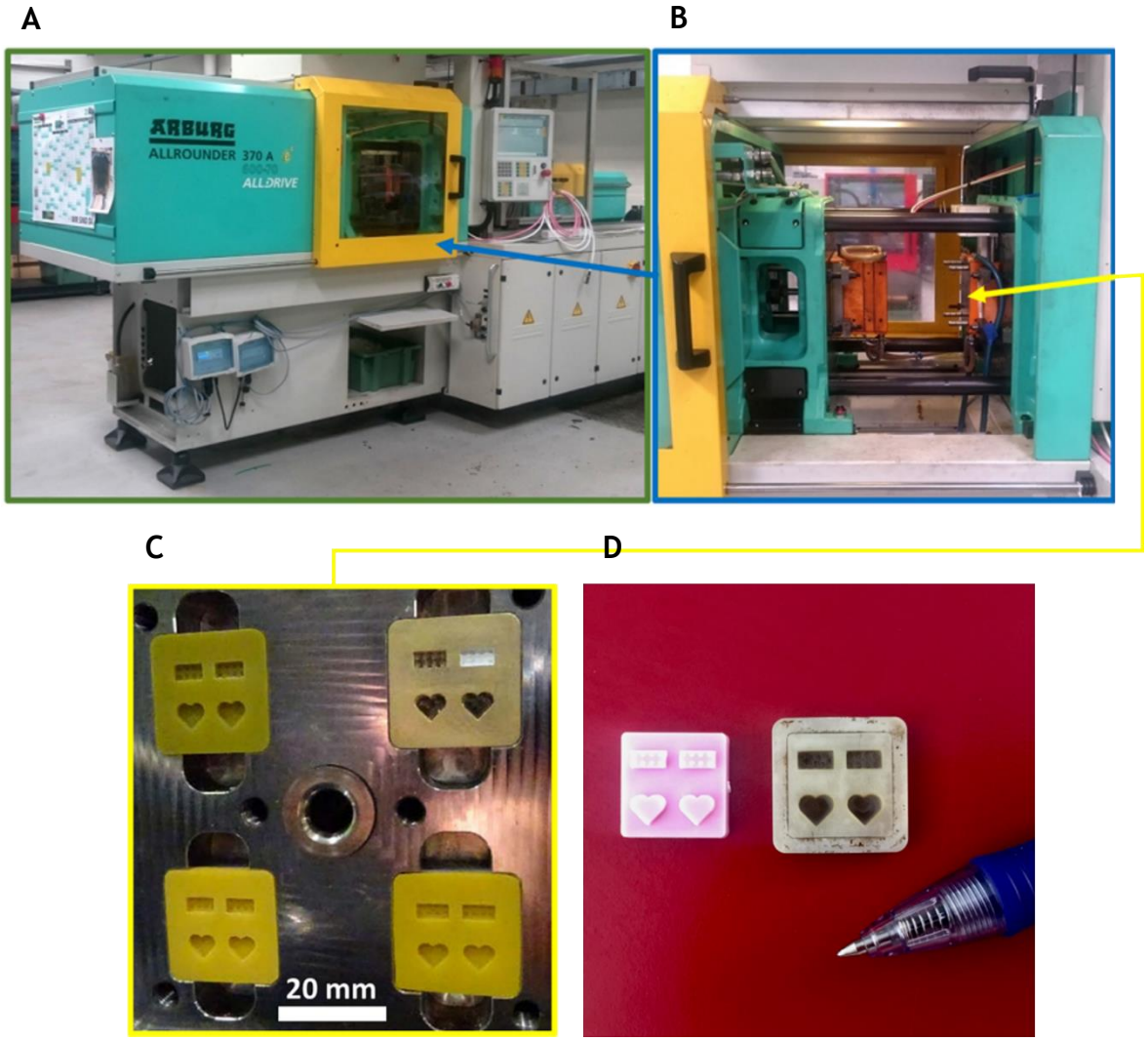

Figure 2.4: A rapid tooling (RT) setup. A, Injection moulding unit. B, Clamping unit open. C, 3D printed tooling inserted into the metallic plate. D, Injection moulded part, on the left, and 3D printed mould, on the right. Images reproduced with permission of Tosello et al [147].

2.1.3.1 Rapid Tooling for Microfluidics

The pathways enabled by RT hold great potential in microfluidics [156]. The value lies in the complementary properties between AM and injection moulding. By using AM in the production of microfluidic RT, issues associated with the biocompatibility of resins and channel drainage are bypassed. Furthermore, RT provides a pathway to realize the complex geometries enabled by AM in a scalable manner. On the other hand, RT brings accessibility and affordability to the fabrication of microfluidic tooling for injection moulding. This way, it makes injection moulding compatible with rapid prototyping, a feature otherwise not possible. Despite presenting an attractive route in the production of cheap and

scalable thermoplastic microfluidics, very limited work has been done towards optimizing RT processes. An interesting approach is, however, presented by Convery et al [156], evidencing the benefits of RT for microfluidics. A commercial SLA printer is explored in the fabrication of moulds, which can be inserted into a metal frame and further fixed onto an injection moulding machine. This describes an efficient setup, capable of accessing the scalability properties of injection moulding, as well as enabling the quick and simple interchange between different 3D printed tooling. Ultimately, it enables rapid prototyping as well as high-volume fabrication. Perhaps the most impressive aspect of this work is the associated lead production time, requiring less than 6 hours to go from a CAD file to a fully functional microfluidic device, whose biocompatibility was verified by culturing organoids.

2.2 Integrated Thermoplastic Microfluidics

Following microfabrication, there are various processes to consider in order to fully functionalise a microfluidic device [157]. Referred to as back-end processes, given they occur during the final stages of microfluidic device integration, these steps play a critical role in determining both the overall manufacturing cost and the performance of the final device [158]. However, back-end techniques are often neglected by the microfluidic research community [159].

Despite the previously mentioned drawbacks, microfabrication with PDMS comes with a well-established range of back-end techniques. Due to its elasticity and conformal properties, PDMS can be easily sealed to itself and other substrates, such as silicon, glass or plastic, without the need for any additional adhesives [159]. Furthermore, sealing properties can be tuned to be either reversible [160], upon natural conformal contact, or permanent [161], after adequate surface treatments, a quality which is desired for different microfluidic applications. Similarly, its conformal properties make PDMS extremely suitable for reversible, press-fit connections with fluidic tubing [159]. Not only does this simplify the integration of fluidics, but it also allows for a higher degree of inlet/outlet (I/O) ports complexity. More so, such connections have been investigated to withstand pressures up to 700 kPa, demonstrating a secure and reliable fluidic interface [162]. The incorporation of porous membranes, essential in both chemical and biological applications [163], is also facilitated using PDMS. Not only does it enable

the quick integration of commercially available membranes, but also the in-house manufacture of PDMS-based membranes, either as a part of the fabrication process or in situ [164]. Finally, its tuneable elastomeric properties enable the easy integration of pneumatic valving and pumps. Quake et al. first introduced the concept of a "microfluidic processor" with the large-scale integration of individually activated valves and microfluidic channels, effectively establishing the microfluidic analogue to a random access memory [43]. Figure 2.5 provides a good example of large microfluidic integration, with multiple tubing plugged into the PDMS substrate and providing flow to the many individually sealed microfluidic channels, multiplexed via a series of pressure-driven valves. This way, a complex microfluidic platform is produced for *in situ* click chemistry, able to carry out 1024 reactions in parallel with reduced reagent consumption and increased screening efficiency [165].

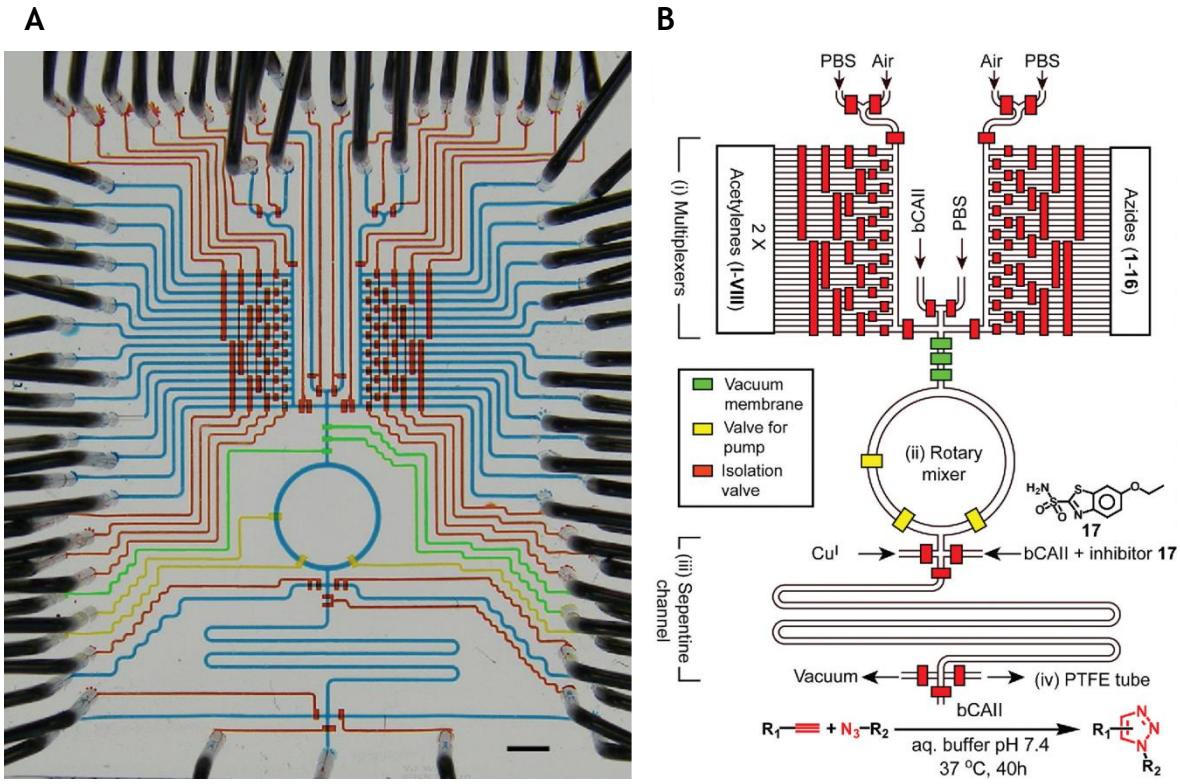

Figure 2.5: Large-scale microfluidic integration. A, 2nd generation integrated microfluidic platform, developed by Wang et al, incorporating multiple microfluidic channels, individually connected to flow and multiplexed using a series of pneumatic valves. Scale bar corresponds to 3 mm. B, Circuit schematics, identifying the various fluidic sections, inlets, valves, multiplexing channels, mixers and outlets, defining a platform for *in situ* click chemistry supporting 1024 chemical reactions in parallel using phosphate-buffered saline (PBS) media and bovine carbonic anhydrous II (bCAII). Images reproduced with permission of Wang et al [165].

The back-end problem is aggravated when transitioning to non-PDMS microfluidic devices. Thermoplastic materials, such as polystyrene, are generally non-conformal, meaning that the bonding procedure becomes more challenging, usually requiring advanced sealing strategies. Common techniques employed to irreversibly seal microfluidic systems include thermal fusion bonding, ultrasonic welding, and adhesive-based approaches [166]. The same techniques can also be adapted to bond porous membranes into a bilayer microfluidic setup. The non-conformal properties of thermoplastics also affect the connection to external microfluidic tubing and pumps. Both reversible and permanent solutions exist, using for instance PDMS gaskets, flanged tubing, magnetic connectors, adhesives, solder or epoxy [159]. However, these solutions are far from being standardized and often lack practicality. Luer Lock and Luer Cone are some of the few standards for fluidic interfacing. However, these are neither suitable with the majority of applications nor compatible for most of the fabrication techniques [159]. The integration of pneumatic valving is an even more challenging topic, with rigid thermoplastic-based solutions being scarce [167]. More common approaches either rely on integrating a soft membrane [168], made from a different material, or manufacturing a device exclusively out of thermoplastic elastomers [169].

This section will address the state-of-the-art of back-end technology for thermoplastic microfluidic integration. It will be divided into three main sub-sections, focusing on bonding and sealing, fluidic interfacing and valving integration. In the topic of sealing, adhesive-based approaches, ultrasonic welding and thermal bonding will be explored as viable solutions in bonding microfluidic channels and porous membranes. Fluidic interfacing will explore popular approaches to establish tubing and open-well fluidic connections. And finally, valving integration will identify existing mechanisms and solutions for fluidic valving in thermoplastic microfluidic systems.

2.2.1 Bonding and Sealing

The functionalization of microfluidic devices typically begins with a bonding stage. A successful seal should ensure: the confinement of solvents, reagents and media in defined volumes, without leakages; the minimization of evaporation; the reduction of contamination and biohazards; and the protection of sensible structures against external factors [159]. Depending on the device's application,

the bonding stage might consist of sealing the channels to a cover layer, or to other microfluidic layers. More so, bonding techniques can also be extended to incorporate other physical components, such as porous membranes, towards achieving more elaborate fluidic, chemical and biological functions and patterns.

There are several sealing strategies available which, depending on the requirements for channel complexity, component integration and material selection, are differently suitable. Adhesive layer, ultrasonic welding and thermal fusion are some of the most popular techniques to bond thermoplastic microfluidics. Each method presents very distinctive characteristics which will be reviewed in the following.

2.2.1.1 Adhesive Layer

Adhesives can be generally split into two categories: dry and liquid. Dry adhesives are more popular in the form of pressure sensitive double-sided tape. They represent a low-cost technique, capable of providing a strong, reliable bond, without any chemical or thermal treatments. They are easy to assemble and compatible with rapid fabrication methods, like laser cutting and xurography [166]. Pressure sensitive double-sided tape is also commercially available in different thicknesses, material composition and adhesive strength [170], typically presenting good optical transparency [171] as well as biocompatibility [172]. Finally, adhesives are also gas permeable, meaning they can compensate the impermeable nature of thermoplastic polymers, a critical factor for cell studies [173]. Liquid adhesives, on the other hand, are applied to the microfluidic substrate and form a strong bond after curing [174]. The curing process can be achieved either through evaporation of solvents or through chemical reactions, induced via thermal or UV exposure [157]. Liquid adhesives are also commercially available with different properties, most of which being optically transparent and many biocompatible. Furthermore, they enable both permanent [175] and reversible bonding [176].

Both dry and liquid adhesives are common techniques in the bonding of thermoplastic microfluidics. They have been used to seal channels in PMMA [177], PS [178], PC [179], cyclic olefin copolymer (COC) [179], cyclic poly(ethylene terephthalate) (PET) [178], and polyformaldehyde (POM) [180], for instance.

Pressure sensitive double-sided tape has further been used to form the microfluidic channels themselves, being sealed at the top and bottom using laser printer transparency film [181]. Membrane integration too, has been achieved using both dry and liquid adhesives. Systems emulating the bone marrow [182] and lung airway [172] have been reported by using porous membranes integrated using pressure sensitive double-sided tape. Similarly, an epoxy-based adhesive was used to bond a nanopore PC membrane to PMMA-based microfluidic devices, using contact printing [183]. Despite their versatility, the application of adhesives tends to share a common downside, associated with being more labour intensive, time-consuming, and less reproducible [170].

2.2.1.2 Ultrasonic Welding

Ultrasonic welding is one of the leading bonding processes in industry, with applications ranging from commodities to the automotive industry, electronics, packaging, and the medical sector [184]. The process generates a permanent joint by plasticising the contact surface asperities via induced vibrational friction heating [185]. This results in a strong and stable weld, once the vibration stops, the joint is cooled, and the pressure is released. An ultrasonic welding machine typically consists of five main components, from which: a power supply, to convert the mains current into kHz-range electrical energy; a piezoelectric transducer, that converts the electrical signal into low amplitude (2.5 – 250 μm) high frequency (20 – 40 kHz) mechanical vibration; a booster, which amplifies and shapes the vibrations; a sonotrode, or welding horn, that applies pressure and transmits the welding energy onto the parts to be fused; and a fixture, or anvil, which prevents the parts from moving during the welding procedure [186]. One advantage of ultrasonic welding is that the equipment required is relatively unexpensive [186]. Another advantage is that the process enables to specifically tailor the weld line. This is achieved by adding protruding features, highlighted in red in Figure 2.6 A and designated as energy directors, which concentrate the ultrasonic vibrations and localize the melting, creating a kind of glue which, once solidified, fuses the contact surfaces together. The usage of energy directors works both to localize the welding and increase its reproducibility [187]. Perhaps the most attractive quality of ultrasonic welding is, however, its scalability. With a characteristic cycle time on the order of a second [188], ultrasonic welding is an extremely high-throughput procedure, suitable for mass production. Finally,

the process is also compatible with a vast range of polymers, further enabling the bonding between different thermoplastic materials that present similar molecular structures and melting temperatures [189].

Ultrasonic welding is also a well-known technique to bond thermoplastic microfluidics [166]. Truckenmuller et al first demonstrated the effective usage of ultrasonic welding to bond microfluidic components [190]. In this case, PMMA and polyether ether ketone (PEEK) were used in the development of a micropump. Zhang et al developed the technique and the usage of energy directors further to weld PMMA-based microfluidic chips, describing a method with high bonding strength and low channel deformability [191]. Kistrup et al, on the other hand, innovated by using the energy directors not only for bonding, but also for the self-alignment of microfluidic chips made from COC [187]. Convery et al. further investigated the dimensions of energy directors in PS-based microfluidic chips as a function of the sealing success and the added height [156] (Figure 2.6 B and C). For that, Ng et al described a setup including dual fixtures and an insert to avoid the flow of molten polymer and create a free conduit to plug microfluidic tubing [186]. The integration of porous membranes onto microfluidic channels has also been successfully achieved using ultrasonic welding [192], despite having limited applications. Runge et al used ultrasonic hot embossing to create the microfluidic channels in a PC substrate, and ultrasonic welding to then integrate a PC porous membrane onto the respective channels and finally seal them against a PC lid [193].

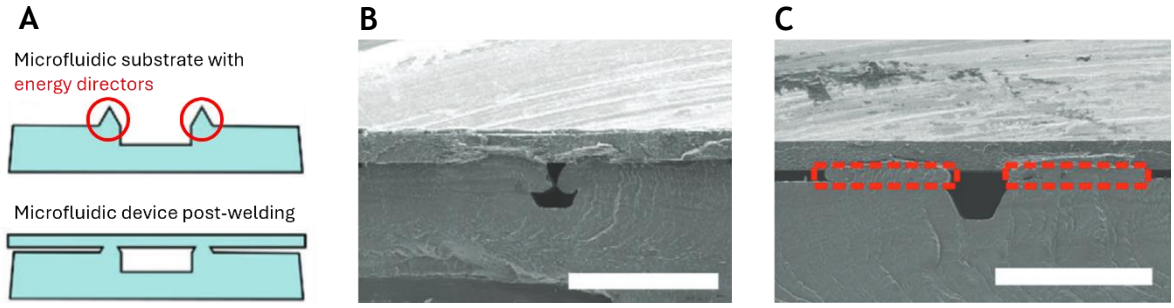

Figure 2.6: Energy directors in microfluidic bonding with ultrasonic welding. A, Illustration representing the geometrical aspect of energy directors, highlighted in red, and their effect on channel geometry post-bonding. B, Oversized energy directors constricting microfluidic channel post-welding. C, Optimized energy director size and offset, minimizing their effect on microchannel geometry. Scale bars in B and C correspond to 1 mm. Images adapted with permission of Convery et al [156].

2.2.1.3 Thermal Fusion Bonding

Thermal fusion bonding consists of heating the substrates near or above *Tg* while applying high pressure to ensure optimal mating contact. This leads to flow of polymer at the contact interface between the substrates, with the interdiffusion of polymer chains forming a strong bond between the mating surfaces after cooling [174]. Under optimal temperature and pressure, the achieved bonding strength can reach the cohesive forces of the bulk material. The equipment for thermal fusion bonding typically consists of two levelled plates, operated by a pneumatic or hydraulic system, to deliver uniform pressure and ensure ideal contact between the two surfaces. Optimally, both plates have a heating element, so that temperature is uniformly distributed across the two mating components, to therefore enhance bonding and avoid the creation of residual stresses. Nevertheless, the complexity of the setup may vary according to the bonding requirements of different materials and applications. This way, simple low-pressure clamps and convection ovens can also be employed towards achieving thermal fusion bonding [192]. The simplicity of the approach and the relatively unexpensive equipment required, are major advantages of thermal fusion bonding. More so, the technique is effective with a vast range of polymers, and it can also be readily applied to bond dissimilar materials [174]. Despite being dependant on the heat transfer rate of polymers and therefore limited to relatively long bonding cycles [95], thermal fusion bonding is a scalable procedure, with the increase of surface area for heat pressing allowing the parallel bonding of multiple components in a single cycle.

These characteristics make thermal fusion bonding the most popular method for sealing thermoplastic microfluidic devices [174]. Successful bonding has been achieved with microfluidic structures made from PC [194], PMMA [195], polylactic acid (PLA) [196], COC [197], PS [198], and more [166]. Nevertheless, the necessity to heat thermoplastic substrates above their *Tg* very commonly leads to channel deformation and, more severely, clogging [95]. Therefore, a great deal of work has been done towards optimizing the bonding parameters, such as temperature, pressure and time, for each different material and application. Alternative methods have also been proposed towards reducing the bonding temperature and pressure, and hence the likelihood of channel deformation. Such methods rely, for instance, on the exposure to UV light or oxygen plasma prior to bonding. UV

light breaks polymeric chains at the surface level, therefore reducing the required bonding temperature whilst increasing the resulting bonding strength [195, 199]. Similarly, by making the surfaces hydrophilic, oxygen plasma has been shown to reduce the bonding time, as well as the required temperature and pressure, ultimately reducing channel deformation [200]. Beyond channel bonding, thermal fusion has also been successful in the integration of porous membranes. Wang et al described a two-step bonding procedure for the integration of a PC porous membrane into a PMMA-based microfluidic device [201]. Kappings et al further reported the incorporation of customizable ion-tracked PC membranes onto a PC substrate via thermal fusion [202].

2.2.2 Fluidic Interfacing

Defining a reliable fluidic interface between device and peripherals, such as tubing and pumps, is an important factor in the functionalization of any microfluidic device. Despite compromising performance, usability and overall cost, the integration of fluidic interconnects is an often-neglected problem [159]. There are several characteristics a fluidic interconnect should present, which include: provide minimal dead volume; be removable, reusable and easy to plug; be low-cost and small, to allow for high density connections; present a reliable seal for a wide range of flow rates; be chemically inert and avoid cross-contamination of samples. A wide variety of fluidic interconnects have been developed, even though most are application specific. A few fluidic interfaces are considered to be standard, notably the Luer Lock and Luer Slip. However, these are not readily compatible with most microfabrication techniques [159]. There is, therefore, no universally compatible fluidic interface, a factor which, most often, compromises microfluidic development.

This subsection will delve into the current state-of-the-art of fluidic interfaces compatible with thermoplastic microfluidics. The techniques presented are subcategorized into tubing interconnects and open-well solutions, and their unique characteristics will be described.

2.2.2.1 Tubing Interconnects

The simplest approach to reversible tubing connections is via the direct insertion of tubing. This implies, however, the existence of a structure, such as a well or a coupler, which enables the press-fit connection of external tubing. Harrison et al described a practical solution to this problem, consisting of drilling a hole at the ends of each channel, effectively creating a well capable of interfacing with capillary tubing [203]. The use of an adhesive layer is also a popular approach towards obtaining a permanent bond directly with fluidic tubing [209], or with connecting components, such as custom-made PDMS interconnects [204] or other standardized components. Perhaps a more sophisticated and standardized approach to reversible tubing connections are the Luer Lock and Luer Slip interfaces. These represent, today, the closest to a standardized interconnect within microfluidics. Despite their acknowledged mechanical and operational robustness, Luer connections have a relatively large footprint. Not only does this lead to undesired dead volumes, but also compromises their integration with systems of high microchannel density. To address this challenge, Etxeberria et al investigated Luer Slip connectors and developed a protocol towards downscaling them [205]. Work on integrating Luer connectors has also been described using ultrasonic welding [206] and monolithic construction via 3D printing [207].

2.2.2.2 Open Well Solutions

Perhaps the most primitive method is, however, the simple creation of wells and the manual loading of media. Despite, or due, to its simplicity, it is a frequently used method [208] whose popularity has been growing recently, particularly in the field of organ-on-chip [209]. The reduction of operation complexity and peripheral's footprint is critical in the field, with a simpler interface representing a far more attractive solution [210]. Before being used, open well-based solutions need to be primed, a process which most users consider constraining [208]. By forcing media in, it is intended to clean the channels from micro-particles and fibres that may have been accidentally introduced through the open wells. Wetting the channels also aims at avoiding air-liquid interfaces from inducing undesired capillary pressure and blocking flow from occurring naturally.

In its simplest form, well-based solutions yield one-off, unidirectional flow. A first example of this was provided by Harrison et al in 1992, where ultrasonically drilled holes enabled electroosmotic flow and capillary electrophoresis for sample separation [15]. One-off, unidirectional fluidic approaches do not allow, however, for continuous operation. This led to the development of various new approaches, using platforms for rotation, 2D and 3D tilting, to obtain continuous flow. Yang et al developed a gravity-driven cell culture chip, which not only allows for simple one-off, unidirectional flow, but also automated, continuous, bidirectional flow, when incorporated with a custom-made rotating platform. When it comes to scalability, automation and physiological versatility, *Mimetas* has been leading the market with their recently developed *OrganoPlate*® product family [211]. These comprise of four different channel designs, each addressing a specific target microenvironment. A custom-made 96-well plate format is further used, pairing up with *Mimetas*' own fluidic interfacing environment for 2D tilting and automated, continuous, bidirectional flow. Another interesting approach was developed by Busek et al, comprising of a pumpless, recirculating organ-on-chip (rOOC) platform [212], Figure 2.7. This work described the usage of continuous pitching and rolling (Figure 2.7 A) and closed-loop channel designs (Figure 2.7 B),

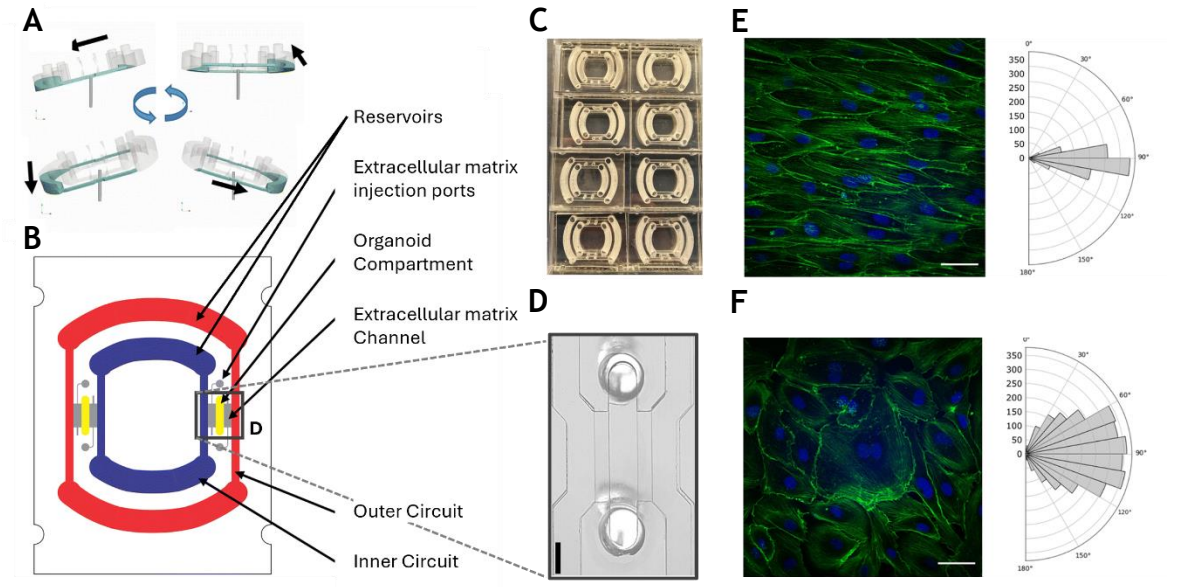

Figure 2.7: Open well fluidic interfacing for gravity-driven flow, with the rOOC platform. A, Continuous pitching and rolling to generate pumpless, recirculating flow. B, General layout of the rOOC platform. C, Several rOOC devices produced using PMMA. D, Higher magnification view of the organoid compartment (centre) and perfusion channels (outer). Scale bar 1 mm. E, Culture of endothelial cells in the rOOC platform evidencing the alignment of actin filaments (green) and nuclei (blue) as a function of flow and shear, this way providing greater resemblance with *in vivo* conditions in large blood vessels. Scale bar 50 µm. F, Culture of endothelial cells under static conditions evidencing significant morphological changes with low cell elongation and thus poorer resemblance with *in vivo* conditions. Scale bar 50 µm. Images adapted with permission of Busek et al [212].

to generate gravity-driven, unidirectional, pulsatile flow. The fluidic pattern generated, as well as the recirculation of cell-produced factors, was argued to contribute to greater physiological relevance. In Figure 2.7 E, it is demonstrated how the exposure to unidirectional flow contributed to the greater elongation and alignment of endothelial cells when compared to static conditions, Figure 2.7 F. By replacing tubing and pumps with a simple 3D tilting platform, this platform simplifies operational requirements, whilst enabling automation, scalability and customized fluidic performance.

2.2.3 Valving Integration

Microfluidic valving is subcategorized into passive and active. Passive valving relies either on internal moving components, designated as mechanical valving, or capillary pressure, non-mechanical valving, to determine the threshold between the on and off states of the valve [213]. Non-mechanical valves are a particularly popular element within microfluidics, as their integration does not require any external component or multiple-layer design, and relies solely on surface tension, contact angle and channel shape. Despite their value and relevance in a wide range of microfluidic applications [214], they present a limited degree of complexity. Active valving, on the other hand, relies on external energy sources, such as electrostatic, electromagnetic, thermal, hydraulic or pneumatic, to control the deformation of a boundary and determine the on and off states of the valve [215]. This way, they enable much greater fluidic control, from which elements for fluidic switching, pumping, and logic may be constructed [216]. This comes, naturally, at the expense of manufacture and operational complexity.

The integration of active fluidic valving has always been a core challenge and aim of microfluidic technology [6]. This ambition stems from the early parallelism between microelectronics and microfluidics, with a true fluidic valve presenting the same fundamental potential to that of a transistor in integrated circuits. PDMS and soft lithography were precursors to a wide surge of innovations in the field, one of which was the mass-scale integration of active fluidic microvalving. The work of Thorsen et al in 2002 pioneered the field by exploring the elastomeric properties of PDMS in the integration of thousands of micromechanical valves and hundreds of individually addressable chambers [43]. The result was a seminal device, operated by a multiplexing system capable of bestowing unparalleled

processing power, defining the microfluidic analogue to a random-access memory. Ultimately, this device was a powerful demonstrator of the pathways enabled by PDMS and soft lithography in microfluidic large-scale integration. Genomics, proteomics, chromatography, protein synthesis, chemical and biological mass screening, are some of the applications enabled by microfluidic large-scale integration systems [217].

2.2.3.1 Active Valving Integration with Rigid Microfluidic Substrates

One of the challenges behind the transition to thermoplastic materials lies exactly in overcoming their rigidity towards finding an alternative route to the integration of active microfluidic valving. Pantoja et al described a viable solution, reporting the fabrication, operation and performance of microfluidic valving made entirely of acrylic [167]. Both the channels and membrane layers were fabricated using a 3D milling machine, whose vertical resolution enabled obtaining a 100 μm thick membrane. Bonding was achieved via solvent-assisted thermal bonding, while using PDMS patches to protect both the membrane and valve inlet from being affected by the solvent. The valve set-up was finalized by gluing the coupler and external pneumatic tubing to the membrane chamber. The described methodology established valving capable of closing and resisting forward liquid pressures up to 17 kPa. A similar but perhaps simpler approach was proposed by Zhou et al, reporting a microfluidic device with integrated valving made entirely of PS [218]. The manufacturing procedure consisted of machining the microfluidic channels onto the PS substrate and sandwiching a 25 μm-thin PS film in between using solvent-assisted thermal bonding. Leak-free valving was described for applied pressures below 41 kPa.

Another approach, and perhaps the most common with thermoplastics, lies in integrating a soft membrane within a rigid device. Various solutions have been reported, using membranes made from PDMS [168, 219], PET [220], Viton [221], thermoplastic polyurethane (TPU) [222] and fluorinated ethylene propylene (FEP) Teflon [223], sandwiched between layers of PMMA, COC and PC. Despite describing an arguably more complex manufacturing procedure, generally involving a higher number of steps and often additional surface chemistry treatments, the resulting platforms are capable of higher fluidic pressures, up to 800 kPa [224]. A practical advantage of this hybrid approach comes with plug-and-play arrangements, such

as the one described by Shaegh et al [222]. This work reported the fabrication of PMMA channels integrated with a TPU elastic membrane, which can be developed as off-the-shelf valve and pump components for easy integration with thermoplastic microfluidics. Describing a similar plug-and-play approach but in a different setup, Au et al developed 3D printed membrane-based valves with Luer connectors for fluidic and pneumatic interfacing [225], Figure 2.8 A to C . The big advantage is that the valve can be easily manufactured with a 3D printer, requiring little labour and expertise, and interfaced with virtually any microfluidic device. This way, digital manufacturing is used to produce a user-friendly interconnect for microfluidic automation.

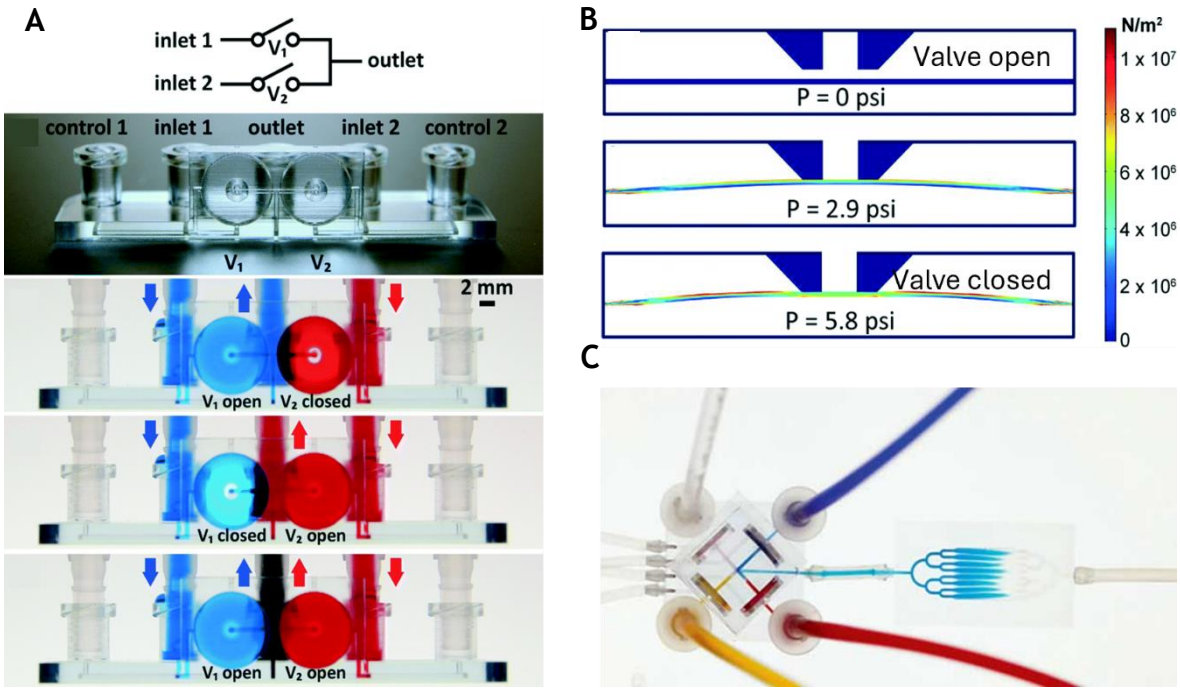

Figure 2.8: 3D printed two-valve pneumatic switch. A, two-valve pneumatic switch, with an illustration of the circuit diagram at the top, the 3D printed component below, and then three individual fluidic states. In B, finite element modelling using COMSOL Multiphysics demonstrates the working principle and operational pressure of the respective 3D printed valve, as seen from a top view. A four-valve switch is further demonstrated, C, evidencing its potential to be easily interfaced with microfluidic device of various kinds. Figures are reproduced with permission of Au et al [225].

2.3 Numerical Modelling of Microfluidics

Numerical modelling methods generally rely on algorithms to solve partial differential equations (PDEs) describing physical, chemical and biological phenomena [226]. The complexity of these PDEs usually means their solution would be virtually impossible to calculate using analytical approaches. For this reason, numerical methods stand as extremely powerful and valuable tools in predicting the behaviour of real-life systems, *in silico*. They also provide

unparallel potential in the design of complex, multiphysics systems, lowering the costs and increasing the efficiency of optimization processes [227].

Numerical modelling is based on the discretization of time and space to solve PDEs, which most frequently implies implementing mesh-based approaches [226]. These approaches consist of prearranging the spatial domain into various, smaller, discrete divisions, known as finite elements. The discretization of space allows the application of simpler polynomial functions to describe the physics associated with each finite element. When composed together into a collective mesh, it enables the calculation of an approximate solution to the real system. The accuracy of the obtained solution increases as the mesh is refined further into smaller elements, resulting in a more precise representation of the true topographical environment. One of the most popular mesh-based approaches is FEM. This technique was founded in the 40s [228, 229] and, since then, has been extensively used transversally across engineering, as well as in various fields of applied sciences. Microfluidics is no exception, with FEM providing a powerful tool not only to investigate fluid dynamics, as a means for Computational Fluid Dynamics (CFD) [230], but also to explore the multi-physics nature of microfluidic devices, for example in regard to mass transfer, thermodynamics, electromagnetics, acoustics, solid mechanics and particle tracing [231].

This section will discuss the basic principles of FEM as well as introduce some of the most relevant solvers in the field of microfluidics. More so, the applicability of FEM in the analysis of fluid flow and mass transfer, as well as in the design optimization process of microfluidic devices will be explored and reviewed.

2.3.1 Finite Element Method

PDEs form the most accurate and complete mathematical descriptors for physical phenomena. For instance, a fluidic field is fully defined according to the balance of mass, momentum and total energy, which in turn is described by the set of PDEs composed by the continuity, Navier-Stokes, and total energy equations [232]. However, the mathematical accuracy of PDEs implies a very strict formulation, making it virtually impossible to find a closed form solution via purely analytical methods. The strength of numerical methods, such as FEM, lie not in finding the

exact solution, but rather in providing a numerical approximation to the system of PDEs, with a controllable and reasonable degree of accuracy.

A physical system defined by PDEs and subjected to constraints, also known as boundary conditions, is designated as a boundary value problem. A boundary value problem is said to be in its strong form when it requires the satisfaction of the PDEs for all points in the physical domain, as well as the satisfaction of the boundary conditions for all points in the boundary domains [233]. The weak form, on the other hand, is obtained by integrating the strong form over its domain and multiplying it by a test, or weight, function. The weight function is critical in ensuring there is a set number of solutions to the integral [234]. Ultimately, this relaxes the requirements for the boundary value problem by implying the existence of an interval of solutions to the problem, whose accuracy increases as the value of the weight function approximates 0. The integral nature of the weak formulation allows for further important adaptations, especially in the realm of discontinuous domains. The principle behind FEM lies exactly in proceeding with a step further in the discretization of the spatial domain. This way, instead of looking for a solution in a continuous domain, the analysis is carried out in a finite number of non-overlapping subdomains, or elements. This is known as the Galerkin approximation. Each element is further connected to one another via nodal points, or nodes, collectively forming a mesh. The solution within each element is then calculated using shape, or interpolation functions, usually of low polynomial degree, which provide the contribution weight of each node for the solution in analysis [235]. This way, the approximate solution provided by FEM converges to the exact solution as the number of finite elements grows. This is known as the completeness requirement of the function space.

A typical FEM numerical routine consists then of the following. First, the spatial domain is discretized into a mesh, composed of several finite elements. Second, the boundary conditions are defined together with the governing equations, corresponding to the appropriate set of PDEs to the multiphysics system in analysis. Each element is then analysed individually, and their associated integral calculated. The final step is the assembly, where the individual contributions of each element are summed together into a single global output, as the FEM converges into the desired solution to the boundary value problem [236].

2.3.2 Microfluidic Simulation using the Finite Element Method

FEM is an extremely powerful tool to study the multidisciplinary nature of microfluidic devices. It allows studying and optimizing the performance and functionality of devices, as a function of design and operational parameters, before they are manufactured, saving time, resources and cost [237]. This way, FEM accelerates innovation and enhances the functionality and relevance of microfluidic devices for biomedical research and diagnostics. More so there is a wide variety of commercially available software for FEM, with distinct solver properties and application purposes [236], making it a widely accessible tool as well. COMSOL Multiphysics is one of the commercially available solvers, specifically designed for the analysis of multi-physics problems. It incorporates several different modules, each designed to simulate a specific physical phenomena, such as fluid mechanics, thermodynamics, solid mechanics, acoustics, electromagnetics, chemical engineering, particle tracing, and many more. This enables the addition of any of these modules to any solution, for a more realistic simulation. Such approach sets it apart from the remaining commercially available FEM solvers and makes COMSOL particularly relevant in expressing the multiphysics nature of microfluidics [238].

2.3.2.1 Fluid Flow, Mass Transport and Design Optimization

Control over fluid flow and mass transport are two fundamental aspects in any microfluidic application. Fluid flow determines velocity fields, pressure gradients, and shear stress. It also regulates the advective delivery of soluble molecules and compounds which, associated with their respective diffusive properties, define mass transport, mixing and concentration gradients. Underlying these properties is geometry, critical in determining the functionality of microfluidic devices by modelling flow and transport. Numerical approaches, and particularly FEM, provide unparalleled power to analyse these intricate dependencies in a cost- and time-effective manner, reducing waste, and upping the analysis to a level of detail unattainable through experimental methods [231, 237]. Some of its most popular applications include the design and optimization of fluidic micromixers [239-241] and gradient generators [242-244], where the unique mixing properties of systems at low *Re* number are explored and harnessed [245, 246]. Droplet formation [247], shear stress distribution [248, 249], and particulate filtering [250], are other

aspects of microfluidics systems often addressed and optimized using FEM approaches. Finally, the integration of porous membranes within microfluidic systems and the investigation of control parameters as a function of fluid and transport kinetics is another popular topic of research with FEM.

2.3.2.2 Porous Membranes

Porous membranes have become essential components in a wide range of microfluidic applications over the years, from chemical to biological engineering. By establishing a porous barrier, they divide the microfluidic environment into separate fluidic channels whilst enabling the selective filtration and exchange of diluted molecules and compounds. Beyond sample filtration, membrane technology has been extensively applied to gas separation, pervaporation, desalination, dialysis, energy generation, microreactor systems, and more [164]. Another prominent application of porous membranes in microfluidic systems is in cell culture and organ-on-a-chip applications [251]. Membranes act as porous scaffolds for cells through which the delivery of nutrients and removal of waste products is possible. Exposure to shear stress can also be regulated and appropriately defined for specific cell types [252]. Membranes also enable the long-term maintenance of co-culture systems [253] being therefore critical in the emulation of complex tissue constructs, such as the gut epithelium, lung and liver.

Selecting the appropriate membrane for a specific microfluidic device is, however, not a trivial task. The first and most common consideration is regarding pore size which, particularly in the realm of OOC, can determine cell transmigration, physical contact and overall biochemical communication, as illustrated in Figure 2.9 [254]. Nevertheless, the properties of membranes present further reaching implications, which are still subject of long consideration and research. The intrinsic properties of the membrane, such as porosity, pore radius and membrane thickness, are known to contribute to modelling porous flow [252] and molecular transport [255]. The morphology of pores contributes to changing the permeation of the membrane [256], and may promote electroosmotic flow, for dual pole nanopores [257]. Surface charge of the membrane is also an important factor, capable of stimulating molecular transport [258]. Beyond the membrane, external factors, such as the channel dimensions and geometry are critical to control fluid flow through the channels and across the membrane [259].

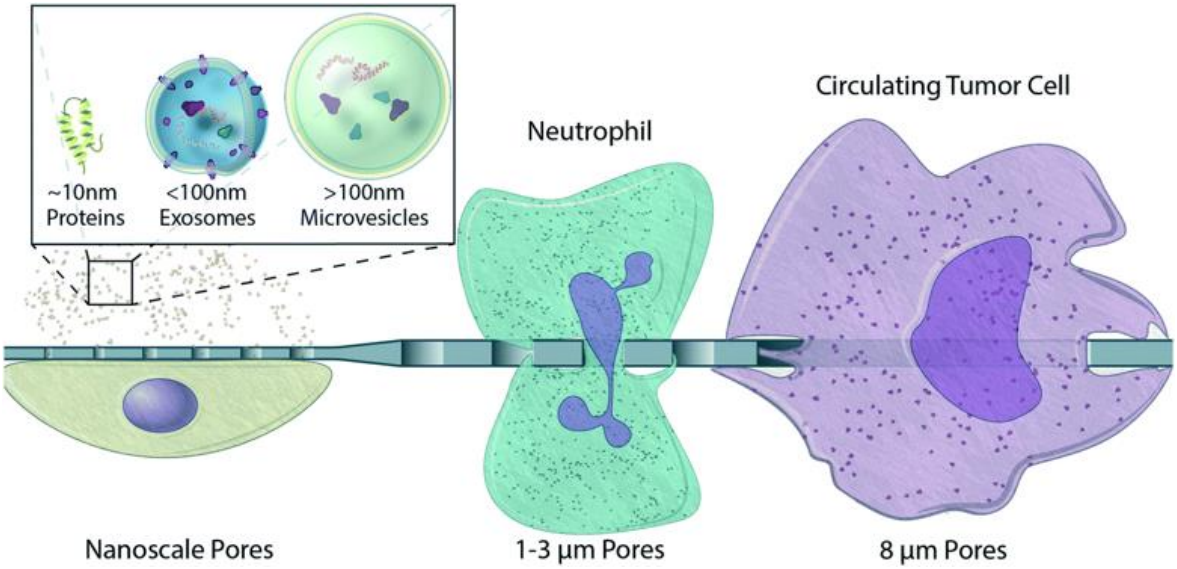

Figure 2.9: Membrane pore size and its effect on transmembrane transit of cells, vesicles and proteins. Image reproduced with permission of Mosvati et al [265].

Changing the pH of the media is also known to influence transport and delivery of molecules through the membrane [260].

Much of this research has been performed with either analytical [255, 261, 262] or FEM models [256, 257, 259, 263-270]. Chung et al proposed a 2D analytical model to predict the amount of convective cross-talk between parallel chambers separated by a porous membrane [252], Figure 2.10 A and B. Essentially, the pores of the membrane were treated as resistors connected in parallel, as illustrated in Figure 2.10 A and B, whose individual resistance to flow, R_p [Pa.s/m^3] can be calculated using Daegan's equation for short through pores:

$$R_p = \frac{\mu}{r^3}\left[3 + \frac{8}{\pi}\left(\frac{L}{r}\right)\right] \quad (1)$$

Where μ [Pa.s] is the fluid dynamic viscosity, r [m] is the pore radius and L [m] is the length of the pores, equivalent to the thickness of the membrane. In this model, the hydraulic permeability of the membrane, K_m [m^2], is therefore obtained by multiplying R_p by the total number of pores across the membrane. Instead, in FEM models, the membrane is treated as a porous media through which K_m can be calculated using Brinkman's equation:

$$K_m = \frac{\mu L P}{\pi r^2 R_p} \quad (2)$$

With *P* being the porosity of the membrane. And finally, this equation is employed to Darcy's Law, which accounts for the flow of media across the membrane, classified as slow flow through the interstices of a fully saturated medium. The equation is formulated as follows:

$$v = \frac{K_m}{\mu L} \nabla p \tag{3}$$

Where *p* [Pa] is the fluidic pressure. Many of these models, applied with FEM software such as COMSOL Multiphysics, are commonly used in literature to complement and corroborate experimental data, such as described by the work of Mosavati et al [265]. As it is observed in Figure 2.10 C and D, such models provide accurate means to simulate flow and transport across porous membranes, even when considering different cell monolayers and co-culture cultured on the membrane.

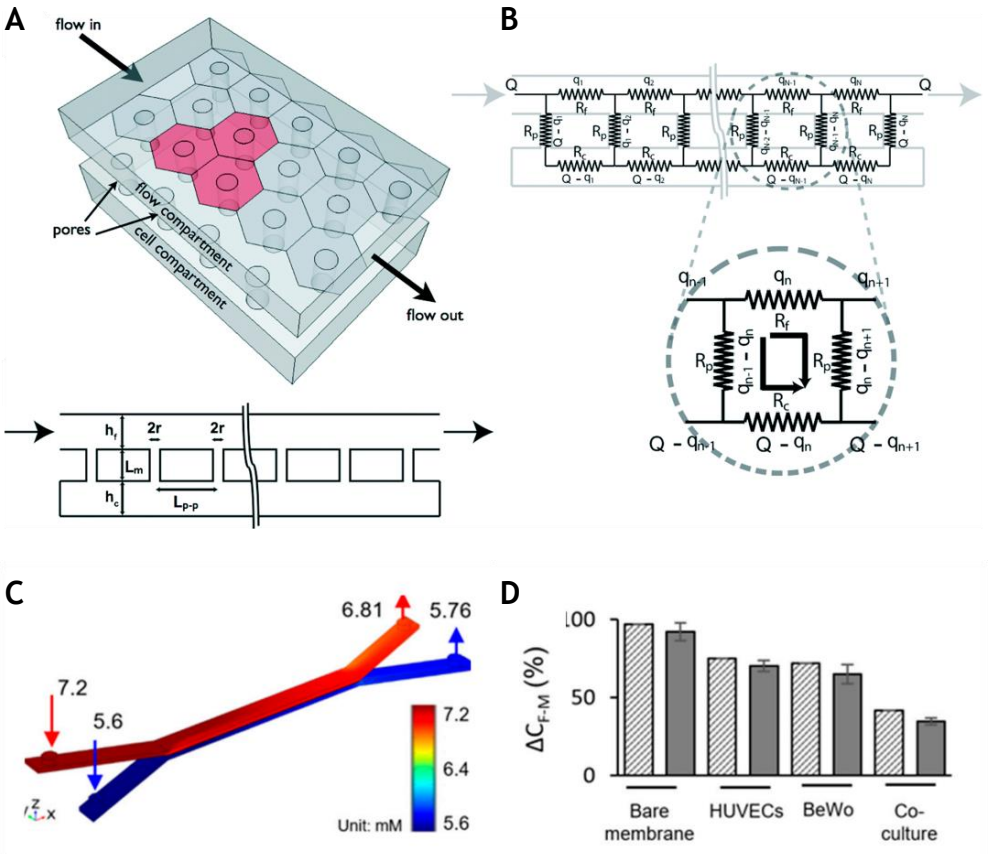

Figure 2.10: Numerical simulation of porous membranes. A, Membrane model geometry proposed by Chung et al. B, Circuit analogue of the membrane porous network and fluidic channels. C, Glucose concentration profiles at a flow rate of 50 µL/h simulated for a membrane lined with a co-culture of human placental choriocarcinoma cells (BeWo) and human umbilical vein endothelial cells (HUVEC). D, Comparison between experimental, in solid fill, and numerical data, pattern fill, of the glucose diffusion rate across the maternal-fetal interface for a 2h experiment. Images in A and B are reproduced with permission of Chung et al [252], and in C and D with permission of Mosvati et al [265].

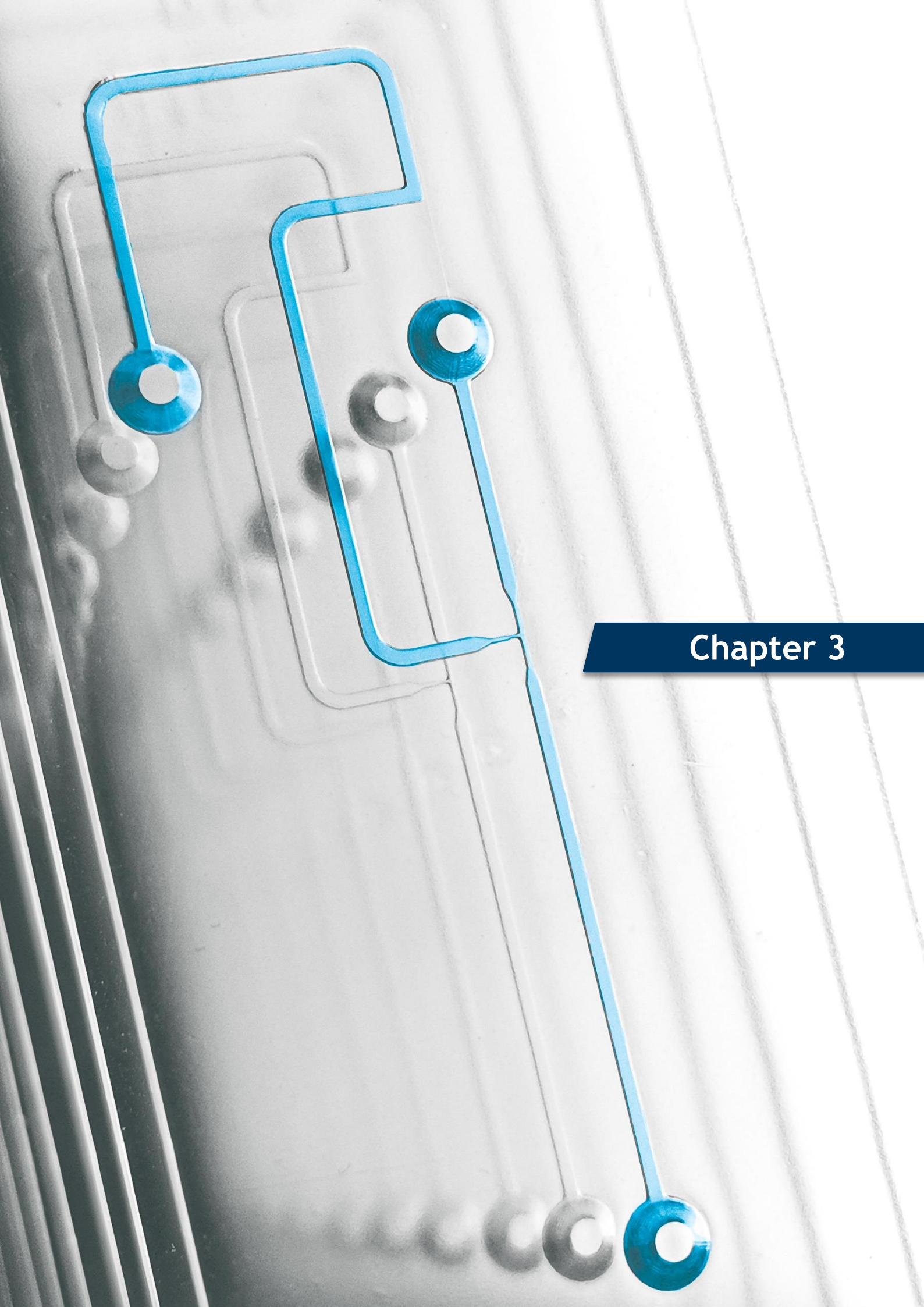

Chapter 3

3 Scalable Microfluidic Fabrication with 3D Printed Rapid Tooling for Injection Moulding

The following Chapter is adapted from Menezes et al, *Advanced Engineering Materials*, **2024**, 26 [271].

3.1 Introduction and Aims

As microfluidic applications continue to expand, so does the necessity to scale up production, a factor which currently forces the field away from PDMS and into thermoplastic materials. From the various high-volume manufacturing procedures thermoplastics provide access to, injection moulding presents the highest potential for automation, reproducibility and scalability [85]. Nevertheless, the high costs associated with traditional techniques for tooling microfabrication, renders this technology unsuitable for rapid prototyping. On the other hand, the development of 3D printing for microfluidics offers rapid, accessible and cheap prototyping, with an unmatched level of geometric complexity and multi-material printing, for a greater range of design possibilities [129]. Despite presenting a significant improvement to soft lithography, 3D printing lacks scalability prowess.

RT surges instead as a method to overcome the challenges associated with both injection moulding and 3D printing, while taking advantage of their complementary properties. This way, it provides a pathway to scale up the complex geometries achieved by 3D printing, whilst greatly reducing the costs associated with the fabrication of tooling and bridging the gap between rapid prototyping and injection moulding for microfluidic applications. In spite of its potential, the technology remains largely underdeveloped, particularly within the microfluidic field. This Chapter will, therefore, explore current protocols for microfluidic RT, and investigate new pathways to establish low-cost, high-quality microfluidic systems, with short lead production times.

3.1.1 Challenges with State-of-the-art Rapid Tooling for Injection Moulded Microfluidics

As discussed in section 2.1.3, RT takes advantage of the complementary properties between 3D printing and injection moulding. This way, it provides a pathway to

scale up the complex geometries achieved by 3D printing, whilst bypassing issues such as resin biocompatibility and channel drainage, known to affect 3D printed microfluidics. Similarly, it also provides an accessible, affordable, and quick method for the production of tooling for injection moulding, bridging the gap between the latter technology and rapid prototyping. Despite its great deal of potential in the production of thermoplastic microfluidics, RT remains largely underdeveloped, with a very limited impact in the microfluidic field.

Griffiths et al 2011 [272] first demonstrated the concept of micro SLA in the production of RT for injection moulding. The printed mould included 100 x 100 μm (height x width) microfluidic channels, and moulding performance was investigated both as a function of tool geometry and process parameters, such as melt temperature, mould temperature, injection speed and injection pressure. Both polypropylene (PP) and PC were used for injection moulding, ultimately demonstrating the viability of SLA-based tooling for the production of microfluidic RT for injection moulding. Nevertheless, severe feature damage after a short but unspecified number of cycles highlighted the limited tool life associated with such method. This work was further progressed in 2012, with the small batch production of polymer micro lens parts manufactured with SLA-based RT [273]. In this study, the thermal properties, durability and dimensional accuracy of the moulds were extensively investigated. The cooling time of the injection moulding cycle was optimized as a function of the material heat capacity. Build orientation was studied as an important parameter defining the replication properties of the mould and hence its durability. And polystyrene replicas were analysed to be 18 – 4% larger than their mould counterpart, even if presenting only marginal changes between different injection moulded parts. Despite the thorough investigation and parameter optimization, tool life remained limited to a total of 5 injection moulded cycles. Further technological progresses were only seen later in 2017, with the introduction of an SLA-based digital light processing (DLP) technique for the fabrication of RT containing a micro pillar array, 200 μm wide and deep [274]. This work, carried out by Zhang et al 2017, explored several process parameters, such as mould temperature and injection speed, as a function of dimensional accuracy and feature replication. Furthermore, the relative position of pillars in relation to the gate was seen as a crucial factor determining melt viscosity and ultimately dimensional accuracy. Importantly, an extended production run of 100

injection moulding cycles was reported. In 2021, Walsh et al investigated which properties are important in determining the suitability of photopolymer resins for injection moulding, as well as optimal printing and post-processing parameters, using an SLA-based machine. A high flexural modulus and elongation were found to increase the probability of injection moulding success. Furthermore, diagonal printing orientation was preferred, for which a scaling factor of 1.09 was required. This way, a systematic workflow was developed to assess and test the compatibility of photopolymer resin materials for RT. Convery et al quickly followed up in 2021 by employing a similar SLA setup to the development of RT for injection moulding, obtaining polystyrene chips sealed via ultrasonic welding into fully functional microfluidic devices [156]. This work addressed different resin materials, printing orientation, dimensional accuracy and the durability of 3D printed moulds, as well as the design implications for ultrasonic welding. Ultimately, channels as small as 100 x 200 μm (height x width) were achieved, and their dimensional accuracy was investigated over an extended tool life of 500 shots. The development of an injection moulded plasmonic sensor, with microchannels produced via SLA-based RT, highlighted the relevance of the reported RT-based manufacturing procedure for the microfluidic field. More so, by successfully culturing organoids over a period of 7 days, the biocompatibility of the devices was further verified.

Despite the presented body of work, to this date, no single protocol has combined both < 100 μm feature resolution and >500 cycle tool life. This aspect is critical in ensuring true microfluidic features (< 100 μm) produced via 3D printing are compatible with small scale injection moulding production (> 500 parts). More so, the optical properties of the injection moulded microfluidic parts, produced via 3D printed RT, lack systematic investigation. This is an especially important aspect for microfluidic systems, given the regular reliance on optical imaging in performing non-invasive analysis across various different fields. Convery et al. briefly addressed this issue, describing the necessity of employing manual polishing to improve the surface roughness of 3D printed moulds, and hence the optical properties of the resulting polymer replicas. Nonetheless this method is unsuitable when fine details or complex structures are involved. Furthermore, it is both laborious and time-consuming, which defeats the purpose of developing a scalable and automatic protocol with RT. Finally, with the exception of Zhang et

al 2017 [274], literature exclusively explored traditional SLA-based equipment in the fabrication of RT. Particularly in the knowledge of the rapid development and proliferation of alternative SLA-based techniques, such as LCD printing, as discussed in section 2.1.2, it becomes increasingly relevant to explore such techniques in the context of microfluidic RT.

3.1.2 Aims

The aims of this chapter are the following:

- Explore LCD printing technology in the development of microfluidic RT, identifying the key benefits and limitations of the technology when compared to state-of-the-art RT protocols with laser-based SLA.

- Explore the influence of different photocurable resins in determining the compatibility of LCD-based microfluidic RT with injection moulding.

- Develop a new RT protocol capable of producing microfluidic moulds with a < 100 µm feature resolution and >500 cycle tool life with high feature reproducibility.

- Identify, characterize and optimize a new approach to the development of optically transparent microfluidic devices using LCD-based microfluidic RT.

- Fabricate and test a functional microfluidic device produced via LCD-based RT.

3.2 Materials and Methods

This chapter addresses the manufacturing of microfluidic devices using RT. It focuses on the development of a protocol capable of delivering microfluidic devices with high feature resolution, scalability, and optical transparency. This way, this section provides a description of the technologies and methods involved in the fabrication and characterization of the obtained microfluidic devices.

3.2.1 Mould Fabrication

Mould design was performed using the CAD software Fusion 360 (Autodesk, US), after which an STL file is obtained. The STL file is then processed using a slicer software that is compatible with the desired 3D printing system. In Section 3.3, a Formlabs Form 3 (Formlabs, US) and a Phrozen Sonic Mini 8K (Phrozen, Taiwan) were employed for RT, using respectively the Preform (Formlabs, US) and Chitubox (Chitubox, China) slicing software. For the following sections and remainder portion of the work, 3D printing was achieved using an Anycubic Photon M3 Premium (Anycubic, China) and the Anycubic Photon Workshop (Anycubic, China) slicer software. The Formlabs Form 3 presents a laser with a spot size of 85 µm and power of 250 mW. Whereas the Phrozen Sonic Mini 8K presents a pixel size of 22 µm, the Anycubic M3 Premium presents a pixel size of 28.5 µm. The power output of each system was measured using a Thorlabs S121C Photodiode Power Sensor (Thorlabs, US), with a value of 1.86 ± 0.0 mW/cm^2 for the Phrozen and 2.39 ± 0.0 mW/cm^2 for the Anycubic.

Moulds were printed without supports and with their base directly on the build platform, for increased geometric accuracy [156]. As illustrated in Figure 3.1 A-B, moulds (Figure 3.1, element 1) were designed to fit a steel frame (Figure 3.1, element 2), with the dimensions of 77 x 29 x 5 mm. The photosensitive resins tested included the Anycubic Standard resin (colour white) (Anycubic, China), the Monoprice Rapid UV Printer Clear resin (Monoprice, US) and the Formlabs Clear resin (Formlabs, US). Their respective mechanical properties are present in Table 3.1. After printing, moulds were removed from the build plate, bathed in isopropyl alcohol (IPA) and agitated for 5 min, using a Form Wash (Formlabs, US). After washing, the moulds were blown dry using an air gun. Finally, full curing was achieved employing UV exposure for 30 min at a controlled temperature of 60 ºC, using a Form Cure (Formlabs, US). Its power output was measured as being 3.57 ± 0.0 mW/cm^2, using a Thorlabs S121C Photodiode Power Sensor (Thorlabs, US).

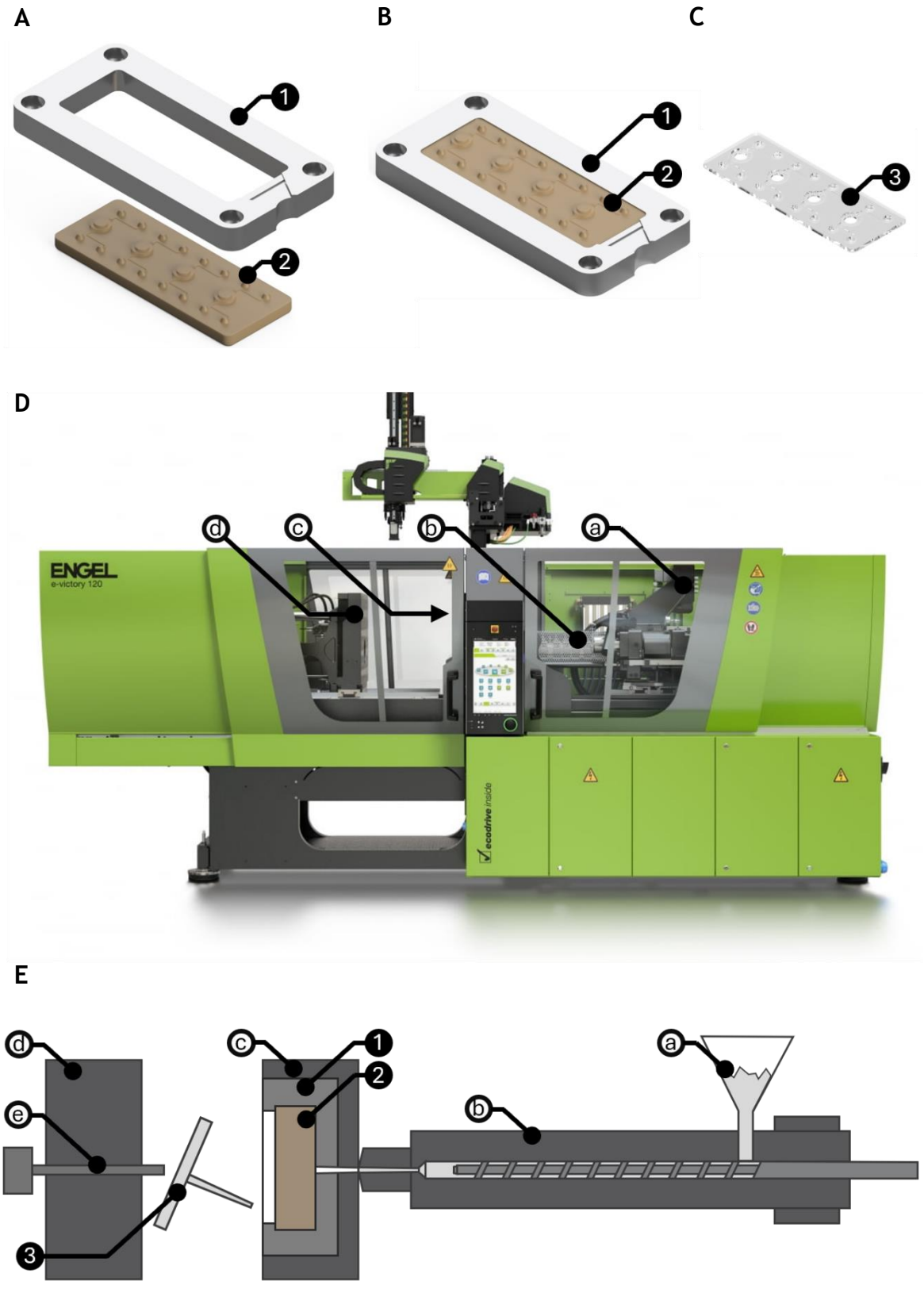

Figure 3.1: Illustration of the SLA-based RT setup as described by Convery et al. The metallic frame, 1, is fitted with the 3D printed tooling, 2, and then fixed to the fixed plate, c. After injection, D, the resulting polystyrene part, 1, is automatically ejected, E. The components identified in A – E fit in the injection moulding machine as labelled in F. Image in D reproduced with permission of Engel [93]. Image in E adapted with permission of Goodship [89].

Table 3.1: Properties of photocurable resins.

Resin		Anycubic Standard White Resin	Monoprice MP Rapid UV Clear Resin	Formlabs Standard Clear Resin
Material Properties	Density [kg/m^3]	1130	-	-
	Viscosity [cP.mPa.s]	200-230	-	-
Curing	Wavelength [nm]	365 - 405	405	-
Tensile Properties	Ultimate Tensile Strength [MPa]	40-50	-	53
	Young's Modulus [GPa]	-	-	2.4
	Elongation at Failure [%]	12-16	-	9
Flexural Properties	Flexural Modulus [GPa]	0.05 – 0.06	-	2.7
Impact Properties	Notched IZOD [J/m]	-	-	27
	Hardness [HS]	84-86	-	-
Thermal Properties	Heat Deflection Temp. at 1.8 MPa [°C]	-	-	65

3.2.2 Injection Moulding

A Victory 28 injection moulding machine (Engel, Austria) (Figure 3.1 D) was used in the manufacture of the polymeric replicas (Figure 3.1 C, element 3). The steel frame (Figure 3.1 B, element 1) with the fitted 3D printed mould (Figure 3.1 B, element 2), was fixed to the moving plate of the clamping unit of the injection

moulding machine as illustrated in Figure 3.1 D. This way, the injection moulding cavity is delimited, on one side, by the surface of the moving plate (Figure 3.1 C, element d), and on the other, by the surface of the 3D printed tooling (Figure 3.1 C, element 2). Laterally, the injection moulding cavity is delimited by the steel frame (Figure 3.1 C, element 1), ultimately providing the dimensions of 75 x 27 x 1.2 mm (length x width x height). The polymer selected for injection moulding was PS (1810 crystal polystyrene, Total Petrochemical and Refining, Belgium) whose qualities make it the prevalent material among commercial labware for cell culture research [96]. PS granules were fed, through the hopper (Figure 3.1, element a) into the injection moulding barrel (Figure 3.1, element b), gradually heated until 210°C and then cooled to 170°C, at the nozzle, to prevent stringing of the sprue. A shot volume of 5.8 cm^3 was then injected at a speed of 4 cm^3s^{-1} into the mould cavity. Holding pressure was maintained at 450 bar for 6 s, after which the clamping pressure was released and the moulds minimally separated, to allow the molten polymer to cool, for 25 s, and ensure its temperature dropped below its glass transition temperature (equivalent to 90°C for PS). Finally, the tool was opened, and the part was ejected, as illustrated in Figure 3.1 C, after which another cycle began. Sprues were manually cut from all injection moulded parts.

3.2.3 Feature Analysis

A multi-purpose calibration template was devised and printed, as illustrated in Figure 3.2 A, where the XY resolution of features was performed, Figure 3.2 A, section b. It included an array of different features, both positive and negative, with different dimensions, as shown in Figure 3.2 B. Top view images of the features were obtained with surface mapping, using an Alicona Infinite Focus G4 (Bruker Alicona, US) with a 5x/0.15 objective (Bruker Alicona, US). The generated images were then imported to ImageJ (National Institutes of Health and the Laboratory, US) software, where the feature measurements were performed.

The analysis of the durability and reproducibility of injection moulded microfluidic channels involved mapping the channels using an Alicona Infinite Focus G4 (Bruker Alicona, US) with a 5x/0.15 objective (Bruker Alicona, US). The generated files were then used in the Vision 64 Map software (Bruker Alicona, US) to obtain the

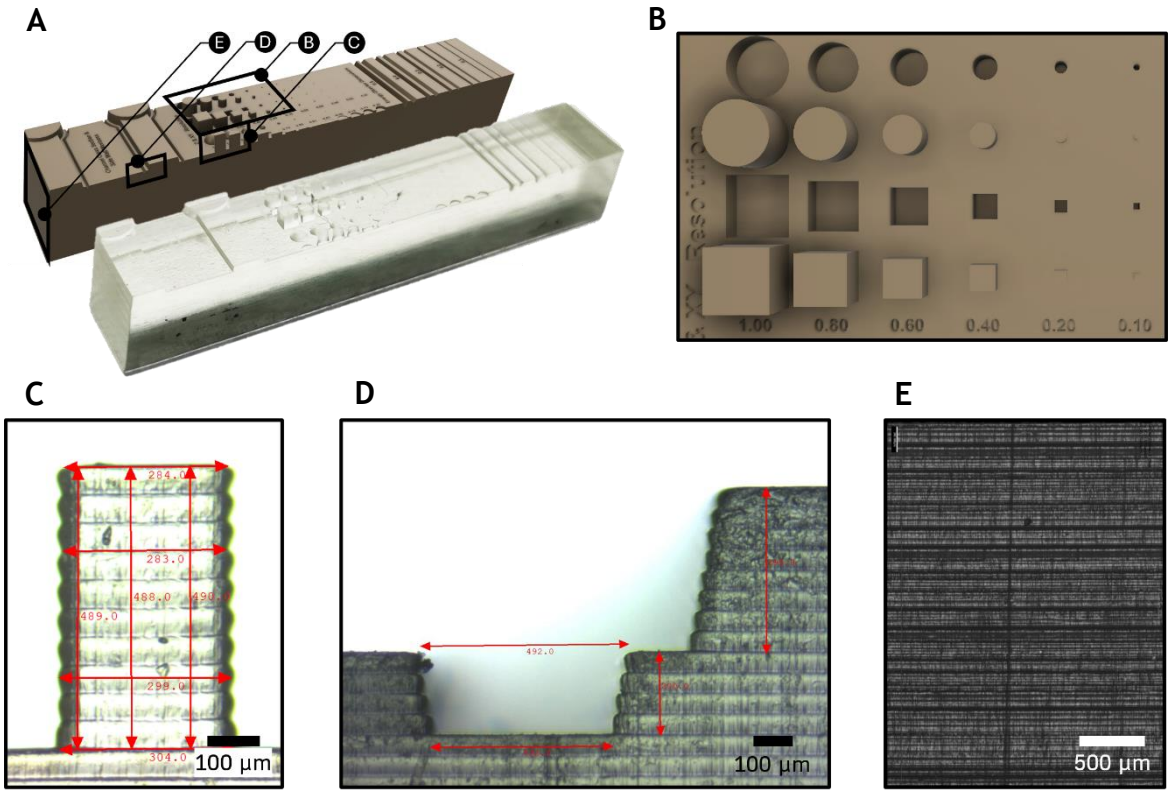

Figure 3.2: Calibration template and its different analysis sections. A, CAD version of the calibration template, in front of its 3D printed counterpart, illustrating the sections meant for, B, the analysis of XY resolution, C, the investigation of vertical resolution, D, the analysis of channel feature cross-sections, and E, the measurement of wall waviness.

channel dimensions, height and width, as a function of the shot number, and characterize reproducibility. The durability and reproducibility analysis of the injection moulded through features was based on using a Leica DM 750M (Leica Microsystems GmbH, Germany) microscope with a 5x/0.12 objective (Leica Microsystems GmbH, Germany). The images were then analysed using the ImageJ (National Institutes of Health and the Laboratory, US) software, and the diameter was measured as a function of the shot number and characterise durability.

The droplet generator channels were imaged at a 20° tilt using scanning electron microscopy (SEM) with a Hitachi SU8240 (Hitachi, Japan) operated at low magnification and an accelerating voltage of 5 kV. Prior to imaging, the samples were sputter-coated with a gold-palladium (80/20) alloy using an Agar Auto Sputter Coater at 20 mA for 40 seconds, resulting in a conductive coating approximately 6 nm thick on the channel surfaces.

3.2.4 Cross-Section Analyses

The multi-purpose calibration template illustrated in Figure 3.2 A was similarly used in the analyses of vertical resolution, Figure 3.2 A, section c, and channel cross-section, Figure 3.2 A, section d. To analyse vertical resolution, the template included extruded features, protrusions and cavities, printed with a diameter of 300 µm and different heights, from -1000 µm to 1000 µm. Furthermore, these features were intentionally placed at the edge of the template, to allow the direct analysis of the cross-section, as observed in Figure 3.2 C, and measurement of vertical dimensional accuracy. Similarly, to analyse the cross-section of microfluidic channel features, these were integrated in the template. The feature layout contained a protrusion 400 µm tall, representative of a microfluidic channel, and a cavity 200 µm deep and 500 µm wide, representative of an energy director [156], both with walls at a 10º draft angle, as observed Figure 3.2 D. Imaging, as observed in Figure 3.2 C and D, was performed using a Leica DM 750M (Leica Microsystems GmbH, Germany) microscope. The images of cross-sections addressing the analysis of vertical resolution and feature geometry, as in Figure 3.2 C, were obtained using a 5x/0.12 objective (Leica Microsystems GmbH, Germany). Further investigation was required in the analyses of cross-sections, particularly to characterize the effects of different light penetration properties associated with each of the different tested photocurable resins. This way, both the sidewall waviness and interlocking angle were measured. Imaging to illustrate the waviness of the sidewall of microchannel features was obtained using a 5x/0.12 objective (Leica Microsystems GmbH, Germany). In turn, the imaging used to calculate the interlocking angle was obtained using a 50x/0.75 objective (Leica Microsystems GmbH, Germany). The interlocking angle was then measured using ImageJ (National Institutes of Health and the Laboratory, US) software.

3.2.5 Surface Measurements

The surface properties of channel sidewalls were analysed using the same calibration template as illustrated in Figure 3.2 A. Surface mapping was performed using an Alicona Infinite Focus G4 (Bruker Alicona, US) with a 10x/0.30 objective (Bruker Alicona, US), and facing the draft wall (with an angle of 10° to replicate the sidewall of channels) of the template, Figure 3.2 A, section e, parallel to the

lens. The obtained images, as presented in Figure 3.2 E, and respective files were then analysed for waviness using the Vision 64 Map software (Bruker Alicona, US).

Surface deflection was measured using featureless moulds. Mapping was done in the opposing ends of moulds using an Alicona Infinite Focus G4 (Bruker Alicona, US) with a 5x/0.15 objective (Bruker Alicona, US). The values for curvature were obtained using the Vision 64 Map software (Bruker Alicona, US), and then imported to MATLAB (MATLAB, US) to reconstruct the surface of the moulds and calculate total deflection.

Surface roughness was measured using similar featureless moulds. Mapping was done using a Bruker Contour GT-X 3D Optical Microscope (Bruker Alicona, US) with a IX5 objective (Bruker Alicona, US). The values for surface roughness, *Ra* [µm], were obtained using the Vision 64 Map software (Bruker Alicona, US).

3.2.6 Tensile Testing

An Instron 3367 (Instron® Mechanical Testing Systems, USA) universal tensile machine was used to characterise the mechanical properties of the 3D printed components. Test specimens were designed and printed in a dumbbell shape, as illustrated in Figure 3.3 A, with a rectangular cross-section of 4 x 2 mm and a gauge length of 29 mm, according to the ASTM-D638 standard. All test specimens were subject to post-processing under UV exposure for 30 min with a curing

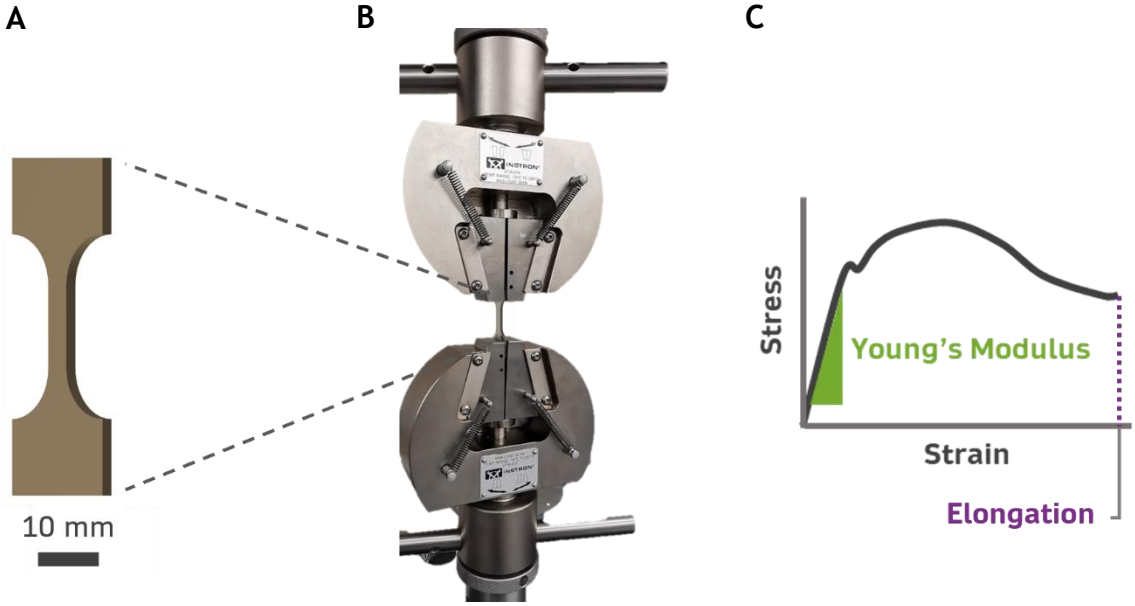

Figure 3.3: Design of experiments for tensile testing. A, CAD of the test specimen. B, Tensile testing setup, with the tensile specimen tightened to the universal tensile machine. C, Illustration of the force displacement data, highlighting the calculation of both the Young's modulus and elongation.

temperature of 60°C. Tensile measurements were performed at a normal loading rate of 1mm/min. An illustration of the tensile testing setup is present in Figure 3.3 B. Force displacement data, as illustrated in Figure 3.3 C, was continuously recorded from the point of the specimen being unloaded to the point of failure. The Young's modulus, *E*, was calculated from the linear elastic region of the stress-strain curves obtained, using $E = \sigma/\varepsilon$, where σ [Pa] stands for the stress applied and ε the strain obtained. Strain was calculated by the ratio between the final displacement, ΔL, and the initial gauge length, L_0, with $\varepsilon = \Delta L/L_0$.

3.2.7 Optical Testing

Optical transparency was measured using 951 USAF wheel pattern test target (Thorlabs, Germany). A featureless injection moulded chip was put on top of the target, as illustrated in Figure 3.4 A, and then imaged using a Leica DM 750M (Leica Microsystems GmbH, Germany) microscope with a 5x/0.12 objective (Leica Microsystems GmbH, Germany). The obtained images were then analysed using ImageJ (National Institutes of Health and the Laboratory, US) software. Optical transparency was measured as a function of resolution, contrast and amplitude. Optical resolution was calculated by determining the smallest discernible group of three lines in the resolution target and, by using the group and element number, applying the following equation:

$$Resolution = group\ number + \frac{element\ number - 1}{6} \quad (4)$$

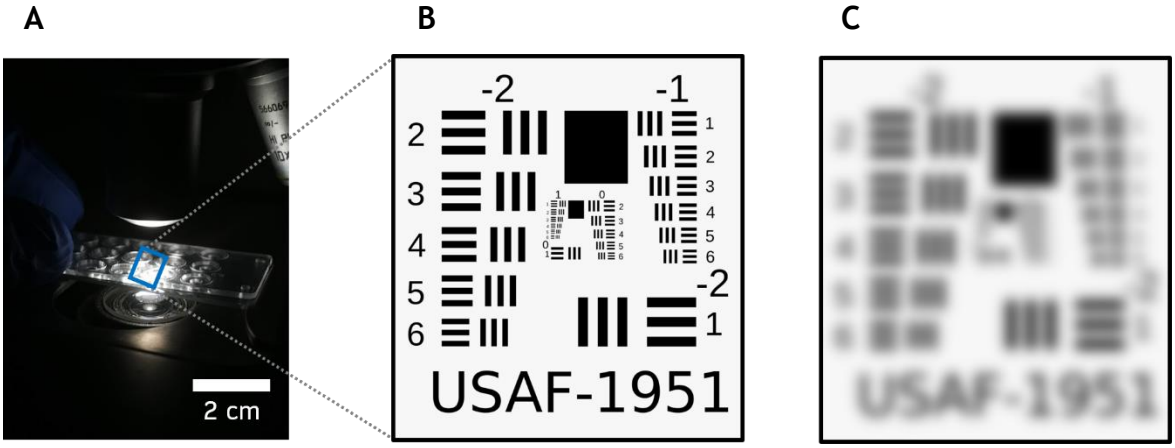

Figure 3.4: Analysis of optical transparency with a resolution target. A, Microscopy setup with the microfluidic chip on top and the target on the bottom. B, Illustration of the resolution test target as seen through an optically transparent sample. C, Illustration of the resolution test target as seen through an opaque sample.

Contrast was calculated instead as the transition slope between a black and a white pattern. In turn, amplitude was measured as the difference between the grey values of a black and a white pattern. Figure 3.4 B and C illustrate the observed differences between an optically clear and an opaque sample.

3.2.8 Statistical Analyses

All statistical analyses were performed using GraphPad Prism v10.4.2 (Dotmatics, US). The choice of statistical test varied based on the experimental design and data structure. In general, comparisons between multiple groups were evaluated using one- or two-way analysis of variance (ANOVA), followed by post-hoc tests such as Tukey's Honestly Significant Difference (HSD) when applicable. A significance level of $\alpha = 0.05$ was used throughout. The data was presented as mean ± standard deviation. Statistical notation was defined as non-significant (ns) for $p > 0.05$; "*", or significant with * $p \leq 0.05$; ** $p \leq 0.01$; *** $p \leq 0.001$; **** $p \leq 0.0001$.

3.2.9 Bonding

Prior to bonding, injection moulded chips were treated with oxygen plasma, at 80 W for 1 min, using a Henniker Plasma HPT-200 (Henniker Plasma, UK). The equipment used for hot bonding consisted of a manual hydraulic press from Specac (Specac, UK), integrated with two parallel 4 x 7-inch hot plates from Devil Press (Devil Press, UK) controlled by a DP40 dual PID controller (Devil Press, UK). Bonding was done for 15 min, at a constant temperature of 79°C, and an initial pressure of 1.1 bar, allowed to decrease throughout time due to the softening of the polymer. Bonding was performed between the manufactured droplet generator components and flat, blank chips. The RT for the respective blank chips was similarly produced via 3D printing, and injection moulded with polystyrene.

3.2.10 Fluidic Perfusion and Droplet Generation

To assess the seal of the microfluidic devices post bonding, diluted colouring dye (MOB Cosmetics, UK) was perfused into the channels by using an AL-300 syringe pump (World Precision Instruments, US). Imaging was performed with a 3.3X Macro Zoom Lens (Edmund Optics, US), with 0.3X to 1X magnification, and a Basler Ace acA1300-200uc Color (Basler AG GmbH, Germany) camera, with 1.3 MP. Image

analysis was then performed using ImageJ (National Institutes of Health and the Laboratory, US) software

To evaluate droplet generation, devices were perfused with an emulsion of fluorinert FC-40 (Sigma-Aldrich, USA) and mineral oil. Imaging was performed using a Zeiss Primovert inverted microscope (Zeiss, Germany) with a 4x/0.10 objective (Zeiss, Germany). Imaging was performed using the Pylon Viewer software (Basler AG, Germany), with an exposure time of 250 μs and an acquisition frame rate of 350 fps.

3.3 Selection of SLA-Based 3D Printing Technique for Rapid Tooling

Within a highly prolific market [275], choosing the right 3D printing system for a given application is not a trivial task. Even if narrowing the options down to SLA-based techniques, which demonstrate better compatibility for RT, there are various methods relevant to consider. Within literature, research in microfluidic RT has been almost exclusively performed using traditional SLA. Nevertheless, technologies based on vat polymerization using LCD systems are becoming increasingly more capable of higher resolution printing, faster cycles, and more affordable pricing. Therefore, an initial assessment was carried out using two different machines based respectively on traditional SLA and LCD systems. This way, state-of-the-art protocols for the development of RT using SLA-based machines, such as the one described by Convery et al [156], were directly compared with LCD-based methods.

The analysis was then focused on providing an initial comparison between the properties of the moulds produced by both SLA and LCD-based methods and determine the most promising in the context of microfluidic RT. Feature quality and resolution, channel cross-section and surface roughness were addressed together with the optical transparency of subsequent injection moulded polymeric parts. For this initial study, a Formlabs Form 3 and a Phrozen Sonic Mini 8K were tested, respectively representing SLA and LCD technology. Formlabs is a well-established 3D printing technology manufacturer, and their Form 3 SLA printer was already explored in the context of microfluidic RT [156, 276]. Phrozen, on the other hand, is another 3D printing manufacturer whose popularity has grown in

recent years as one of the market leaders in the production of affordable, high-quality LCD printers. Additionally, two different photocurable resins were tested. One, the Formlabs Clear (FC) resin, is manufactured by Formlabs specifically for their own brand of SLA systems. The other, the Monoprice Clear (MC) resin, is an affordable option for generic 3D printing systems, despite primarily targeted at LCD or DLP systems.

The hardware and software environment developed by Formlabs is primarily industry-oriented, with a focus towards improving user-experience, reliability, and printing success. This way, Formlabs printers are standardized to operate exclusively with their own specific range of materials, having a predefined set of printing parameters associated to each which, with the exception of layer height, are not modifiable. On the other hand, the environment provided by Phrozen, as well as most of the LCD systems available in the market today, is more oriented towards individual developers, therefore valuing printing versatility and freedom over standardization. In the context of this experiment, this ultimately meant that, while the Form 3 printer was restricted exclusively to the FC, the Phrozen Sonic Mini 8K was tested with both resins. This way, three setups were tested: SLA with FC (SLA-FC), LCD with FC (LCD-FC), and LCD with MC (LCD-MC). The printing parameters for the SLA-FC setup were predefined from the manufacturer, with the exception of layer height, which was set at 25 μm for maximum resolution.

Instead, the LCD-FC and LCD-MC setups required prior testing to determine, most importantly, the minimum layer exposure enabling reliable printing. This way, it was determined that, for the LCD-FC setup a minimum layer exposure of 10 s was required, and for the LCD-MC setup a layer exposure of 8 s was sufficient to provide reliable results. Layer height, on the other hand, was determined according to the resin manufacturer instructions, being set at 25 μm for the FC and 50 μm for the MC. A list of the parameters used can be found in Table 3.2.

3.3.1 Feature Resolution and Channel Cross-Section

To address feature resolution in the X-, Y- and Z-axis, as well as the ability to realise microfluidic channels, a calibration template was devised and printed, as illustrated in Figure 3.5. It contained a standard XY resolution target, view 1, with different-shaped features varying in diameter from 1000 to 10 μm. It incorporated

Table 3.2: List of printing parameters for the different printing setups.

Printing Technology	**SLA** Formlabs Form 3		**LCD** Phrozen Sonic Mini 8k	
Resin Material	Formlabs Clear		Formlabs Clear	Monoprice Clear
Layer Height [µm]	25	Layer Height [µm]	25	50
Fill Exposure [mJ/cm^2]	-	Layer Exposure [s]	10	8
Early Exposure [mJ/cm^2]	-	Bottom Layer Exposure [s]	35	40
Number of Bottom Layers	-	Number of Bottom Layers	6	10

as well simple extruded features with a fixed width of 300 µm but different heights, varying from 50 to 1000 µm, both in the positive range, for protrusions, and negative, for cavities. The respective features were also purposefully extruded at the edge of the template, to allow the analysis of their respective cross-section, view 2, and the direct measurement of height. Finally, the calibration template also integrated a feature representative of a general-purpose microfluidic channel, whose cross-section is viewed in view 3. The chosen channel layout contained a protrusion 400 µm tall, representative of a microfluidic channel, and a cavity 200 µm deep and 500 µm wide, representative of an energy director [156], both with walls at a 10º draft angle. By allowing the direct observation of the channels' cross-section, this template was designed to evidence the ability of each protocol in realizing general-purposed microfluidic features for RT.

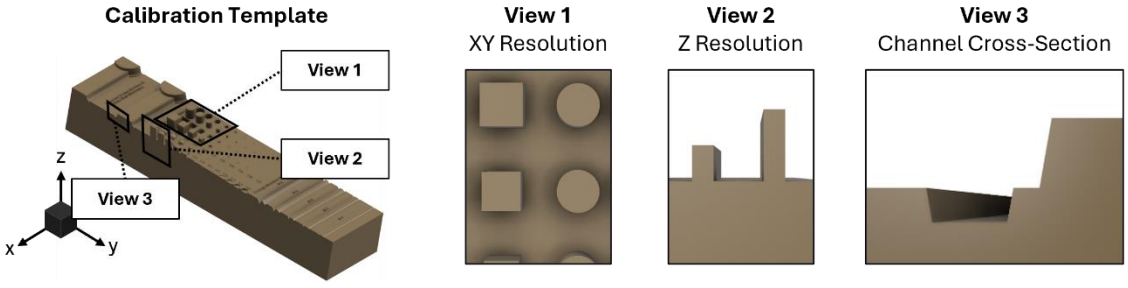

Figure 3.5: Calibration template and its multiple views designed to assess the XY resolution, view 1, Z resolution, view 2, and the cross-section of channels, view 3.

In Figure 3.6 A, view 1 of the calibration template is analysed for the various tested setups. It highlights the varying levels of feature quality and geometric accuracy obtained for the different setups. An analysis first to feature quality, evidences that, for the SLA-FC setup, not only are edges rough and imprecise, but the surface finish is poor as well, with high levels of surface roughness. The LCD-FC setup improves marginally on feature quality, with a higher surface finish and clearer edges. Nevertheless, there are various visible indentation in the presented features, a factor indicative of under exposure. Optimal feature quality was obtained using the LCD-MC setup, providing a glossy surface finish, with barely any visible roughness, along with accurate geometric shapes and clear edges. An analysis to feature resolution further demonstrates the superior performance of the LCD-MC setup, which presents high geometric accuracy down to 50 µm wide features. Instead, the SLA-FC setup reaches a resolution limit somewhere in the range between 500 to 250 µm wide features, presenting below this interval a high offset between CAD and printed dimensions. The LCD-FC setup is in turn observed to be incapable of realising features ≤ 100 µm, and presents a high offset between printed and CAD dimensions, throughout the entire tested range. Geometric accuracy is better illustrated in Figure 3.6 B, where printed dimensions are compared to their corresponding CAD value, for all three setups. This figure evidences first the superior performance of the LCD-MC setup, with a feature resolution and noteworthy precision down to 50 µm, only failing with diameters of 10 µm. And second, it highlights the limitations of the SLA-FC and LCD-FC setups. It is visible that the SLA-FC setup begins to underperform for features < 300 µm, reaching a resolution limit at approximately 200 µm, after which feature width remains in the interval between 150 – 225 µm, regardless of the CAD dimension. On the other hand, Figure 3.6 B also highlights the consistent offset between CAD and printed dimensions for the LCD-FC setup, where features are systematically printed smaller than their CAD counterparts. This evidence is highly indicative of underexposure, suggesting that the printing parameters, and particularly layer exposure, should be optimized for the LCD-FC setup.

An analysis to view 2 of the calibration template, in Figure 3.7 A, highlights a different set of characteristics. Particularly, it demonstrates the differences in the cross-sectional profiles of features printed with SLA and LCD and, by doing so, the differences between the two methodologies involved. The systematic

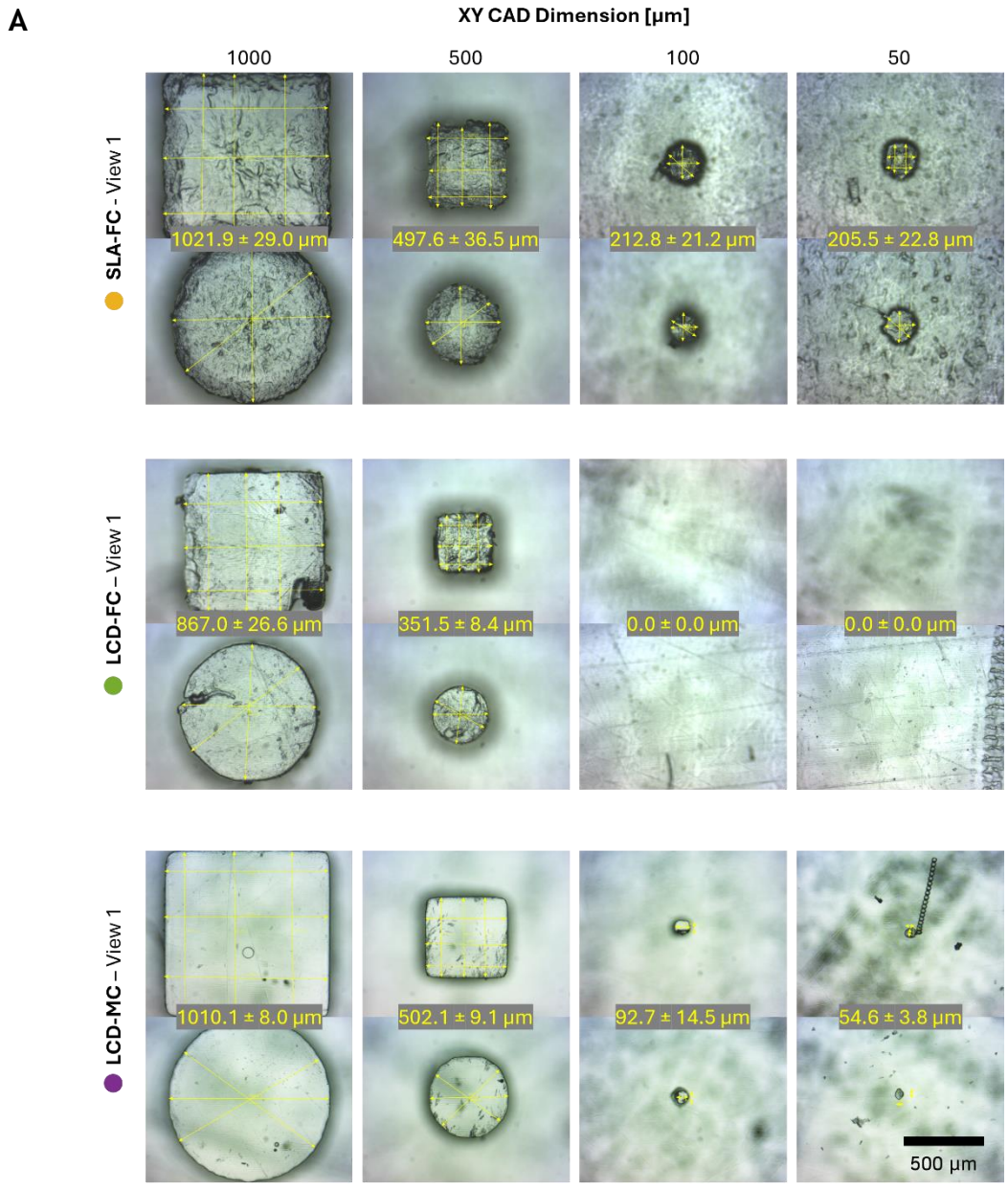

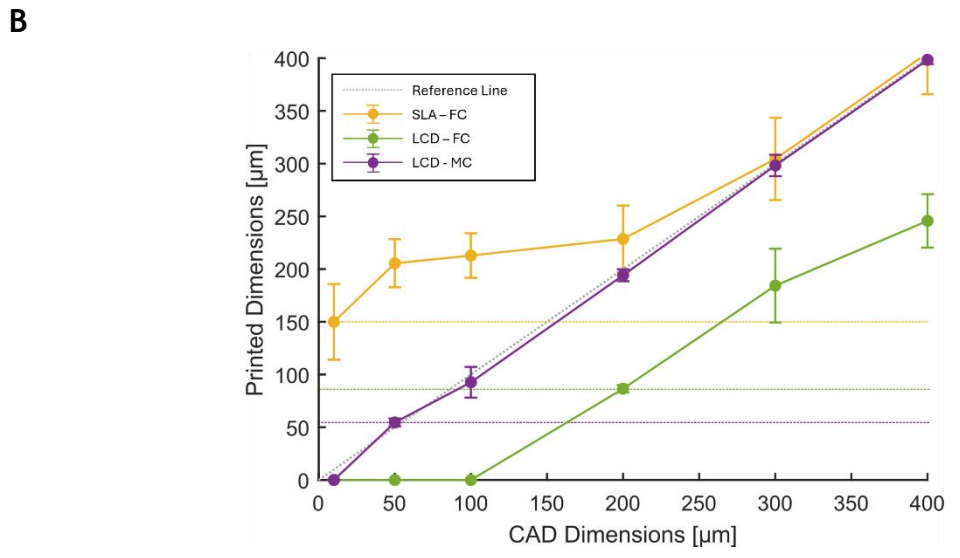

Figure 3.6: Analysis of XY feature resolution, using view 1 of the calibration template, in relation to the tested setups. A, Arrays of printed features, labelled with their measured width, used to assess XY resolution and geometric accuracy across all tested setups. B, Geometric accuracy of each setup, comparing printed feature dimensions to corresponding CAD designs.

horizontal layering visible in the LCD-FC and LCD-MC samples comes as a result of the one-off exposure, cyclically performed for each layer. The high stratification it generates, also allows to easily identify printing parameters such as layer height, in this case, equivalent to 50 µm for the LCD-MC setup, and half (25 µm) for the LCD-C. More so, by analysing the profile of each layer, the nature of the photopolymerization process is highlighted, as well as if layers have been over- or underexposed. It can be observed, for instance, that while features printed with the LCD-MC setup evidence a round, bulbous profile with each layer, features printed with LCD-FC display instead a smoother profile. Whereas the former may be a sign of overexposure, with excessive photopolymerization resulting in the lateral expansion of layers, the latter is usually a manifestation of underexposure. On the contrary, traditional SLA is based on laser rastering to achieve vat polymerization. This way, the cross-sectional profile does not evidence such defined stratification in the XY plane, but a high repeatability of patterns and resulting stratification along the Z-axis instead. The vertical resolution of both cavities and protrusions is displayed in Figure 3.7 B and C respectively. Both figures highlight the superior geometric accuracy of the LCD-MC setup in the Z-axis, this time however closely matched by the SLA-FC setup as well. The LCD-FC setup shows on the other hand a systematic offset, where features are consistently printed below their attributed heights. This is again evidence of underexposure and suggests further work in parameter optimization.

The properties described in Figure 3.6 and Figure 3.7 and their influence in microfluidic channel fabrication are displayed in Figure 3.8, where the cross-sectional profiles of channel features printed with each setup are visualized with view 3 of the calibration template. Despite maintaining feature height with rigorous accuracy, the SLA-FC displays low accuracy in the width of features. More so, the setup visibly struggles to realize clean features, with sharp angles and edges, as well as flat surfaces. Instead, a significant rounding of edges and surfaces is observed. Greater geometric rigour is observed for both LCD setups, with the LCD-MC setup providing once again the best performance. With this setup, it is observed that vertices are sharp, and surfaces are flat and parallel. The high stratification of layers generates, however, sidewalls that present significant waviness, due to the lateral expansion of layers during

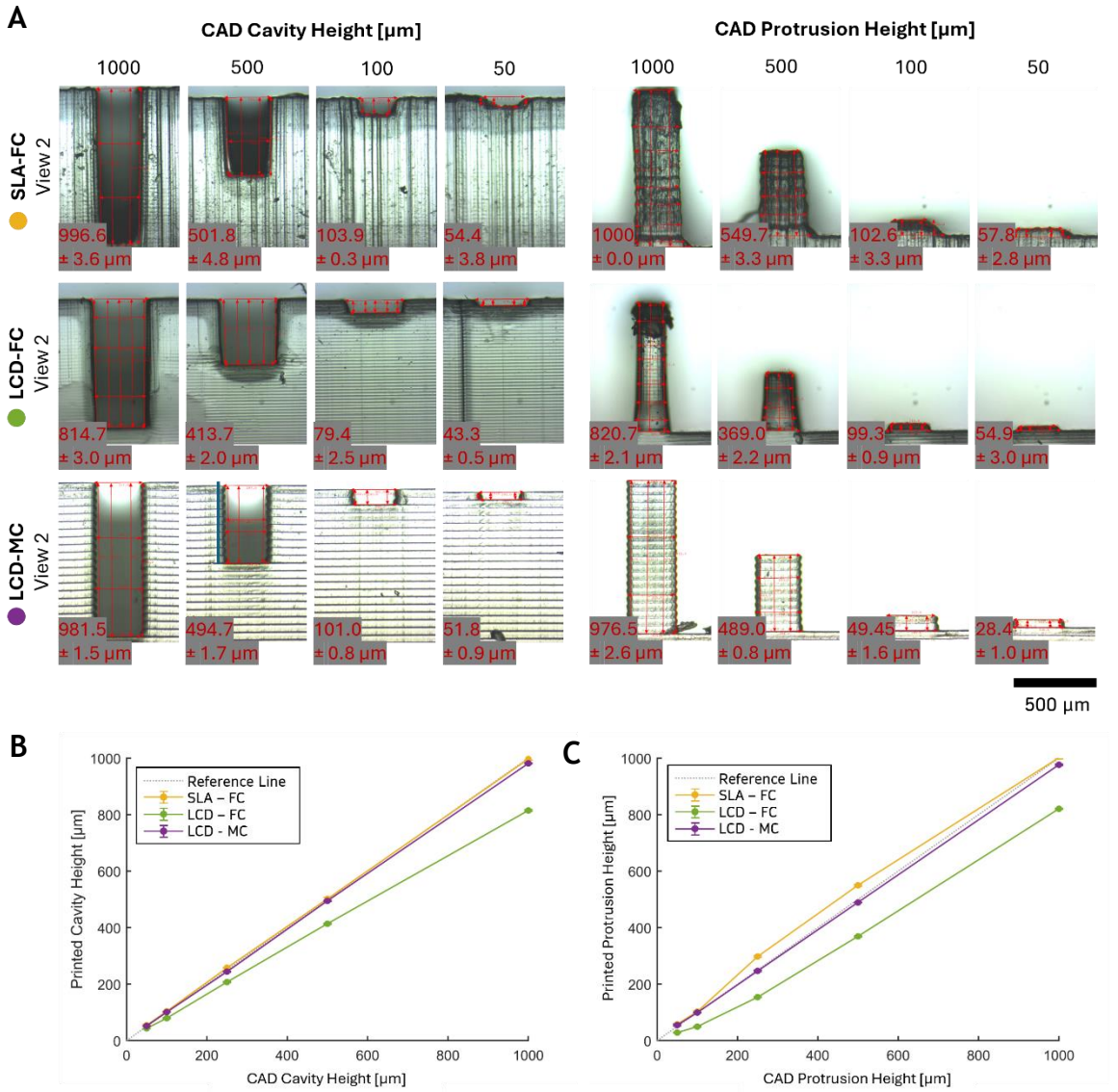

Figure 3.7: Analysis of feature height in the Z-axis, using view 2 of the calibration template, in relation to the tested setups. A, Arrays of printed cavities and protrusions, labelled with their measured heights, used to assess resolution in the Z-axis across all tested setups. B, Geometric accuracy of cavities in the Z-axis across all tested setups, comparing the height of printed cavities with their corresponding CAD value. C, Geometric accuracy of protrusions in the Z-axis across all tested setups, comparing the height of printed protrusions with their corresponding CAD value.

photopolymerization. This effect is reduced for the LCD-FC setup, in part due to both to the smaller layer height employed and the underexposure of layers as previously mentioned. This ultimately generates smoother sidewalls, with less evident stratification and lateral expansion of layers.

These tests allow the conclusion that LCD technology is generally the most promising. The LCD-MC setup provided the highest geometric accuracy and great potential for microfluidic RT. The LCD-FC setup evidenced as well high potential for microfluidic channel fabrication, despite displaying signs of underexposure, which encourage further investigation and optimization of printing parameters.

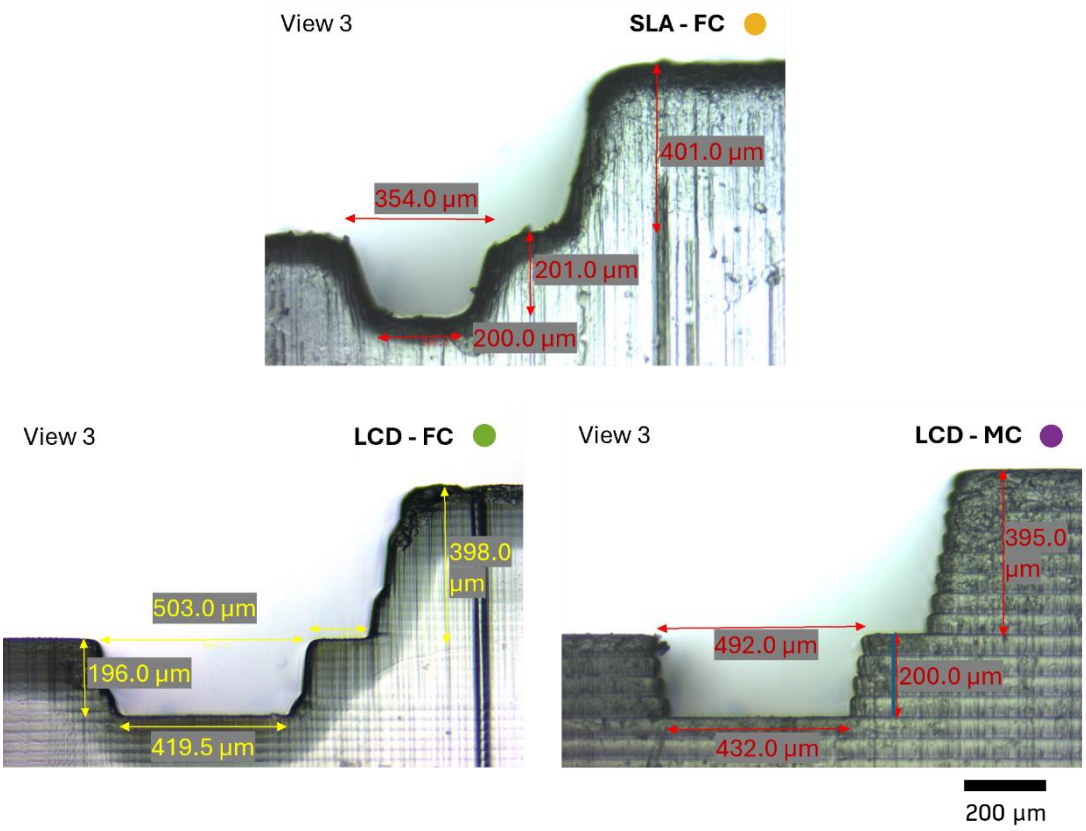

Figure 3.8: Cross-sectional analysis of microfluidic channel features, using view 3 of the calibration template, in relation to the tested setups.

3.3.2 Surface Roughness and Optical Transparency

Another important aspect to address is the surface roughness of moulds produced via 3D printing. Especially in the context of RT, the surface roughness of moulds directly influences the surface roughness of the injection moulded parts, which in turn affects their optical properties. Particularly in the realm of microfluidic applications, substrate transparency is a critical aspect to enable the compatibility with optically based analytical techniques, popular across all branches of the field. To rank the surface roughness of moulds produced according to the different printing setups in analysis, as well as the optical transparency of the resulting polymer devices, different microfluidic layouts were printed and subsequently injection moulded. Beyond the setups previously introduced, moulds produced with the SLA-FC setup were further subdivided into non-polished (SLA-FC-NP), and polished (SLA-FC-P). This way, manual polishing is contemplated as a means of decreasing the surface roughness of moulds and increasing the subsequent optical transparency of the polymer chips, as reported by Convery et al [156]. The respective microfluidic moulds are presented in Figure 3.9 A.

A preliminary visual analysis of the moulds, Figure 3.9 A, shows some of the distinct properties associated with each of the surfaces. It is possible to observe that both the SLA-FC-NP and the LCD-FC reflect significantly less light and present a distinctively matte surface finish. This quality also makes the channels and features on the surface of the moulds less visible. In turn, a comparison between the SLA-FC-NP and the SLA-FC-P moulds demonstrates the ability of manual polishing to increase surface quality, as evidenced by the greater reflection of light displayed by the SLA-FC-P mould. Nevertheless, manual polishing generates inconsistent results across the surface, and is greatly dependant on the density of features in the respective surface. This is possible to observe in Figure 3.9 A, given that from the centre of the chip, where polishing is easier, to the extremities, where polishing is more difficult due to the existence of taller features, the quality of the polishing decreases. More so, not only is the structural integrity of microfluidic features at risk with manual polishing, but also, tight corners, vertices and cavities may be impossible to reach. Finally, the process itself relies greatly on manual labour, and it is very time-consuming as well (approximately 30 min to obtain the surface finish presented in Figure 3.9 A). On the other hand, the mould produced by the LCD-MC setup provides a high surface quality, with a consistent glossy finish across the mould and without requiring any additional polishing.

An analysis based on optical profilometry cements and quantifies these properties. As shown in Figure 3.9 B, the surface topography of each mould was individually mapped towards providing a 3D model from which roughness profiles and the value for *Ra* were retrieved, as shown in Figure 3.9 C. These measurements confirm the previous observations. It is possible to observe that both conditions with the FC resin present similar properties, with the SLA-FC-NP displaying the roughest surface, with *Ra* = 2.1 ± 0.1 µm, and the LCD-FC a slightly smoother topography, with *Ra* = 2.0 ± 0.2 µm. A significant improvement is obtained by polishing the moulds with the SLA-FC-P setup, resulting in a lower surface roughness equivalent to *Ra* = 1.1 ± 0.2 µm, as observed in Figure 3.9 C. However, the lowest value for roughness

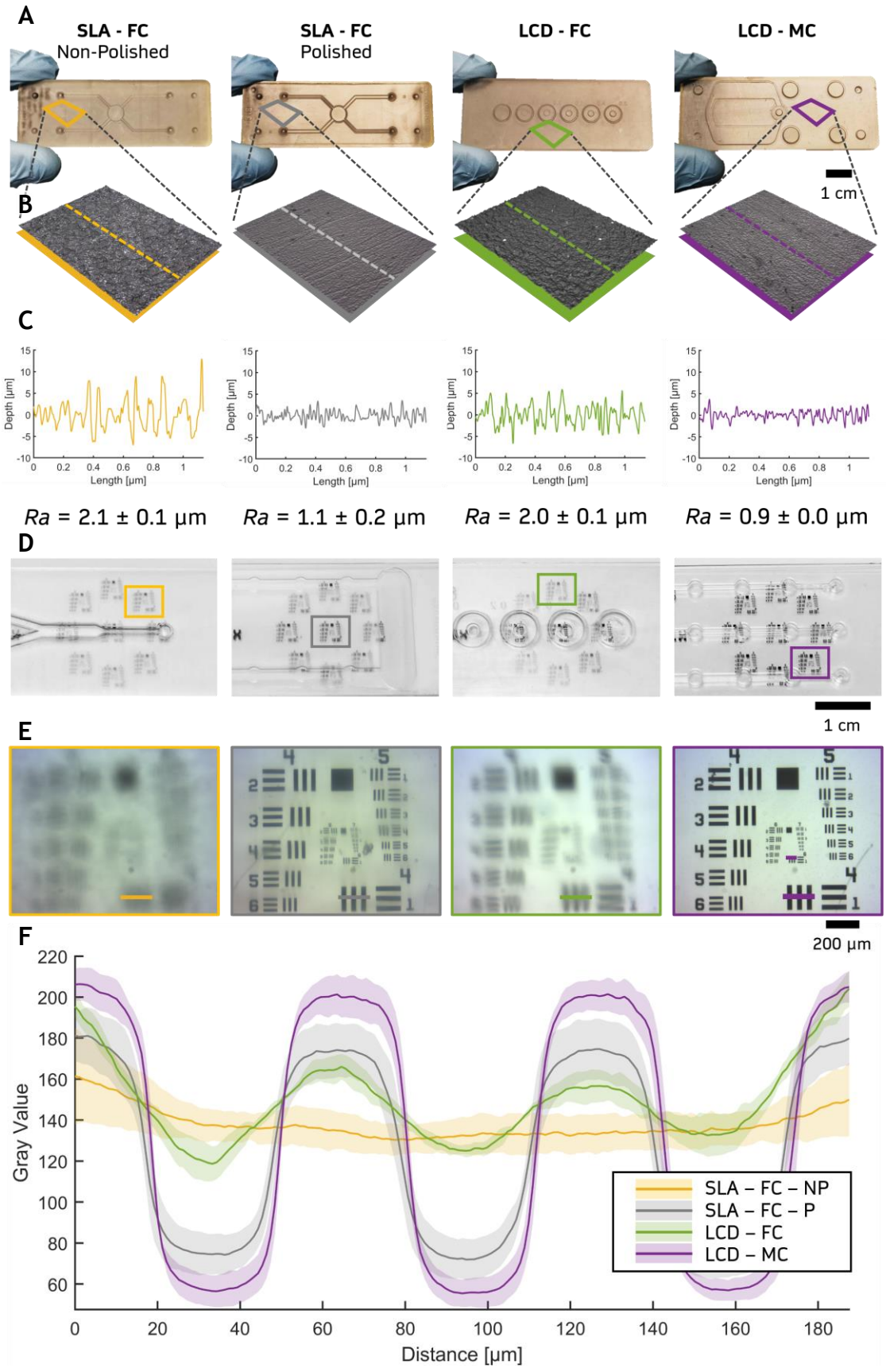

Figure 3.9: Surface roughness of moulds and optical transparency of injection moulded devices. A, Microfluidic RT moulds produced with the four different setups. B, 3D topography maps, obtained via optical profilometry, characteristic of each individual surface. C, Surface roughness profile and *Ra* value associated with each mould. D, Injection moulded polystyrene chips stacked on top of a resolution target. E, Higher magnification view over a single resolution pattern as analysed through the chip. F, Line resolution plotted as a function of grey value for the coarser zebra pattern of the optical target.

was recorded for the LCD-MC setup, with *Ra* = 0.9 ± 0.0 µm. Also, as observed by the standard deviation, results for roughness were very stable across the surface, evidencing great surface homogeneity as well.

The polymer chips obtained from the moulds in Figure 3.9 A are presented in Figure 3.9 D. The chips were placed on top of a resolution target, whose features are magnified in Figure 3.9 E, to provide a better analysis of optical resolution. It is possible to observe that optical transparency follows a similar trend to surface roughness. Both SLA-FC-NP and LCD-FC exhibit a low optical transparency, as evidenced by the poor visibility of the patterns on the resolution target, Figure 3.9 D. However, whereas the chips produced with the LCD-FC setup are capable of resolving features down to a resolution of 28-line pairs per millimetre (lp/mm), Figure 3.9 D, the chips obtained with the SLA-FC-NP setup exhibit a lower optical resolution, < 16 lp/mm, being incapable of resolving any feature from the target. An improvement to optical quality is observed with the SLA-FC-P setup. However, not only is optical clarity inconsistent across the substrate, Figure 3.9 D, being more effective in open surfaces than in areas close to channels or features, but there is a significant amount of imperfections and artefacts visible through microscopic as well, Figure 3.9 E. Nevertheless, the SLA-FC-P setup is capable of obtaining a resolution of 181 lp mm^{-1}. The results provided by the LCD-MC setup are more consistent. As it is possible to observe in Figure 3.9 D, the mould generated by the setup exhibits high optical clarity and great homogeneity across the entire surface and channels. A higher magnification view over a single resolution pattern, Figure 3.9 E, further demonstrates the superior optical quality generated by the LCD-MC setup, capable of resolving the maximum resolution of the test target, equivalent to 228 lp mm^{-1}.

To deepen the analysis on optical transparency, ImageJ was used to plot a line profile over the coarser zebra pattern, as highlighted in Figure 3.9 D, and address line resolution. This way, in Figure 3.9 E, it is possible to observe the intensity profile of the grey value along the plotted line, with each depression and crest representing respectively the white spacing and the black line. In this plot it is possible to observe that, while the SLA-FC-NP polymer chip is incapable of distinguishing between the different optical features, the LCD-FC chip exhibits an improvement, being capable of faintly distinguishing between the white lines (the peaks) and the black lines (the valleys). Better defined features are observed for

the SLA-FC-P setup, even though the highest quality is found for the LCD-MC setup. It is possible to observe that, not only is contrast superior for the LCD-MC polymer chip, as denoted by the steeper transition phases between white and black lines, but also amplitude, as evidenced by the greater magnitude between each peak and valley.

It is therefore possible to conclude that, regarding surface finish quality and subsequent optical transparency of polymer chips, LCD technology is the most promising. Low surface roughness values were obtained, directly after printing and without any additional procedures. This stands as a highly attractive feature for microfluidic RT and already an improvement to current state-of-the-art RT technologies. The LCD-MC setup was particularly promising in this aspect, providing the lowest roughness values and highest transparency of resulting polymer chips.

3.4 Resin Selection and Injection Moulding Compatibility

The previous tests led to the conclusion that LCD is the most promising technique for microfluidic mould fabrication. However, to ensure that the technology is indeed suitable for RT, the performance of the moulds during injection moulding must be investigated. Two aspects are particularly crucial to ensure their compatibility. These are firstly the ability to ensure mould release, greatly dependant on mould design and material and decisive in ensuring automation, and secondly tool life, similarly dependant on mould material and properties and fundamental in assuring scalability.

Therefore, to investigate both these aspects and ensure the compatibility of LCD technology for RT, LCD-printed microfluidic moulds were produced and explored in further depth in injection moulding. Beyond the previous two setups, LCD-FC and LCD-FC, both using transparent materials, a third was additionally introduced, using a pigmented resin formula to address the consensus over the usage of pigments to absorb light and improve feature resolution [277, 278] and investigate its implications for RT. Therefore, the Anycubic White (AW) resin was included in the following experiments, and parameters were determined according to the manufacturer instructions. More so, the LCD printer was updated to the Anycubic Photon M3 Premium, providing similar XY pixel resolution to that of the Phrozen

Sonic Mini 8K (28.5 μm to 22 μm), but increased vertical resolution (5 μm to 10 μm), wider printing volume (6.7 L to 2.1 L) and faster printing (93.9 mm/hr to 80 mm/hr).

This way, the respective LCD printer and the three photocurable resins involved, AW, MC and FC, were employed in printing RT containing a general-purpose microfluidic channel network, as shown in Figure 3.10 A. Channels presented a dimension of 500 x 500 μm (height x width) and contained a main chamber with a diameter of 4 mm. The respective microfluidic features were further designed with a draft angle of 10° to facilitate mould release, in alignment with current literature [156]. Testing involved assessing the mould release success rate and durability of each respective mould during a small injection moulding session of 50 cycles. The primary goal was to address material selection within the context of LCD RT, identify relevant properties and their respective implications for automation and scalability, and ultimately determine the most suitable resin material.

3.4.1 Mould Release and Side Wall Surface Properties

As expressed in greater detail in Section 2.1.1.1, the last stage of the injection moulding cycle is ejection. It consists of detaching the cooled polymer part from the mould by releasing the clamping force and opening the mould, and lastly using automated ejector pins to push the part outwards. While ejection is occurring, the next cycle has already begun. Therefore, ensuring all steps during the ejection stage take place systematically without issues is critical towards securing the automation of the whole procedure. From the respective steps, mould release is perhaps the one more tightly dependant on the properties of the mould and, in the case of RT, the properties of the 3D printed tooling. Therefore, the relevant properties contributing to or limiting mould release should be appropriately investigated. The draft angle of side walls is a design feature with well-documented influence in reducing friction between the polymeric part and the mould and ensuring successful mould release across all types of injection moulding tooling [279]. Similarly, 3D printed RT has also been shown to benefit from a draft angle ≥ 5° to ensure successful mould release [156]. However, when transitioning to LCD-based technology for tool making, the consequences of using extremely laminated moulds, with sidewalls presenting the bulbous profiles briefly identified

in Section 3.3.1, must be carefully investigated. Therefore, all three materials were evaluated by subjecting each respective mould to a run of 50 consecutive injection moulding cycles. Then, mould release success rate was investigated and further correlated with the relevant mould properties.

While the different materials were used to produce the same channels, as illustrated in Figure 3.10 A, their performance on automatic mould release was vastly different, as portrayed in Figure 3.10 B. It is possible to observe that, whereas the FC mould demonstrates a mould release success rate of 100 ± 0.0%, the AW and MC are significantly below this value, exhibiting a mould release success rate of respectively 22 ± 0.1% and 32 ± 0.1%. To understand the factors determining the discrepancies in performance between the three different resins, the cross section of channels of each respective mould were analysed, as shown in Figure 3.10 C. The figure highlights critical differences in channel sidewall waviness between the FC, AW and MC moulds. Both the AW and MC exhibit high stratification of layers. However, whereas the AW displays a distinctively rough surface and irregular pattern, the MC exhibits a regular profile despite laterally salient layers. Both surfaces define a significantly wavy surface, prone to increase the friction between the mould and the polymeric part and decrease the success rate of mould release. The values for waviness can be respectively observed in Figure 3.10 D, with the AW presenting a waviness of 3.1 ± 0.4 μm and the MC of 3.0 ± 0.2 μm. On the other hand, a significantly lower side wall waviness is observed for the FC mould, with a measured value of 1.9 ± 0.4 μm, representative of the smoother profile observed in Figure 3.10 C. The effects of the high stratification and lateral expansion of layers is better visualized when analysing the cross sections of each individual layer more closely. Beforehand, it is also important to distinguish between a draft and an interlocking angle. A draft is when the angle between the perpendicular to the mould's surface and the sidewall is negative, which results in the reduction of friction and promotion of mould release during injection moulding. On the other hand, an interlocking angle is when this angle is positive, therefore creating cervices which contribute to locking the cooled polymer to the mould during injection moulding, and reduce the likelihood of automatic mould release. These crevices, which result from asymmetrical photopolymerization across a single layer (where the regions near the light source benefit from greater photopolymerization, and subsequent lateral expansion of

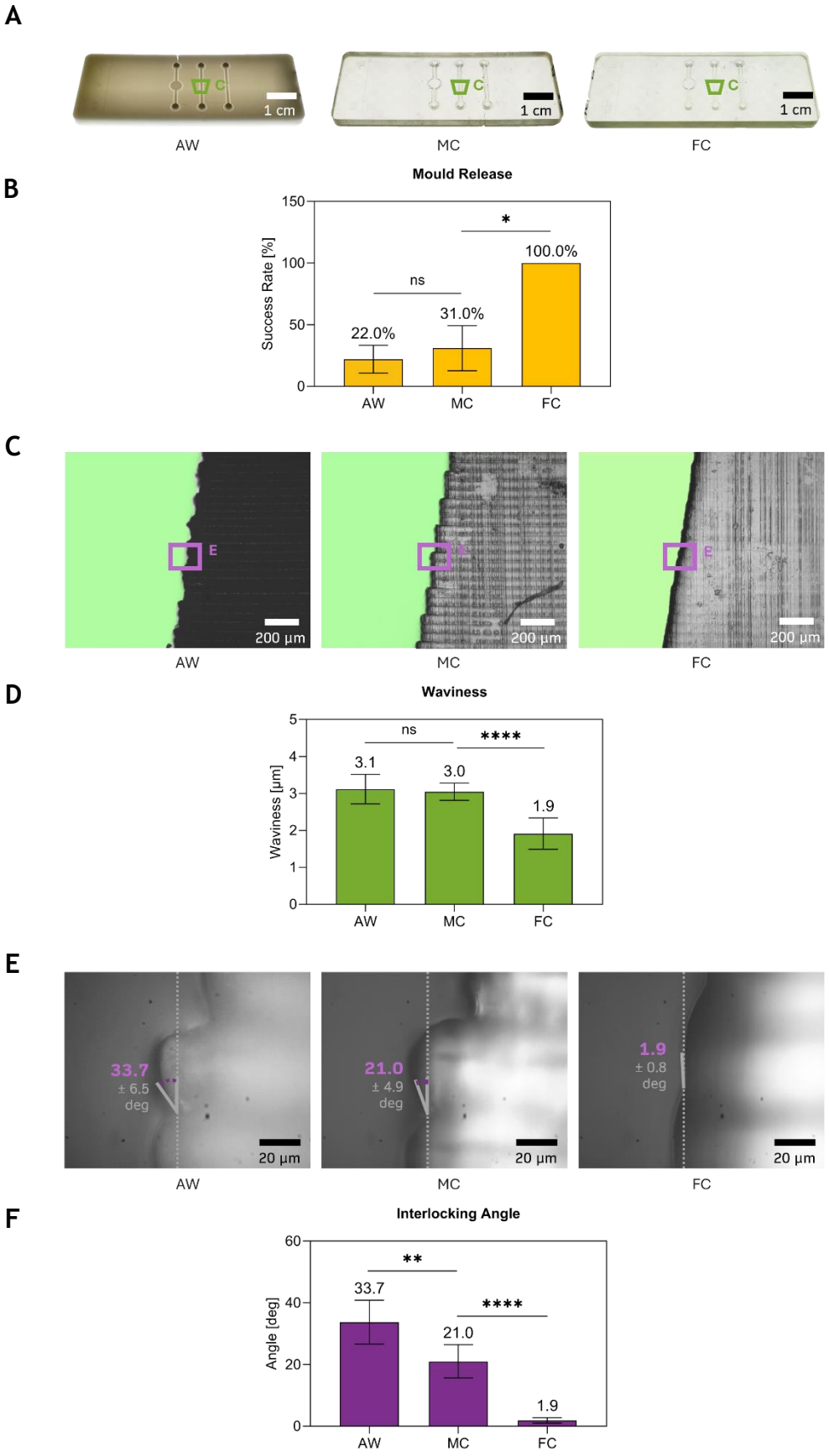

Figure 3.10: Mould release as a function of wall waviness and interlocking angle. A, Moulds produced using the three tested resins. B, Mould release success rate measured for each of the tested resins. C, Close-up of the cross-sectional sidewalls of channels. D, Sidewall waviness measured for each of the tested resins. E Higher magnification view over the lateral profile of a single printed layer. F, Interlocking angle measured for each of the tested resins.

the material, than those further away) are better visualized in Figure 3.10 E. They define higher interlocking angles, of 33.7 ± 6.5° and 21.0 ± 4.9° for the AW and MC moulds respectively, as shown in Figure 3.10 F. On the contrary, the FC mould displays a smoother profile, with less salient layers, as observed in Figure 3.10 E, resulting in a much lower interlocking angle, close to the vertical at 1.9 ± 0.8°, as displayed in Figure 3.10 F. Ultimately, this defines a profile which promotes mould release, and explains the results obtained in Figure 3.10 B. It is therefore possible to conclude that the FC resin appears to be the most suitable to increase the success rate of mould release, and therefore, ensure the automation of the injection moulding procedure.

3.4.2 Tool Life and Surface Deflection

The properties of the mould are equally as important in determining the length of the production run, and hence the scalability of the injection moulding procedure. As highlighted in greater detail in Section 2.1.1.3, traditional tooling for injection moulding is made of steel, to ensure properties, such as high rigidity, yield strength, toughness, wear resistance, and thermal conductivity, that may contribute to the longer durability of the tool. On the other hand, RT, made from 3D printed components, are well-known to provide poorer mechanical properties, as described in Section 2.1.3, ultimately leading to a significantly limited tool life. These lower mechanical properties are, however, linked not only to the material involved, but also to the 3D printing process itself. As explained in Section 2.1.2.1, during SLA-based 3D printing methods, such as LCD, the photocurable resin is selectively exposed to UV light, forcing photopolymerization to occur, layer by layer, until a solid 3D component is obtained. During photopolymerization, the prepolymer transitions from a liquid to a solid state, as the polymer chains cross-link to form long-chain macromolecular polymers [280]. This reaction is induced by photoinitiators and is exothermal, involving sudden thermal expansion and contraction [281]. Both the structural change at the molecular level, and the exothermal nature of the process, contribute to the inevitable shrinkage of the solid-state polymer. If shrinkage is poorly controlled, due to inappropriate printing parameters or a less adequate resin formulation, it can lead to high interfacial stress between layers, not only affecting the physical appearance of the component due to wrapping, but also affecting its mechanical properties. Ultimately, for RT, it means that tool life may be compromised. To investigate

the durability of the three different resins, each mould was subjected to continuous injection moulding until fracture, to characterize their respective tool life. The geometry of the tested moulds was similar to that of the moulds presented in Figure 3.10 A.

The results on tool durability are present in Figure 3.11 A. Both the AW and MC moulds exhibit a poor performance, withstanding respectively only 11 ± 6 and 16 ± 5 injection moulding cycles, after which they suffered significant mould damage. Ultimately, such a limited tool life renders these resins incompatible with long-term, continuous production. On the other hand, the FC displays a superior performance characterized by a distinctively higher durability, enduring up to 500 injection moulding cycles without any severe damage or failure. Beyond the various mechanical properties involved, it was observed that interfacial stress, reflected by surface deflection, presented a significant role in the development and propagation of fractures. As observed in Figure 3.11 B, the moulds display varying levels of surface deflection, with the FC displaying the lowest value, of 0.15 ± 0.1 mm. The values for the AW and MC are significantly superior, at 0.68 ± 0.3 mm and 0.46 ± 0.3 mm, respectively. These results suggest that the latter resins experience higher levels of interfacial stress, which ultimately contributes to the propagation of fractures, particularly when under the cyclic temperature and pressure characteristic to the injection moulding procedure. This way, tool life is significantly compromised and reduced. On the other hand, the FC mould experiences a significantly lower surface deflection, which reflects lower levels of interfacial stress. This contributes to its superior performance on tool durability and, ultimately, its higher compatibility to endure long-term, continuous injection moulding production.

Consequently, it can be concluded that the FC resin provides the best durability and hence tool life, and is therefore the more suitable material to secure the scalability of injection moulding when using RT.

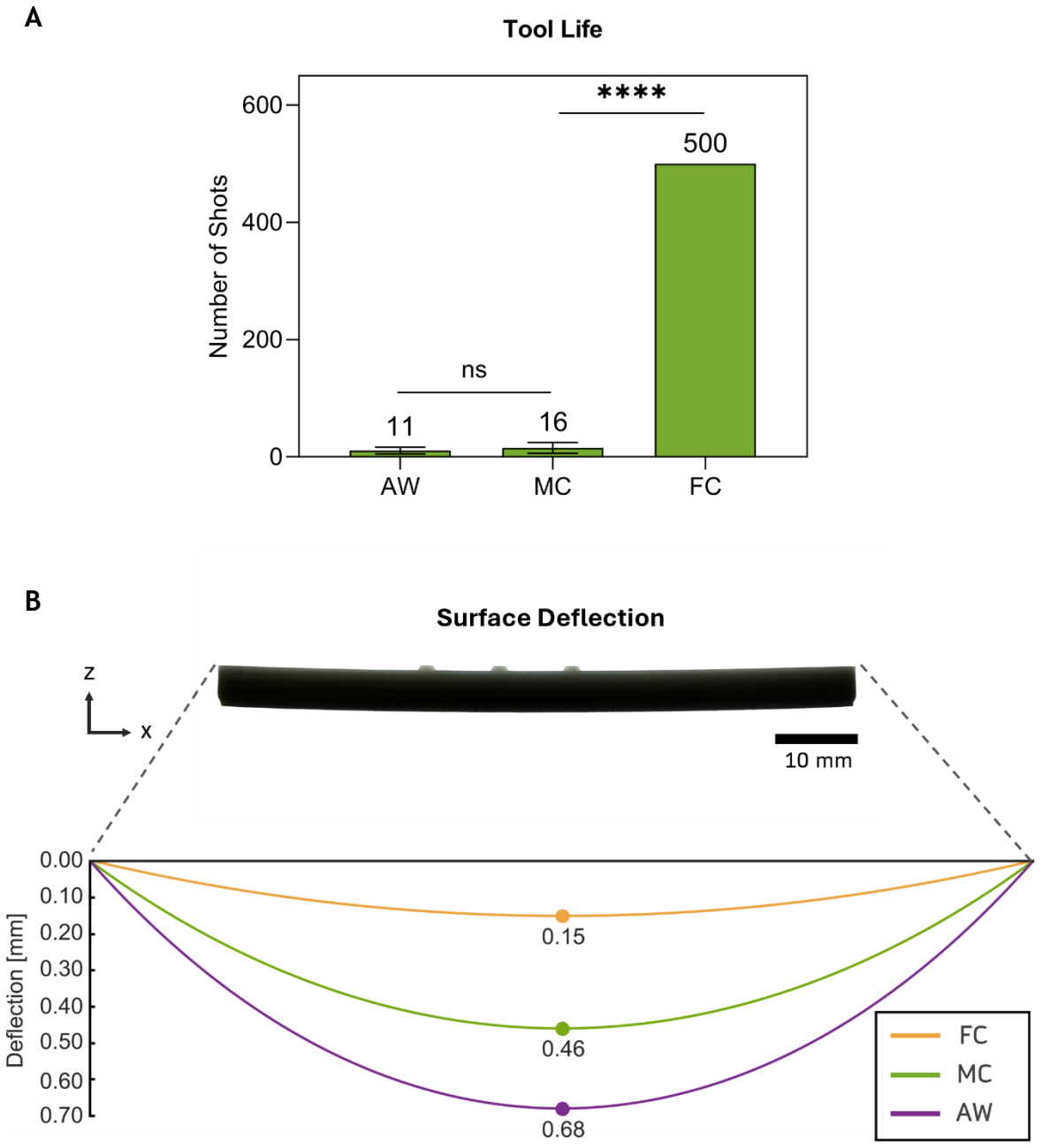

Figure 3.11: Tool life investigated as a function of surface deflection. A, Tool life measured as a function of number of injection moulded shots and plotted for each of the tested resins. B, Side view of the AW mould, illustrating its surface deflection, and below, the total surface deflection measured for each of the tested moulds.

3.5 Impact of Layer Exposure

From the various slicing parameters available, the most impactful is layer exposure. Within general slicing software, layer exposure is defined as a time interval, determining the period which the LCD screen is turned on and, consequently, the prepolymer resin is exposed to UV light for each layer. Depending on the power output of the LCD screen, layer exposure determines the total amount of energy transferred to the prepolymer resin for

photopolymerization to occur. It is a fine balance determining optimal energy dosage and, therefore, optimal layer exposure. If the energy dosage is insufficient, then the model will experience underexposure, manifested by soft spots, uncured sections, undefined geometries, failed features or an entirely failed print. On the other hand, if the energy dosage is excessive, then the model will experience overexposure, evidenced by over dimensioned features, compromised geometry, and resulting in a more brittle component that is more prone to breaking.

The conclusions drawn from Section 3.4 suggest the most suitable resin to ensure compatibility with injection moulding is the FC. Not only does it promote mould release, but it also provides an extended tool life. Therefore, and given the compatibility with injection moulding is a compulsory aspect for RT, the experiments that follow will exclusively explore the FC resin. Nevertheless, this particular resin demonstrated clear signs of underexposure, following the analysis in Section 3.3. It was observed that, not only did some of the features display visible indentation, but also, dimensional accuracy presented a systematic offset in all axis, with features being consistently printed smaller than their CAD counterparts. Both occurrences suggest underexposure, and therefore imply deeper investigation and optimization of printing parameters, and particularly, layer exposure. This section will therefore address this aspect and explore the effects of layer exposure in modifying the properties of the mould.

To analyse surface roughness, blank moulds featuring a flat, empty surface were devised and printed, whereas templates similar to those displayed in Figure 3.10 A were used to investigate feature geometry and dimensional accuracy. More so, each mould and template were respectively printed for an array of different layer exposures, ranging from 10 to 70 s. To further evaluate optical transparency as a function of surface roughness and layer exposure, each of the blank moulds, printed at different exposure rates, were injection moulded, and their polymer chips evaluated using a testing target, as described in Section 3.2.7.

3.5.1 Surface Roughness and Optical Transparency

Optically based analytical techniques are fundamental for the majority of microfluidic applications. Therefore, substrate transparency is an imperative

aspect that should be ensured with the appropriate selection of material and fabrication procedure. Similarly, in the process of establishing RT as a viable candidate for the fabrication of microfluidics, the development of methods capable of systematically achieving appropriate optical transparency is an essential aspect. Nevertheless, current literature provides very limited work in this regard, with the only suggested approach being manual polishing [156]. However, as shown in Section 3.3.2, manual polishing has several drawbacks. First, it is both time consuming and laborious, this way defeating the purpose of establishing a scalable, automatic fabrication method. And second, not only does it compromise the structural integrity of microfluidic features, particularly when high aspect ratio features are involved, but also, as demonstrated in Figure 3.9, generates inconsistent results across the mould's surface. Therefore, a more practical and systematic approach to reducing the surface roughness of moulds and increasing the optical transparency of the subsequent polymer chips should be developed towards the successful establishment of RT for microfluidics.

It was found that, to improve on surface roughness and optical transparency, layer exposure presents a reliable and effective pathway. As Figure 3.12 A demonstrates, there is a direct correlation between layer exposure and surface roughness. As layer exposure increases so does surface quality, with surface roughness following the inverse trajectory. In Figure 3.12 B, high-resolution 3D topographical maps are displayed, evidencing the effects of layer exposure in reducing surface roughness at length scales similar to those of single cells. This relation is better illustrated in Figure 3.12 C, where surface roughness is plotted as a function of layer exposure. It is possible to observe that by increasing layer exposure, it is possible to significantly decrease surface roughness. This decrease is particularly significant between 10 s to 50 s of layer exposure, with surface roughness reducing from Ra = 1.1 ± 0.1 µm to Ra = 0.2 ± 0.0 µm, respectively. Beyond the value of 50 s, roughness was seen to fluctuate and marginally increase. In the same plot, a reference to the surface roughness of the perfluoroalkoxy alkane (PFA) film used in the printing vat can further be seen, with a value of Ra = 0.2 ± 0.0 µm. This was included to provide a baseline value for roughness, to which the printed surfaces tend with the increase of layer exposure and enhancement of vat polymerization.

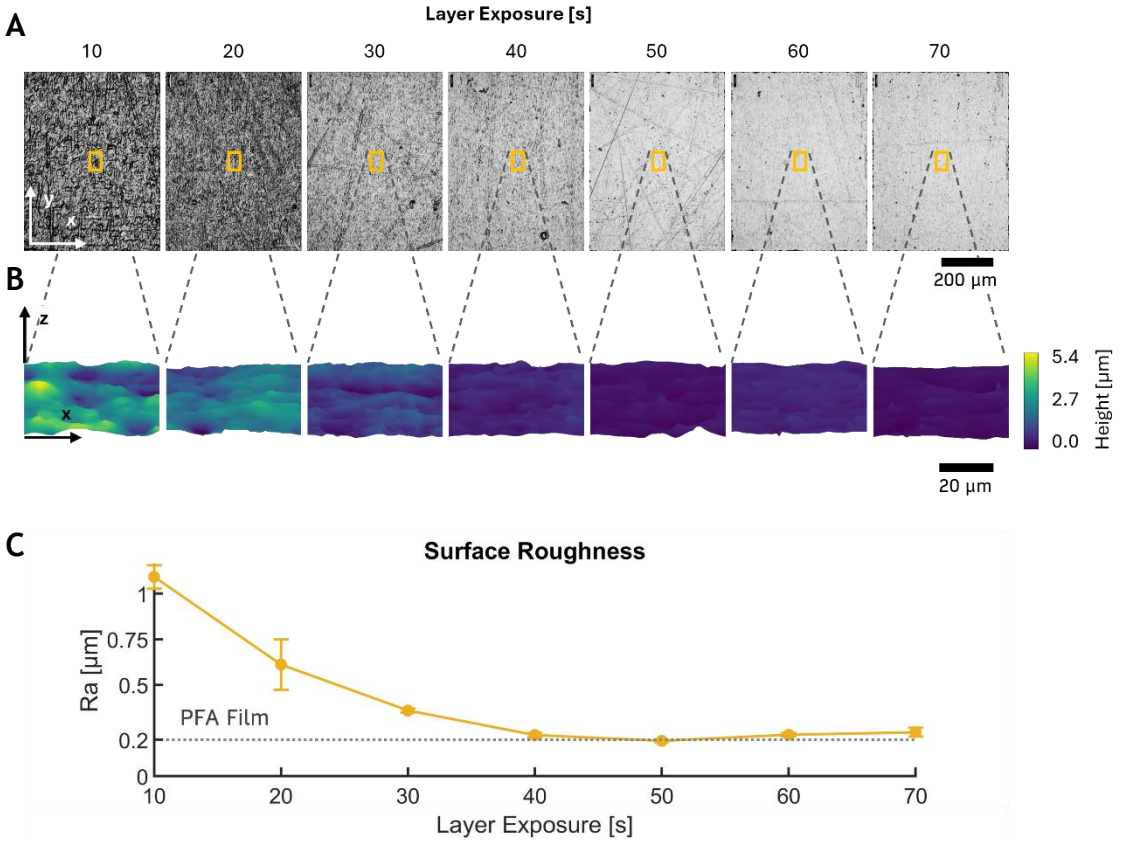

Figure 3.12: Effect of layer exposure on printed mould surface roughness. A, Surface maps evidencing the influence of layer exposure on surface roughness. B, High-resolution 3D topographical maps, 50 µm wide, demonstrating surface roughness at a length scale similar to that of a single cells. C, *Ra* as a function of layer exposure, and with reference to the surface roughness value measured for the PFA film used in the printing vat.

Following injection moulding with the respective moulds, it was further observed that optical transparency follows the same trend. As seen in Figure 3.13 A and B, the optical transparency of injection moulded substrates is enhanced for moulds printed at a higher layer exposure. Above a layer exposure of 20 s, chips achieve a resolution of 228 lp/mm, equivalent to the maximum level measured by the optical target. To provide a more significant measure of resolution and transparency, a similar approach to that described in Section 3.3.2 was here as well employed. This way, a line was plotted over the coarser zebra pattern, as illustrated in Figure 3.13 B, and the grey value intensity along the line retrieved. The obtained profile was then used to calculate line contrast and amplitude, and plot them as a function of layer exposure, as demonstrated in Figure 3.13 C and D. It is shown that, as layer exposure increases so does contrast and amplitude. This increase is sharpest from 10 s to 40 s, and more moderate from 40 to 70 s. Ultimately, the replicas produced from moulds printed with a layer exposure of 70 s exhibit a line contrast of 47.6 ± 5.3 grey scale/mm and an amplitude of 169.0 ± 1.6 grey scale. Such values are comparable to those of a standard glass

microscopic slide, showcasing under the same conditions a line contrast of 52.5 grey scale/mm and an amplitude of 177.0 ± 0.8 grey scale, as included in Figure 3.13 D.

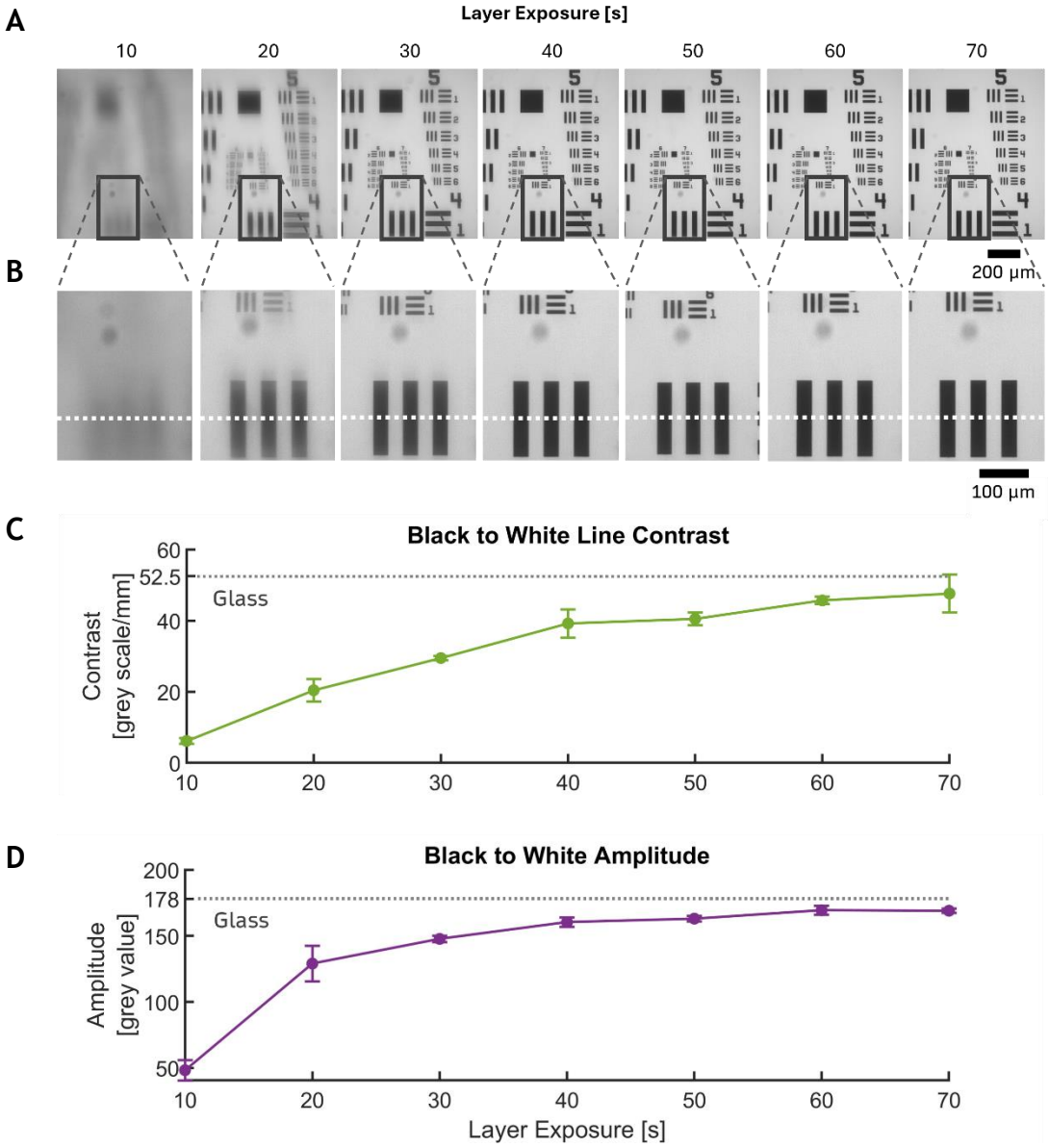

Figure 3.13: Effect of layer exposure on polymer part transparency. A, Optical transparency investigated as a function of layer exposure, using an optical target as reference. B, Higher magnification view of the coarser optical pattern in the resolution target, evidencing the line from which the values for contrast and amplitude were measured. C, Line contrast as a function of layer exposure, with reference to the contrast value measured for glass. D, Black to white amplitude as a function of layer exposure, with reference to the amplitude value measured for glass.

3.5.2 Dimensional Accuracy and Feature Resolution

As defined in Section 1.1, microfluidics is the field of research which operates minute amounts of fluid in micro scale channels, defined as ranging from 0.1 to

100 µm [3]. A true microfluidic system and a viable fabrication procedure should, therefore, comply to these requirements. The sub 100 µm boundary remains, nevertheless, a challenge for present day SLA-based 3D printed microfluidics [146], with most methods requiring either a modified SLA setup or the development of specific resin formulas, to overcome the respective barrier. Part of the challenge lies in producing closed channels, at the respective dimensional range, without the risk of clogging, due to resin trapping and curing. To this, microfluidic RT provides a solution. By printing a mould, as illustrated by Figure 3.1 in Section 3.2.1, rather than a fully functional microfluidic device, it does not involve the fabrication of sealed channels, and therefore relaxes these requirements. Nevertheless, and perhaps reflecting the limited amount of work published in the field, this aspect has not contributed to increase channel resolution in microfluidic RT. Instead, feature resolution in moulds produced for RT remains similarly at 100 µm, as reported at the start of this chapter. To assess dimensional accuracy as a function of layer exposure and to provide a measure of feature resolution for the current setup, a template similar to that presented in Figure 3.5 was printed for the different analysed layer exposures, ranging from 10 to 70 s. By incorporating both protrusions, features presenting a positive height, and cavities, features presenting a negative height, the effect of polarity was also investigated.

This way, results were obtained characterizing the effects of layer exposure in determining the dimensional accuracy for both cavities, Figure 3.14, and protrusions, Figure 3.15 The array of different squared-shaped cavities, printed with different dimensions, from 100 to 1000 µm, for the various analysed layer exposures, is present in Figure 3.14 A. In Figure 3.14 B, cavity width is measured and plotted as a function of layer exposure and according to the different feature sizes. In Figure 3.14 C, the offset between the printed and CAD width is plotted, to highlight dimensional accuracy. One of the first points to discuss is the inability of the current setup to print cavities with a width < 400 µm, regardless of the layer exposure applied, as shown in both Figure 3.14 A and B. Above this range, results demonstrate that cavity geometry, Figure 3.14 A, resolution, Figure 3.14 B, and dimensional accuracy, Figure 3.14 C, undergo a significant decline with the increase of layer exposure. A layer exposure of 10 s results in accurate dimensions, with an offset of, on average, -30.1 ± 24.5 µm in relation to the original CAD

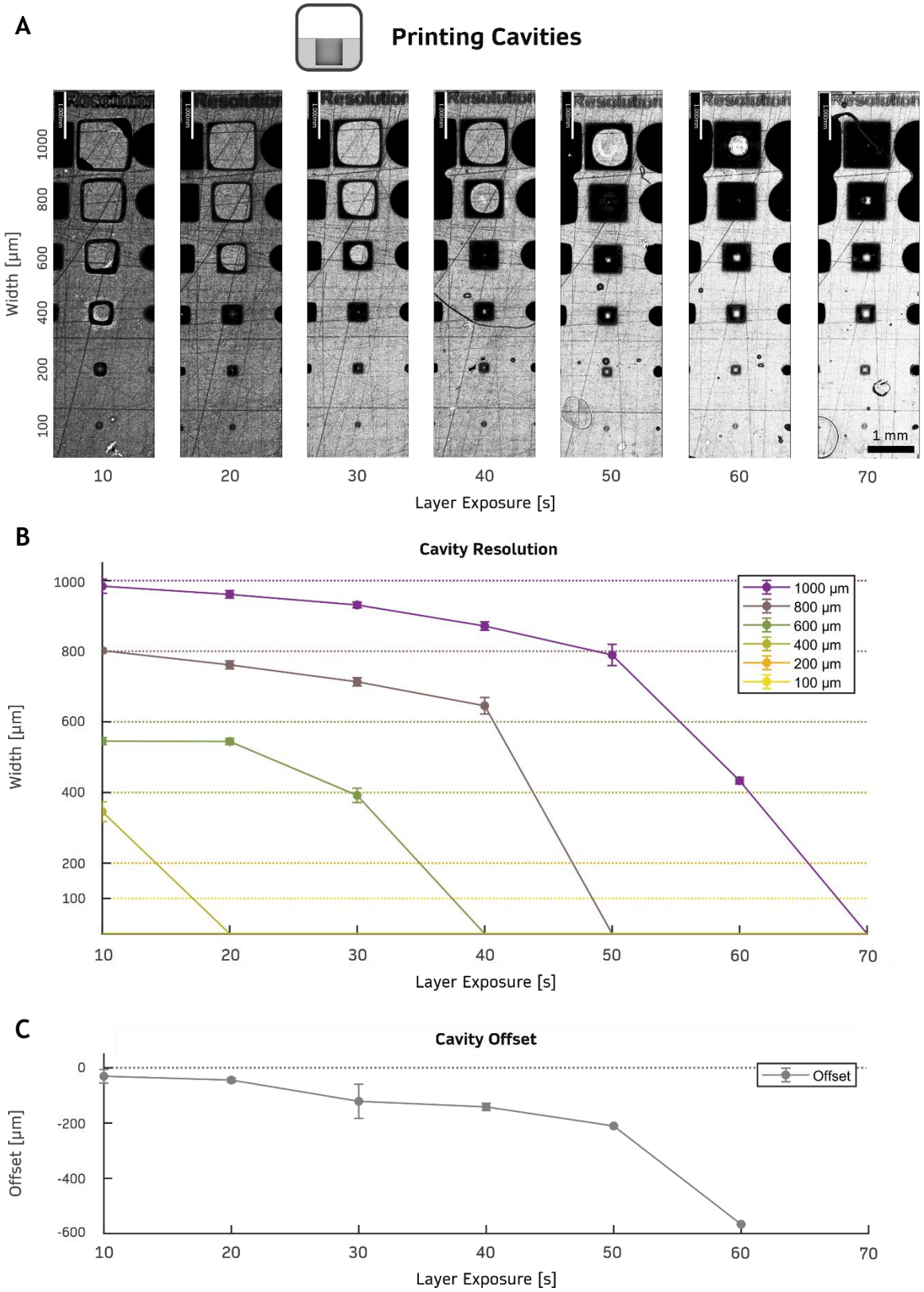

Figure 3.14: Effect of layer exposure on the dimensional accuracy of printed cavities. A, Array of cavities with widths from 100 to 1000 µm, printed with layer exposures from 10 s to 70 s. B, Resolution of cavities as a function of layer exposure. C, Dimensional accuracy of cavities, as measured by the average offset between CAD and printed dimensions, according to layer exposure.

dimensions. Curved walls and rounded edges suggest, nonetheless, a slight underexposure. Feature geometry improves with the increase of layer exposure, displaying finer edges and sharper corners for a 20 s exposure. However, it comes at the expense of cavity resolution, unable of resolving features 400 μm wide. A slight decline is also observed in the dimensional accuracy of cavities ≥ 600 μm. This effect enhances with the increase of layer exposure, with light scattering induced by overexposure reducing the overall level of detail. With a layer exposure of 70 s, results evidence the inability of resolving cavities as wide as 1000 μm.

A similar analysis is presented for printed protrusions which exhibit, nonetheless, a different relationship to the effects of layer exposure. Figure 3.15 A displays the array of square-shaped protrusions printed with different dimensions, from 100 to 1000 μm, for the various analysed layer exposures. In Figure 3.15 B, the width of protrusions is plotted according to the different feature sizes and as a function of layer exposure, and in Figure 3.15 C, the offset between the printed and CAD width is displayed. It is possible to observe that, contrary to cavities, the dimensional accuracy of protrusions improves with the increase of layer exposure. This is due to the effects of overexposure in increasing photopolymerization and expanding the material. Opposing feature polarities further means that, whereas for cavities an increase of layer exposure compromises their resolution by narrowing the spacing between walls, for protrusions, it results instead in the increase of their feature width. The latter effect is particularly evident in Figure 3.15 B and, importantly, it results in the increase of dimensional accuracy for this setup. It is possible to observe that with a layer exposure of 10 s, dimensional accuracy is low, with the width of protrusions exhibiting an average offset of -152.2 ± 17.4 μm to the original CAD file. On the other hand, at 70 s, dimensional accuracy is more accurate, already presenting a positive offset equivalent to 4.5 ± 10.6 μm. Nevertheless, dimensional accuracy is optimal for the layer exposure of 60 s, with a minimal average offset of 0.1 ± 8.5 μm recorded. Finally, it is noteworthy that the current setup achieves feature resolutions of < 50 μm, Figure 3.15 B.

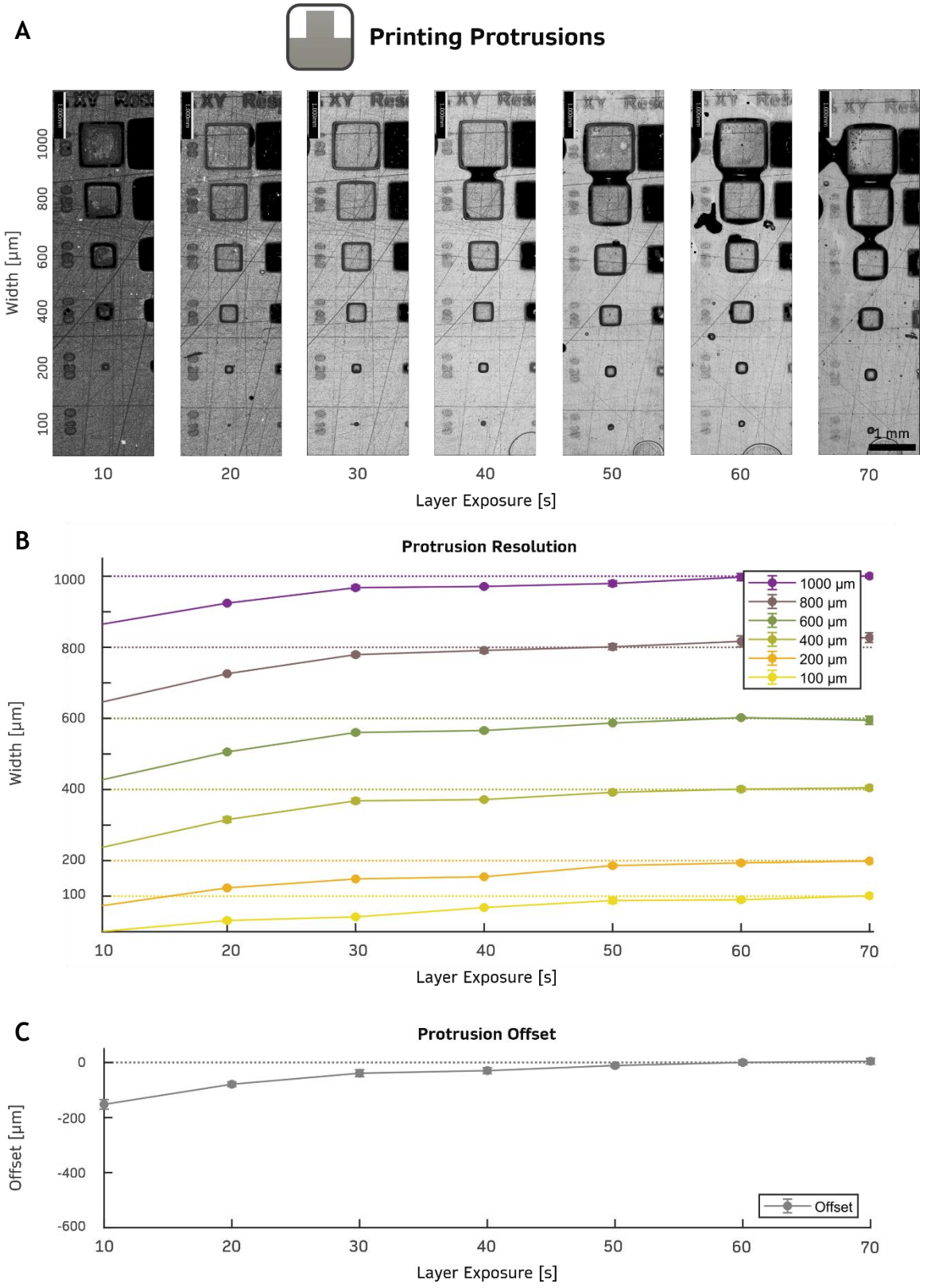

Figure 3.15: Effect of layer exposure on the dimensional accuracy of printed protrusions. A, Array of protrusions with widths from 100 to 1000 µm, printed with layer exposures from 10 s to 70 s. B, Resolution of protrusions as a function of layer exposure. C, Dimensional accuracy of protrusions, as measured by the average offset between CAD and printed dimensions, according to layer exposure.

3.6 Mechanical Properties and Feature Reproducibility

Section 3.4.2 provided a measure for tool life as a function of the selected prepolymer resin. It described a preliminary procedure to select the most promising resin for scalable manufacturing, using surface deflection as an indicator for the different levels of interfacial stress experienced by the different moulds. However, durability and tool life are, to a much greater degree, dependant on the mechanical properties of the mould. As discussed in Section 2.1.1.3, properties such as rigidity, yield strength, toughness, wear resistance, thermal conductivity and thermal expansion, are some of the factors taken into consideration during mould design and fabrication. The ability to address each of these properties individually, through various different alloys, is what ultimately makes steel the material of choice for tool fabrication in injection moulding.

In the context of microfluidic RT, the development of a material capable of similarly addressing these properties remains an ongoing challenge. A very interesting study, highlighted in the introduction of this chapter, was conducted by Walsh et al 2021, investigating the most relevant mechanical properties determining the success of microfluidic RT for injection moulding [276]. From the various properties analysed, the flexural modulus (equivalent to the modulus of elasticity, or Young's modulus, for isotropic materials such as most polymers) and elongation were found to be the most important, ensuring a material less likely to experience failure and more prone to increase mould release. Control over these properties is especially relevant at the length scale of microfluidic features, where fine details are critical in ensuring the functionality of devices. Furthermore, it is the ability to ensure the precise reproducibility of the respective microfluidic features, over the course of continuous injection moulding operation, that defines the scalability of the procedure.

This section therefore addresses methods to control and modify the mechanical properties of 3D printed moulds, as well as the resulting reproducibility of microfluidic features during injection moulding. To do so, a tensile specimen was printed and post-processed according to different curing parameters, such as temperature and exposure to UV light. In agreement with literature, the respective parameters were found to provide significant control over the mechanical properties of the mould, including the Young's modulus and

elongation. This analysis provided ground data to determine the optimal post-processing parameters for the presented microfluidic RT setup, capable of maximizing the mechanical properties of the 3D printed mould. Using the respective protocol, different microfluidic features, including channels and I/Os, were incorporated in a mould according to various orientations and draft angles to be tested with injection moulding. The mould was tested over a short production run of 500 injection moulding cycles, and features were analysed for durability and reproducibility by investigating their respective dimensional and geometric accuracy as a function of the cycle number.

3.6.1 Post-Processing Parameters and Mechanical Properties

The process of SLA is known to only partially polymerise the liquid-state resin, generating a polymer known to be in a green state [126]. Green state polymers are generally characterized by having a tacky surface and a reduced rigidity. Only through post-processing techniques, such as thermal and UV exposure, the residual photoinitiators can be activated to cross-link the remaining polymeric chains and achieve a greater level of polymerization. By doing so, the structure of the polymer is strengthened and its mechanical properties are increased [127]. The polymer is then known to be in a cured state. Precise control over post-processing parameters is therefore critical in ensuring the suitable mechanical performance of cured state components. Particularly in the context of microfluidic RT, the optimization of the post-processing protocol is key in determining the durability and reproducibility of features. To investigate the effect of UV exposure and curing temperature in regulating the mechanical properties of the post-processed polymer, tensile testing was performed. Tensile specimens, as previously illustrated in Figure 3.3 A, were therefore prepared and post-processed according to individual values for curing time, 15, 30 and 45 min, and temperature, 45, 60 and 75°C. Each tensile specimen was then evaluated using a universal tester, as demonstrated in Figure 3.3 B, and their mechanical performances were recorded as a function of their respective post-processing protocol. From the obtained stress-strain curves, mechanical properties such as the Young's modulus and elongation were calculated, as illustrated in Figure 3.3 C, this way assessing both the stiffness and ductility of 3D printed tooling.

The compiled results describe both the changes in Young's modulus and elongation according to the different tested post-processing protocols, as shown in Figure 3.16 A and B, respectively. It is possible to observe, in Figure 3.16 A, that despite the different tested protocols, the Young's modulus remains relatively stable, presenting only minor variation. Nevertheless, the conditions yielding a higher modulus, of 3.4 ± 0.1 GPa, and therefore greater stiffness, are those characterized by a curing time of 30 min and a temperature of either 60 or 75°C. On the other hand, Figure 3.16 B demonstrates that elongation is more susceptible to post-processing parameters. It is observed that, as the curing temperature increases, the mechanical properties generally shift from ductile to brittle. Regarding the curing time, it is observed that a duration of 60 min generally yields better results, with the exception of the protocol done at 75°C. Towards enhancing elongation and therefore increasing the likelihood of injection moulding success [276], results determine that the optimal post-processing conditions are described by a curing time of 30 min and a curing temperature of either 45 or 60°C. Such conditions yield an elongation value of 3.4 ± 1.2% and 3.4 ± 0.7% respectively. Having both the Young's modulus and elongation in consideration, the optimal post-processing protocol for the current setup, ensuring both stiffness and ductility, is described by a curing time of 30 min and a curing temperature of 60°C.

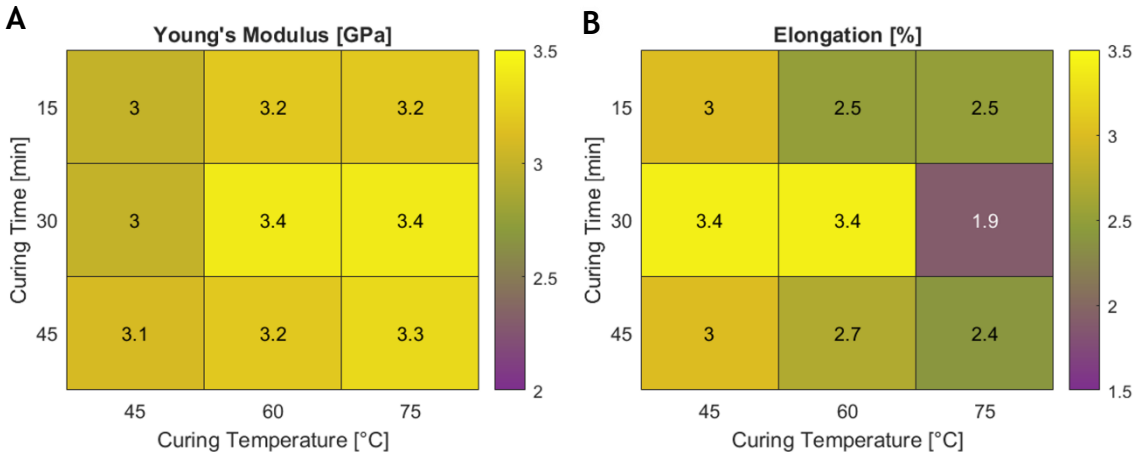

Figure 3.16: Mechanical properties as a function of post-processing parameters. A and B, Values obtained for the Young's modulus and elongation, respectively, as a function of both the curing temperature and curing time.

3.6.2 Feature Properties and Reproducibility

The design of microfluidic devices incorporates a wide variety of different geometric features with unique fluidic purposes. From microfluidic channels, intersecting junctions, mixing and reaction chambers, I/Os, to higher degree

elements, such as valves, filters and sensors. An analysis to feature reproducibility should, therefore, address to some degree this geometric variety as well. The two most fundamental elements in any basic microfluidic network are the microfluidic channels and the I/O ports. While fabricating microfluidic channels with RT is a relatively trivial task, consisting of extruding protrusions with the desired shape and dimension, and the opposing polarity to that of the final polymer substrate, obtaining I/O ports is not. It involves creating high aspect ratio protrusions, extruded to the height limit of the mould cavity, to block the local flow of polymer melt during the mould filling stage, and create a through hole across the polymeric replica. Incorporating such features provides broad benefits to the scalability of microfluidic devices fabricated via RT. Not only does it systematize the creation of I/O ports into the final polymer devices, something not yet reported within microfluidic RT, but provides as well the potential of saving up to an hour per every 100 polymer chips produced [156], avoiding the labour associated with manually drilling the holes for every individual device.

The fabrication of I/O ports with RT involves two major challenges. First, features need to be designed with a height similar to that of the injection moulding cavity. However, the feature should not directly contact the opposing surface of the cavity, to avoid tool damage resulting from the cyclic, high pressure opening and closing of the moulds. Therefore, minimal spacing should be considered between the top surface of the I/O feature and the opposing surface of the mould cavity, to avoid direct contact between the tools whilst preventing the local flow of molten polymer. Second, in order to operate at a height similar to that of the mould cavity, I/O features have to necessarily possess a high aspect ratio. This further means that such features are more prone to wear and tear, due to the increased surface area of their side walls and the additional friction involved during the mould release stage of the cooled polymer. This way, both challenges involve careful geometric consideration regarding the height of features and their appropriate draft angle, towards allowing the scalable creation of I/O through holes without the risk of tool damage.

Therefore, a preliminary study was conducted, focused on determining the optimal I/O feature height to obtain through holes on the polymer substrate. With this purpose, a mould was designed, Figure 3.17 A, and printed, Figure 3.17 B, with I/O features displaying a height gradient from 900 to 1150 μm. The mould

was further designed to incorporate a draft angle gradient, as the figure also displays. After injection moulding, and by analysing the resulting polymer chips, it was possible to analyse which geometric parameters enabled to obtain I/O ports. As Figure 3.17 C demonstrates, a minimal height of 1050 µm is necessary (corresponding to a spacing to the opposing surface to the tool of 150 µm) to obtain through holes for I/O ports in the polymer chips. It is also observed that the draft angle possesses no significant influence in establishing through holes, given that regardless of its value, and for a similar height, results do not change. However, the relevance of including a higher draft in reducing friction and therefore increasing the durability of I/O features, will be studied in the experiment that follows.

With a protocol to create microfluidic channels and I/O features via RT, a mould was designed, as illustrated in Figure 3.18 A, to integrate both features and analyse their reproducibility during injection moulding. The mould was then tested over a short production run of 500 injection moulding cycles, during which the reproducibility of features was evaluated by investigating dimensional accuracy and geometric integrity as a function of the cycle number. Microfluidic channels were designed to be 200 x 500 µm (height x width) and were printed both

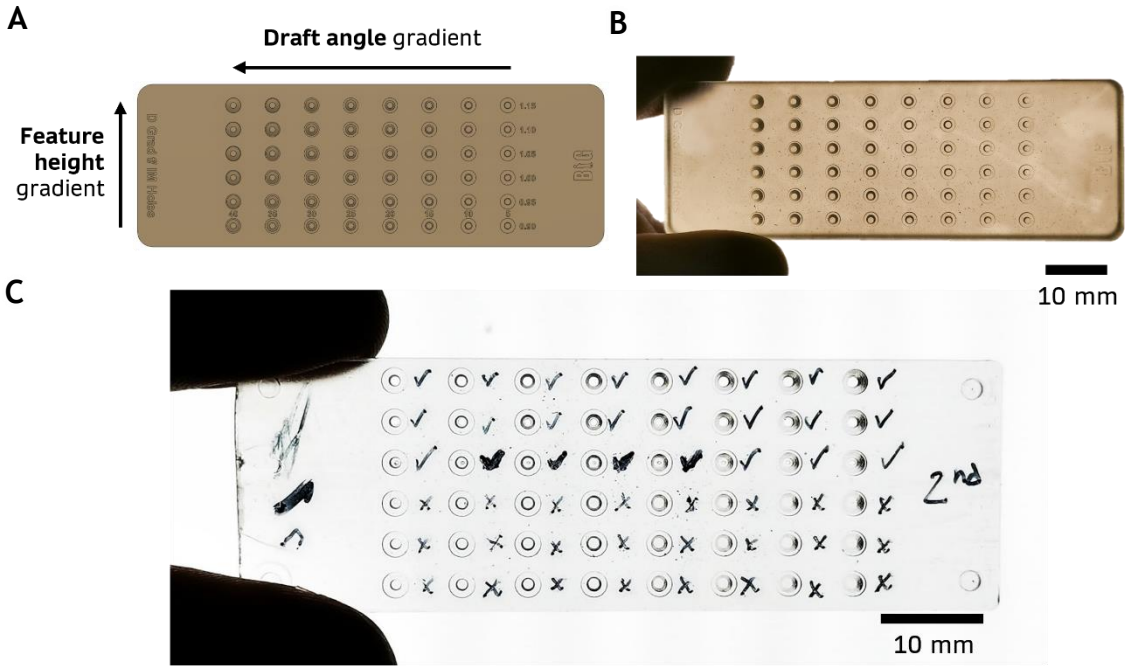

Figure 3.17: Fabrication of through holes with RT. A, CAD illustration of the mould investigating feature height and draft angle in the fabrication of through holes. B, The same mould after printing. C, The resulting injection moulded polystyrene chip highlighting, with a check, the parameter combinations resulting in a thorough hole and, with a cross, those which not.

parallel and perpendicular to the flow of molten polymer, elements b) and c) in Figure 3.18 A respectively, to assess the influence of feature orientation in durability. In turn, I/O features were printed with the dimensions of 1050 x 1000 µm (height x width) and a draft angle of 10° and 20°, elements d) and e) in Figure 3.18 A respectively, to address the influence of including a higher draft to reduce friction and increase feature durability.

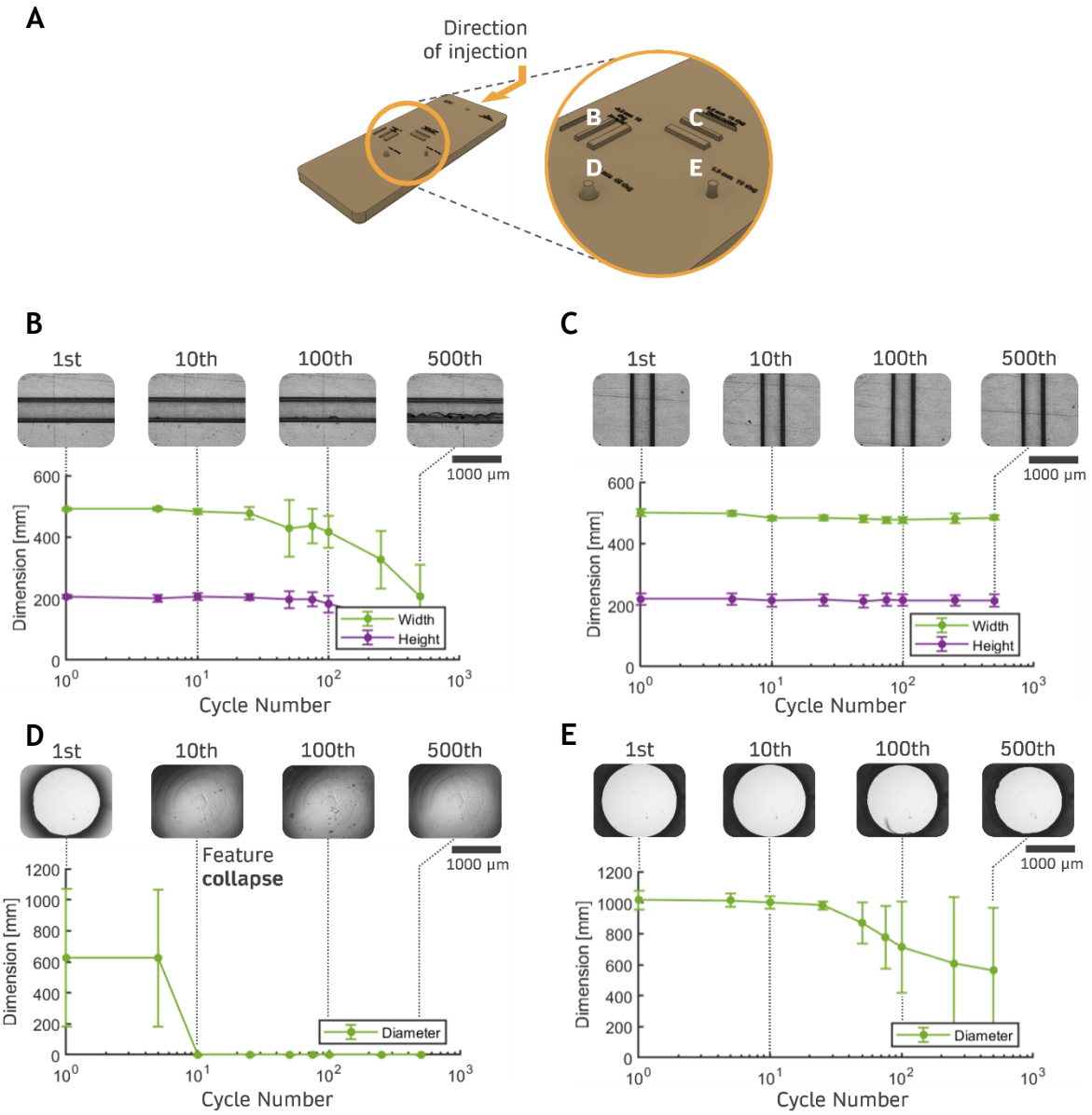

Figure 3.18: Feature reproducibility and durability as a function of design properties. A, CAD image of the mould used for the feature durability testing, providing a higher magnification view of the features under analysis as well as their respective orientation and geometric variations tested. The durability of channel features is plotted as a function of both width and height for features oriented, B, parallel and, C, perpendicular to the stream of molten polymer. Above each graph, images illustrate the degradation of features along the injection moulding test. The durability of pillars is measured as a function of diameter and expressed for a draft angle of, D, 10° and, E, 20°.

The results for channels parallel to the flow of polymer, Figure 3.18 B, demonstrate that reproducibility remains stable, despite only a minor decay, for the first 100 cycles. Onwards though, features undergo rapid deterioration. At the 500th cycle, the average height of the channels has reduced to 131.6 ± 29.2 μm and the width to 207.1 ± 103.3 μm, representing a percentage change of 36.1 ± 14.2% and 57.7 ± 21.1%, respectively. The change in orientation to perpendicular provides a wide increase in reproducibility, Figure 3.18 C. Results demonstrate that both the average height and width of channels remain very stable for the whole production run, presenting a percentage change of 2.5 ± 9.3% and 3.1 ± 1.7%, respectively. The reproducibility of I/O features with a 10° draft exhibits a much more fragile behaviour, Figure 3.18 D. Not only is the width of the feature compromised after the first cycle, presenting an average diameter of 625.5 ± 442.4 μm, but more critically, the feature is unable of sustaining more than 5 cycles before collapsing. A change in draft to 20° provides a great increase in robustness and thus reproducibility, Figure 3.18 E. Results demonstrate that the feature remains sound for the whole production run, nonetheless presenting a percentage reduction in diameter corresponding to 45.6 ± 39.7% after 500 cycles, with a final value of 553.8 ± 403.6 μm. This reduction is sharpest after the 25th cycle, from which feature diameter evidences a high degree of variability between different moulds.

3.7 Proof-of-Concept for Microfluidic Fabrication

Extensive characterization was performed to demonstrate both the compatibility, quality, and reproducibility of the current LCD-based RT method. In turn, to demonstrate its potential in the context of microfluidics, three different proof-of-concept devices were designed, manufactured and tested. These consist of single layer designs, defining a microfluidic maze, mixer, and droplet generator. Each design intends to highlight a different aspect of the current manufacturing procedure, by presenting different levels of geometric, manufacturing, and function complexity. The fabrication of the three respective devices followed the guidelines provided in the previous sections. This way, the prepolymer resin selected for mould fabrication was the FC, to ensure optimal mould release and tool life, as according to Figure 3.10 and Figure 3.11. To optimize printing time, multi-parameter slicing was performed. All layers prior to the surface of the mould were printed with the minimal exposure time of 30 s, whereas for the single

surface layer, exposure was increased to 70 s, ensuring improved surface properties and optimal optical transparency, as according to Figure 3.13. In turn, the layers equivalent to the channels were printed with a reduced layer exposure of 50 s, to save time whilst providing precise dimensional accuracy, as described in Figure 3.15. Layer exposure was then increased again to 70 s for the layer equivalent to the upper surface of the channels, to optimize channel transparency. Finally, for the layers that follow, layer exposure was again reduced to 30 s, for time efficiency. Finally, after printing, moulds were washed for 10 min in a bath of IPA and post-processed for 30 min under UV exposure and a curing temperature of 60°C, to optimize their stiffness and ductility as according to Figure 3.16.

3.7.1 Fabrication of a Microfluidic Maze

The successful fabrication of a microfluidic maze demonstrates the ability of the manufacturing procedure to produce dense networks of precise microfluidic channels, by easily converting complex designs into a polymer substrate. Additionally, it also shows the ability of the produced devices in generating the appropriate pressure gradient, from inlet to outlet, once the channels are sealed. Beyond the design aspects relevant to the proof-of-concept, a microfluidic maze is also valuable in the context of biological research, being particularly interesting in the investigation of migration patterns of cells during chemotaxis [282, 283].

The design of this microfluidic maze was adapted from an svg file generated online, Figure 3.19 A, and translated using CAD software into the equivalent channel network. The respective channel network was then integrated within the template mould used in the current RT setup, defining channels to a dimension of 300 x 400 µm (heigh x width). And finally, after injection moulding, the respective mould generated the microfluidic polystyrene maze presented in Figure 3.19 B. This way, it is shown how the procedure enables to quickly convert any design, and foreign file, into a fully functional microfluidic devices. More so, and as observed in Figure 3.19 C and D, the pressure-driven flow accurately finds its way across the maze by following the paths of least fluidic resistance, until successfully finding the outlet, Figure 3.19 E. Ultimately, demonstrating the path of greater

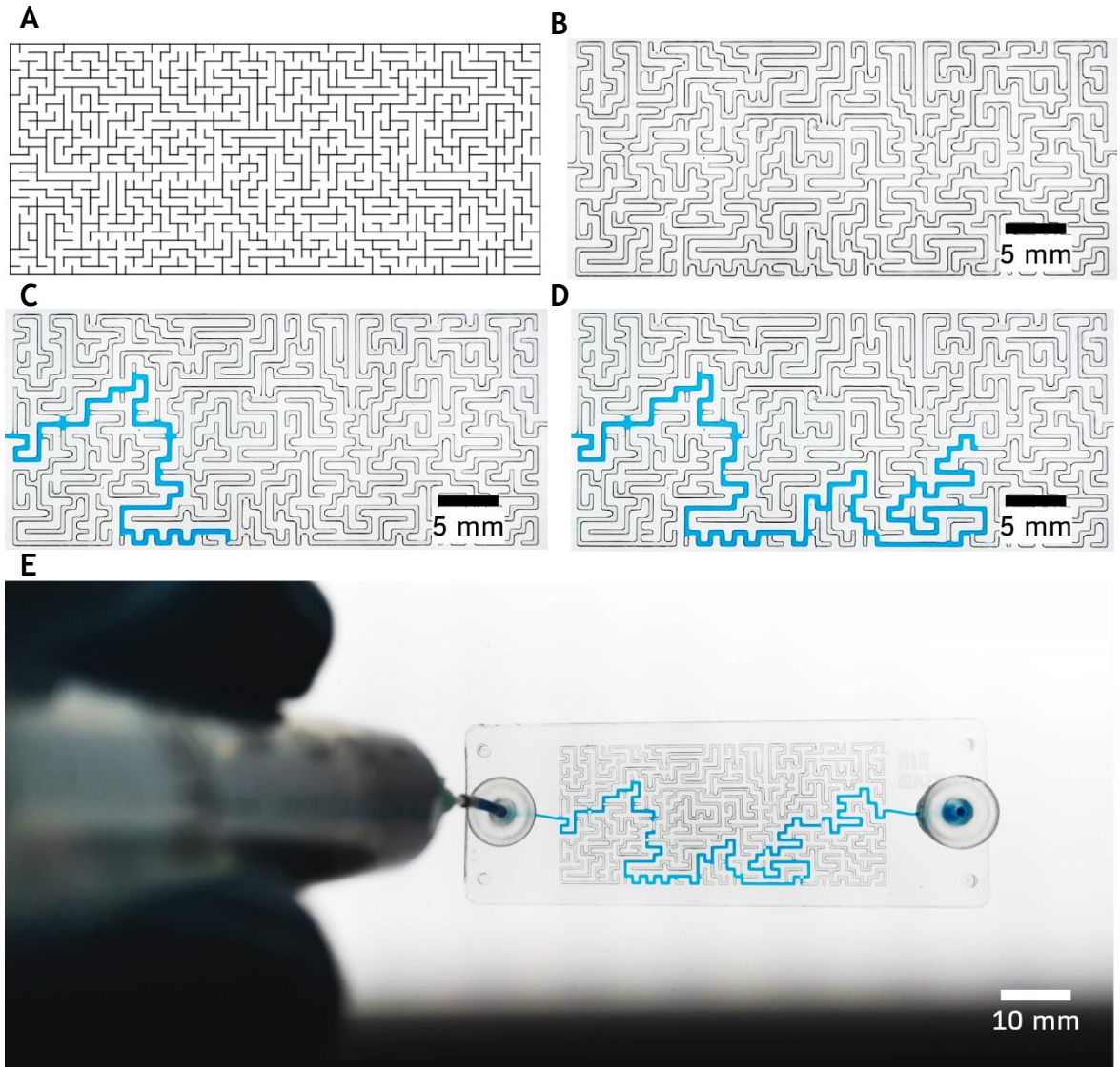

Figure 3.19: Fabrication and testing of a microfluidic maze. A, Svg file of an automatically generated maze. B, Adaptation of a similar svg file into a microfluidic maze produced via RT. Perfusion of dissolved blue dye demonstrating the ability of flow to find the path of least fluidic resistance, at one third of the way, C, two thirds of the way, D, until finally completing the whole maze, E.

efficiency across the maze, highlights the success of the developed device in precisely defining the pressure gradient between inlet and outlet.

3.7.2 Fabrication of a Microfluidic Mixer

Due to the inherent laminar properties of flow at a low *Re* number, and the resulting reliance on slow diffusive transport as the primary mechanism for molecular mixing, microfluidic mixing is often challenging [284]. Several design solutions have been proposed to enhance microfluidic mixing based on channel geometry, from which the staggered herringbone design, first reported in 2003 by Stroock et al [285], is highlighted. The interest behind this design for the current

proof-of-concept is that the respective geometry is particularly difficult to achieve using traditional microfabrication. To fabricate the characteristic bas-relief staggered herringbone patterns on top of the microfluidic channels, two individual photolithography steps with SU-8 are required [285], which significantly increase the complexity and labour of the microfabrication process. The advantage of the current manufacturing procedure is that it allows the integration of the hierarchical features without any additional steps or changes to the manufacturing procedure, due to the unique capability of 3D printing to produce complex microstructures and geometries.

A new mould was thus designed, including both a flat channel and an asymmetric staggered herringbone mixer, Figure 3.20 A. Channels were defined with a dimension of 300 x 600 µm (height x width), and a total mixing length of 53 mm. In turn, the staggered herringbone features were patterned with dimensions of 150 x 200 µm (depth x width). The final polymer device, filled with diluted dye, both blue and red, is shown in Figure 3.20 B. By perfusing the dyes at a steady flow rate of 10 µL/h, it was possible to briefly test the performance of the staggered herringbone mixer against flat channel. Figure 3.20 C shows that the mixing length of the flat channel mixer was not sufficient to significantly mix the two different dyes at the rate of 10 µL/h. This is better illustrated by the plots in Figure 3.20 D and E, where the colour intensity of both dyes is plotted for both the start and end of the channel, respectively, demonstrating that, despite changes in the gradient of the curves, the maximum intensity value for each colour does not change. In turn, Figure 3.20 F demonstrates that the herringbone design provided greater mixing. This is particularly evident when comparing Figure 3.20 G and H, where it is possible to observe a great reduction in the maximum colour intensity of both dyes, therefore determining a greater mixing performance.

3.7.3 Fabrication of a Droplet Generator

Droplet generation is perhaps one of the most important branches of microfluidics, with widespread application in a variety of fields, from single-cell analysis to gene sequencing and real-time diagnosis [286]. It consists of exploring the fluid instabilities of emulsions into forming monodisperse droplets, which can be produced in large numbers and with precise control over their individual volume. To ensure an appropriate performance, droplet generators are typically required

to present ≤ 100 µm channels, which enhance hydrodynamic forces to segregate the dispersed and continuous phases. For this reason, successfully producing a functional microfluidic droplet generator, provides strong evidence of the ability of the current manufacturing procedure to fabricate true microscale channels.

Therefore, a droplet generator was designed and manufactured as proof-of-concept. Its geometry, Figure 3.21 A, featured a T-junction, with 50 x 100 µm

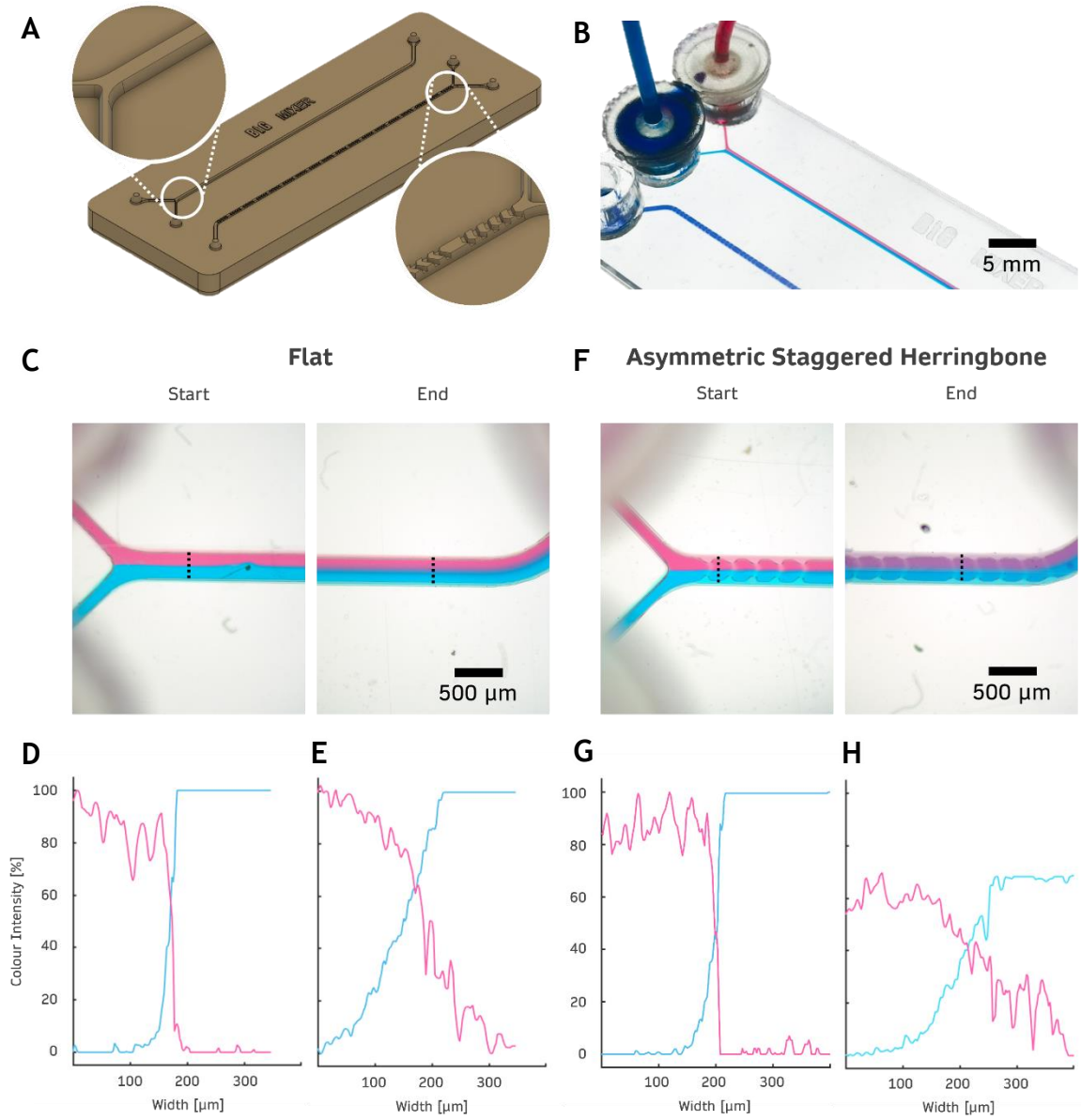

Figure 3.20: Fabrication and testing of a microfluidic mixer. A, CAD of the RT mould containing both a flat channel mixer (top left) and an asymmetric staggered herringbone mixer (bottom right). B, Polystyrene micromixer device after bonding, filled with blue and red coloured dye. C, Flat channel mixer with both dyes being perfused at 10 µL/h. The probe line in dotted black provides the data set from which E and F are plotted, highlighting the reduced mixing occurring from the start to the end of the channel respectively, as measured through the colour intensity. F, Staggered herringbone mixer with both dyes being perfused at 10 µL/h. The probe line in dotted black provides the data set from which G and H are plotted, highlighting the significant changes occurring in mixing from the start to end of the channel respectively, as measured through the colour intensity.

(height x width) channels for the flow of the continuous phase, element 1 Figure 3.21 A, and an orthogonally oriented constricting channel, element 2 Figure 3.21 A, with a 50 x 50 µm (height x width) for the inlet of the dispersed phase, and ultimately, the generation of droplets. More so, the respective 50 µm wide channel was positioned transversal to the flow of molten polymer, during injection moulding. This way, and according to the results described in Figure 3.18, optimal feature durability was ensured. Results demonstrate that, not only was the current RT protocol capable of resolving 50 µm wide channels, Figure 3.21 B, but also, the respective channels withstood a small-scale production run of 500 shots, evidencing no detectable damage, Figure 3.21 C. A further analysis of the mould demonstrates, nevertheless, minor deterioration in the outlet feature and sections of the larger channels, Figure 3.21 D.

To validate the functionality of the droplet generator, channels were sealed against a flat PS layer, following treatment with oxygen plasma, for increased hydrophilicity. The respective flat polystyrene layer was similarly produced via RT for injection moulding. The obtained devices were initially tested for leakage, Figure 3.21 E, with a solution of blue-coloured dye evidencing successfully sealed channels, Figure 3.21 F. Finally, droplet generation was tested with an emulsion of CFC-40 (continuous phase) and mineral oil (dispersed phase), perfused respectively through inlets 1 and 2. Results demonstrate successful droplet generation, with the diameter and mixing rate being a function of the ratio between the flow rate of inlet 1 and 2, thus Q_{in1}/Q_{in2}. It is observed that when $Q_{in1}/Q_{in2} >> 1$, droplets are small and the mixing rate between dispersed and continuous phase is low, Figure 3.21 G. In turn, with the decrease of Q_{in1}/Q_{in2}, tending to 1, droplets become wider and the mixing rate increases, Figure 3.21 H. These results are in accordance with literature [247], and validate this way the performance of the droplet generator.

Finally, it is also important to note the time frame associated with the fabrication of the respective microfluidic droplet generator. Using the current RT procedure, it was possible to define a total lead production time, from CAD to a fully functional microfluidic device, of just 159 min (2 h 39 min). If considering the full production run, and therefore from CAD to 500 replicas, the total lead production time was of 504 min (8 h 04 min). Table 3.3 showcases in greater detail the time frames associated with each process stage, from design

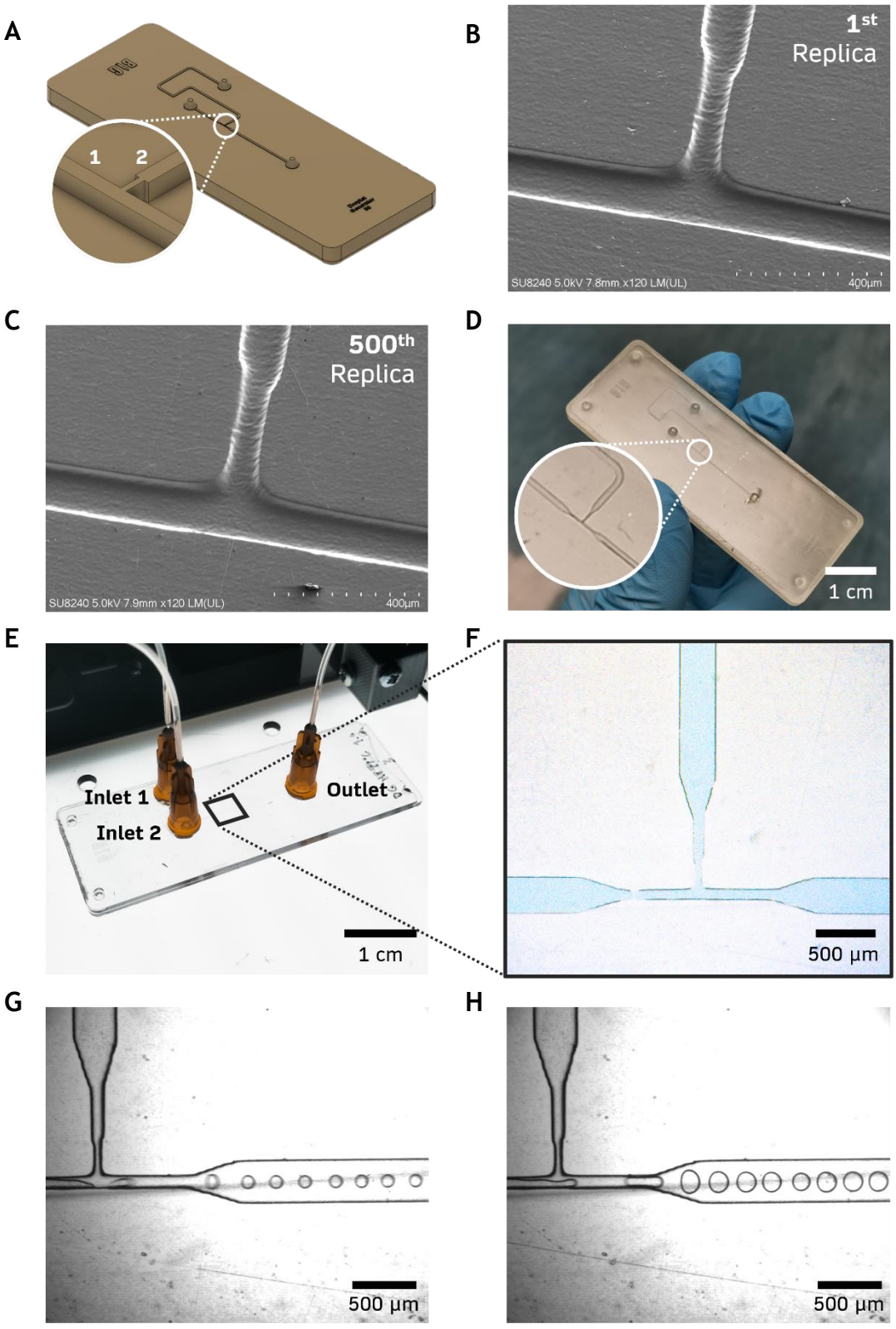

Figure 3.21: Fabrication and testing of microfluidic droplet generator. A, CAD of the droplet generator mould, highlighting the T-section, where the 50 x 100 µm (height x width), element 1, and 50 x 50 µm (height x width), element 2, channels converge. B, 3D printed mould after 500 injection moulding cycles, presenting only minor wear and tear near the outlet feature and on the wider channel sections. C, Scanning electron microscopy (SEM) image of the 1st thermoplastic replica, highlighting the T-section. D, SEM image of the 500th thermoplastic replica, highlighting the T-section and evidencing no visible damage. F, Fully functional droplet generator device, after hot bonding, perfused with blue-coloured dye and demonstrating successfully sealed channels. G, Droplet generation with Qin1/Qin2 >> 1 resulting in small droplets and a low mixing rate. H, Droplet generation with Qin1/Qin2 ≈ 1 resulting in wider droplets and a higher mixing rate.

to production, post-processing and injection moulding. It is also noteworthy that the cost to manufacture a single mould is approximately equivalent to £1. By considering the performance achieved by both the device and manufacturing procedure, a significant proof-of-concept is provided to the ability of the presented RT method in fabricating true microfluidic channels (≤ 100 µm) in a scalable (≥ 500 replicas) and cost-efficient manner, a novel feat within state-of-the-art microfluidic RT.

Table 3.3: Process stage and associated minimum lead time.

	Process Stage	Minimum Lead Time [min]
CAD to Device	CAD Design	10
	3D Printing	97
	IPA Washing	5
	Post-Processing	30
	Injection Moulding (1 shot)	1
	Oxygen Plasma	1
	Hot Bonding	15
	Total Time	**159 (2 h 39 min)**
CAD to 500 parts	Injection Moulding (499 shots)	345
	Total Time	**504 (8 h 04 min)**

3.8 Conclusion

To address the challenge of scalable production within microfluidics, the presented work investigated the benefits of 3D printed RT, as a viable method in the production of thermoplastic devices. By doing so, a novel method based on LCD RT was developed, capable of producing durable tooling for injection moulding, that is compatible with automation, with controlled surface roughness, high feature resolution and high feature reproducibility. In turn, this allowed the production of high quality, optically transparent, sub 100 µm feature resolution microfluidic devices. As proof-of-concept, three distinct devices were designed, manufactured and tested, demonstrating the potential of the presented manufacturing procedure for both quick prototyping and scalable fabrication.

Initially, a state-of-the-art RT setup was tested and adapted to operate with both its described SLA-based 3D printing system and a recent LCD 3D printer. This way, a direct comparison was established between the two technologies, which allowed to determine LCD printing as being the most promising technology in the context

of microfluidic RT. Its key qualities were the ability to provide higher feature resolution, greater geometric accuracy, and improved surface quality, which ultimately resulted in higher transparency microfluidic devices without the need for additional post-processing step.

Various parameters were then explored to improve the compatibility, quality, and reproducibility of LCD-based RT for injection moulded microfluidics. It was observed that both the sidewall waviness and the interlocking angle of layers play a critical role in ensuring mould release when using LCD-based RT for injection moulding. By reducing the sidewall waviness to 1.9 ± 0.4 μm and the interlocking angle to 1.9 ± 0.8° it was possible to ensure a mould release success rate of 100 ± 0.0%. In turn, surface deflection was observed to contribute to greater tool durability, as an indicator of lower interfacial tension. By keeping surface deflection below 0.15 mm, it was possible to extend tool life above 500 injection moulding cycles.

The impact of layer exposure was also investigated. It was observed that, not only is appropriate layer exposure critical in ensuring precise dimensional accuracy, but also, and importantly, it contributes to the regulation of the surface roughness of 3D printed moulds as well. By increasing layer exposure, and therefore enhancing the energy dosage for photopolymerization, it was observed that the surface properties of 3D printed moulds approximated those presented by the PFA film used in the printing vat. This way, by enhancing and controlling layer exposure, it was possible to reduce surface roughness from Ra = 1.1 ± 0.1 μm to Ra = 0.2 ± 0.0 μm. In turn, by decreasing surface roughness, the optical transparency of the resulting injection moulded polystyrene devices increased. This was evidenced by a > 228 lp/mm line resolution and an image contrast and amplitude of 47.6 ± 5.3 grey scale/mm and 169.0 ± 1.6 grey scale respectively. Increasing the layer exposure also improved the dimensional accuracy of printed protrusions, enabling < 50 μm feature resolution. However, the opposite effect was observed when resolving cavity features, with the dimensional accuracy and resolution greatly declining with the increase of layer exposure.

The effect of post-processing protocols, following 3D printing, were also investigated as a means to increase mechanical properties and ensure greater feature durability and reproducibility. Post-processing with UV exposure was

found to be optimal for a temperature of 60 °C and a period of 30 min, improving both the Young's modulus and elongation to the values of respectively 3.4 ± 0.1 GPa and 3.4 ± 0.7%. This ultimately contributed to feature durability above 500 injection moulding cycles, but also highlighted existing interdependencies with design parameters. The reproducibility of microfluidic channels was shown to be optimal for an orientation perpendicular to the flow of molten polymer, presenting a change in height and width equivalent to 2.5 ± 9.3% and 3.1 ± 1.7% after 500 injection moulding cycles. In turn, a draft angle of 20° enabled I/O features to withstand 500 cycles, with a reduced percentage change in diameter of 45.6 ± 39.7%.

As proof of concept, three distinct microfluidic devices were designed, manufactured and tested. These consisted of a microfluidic maze, mixer, and droplet generator. The microfluidic maze highlighted the ease in converting designs into microfluidic tooling and demonstrated the ability of the current RT setup in producing dense networks of precise microfluidic channels, capable of delivering the suitable pressure drop from inlet to outlet. The microfluidic mixer, in turn, demonstrated how the current RT protocol facilitates the manufacturing of advanced channel designs with hierarchical features which, via more traditional fabrication approaches, would involve multiple fabrication steps at the cost of time and labour. This example was achieved by producing an asymmetric, staggered herringbone microfluidic mixer, and demonstrating its mixing performance against a normal mixer with a flat channel surface. Finally, the microfluidic droplet generator testified the capacity of the current LCD-based RT setup in producing channels down to 50 µm in resolution and scaling their production above 500 injection moulding cycles. The droplet generator featured a junction with a 50 x 50 µm (height x width) channel, whose reproducibility evidenced no significant geometric change nor feature damage after the small-scale production. The high feature resolution (≈ 50 µm) and feature durability (> 500 injection moulding cycles) obtained, present a novel feat within state-of-the-art microfluidic RT. The obtained thermoplastic chips were further bonded and tested for their performance in droplet generation.

Finally, this manufacturing procedure enabled a lead production time, from CAD to a fully functional device, of only 159 (2 h 39 min), and from CAD to 500 replicas of 504 min (8 h 04 min). Its exceptionally quick turnaround time and low

fabrication costs (approximately £1 per mould) establish, this way, a manufacturing procedure with an extraordinary potential for rapid prototyping and high-volume manufacturing. The best example for this statement is provided in Figure 3.22, where approximately two thirds of the chip production associated with this PhD degree was gathered and assembled. The respective figure contains hundreds of microfluidic moulds, most of which were analysed, some injection moulded, and a more exclusive group assembled as microfluidic devices and tested with fluid flow and biology. Such numbers, and the benefits they provide for design optimization, would be inconceivable with traditional microfabrication approaches.

Figure 3.22: Hundreds of microfluidic moulds, representing an estimate of two thirds of the total chip production associated with this four-year PhD degree.

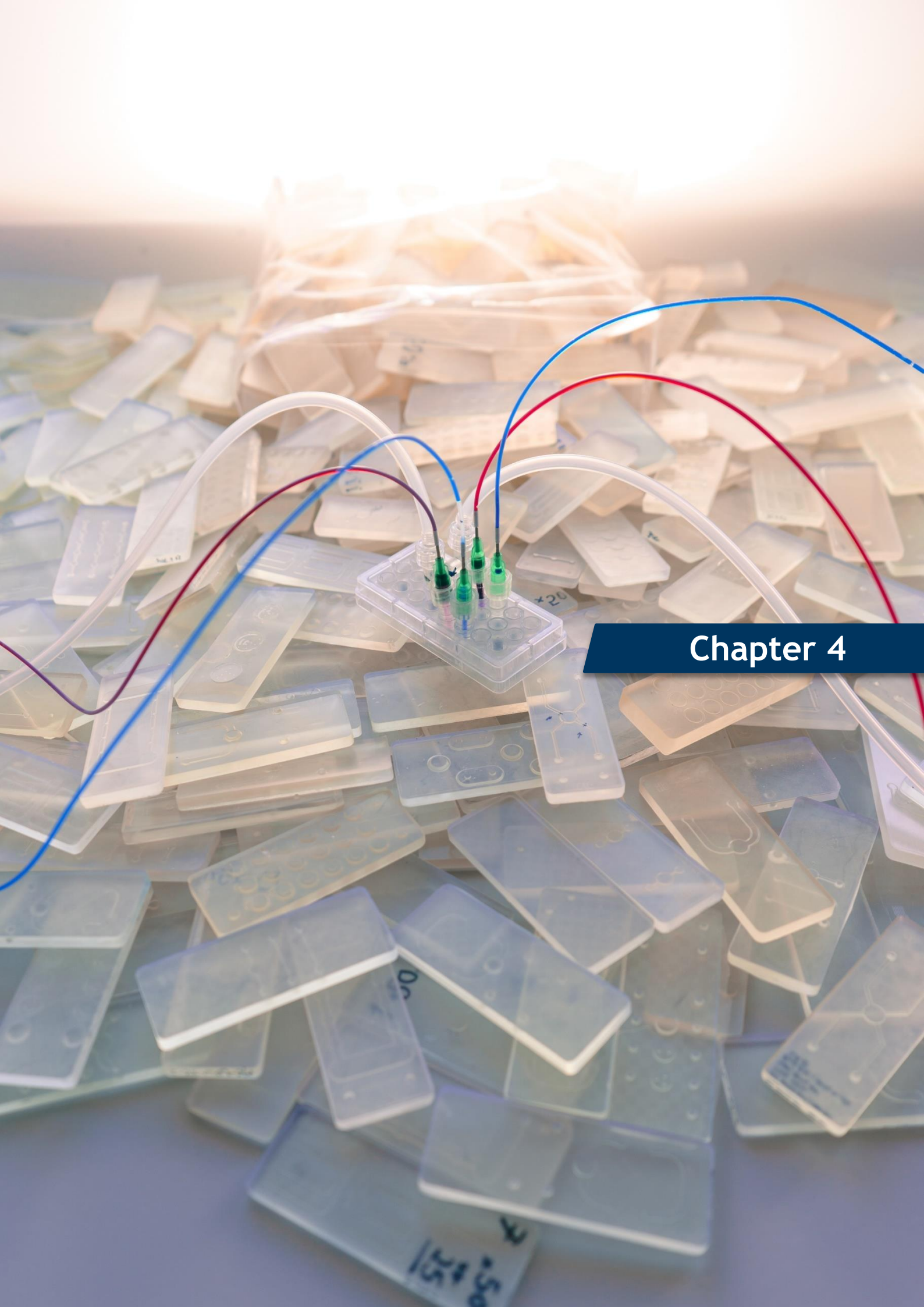

Chapter 4

4 Bonding, Interfacing and Valving for Microfluidic Integration with Polystyrene Devices

4.1 Introduction

Back-end processes for microfluidic integration have a wide impact on the manufacturing costs, usability and performance of microfluidic devices [158]. Nevertheless, this topic is often overlooked by the research community [159]. Microfluidic integration is particularly challenging with thermoplastic materials. Due to their low elasticity and non-conformability, thermoplastics are generally incompatible with the vast majority of techniques used with PDMS for bonding, fluidic interfacing and valving. This prompted the investigation and development of alternative procedures which, in part due to the lack of convergence in thermoplastic material selection, are far from being standardized and are often material and application specific. This lack of standardization implies that the development of a novel microfluidic platform is generally followed by the investigation of suitable integration strategies specific to the respective platform and its unique properties and qualities.

Therefore, following the development of a novel protocol based on RT for the fabrication of polystyrene microfluidics, as described in Chapter 3, this chapter focuses on exploring and developing viable integration techniques for the current devices. Integration will encompass channel bonding, porous membrane integration, fluidic interfacing and valve integration. Due to the vast number of microfluidic devices produced during this PhD, as highlighted in the conclusion of Chapter 3, this Chapter adopts a more exploratory character.

4.1.1 Challenges with Thermoplastic Microfluidic Integration

For microfluidic channel bonding there is a wide variety of well-established technologies [166] that were reviewed in Section 2.2.1. The challenge lies, therefore, in investigating these technologies and adapting them to suit the particular polystyrene-based microfluidic devices produced with the RT method developed in Chapter 3. Similar technologies are employed in the integration and bonding of porous membranes, which are also well, yet less extensively reviewed [192]. However, the challenge lies not only in investigating and optimizing the

current technologies, but also in determining a suitable microfluidic architecture allowing the integration of porous membranes without compromising its porous network nor the bonding between layers. As reviewed in Section 2.2.2, there are various solutions to fluidic interfacing, which are, nevertheless, primarily application and material specific, and therefore generally non-standardized. Furthermore, the interest behind various modes of fluidic perfusion, particularly pressure- and gravity-driven flow, expands microfluidic function and challenges the standardization of fluidic interfacing. Finding a solution which can both provide a convenient and reliable interconnect, as well as a versatile interface, to incorporate various modes of perfusion, would provide a significant progress in fluidic interfacing. Additionally, the integration of dynamic valving within thermoplastic microfluidic systems is a more challenging topic, due to the inherent stiffness of materials such as polystyrene. As discussed in Section 2.2.3.1, there are two main approaches. One, consists of exploring the elasticity of thermoplastic substrates at low thickness, and integrating these films within devices made entirely from the same material [167, 218], to facilitate integration. The other, and more popular, consists of integrating a soft material within the rigid thermoplastic microenvironment. Perhaps at the expense of additional fabrication and integration procedures, such approaches are capable of achieving higher membrane deflection, at lower pressures, and therefore enhancing valving performance [168, 219-221]. Furthermore, the possibility of developing plug-and-play approaches provides great potential when it comes to flexible integration [222].

Furthermore, it is crucial to ensure that the selected back-end processes are easy to integrate and do not compromise on fabrication scalability. This is one of the key aspects advocating the transition to thermoplastic materials, and should therefore be preserved. Therefore, the selection of back-end processes should reflect this consideration and evaluate parameters such as process time, equipment requirements, and the scalability of the process.

4.1.2 Aims

The aims of this chapter are the following:

- Explore and optimize different bonding strategies to seal channels and porous membranes with the current RT-based polystyrene microfluidic devices, identifying the key benefits and limitations associated with each technology.

- Explore different strategies to fluidic interfacing, and develop approaches capable of integrating different modes of fluidic perfusion, based on pressure- and gravity-driven technologies.

- Develop an approach to plug-and-play dynamic valving compatible with the current RT-based polystyrene microfluidic devices, and validate its respective valving performance

4.1.3 Overview of Chapter

This chapter reports the investigation and development of techniques to microfluidic integration, related to channel and porous membrane bonding, fluidic interfacing, and dynamic valving integration. It starts by describing the associated materials and methods involved in the development and analysis of the respective techniques. It then addresses channel sealing by exploring different bonding strategies, based on adhesives, thermal fusion bonding and ultrasonic welding. A similar set of techniques is then used to investigate the integration of porous membranes, together with the development of a suitable microfluidic layout. Afterwards, different approaches to fluidic interfacing are explored, based on irreversibly fixing dispense tips and Luer connectors to the current microfluidic platforms. The integration of an injection moulded 96-well plate adapted to the format of a standard lab slide is then investigated as a versatile approach to fluidic interfacing, compatible with both pressure- and gravity-driven microfluidics. Finally, 3D printing with elastomers is explored to the development of flexible membranes, capable of providing a hybrid solution to dynamic valving within thermoplastic microfluidics. The properties of these membranes are explored and characterized, after which valving was tested for fluidic switching and the generation of dynamic concentration gradients.

4.2 Microfluidic Bonding

To investigate multi-layer bonding with PS microfluidic layers and porous membranes, three different bonding technologies were explored. These were based on adhesive bonding, ultrasonic welding and thermal fusion bonding. Adhesive bonding was further split into dry adhesives, specifically pressure sensitive double-sided tape as a strategy to seal microfluidic channel layers, and UV-curable liquid adhesives, to instead bond porous membranes to the PS substrate.

4.2.1 Materials and Methods

The strategies implemented to investigate each of the respective bonding technologies will be identified and described in the following section.

4.2.1.1 Bonding with Adhesive Layers

Adhesive bonding was tested in the form of both dry and liquid adhesive. Dry adhesive bonding was used to seal microfluidic channels. In turn, liquid adhesive was explored to bond porous membranes.

Two types of dry adhesives were used. These were the Double-Sided Adhesive Tape, Two-Sided Protective Foil from the Microfluidic ChipShop (Microfluidic ChipShop GmbH, Germany), here forwards designated as Microfluidic ChipShop tape, and the Transfer Tape 467MP from 3M (3M, US), series 7952MP, here forwards designated as 3M tape. Whereas the Microfluidic ChipShop tape is 140 µm thick, the 3M tape is 50 µm. In the process of bonding microfluidic channels, the respective tapes were cut using laser cutting. The system employed for laser cutting was a Full Spectrum Laser (Full Spectrum, US), model HL40-5G-110. It uses a water-cooled CO_2 laser, with a rated power of 40 W, a focused beam spot size of 50 - 127 µm, and a maximum XY resolution of 1000 dpi. The process of laser cutting starts by designing the desired shape in CAD software, in this case Fusion 360, and exporting the respective drawing as a DXF file. The file is then processed by the vector graphics software Corel Draw X5 (Corel Corporation, Canada) and finally exported to the interfacing software Retina Engrave v4.404 (Full Spectrum, US), native to the laser cutting system. In the respective software, vector mode is selected, with four main process parameters being explored and defined

according to the different substrates used. These parameters were respectively the velocity of the laser [%], laser power [%], number of passes, and laser intensity [%]. For both tapes, performing a single pass with a laser power of 60%, cutting speed of 60%, and a laser intensity of 100% was observed to be sufficient to obtain a clean through cut. After cutting, one of the release liners is removed and the tape is carefully attached to the microfluidic substrate, to match the pattern on the tape to that of the channels. Afterwards, the release liner on the opposing surface is also removed, so that the microfluidic substrate is bonded against a second layer, this way sealing the respective channels. To remove air bubbles that form at the adhesive interface, cold pressing was employed. This was done by applying a pressure of 2.5 bar for 1 min.

The liquid adhesive used was the Norland Optical Adhesive 73 (Norland Product Inc., US). The adhesive cures under UV exposure, it is optically clear, and meant to provide a strong bond between polymer substrates. The process of bonding and curing porous membranes consisted of depositing the liquid adhesive on the desired section of the microfluidic substrate, placing the membrane on top, and curing the adhesive under UV exposure. Curing was done for 1 min using a 405 nm wavelength UV light source with a power output of 1.68 ± 0.0 mW/cm^2.

4.2.1.2 Bonding with Ultrasonic Welding

Ultrasonic welding was explored in the bonding of both microfluidic channels and porous membranes. The system used was a Rinco Ultrasonics AG Standard 3000 (Rinco Ultrasonics AG, Switzerland). From the various available modes of control, two were primarily used in this project. These were respectively the energy mode, which provides control over the welding energy, E_{USW} [Ws], and the time and energy mode, which provides control over E_{USW} and the welding time, t_{USW} [ms], both of which must be reached before the welding procedure is finished. In the bonding of channels, the time and energy mode proved the most efficient. In the bonding of porous membranes, it was instead the energy mode. The values for both E_{USW} and t_{USW} will be detailed in the results section, for both the bonding of channels and porous membranes. In general, for both applications, ultrasonic welding was performed at a pressure, P_{USW}, of 3.6 bar, and a hold time of 2 s. More so, the throttle, controlling the velocity of approach of the horn, V_{USW}, in the last 30 mm of travel, was set to 5. Given the ultrasonic vibrations applied

during the welding procedure, the parts must be appropriately secured to the anvil. Initially, the microfluidic components were secured to the anvil by using Scotch Tape (3M, US). To provide, however, a more precise and systematic means to securing the microfluidic chips, 3D printing was employed to print a fixture fitting tightly against the anvil, to ultimately secure the chips together. 3D printing was performed using Formlabs Form 3 (Formlabs, US) with Formlabs Clear resin (Formlabs, US). To bond membranes, a specific fixture was designed to press the membrane against the microfluidic layer, only touching the area respective to the weld. This fixture was also produced via 3D printing, using either the equipment above described, or an Anycubic Photon M5s (Anycubic, China) with Monoprice Rapid UV Printer Clear resin (Monoprice, US). Finally, to achieve appropriate welding, energy directors were integrated into the microfluidic layers, to bond both the microfluidic channels and porous membranes. The design of the energy directors followed the guidelines provided by Convery et al 2023 [156], and the dimensions were designed according to printing parameters, as it will be described in the results section.

4.2.1.3 Bonding with Thermal Fusion

Thermal fusion was also investigated in the bonding of microfluidic channels and porous membranes. For such, a custom-made heat press was developed, as illustrated in Figure 4.1 A and fully assembled in Figure 4.1 B. It consisted of two 30 mm thick, machined aluminium plates, bolted to each other using M12 Rods (RS Group plc, UK), and encased by acrylic layers. Inside, it housed two parallel 4 x 7-inch hot plates from Devil Press (Devil Press, UK) controlled externally via a DP40 dual PID controller (Devil Press, UK), Figure 4.1 C. Whereas one of the hot plates was fixed to the bottom aluminium plate, the other was bolted to the rod of a pneumatic cylinder. This consisted of a 125 mm bore pneumatic cylinder (Hydraulic Megastore Ltd, UK), with a 50 mm stroke. Pneumatic lines connected the cylinder to a Bambi BB24V Silent Air Compressor (Bambi Air Compressors, UK), Figure 4.1 D. It is important to distinguish between the cylinder pressure, P_c, and the process pressure, P_{TF}. Whereas P_c is equivalent to the pressure delivered by the compressor, P_{TF} depends on the bore size, BS, and the surface area of the microfluidic devices, SA. To calculate the P_{TF}, the expression $P_{TF} = (P_c \times \pi \times (BS/2)^2)/A_{mic}$ must be employed. Between the compressor and the pneumatic cylinder, an air pressure regulator (Haofy, China) was installed, Figure 4.1 E, as

well as an electric solenoid (WJUAN, China), to control the activation and deactivation of the pneumatic cylinder. The electric solenoid was connected to a delay relay module (Hsthe Sea, China) to allow the activation of the pneumatic cylinder according to a set period of time, t_{TF} [min]. Furthermore, a safety switch was included in the acrylic cover of the heat press, so that the press could only be activated when fully enclosed.

Prior to bonding, microfluidic layers were treated with oxygen plasma, at 80 W for 1 min, using a Henniker Plasma HPT-200 (Henniker Plasma, UK). Bonding was performed initially with the substrates directly sandwiched by the heat plates, but then enclosed by two carrier layers on both sides, to increase the optical quality of the resulting devices. The carrier layers were respectively a PC film, 18 µm thin, and an acrylic layer, 2 mm thick, both laser cut to fit exactly the same shape as the microfluidic chips. Over the course of this work, thermal fusion was, in general, performed for t_{TF} = 20 min, to ensure appropriate heat transfer across

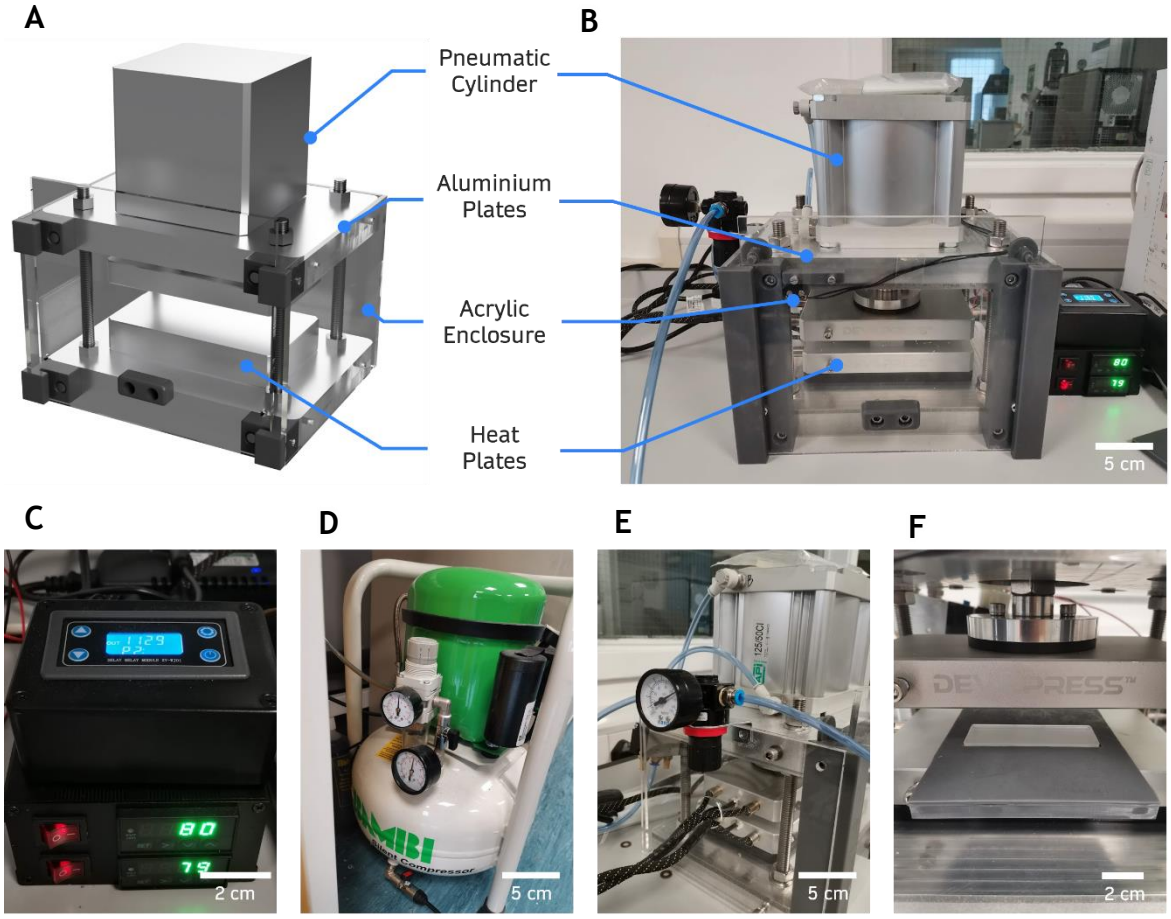

Figure 4.1: Setup for thermal fusion bonding. A, Render of the heat press and, B, its corresponding fully assembled system, identifying the pneumatic cylinder, machined aluminium plates, acrylic enclosure and heat plates. C-F, Delay relay module and DP40 dual PID controller, air compressor, air pressure regulator (maximum pressure range up to Pc =), and 3D printed fixture respectively.

the substrates. The process temperature, T_{TF} [°C], and P_{TF} were defined according to the various tested substrates, as it will be described in the results section. To ensure the alignment of the chips during the bonding procedure, a fixture was 3D printed, as shown in Figure 4.1 F, using the Formlabs Form 3 (Formlabs, US) with the Formlabs Tough 2000 resin (Formlabs, US).

4.2.1.4 Selection, Handling and Cutting Porous Membranes

The techniques mentioned above were also employed in the bonding of porous membranes. Two types of membranes were included in the investigation of membrane bonding and the development of membrane integrated microfluidic devices. These were commercially available hydrophilic polyester (PETE) track etched (TE) membranes (Sterlitech, US), and custom-made PS electrospun (ES) membranes, fabricated at the University of Edinburgh. The PETE-TE membranes were further analysed according to multiple properties. These were the pore size, analysed for 3.0 µm and 0.4 µm, and transparency, with both non-transparent and transparent membranes being investigated. Transparency, in this case, is partly determined by porosity, with non-transparent membranes presenting a higher porosity (14.1% for the 3.0 µm and 12.6% for the 0.4 µm) and transparent ones lower (4.2% for the 3.0 µm and 0.3% for the 0.4 µm)

Two processes were considered and tested in the cutting of porous membranes, to fit the size of their respective microfluidic chambers. The first was laser cutting which was however only employed in the cutting of PETE-TE membranes. The parameters employed in the cutting of the respective membranes will be briefly addressed and explored in the results section. Another process was manual hole punching, using a set of circular, hollow punch tools, with a diameter ranging from 0.5 mm to 6 mm. The cutting process consisted of using the respective hollow punch tools, together with a hammer, to obtain a clean, circular cut of the porous membranes. This process was tested and used for both the PETE-TE and PS-ES membranes.

4.2.2 Strategies for Microfluidic Channel Bonding

As expressed in Section 2.2.1, a successful seal should ensure the confinement of solvents, reagents and media, in the defined volumes of the microfluidic channels,

without leakages [159]. Similarly, appropriate bonding should preserve the structural integrity and geometry of microfluidic channels and further features. Therefore, two fundamental measures of a successful bonding procedure are the evaluation of fluidic confinement, by testing microfluidic channels for leakage, and the investigation of channel deformation. Accordingly, these were the two variables analysed in the investigation of an optimal protocol for the bonding of the current PS microfluidic devices. In turn, these variables were investigated as a function of the control parameters associated with each of the technologies tested.

4.2.2.1 Channel Bonding with Pressure Sensitive Double-Sided Tape

The steps associated with bonding microfluidic substrates (filled in grey, Figure 4.2 A) with pressure sensitive double-sided tape (filled in yellow, Figure 4.2 A,) are shown in Figure 4.2 A. First, the tape is aligned and placed on the surface of the microfluidic substrate (Figure 4.2 A, step 1). Second, pressure is applied to promote conformal contact between the adhesive and the microfluidic layers and achieve bonding (Figure 4.2 A, step 2). Pressure can be either applied manually or via cold pressing. In this work, cold pressing was employed (as illustrated in Figure 4.2) to provide higher pressure and a more homogenous distribution. Finally, the pressure is released and the bonded microfluidic device is obtained (Figure 4.2 A, step 3). Figure 4.2 A also highlights the process parameters explored in black font, and other relevant parameters in grey font.

Figure 4.2 B and C evidence two similar microfluidic channels bonded using the Microfluidic ChipShop and 3M tapes. These tapes present slightly different appearances, with the Microfluidic ChipShop tape displaying a faint yellow tone, while the 3M tape is clearer. While the yellow tone of the Microfluidic ChipShop tape presents a less desired feature for microfluidic systems, both tapes showcase good optical transparency. However, two of the key challenges associated with handling and bonding with tape are evidenced by Figure 4.2 D and E. First, the tendency to create air pockets between the adhesive and microfluidic substrate interfaces, further compromising on optical clarity. For both cases, illustrated in Figure 4.2 D and E, cold pressing was employed, at 3.3 bar for 1 minute. Nevertheless, it is still visible the abundance of air pockets around the channels resulting in poor channel confinement as shown in Figure 4.2 E. The variability of

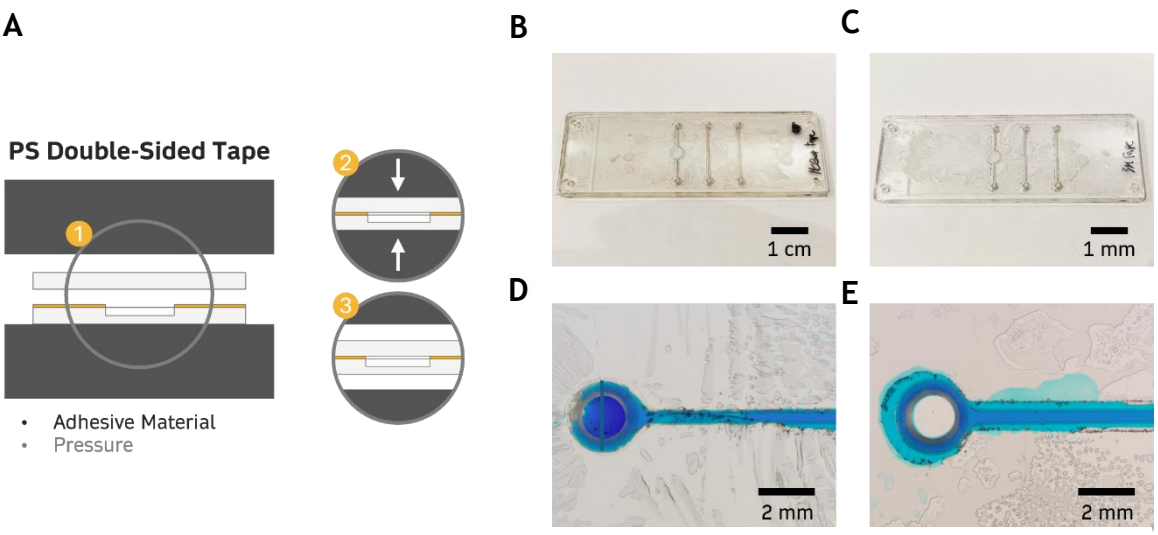

Figure 4.2: Channel bonding with pressure sensitive double-sided tape. A, Illustration of the bonding procedure, involving, 1, attaching the laser cut adhesive layer to one of the microfluidic layers, 2, pressing both microfluidic layers together, after which, 3, the bonded device is obtained. The figure also illustrates the two main parameters explored, namely the adhesive material and the pressure employed during cold pressing. B and C, Bonded devices, using respectively the Microfluidic ChipShop and 3M tapes. D and E, Higher magnification view over the blue media filled channels, highlighting the formation of air pockets, low accuracy in tape placement, and the existence of leakages.

the procedure also compromises on the accuracy and repeatability of bonding, given that it typically involves manual alignment and placement of the tape. In Figure 4.2 D it can be observed that parts of the tape overlap the channel, in the section close to the inlet. Instead, Figure 4.2 E evidences poor geometric accuracy between the tape and channel outline.

Ultimately, the figures illustrate that, despite obtaining reasonably good channel confinement and optical transparency, bonding with tape is significantly affected by the manual labour involved and its resulting variability and low accuracy. This way, while being an extremely useful tool for rapid prototyping, bonding with tape is less suitable for final microfluidic products, where scalability and reproducibility are key requirements.

4.2.2.2 Channel Bonding with Ultrasonic Welding

The process associated with ultrasonic welding is described in Figure 4.3 A. The substrates are put together on top of the anvil (Figure 4.3 A, step 1), with the microfluidic layer typically presenting energy directors (represented by the triangular features on the bottom, grey-filled layer, Figure 4.3 A) around the perimeter of the channels. Then, as the horn approaches the components, the parts are compressed together according to a predefined pressure, P_{USW} (Figure

4.3 A, step 2). Finally, energy transferred via ultrasonic vibrations, E_{USW}, plasticises the energy directors to form a joint between the two surfaces, after which the pressure is released and the bonded device is obtained (Figure 4.3 A, step 3). Figure 4.3 A also highlights, in black font, the process parameters explored by this work and, in grey font, other parameters of relevance.

A first approach to ultrasonic welding with the current PS microfluidic channels involved exploring some of the procedures outlined in literature, particularly the protocol defined by Convery et al 2023 [156]. Therefore, energy directors were printed with a dimension of 350 x 200 µm, and bonding with ultrasonic welding was tested using the Energy Mode for a range of different values for E_{USW}, from 30 to 70 Ws, as Figure 4.3 B demonstrates. However, sealing was unsuccessful across all testing conditions, as evidenced by the leakage of media over the surface of the PS chips. A closer look to some of the leakage source points, Figure 4.3 C, and their respective location on the original 3D printed mould, Figure 4.3 D, highlights the correlation between poorly printed energy directors and a compromised seal. As established in Chapter 3, Figure 3.14, one of the key limitations of the current 3D printing procedure is in printing fine cavities, such as energy directors. This way, to compensate for low geometric and dimensional accuracy, particularly for cavities below 400 µm (as highlighted in Figure 3.14, Chapter 3), and ensure the appropriate printing of energy directors, these were over dimensioned to 500 x 500 µm instead. Despite presenting a more reliable seal, Figure 4.3 E and F highlight other critical challenges associated with the ultrasonic welding setup involved. Not only is the weld in Figure 4.3 E inconsistent, both in terms of its width and optical clarity, but also the obtained surface quality is low, presenting visible scratches, as shown in Figure 4.3 F. These issues were observed to result from poor fixation of the components, in relation to one another and in relation to the horn respectively.

To avoid the relative movement of parts, between themselves and in relation to the horn, a modified setup was defined, as illustrated in Figure 4.3 G. This setup included a fixture, Figure 4.3 H, 3D printed to fit tightly against the anvil and provide a secure fit to the microfluidic chips, to prevent their movement in relation to the welding horn. The setup also included features for self-alignment implemented directly on the microfluidic chips, as highlighted in yellow in Figure 4.3 G and I, this way preventing the movement of the microfluidic chips in relation

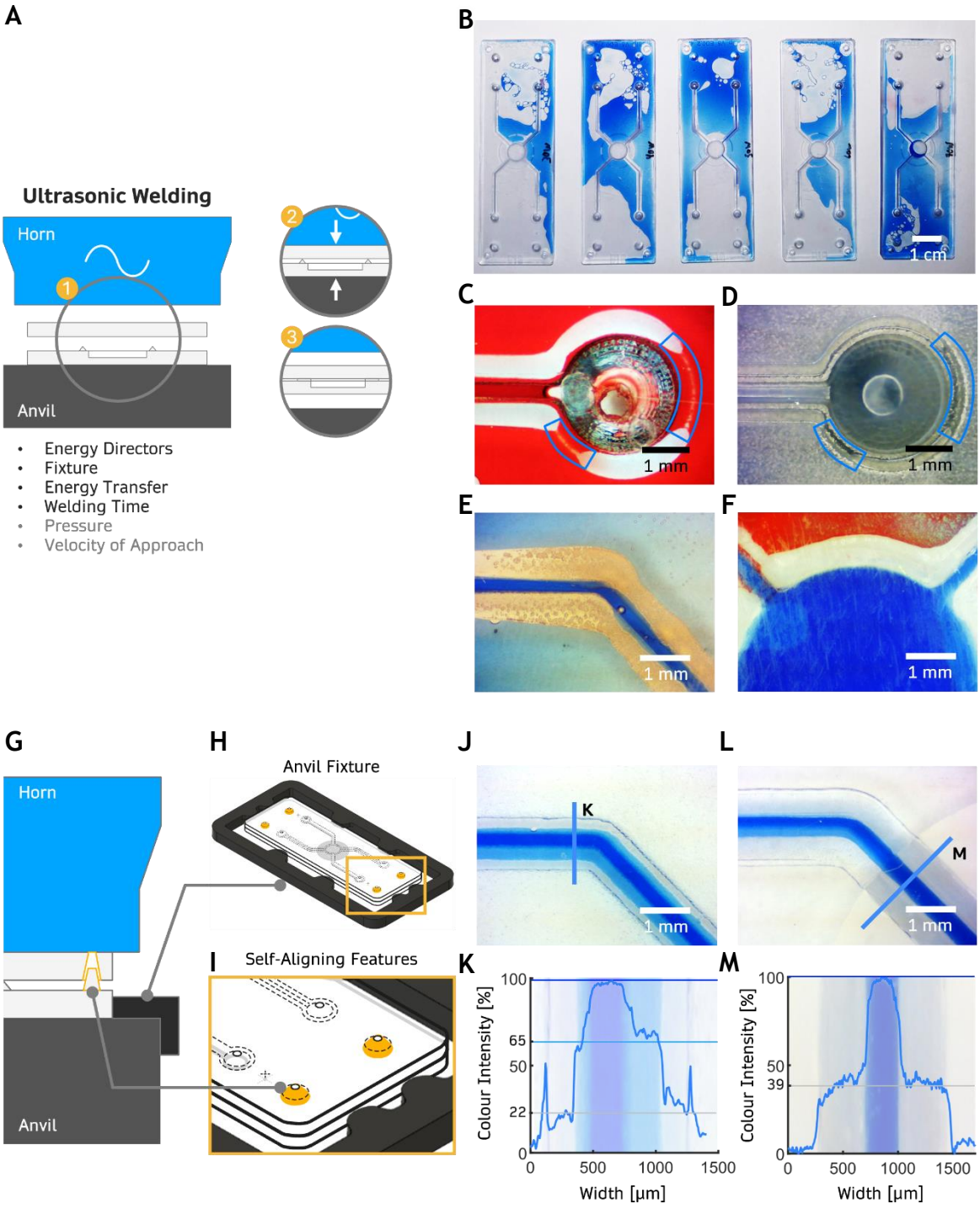

Figure 4.3: Channel bonding with ultrasonic welding. A, Procedure and setup involved in ultrasonic welding, highlighting in black font the main parameters explored, and in grey, other parameters of relevance. Step 1 represents the assembly, step 2 the bonding, and step 3 the release of pressure and obtention of the bonded device. B, Testing energy transfer as a function of sealing success. C, Leakage source associated with respective energy director defect, D. E and F, Low quality of welding seal and surface due to poor fixation of the chips. G, Updated setup for ultrasonic welding, highlighting a fixture for the anvil, H, and self-alignment features included directly on the devices, I. J, Higher quality seal with, however, incomplete bonding of the energy directors. K, Colour intensity profile across the channel and welding joint for the device in J.L, Successful seal, with welding joint providing appropriate media confinement. M, Colour intensity profile across the channel and welding joint for the device in J.

to one another. The implementation of both strategies improved the bonding quality by increasing the uniformity of the weld joint and enhancing the surface quality of the devices, as shown in Figure 4.3 J. However, the figure also demonstrates the incomplete welding of the energy directors, as evidenced by the narrow weld joints and the formation of shallow peripheral channels next to the main channel. This is visible due to the different colour intensities of the flowing medium. By plotting the colour intensity profile across the channels and weld joints, Figure 4.3 K, it is possible to observe the existence of three distinct plateaus, corresponding respectively to the weld joint (lower colour intensity, at approximately 22%), the shallow peripheral channel (medium colour intensity, at approximately 65%), and the main channel (higher colour intensity). Furthermore, it is possible to observe that the width of the weld joint is approximately equivalent to 250 µm, which further evidences the incomplete bonding of the energy directors. Ultimately, the inappropriate bonding results in the formation of the respective shallow peripheral sections, compromising on microfluidic channel accuracy and potentially performance. Higher precision in the welding of the energy directors was obtained by switching to the Time and Energy Mode, and defining a set target E_{USW} and t_{USW}. This way, by employing E_{USW} = 50 Ws for t_{USW} = 300 ms, it was possible to obtain a more reliable seal, capable of more accurately confining the medium to the volume of the channel, as shown in Figure 4.3 L. An analysis to the colour intensity across the channels and weld joints, Figure 4.3 M, further demonstrates that, by highlighting the existence of a well-defined channel, at a higher colour intensity, and well-defined welds, at a medium colour intensity of 39%. More so, it demonstrates the suitable bonding of the energy directors, with the weld joints presenting a width of approximately 500 µm, similar to that of the energy directors. These parameters defined the optimal protocol to obtain successful and reliable seals using ultrasonic welding with the current PS microfluidic chips. This protocol was further characterized by P_{USW} = 3.6 bar and V_{USW} = 5.

4.2.2.3 Channel Bonding with Thermal Fusion

The process of thermal fusion bonding is described in Figure 4.4. The heat plates (filled in dark grey) are first warmed up to a set processing temperature, T_{TF}, after which the microfluidic chips are aligned and placed in between (Figure 4.4 A, step 1). Then, a defined value of pressure, P_{USW}, is applied to the plates, which in turn

compresses the chips against one another (Figure 4.4 A, step 2). Pressure and temperature are maintained at their predefined values for a set period of time, t_{TF}, causing the contact surfaces of the thermoplastic layers to bond. Once the set process time finishes, pressure is released and the bonded device is obtained (Figure 4.4 A, step 3). Figure 4.4 A also highlights, in black font, the process parameters explored by this work and, in grey font, other parameters of relevance.

Initial attempts to bond the current PS microfluidic devices using thermal fusion were based on parameters provided by literature. One such study is provided by Young et al 2011 [198], reporting the bonding of PS-based microfluidic devices using thermal fusion with T_{TF} = 90°C (close to PS's glass transition temperature, of 92-100°C [174]) and t_{TF} = 30 min. Replicating the respective parameters, at a pressure of P_{TF} = 46.9 bar, proved too violent for the current microfluidic chips, resulting in evident over bonding and the collapse of the microfluidic channels, as observed in Figure 4.4 B. A second iteration to the parameters employed involved a reduction of the process temperature, to T_{TF} = 79 °C, and changing t_{TF} to 20 min. Despite preserving the structure of the channels better, Figure 4.4 C highlights the effect of the current setup in decreasing the surface quality of the devices. This is better observed in Figure 4.4 D, which evidences a blurry quality and poor transparency, despite demonstrating a higher seal quality, given the appropriate confinement of the medium inside the channels. The low optical performance is due to the fact that, at such high temperatures, the heat plates essentially perform hot embossing, transferring the micro topographies of their surfaces into the chip substrate. Ultimately, this comes at the expense of surface quality and optical transparency, as seen in Figure 4.4 C and D, respectively.

To improve this aspect, the setup was updated to the one illustrated in Figure 4.4 E, integrating both an 18 µm thin PC film (filled in blue) and an 2 mm thick acrylic sheet (filled in yellow), at the top and bottom of the PS microfluidic layers. The purpose of the PC film was to establish a layer whose glass transition temperature is significantly higher than that of the PS (145-148°C > 92-100°C [174]). This way not only is the PC layer preserved during the bonding procedure and prevented from bonding to the PS substrate, but also, it implies that the PS surface will conform itself to the PC layer and acquire its surface properties. The function of

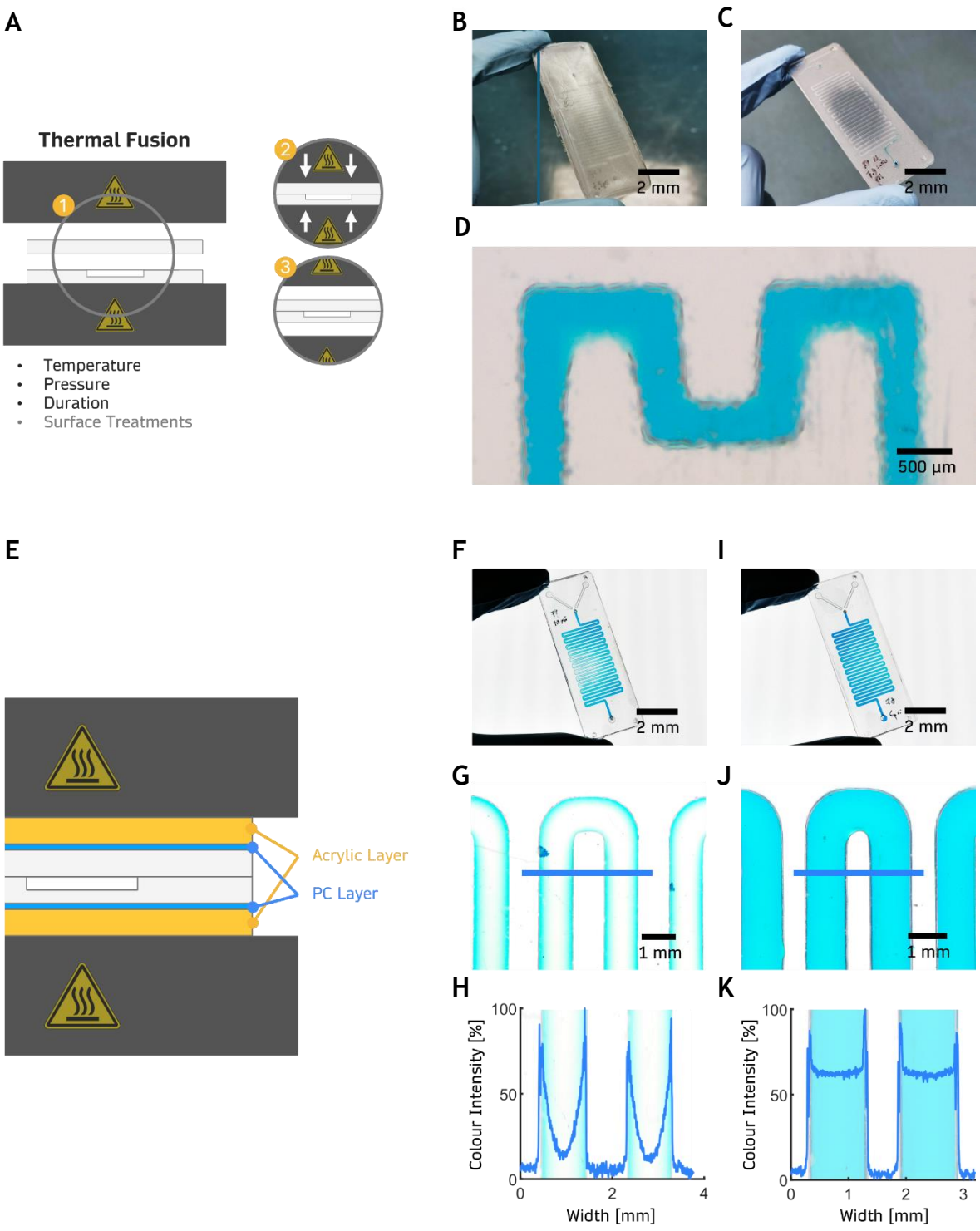

Figure 4.4: Channel bonding with thermal fusion. A, Procedure and setup involved in thermal fusion bonding, highlighting in black font the main parameters explored, and in grey, other parameters of relevance. Step 1 represents assembly, step 2 the bonding, and step 3 the release of pressure and obtention of the bonded device. B, Over bonded device, with no visible channels. C, Bonded device with poor surface quality due to hot embossing with heat plates. D, Low optical properties due to hot embossing with heat plates. E, Improved setup, integrating both a PC film and acrylic layer as carriers, to enhance the surface quality of the bonded chips. F, Higher quality bond, displaying, nevertheless, slight over bonding. G, Higher magnification view of the channels filled in blue-coloured media, highlighting the deformation of the channel. H, Colour Intensity plot, providing a visual approximation to the channel cross section geometry, and highlighting its curved top surface. I, Bonding achieved with optimal parameters, displaying an uniform high-quality seal, further demonstrated by observing the channels with higher magnification, J. K, colour intensity plot as a function of width, evidencing the preservation of the cross-section geometry of channels.

the acrylic layer is just to serve as a buffer and conserve the surface properties of the PC layer. This setup provided significant improvements in the optical quality of the bonded devices, as demonstrated in Figure 4.4 F. However, the figure also highlights evidence of over bonding, particularly around the centre of the device. By taking a closer look at the serpentine channels filled with blue-coloured medium, Figure 4.4 G, the over bonding of channels becomes more evident, with the medium flowing only on the edges of the channels. By plotting the colour intensity as a function of width, it is possible to approximately visualise the geometry of the channels' cross-section which, as Figure 4.4 H highlights, presents a curved top surface, almost touching the bottom surface of the channel at the middle point. This is an effect of excessive temperature and pressure, suggesting a decrease to both parameters. Therefore, in Figure 4.4 I pressure was reduced to P_{TF} = 35.7 bar and temperature to T_{TF} = 78°C, resulting in better bonding uniformity. This is especially visible in Figure 4.4 J, given that channels present a high-quality seal with little to no channel deformation, as better observed by the colour intensity plot presented in Figure 4.4 K. More so, the respective channel layout highlights the capacity of thermal fusion to provide a reliable seal with high density channel networks. The same device geometry would be more challenging to achieve with ultrasonic welding, for instance. This protocol defined the optimal setup based on thermal fusion to bond the current PS-based microfluidic devices.

4.2.3 Strategies for Porous Membrane Bonding

The function of the membrane is to provide a porous barrier to the flowing media, solvents and reagents. The processes involved in the integration of the porous membrane should ensure three fundamental aspects. First, that the integration of the membrane does not compromise the bonding of the channels. Second, that the membrane is rightfully sealed against the substrate and provides the appropriate confinement of media. And third, that integration does not come at the expense of the structural integrity of the pores, and instead preserves its porous network and the permeability properties of the membrane.

The first important aspect to consider is therefore the design of a suitable microfluidic layout, enabling the integration of porous membranes without compromising on channel bonding. Perhaps the most common approach in literature for the fabrication of microfluidic devices with integrated porous

membranes consists of sandwiching a porous membrane between two separate channel layers [192]. This approach is illustrated in Figure 4.5 A, demonstrating in step 1 the three different layers involved, with the porous membrane highlighted in blue, and in step 2 the final bonded device, with two separate, parallel microfluidic channels, connected only via the porous barrier of the membrane. The respective microfluidic layout was initially tested in the development of microfluidic devices with integrated membranes, using ultrasonic welding as the

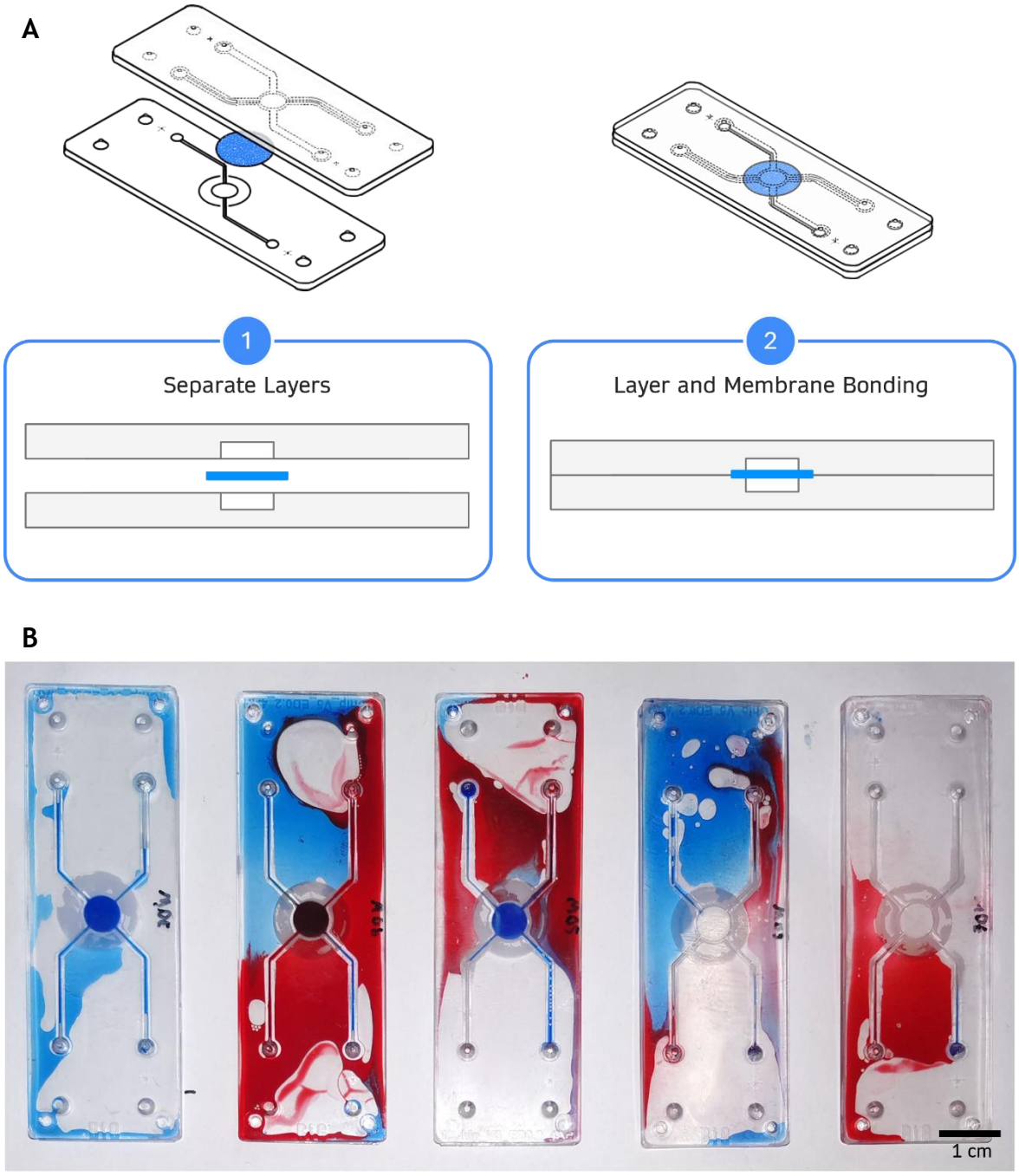

Figure 4.5: Conventional microfluidic design for porous membrane integration. A, 3D view (top) and 2D cross sectional view (bottom) of the microfluidic layout and steps involved in common integration approaches present in literature. B, Ultrasonic welding attempts, using a range of energy transfer values from 30 to 70 Ws, at bonding devices with integrated membranes using the previously described microfluidic layout.

bonding method. However, the sealing of microfluidic channels was consistently unsuccessful, as shown in Figure 4.5 B for different energy transfer values, ranging from 30 to 70 Ws. It was observed that the membrane made it more difficult to achieve appropriate bonding between the three different layers, as highlighted by the poor media confinement and subsequent leakage, and the setup compromised the structural integrity of the membrane. This was observed by the appearance of cuts and general damage to the surface of the membrane.

To address this challenge and provide a setup capable of integrating the porous membranes without compromising the bonding of the microfluidic channels, a three-layer microfluidic layout was developed, as schematically presented in Figure 4.6. This figure illustrates the microfluidic layers (filled in grey) and the porous membrane (highlighted in blue), as well as the steps involved in the bonding procedure, until obtaining a fully functional membrane-integrated microfluidic device. A key aspect to this layout is the ability to individually bond porous membranes to their respective microfluidic layer prior to the bonding of the channels. Not only does this allow for a better characterization of the properties of the membranes post-bonding, but also, it does not interfere with the subsequent bonding of the channel layers, as the porous membrane is sealed within its own separate chamber.

One key implication of this setup is the necessity to precisely cut membranes according to the dimensions of their respective allocated chamber. Two processes were therefore tested for membrane cutting. These were laser cutting and manual hole punching. A brief investigation over the optimal cutting procedure and respective process parameters is presented in Figure 4.7, in this case, for PETE-TE membranes. To serve as control, Figure 4.7 A demonstrates the membrane and respective edge as they are provided from stock. The results with laser cutting

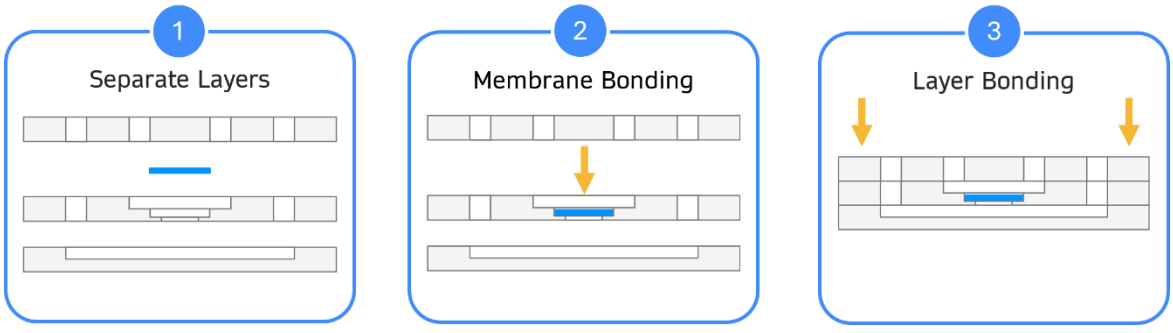

Figure 4.6: Suggested three-layer microfluidic layout (step 1) for individual bonding of porous membranes (step 2), prior to the bonding of the channels (step 3).

are observed in Figure 4.7 B. First, to obtain a clean cut without unnecessary damage and considering the low thickness of the membrane, laser power was reduced to a minimal of 5%. Then, both laser speed and current intensity were explored as a function of the edge quality. As observed in Figure 4.7 B, whereas a high cutting speed significantly affects the accuracy of the cut, a low speed results in a smoother and more continuous geometry. Decreasing the laser speed beyond necessary, however, contributes to bloating the edges of the membrane, due to prolonged exposure to the laser, and increases the process time. Therefore, an optimal cutting speed was found at 40%. In turn, by reducing the laser current intensity, the cut becomes increasingly less clean, as observed in Figure 4.7 B for the condition at 60%. Thus, an optimal cut was obtained for a current intensity of 100% instead. Nevertheless, a cleaner and more accurate cut was obtained with manual hole punching. As observed in Figure 4.7 C, the respective technique provides higher precision on edge quality, resembling that from stock. Therefore, manual hole punching was selected as the preferred procedure for membrane cutting, having also displayed equally good and systematic results in cutting PS-ES membranes. All porous membranes were cut to fit the dimensions of their allocated chambers, and therefore according to an outer diameter of 6 mm.

The process of bonding the porous membranes to the PS microfluidic substrates was investigated for liquid optical adhesives, thermal fusion bonding and ultrasonic welding. Additionally, both the PETE-TE and PS-ES membranes were individually studied, identifying the unique characteristics of each and respective challenges in bonding.

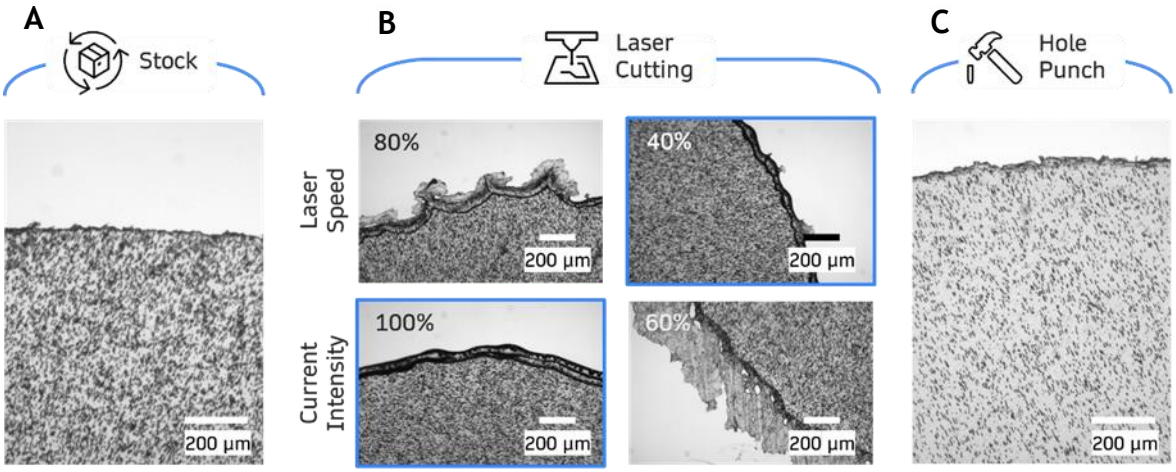

Figure 4.7: Parameters and strategies investigated to cut porous membranes. A, Edge of the membrane as provided in stock. B, Cutting accuracy and edge quality as a function of the laser cutting speed and current intensity, for a laser power of 5% and a single pass. C, Membrane cut using manual hole punching.

4.2.3.1 Porous Membrane Bonding with Optical Adhesive

The process of bonding the porous membrane to its respective PS microfluidic layer using an UV-curable optical adhesive is illustrated in Figure 4.8 A. The process starts by placing the liquid optical adhesive (filled in yellow) in the recess allocated for the membrane (Figure 4.8 A, step 1), using a stamp. Then the membrane is placed on top of the liquid adhesive, which is later cured using UV radiation for a set interval of time (Figure 4.8 A, step 2). After UV exposure and the respective polymerization of the liquid adhesive, a solid bond is achieved between the membrane and the microfluidic layer (Figure 4.8, step 3).

A preliminary investigation was performed to assess the minimum amount of time required to fully cure the layer of the liquid adhesive. It was observed that a total of 50 s was sufficient to fully cure the liquid adhesive and establish a solid bond between the membrane and the microfluidic substrate. In Figure 4.8 B-E the results of bonding PETE-TE membranes are shown. A bright-field image is presented in Figure 4.8 B, providing an overview of the entire membrane chamber, post membrane bonding. It is possible to observe a lack of contrast between the channel and the membrane edges, resulting from adhesive wetting. However, it is only by taking a closer look, using SEM, that it is possible to observe the properties of the obtained bond. Figure 4.8 C highlights the interface between the bonded, peripheral area (at the bottom), which displays no pores, and the effective membrane area, where the pores are maintained. However, by looking at the centre of the membrane, Figure 4.8 D, it is possible to observe that, while some pores present a dark tonality, others display a lighter tone. A higher magnification view over the respective pores, Figure 4.8 E, demonstrates that, while some pores are open, therefore presenting a darker appearance due to the depth of the pore, others are closed, which result in a lighter tonality instead, due to the surface reflection of light. This was observed to result from resin impregnation of the membrane prior to curing the liquid adhesive, wetting sections of the membrane, filling the pores, and ultimately, compromising its permeability.

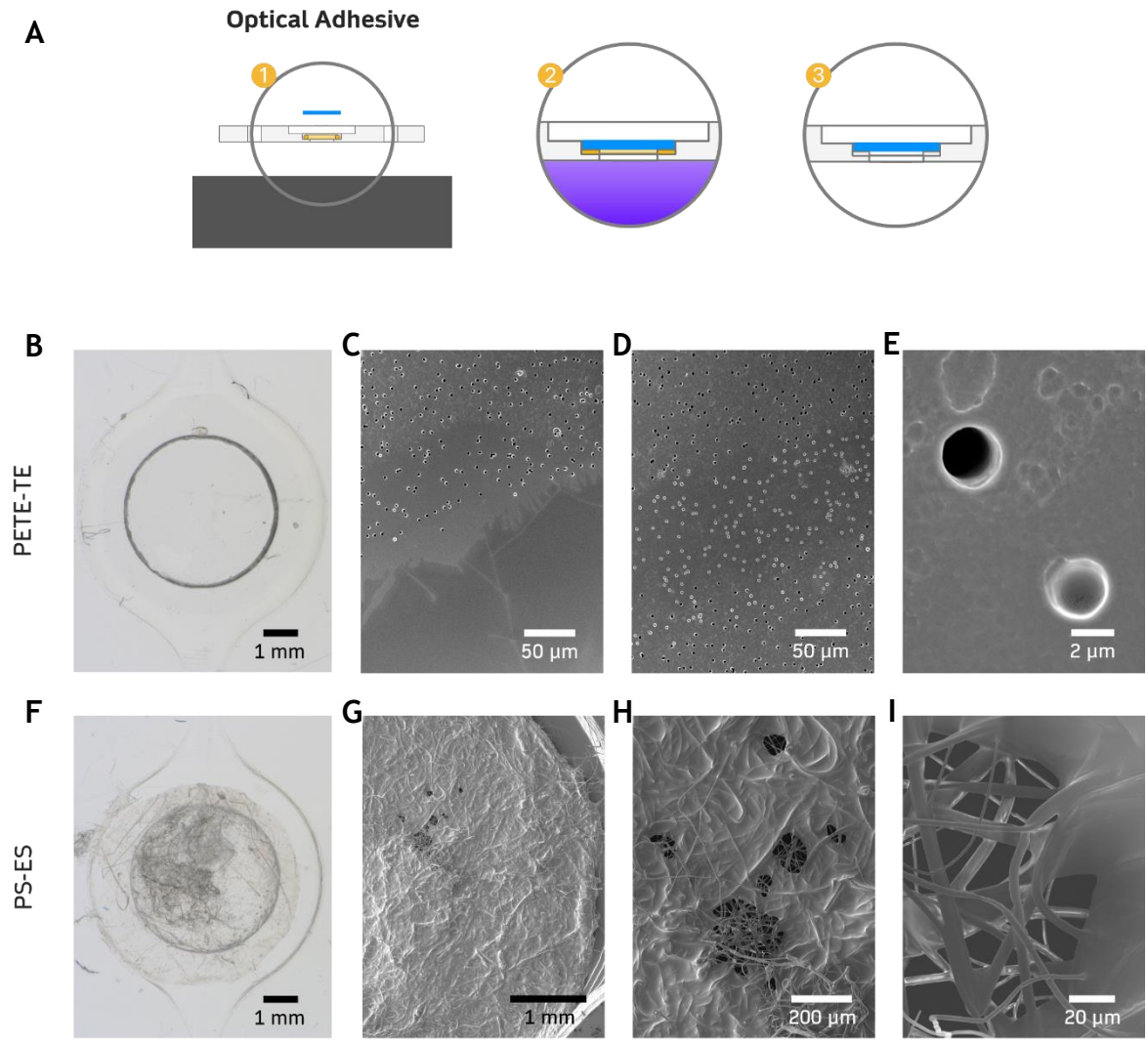

Figure 4.8: Bonding porous membranes with liquid optical adhesive. A, Protocol for bonding, with step 1 consisting of assembly and liquid adhesive stamping, step 2 curing with UV exposure, and step 3 the final bonded composite. B-E, Properties of the PETE-TE membrane bonded with liquid adhesive, from chamber overview to the analysis of individual pores. F-I, Properties of the PS-ES membrane bonded with liquid adhesive, from chamber overview to the analysis of individual fibres.

Greater implications due to undesired wetting of the membrane prior to curing were observed for the PS-ES membranes. The bright field overview of the membrane bonded to its respective chamber is provided in Figure 4.8 F, highlighting a non-uniform surface. Only through SEM imaging, however, it is possible to observe the full implications of using the liquid optical adhesive for bonding. As Figure 4.8 G highlights, bonding the membrane with the liquid adhesive results in the impregnation of the membrane which, after curing, results in a solid surface, with barely any permeability. A higher magnification view over some of the permeable sections is provided in Figure 4.8 H, where the differences between the solid, impregnated surface, and the open, fibrous areas are observed. An even closer look at the PS fibres, Figure 4.8 I, provides a better example of fibre impregnation. As the figure demonstrates, the fibres exhibit a

round, glossy look, due to the cured polymer they are involved in. Furthermore, wider filaments evidence the bonding of multiple fibres together during the polymerization of the adhesive.

Ultimately, these results highlight the nature of bonding porous membranes using liquid optical adhesive. This procedure was seen to be prejudicial to both tested membranes. For the PETE-ES membrane, the spreading of the liquid adhesive prior to bonding resulted in closing some of the pores. However, a much deeper effect was observed for the PS-ES membrane, with its fibres being rapidly wet by the liquid adhesive, prior to UV exposure, and ultimately compromising the permeability of the membrane almost entirely.

4.2.3.2 Porous Membrane Bonding with Thermal Fusion

The setup developed to bond porous membranes using thermal fusion is illustrated in Figure 4.9 A. It included PC washers (filled in grey, Figure 4.9 A, step 1) to press the membrane against the microfluidic substrate and avoid the contact between the remaining surfaces and the bottom heat plate. This way, pressure and temperature are only applied in the periphery of the membrane (an area equivalent to 12.4 mm^2) preserving its centre and localizing the bonding (Figure 4.9 A, step 2). After the set time, pressure is released and the microfluidic layer with a bonded porous membrane is obtained (Figure 4.9 A, step 3). For the present tests, a channel layout was designed enabling bonding four membranes at a time, in 4 separate membrane chambers.

Preliminary testing involved reducing the total force delivered by the pneumatic press, to adequately compensate for the small area involved in bonding. Good results were observed by restricting the compressor to a minimal air pressure of P_c = 1.0 bar, corresponding to P_{TF} = 242.6 bar. T_{TF} and t_{TF} were maintained at the values of 78°C and 20 min, respectively. To ensure the bonding between the PETE-TE membrane and the PS microfluidic layer, it was further necessary to treat the surfaces of both substrates with oxygen plasma. This is due to the fact that PS and PETE present different molecular polarities, with PETE being polar and PS non-polar, making it challenging to obtain a covalent bond between the two materials without adequate surface treatments [287]. By performing oxygen plasma treatment, polar functional groups, such as hydroxyl (*-OH*), carboxyl (*-COOH*) and

carbonyl (-*C*=*O*) are introduced to the surfaces of both materials, increasing the surface energy and polarity, and ultimately enhancing adhesion [288]. This way, to obtain an appropriate bond between the PETE-TE membranes and the PS channels, oxygen plasma treatment was performed for 1 min at 160 W. Below this value, membrane bonding was either achieved partially or not at all.

The protocol including oxygen plasma treatment prior to thermal fusion was successful in bonding the PS microfluidic layer and the PETE-TE membrane together, as observed in Figure 4.9 B. This figure also evidences the existence of a circular weld in the periphery of the membrane, in lighter grey. This weld is also visible using SEM, as shown in Figure 4.9 C. The surface captured in the figure highlights three tones of grey, with the lighter tone (on the right side) representing the free-standing surface of the membrane, and the darker tone (in the middle) the surface of the membrane overlapping the membrane chamber. The medium tone (in the left) represents the surface of the weld, which exhibits the existence of pores and therefore suggests a less consolidated bond. By analysing the centre of the membrane instead, Figure 4.9 D, it is observed that the porous network of the membrane remains intact, despite the surface treatment and bonding procedure. This provides evidence to the preservation of the permeability properties of the membrane. Finally, an analysis to the cross section of the membrane, Figure 4.9 E, further demonstrates the preservation of the pores, which traverse the membrane from the top to the bottom surface.

Due to the material compatibility, bonding with the PS-ES membranes did not require additional treatments. Instead, a strong, reliable seal was achieved, evidenced in Figure 4.9 F. It can be observed that while the membrane presents its characteristic network of fibres in the middle, a distinct bond is present at the periphery, indicated by the lighter grey. An analysis based on SEM, Figure 4.9 G, further highlights the clear boundaries existing between the different interfaces. From top to bottom, the following features can be observed: the surface of the channels, the side wall, the bottom surface of the membrane chamber, the external contour of unbonded membrane fibres, the bonded section, and finally the free-standing area of the membrane. A higher magnification view further demonstrates the interface between the bonded (bottom) and the free-standing surfaces of the membrane (top), Figure 4.9 H. This interface is characterized by the transition between an uniform surface to a dense network of fibres,

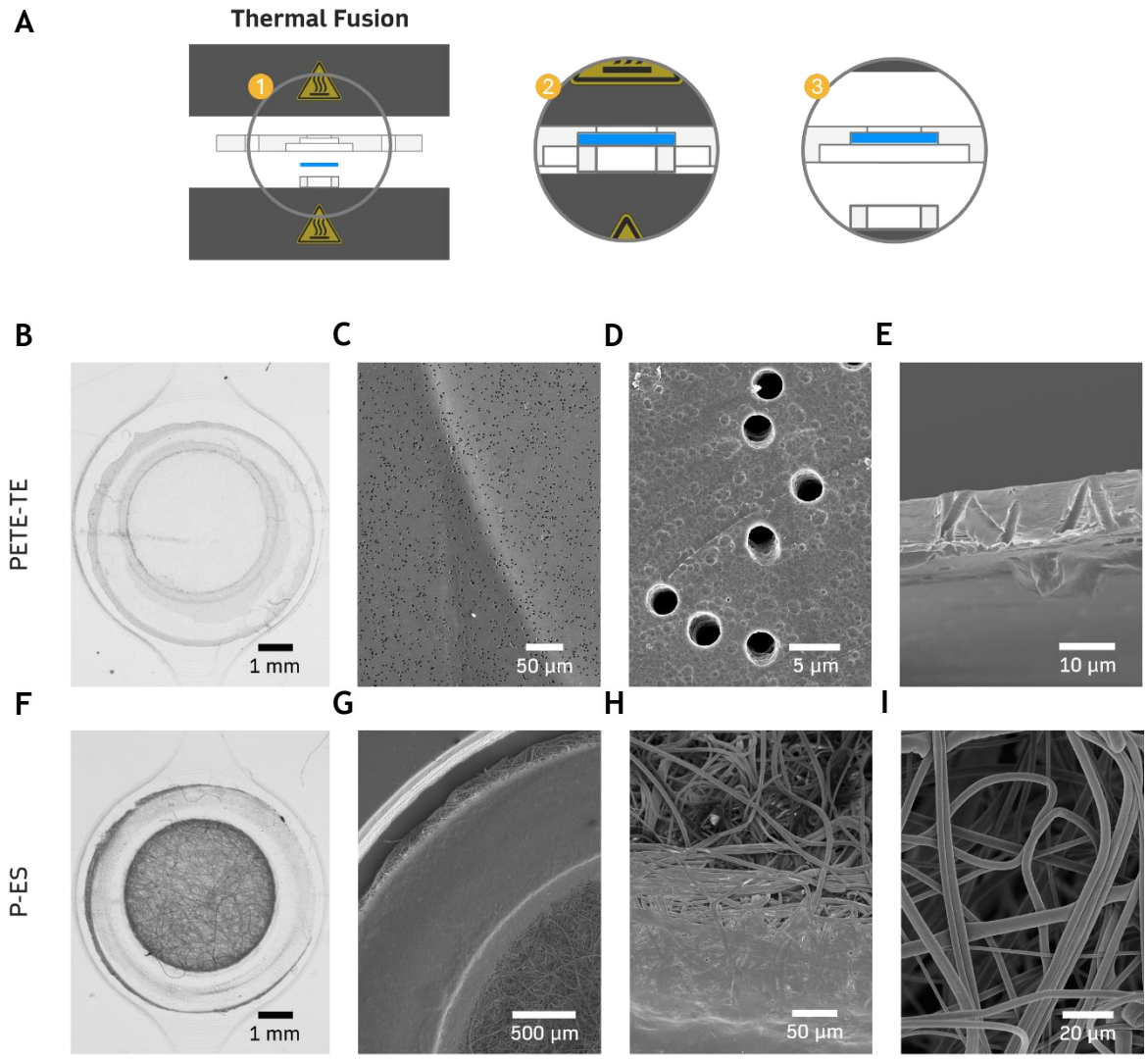

Figure 4.9: Bonding porous membranes with thermal fusion. A, Protocol for bonding, with step 1 representing the assembly, step 2 the bonding procedure, and step 3 the obtention of the final composite layer. B-E, Properties of the PETE-TE membrane sealed with thermal fusion, from chamber overview to the analysis of individual pores. F-I, Properties of the PS-ES membrane bonded with thermal fusion, from chamber overview to the analysis of the fibrous network.

respectively. Figure 4.9 I takes a closer look at the intertwining PS fibres, evidencing the nature of the electrospinning process in the fabrication of the respective membranes, and emphasizing on the preservation of the fibrous network.

Ultimately, results demonstrate that thermal fusion is highly suitable to bond the current PS microfluidic substrates with PS-ES membranes, obtaining strong and reliable seals, while preserving the dense network of fibres characteristic to the respective membranes. However, the procedure proved less effective with PETE-TE membranes, requiring additional surface treatments such as oxygen plasma and resulting in more fragile seals.

4.2.3.3 Porous Membrane Bonding with Ultrasonic Welding

The setup for ultrasonic welding porous membranes is illustrated in Figure 4.10 A. It includes a fixture (filled in yellow), fitted to the anvil, produced via 3D printing and specifically designed to press the membrane against the microfluidic substrate during welding (Figure 4.10 A, step 2). To do so, it integrates a protrusion with a similar size and shape to that of the membrane chamber. Furthermore, it includes a cavity in the centre, so that the membrane is only pressed in its outer perimeter, this way promoting welding exclusively in the respective area. Furthermore, the protrusion is designed to be taller than the microfluidic layer, so that only the membrane surface is under pressure. After welding, the pressure is released and the bonded component is obtained (Figure 4.10 A, step 3).

A preliminary study was initially conducted to determine the process parameters ensuring the successful welding of the PETE-TE membranes. From this study it was observed that, despite the opposing polarities of the PETE and PS materials, as previously mentioned, ultrasonic welding did not require surface treatments such as oxygen plasma to bond the two substrates. Instead, it was determined that using the Energy Mode and employing E_{USW} = 40 Ws, together with P_{USW} = 3.6 [bar] and V_{USW} = 2.5 generated a reliable seal, as shown by the uniform weld on the periphery of the membrane in Figure 4.10 B. An analysis via SEM provided further evidence to the strength of the weld. As shown in Figure 4.10 C, there is a clear distinction between the solid, bonded surface, at the top, and the free-standing membrane, at the bottom, which displays its characteristic network of pores. A higher magnification view over the centre of the membrane, Figure 4.10 D, and a closer look at the cross section of the membrane, Figure 4.10 E, further demonstrate the structural integrity of the pores. Additionally, the size of the pores, measured at 2.9 ± 0.1 µm, match those provided by datasheet (3 µm), this way presenting further evidence of the preservation of the membrane's permeability properties.

Ultrasonic welding was further observed to be capable of stretching the PETE-TE membranes as a function of process parameters, particularly the welding energy. Results demonstrate that, while at E_{USW} = 20 Ws the welded membrane presents a very significant curvature, Figure 4.10 F, at E_{USW} = 160 Ws the surface of the membrane flattens, Figure 4.10 G. By plotting the waviness profile associated with

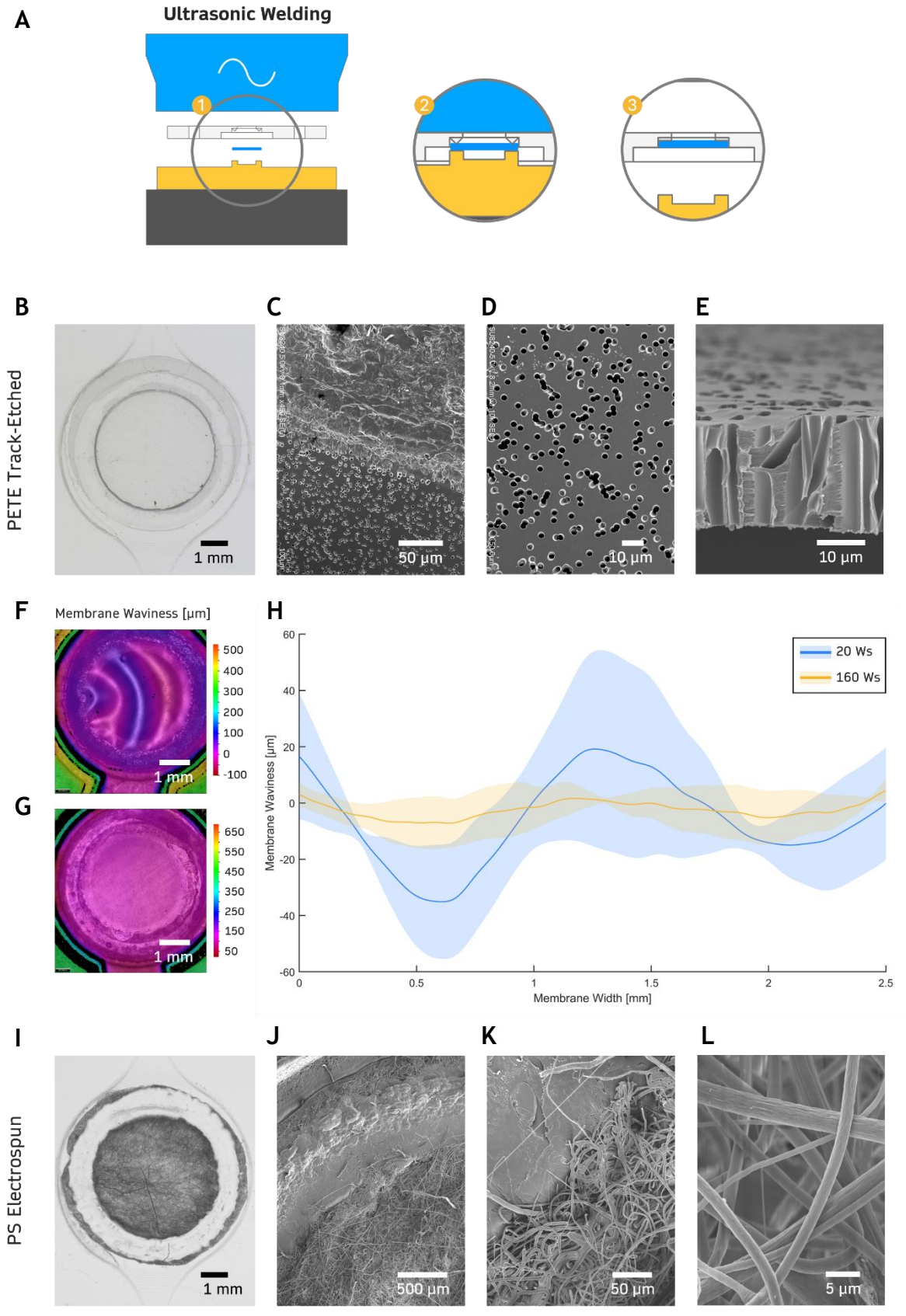

Figure 4.10: Bonding porous membranes with ultrasonic welding. A, Protocol for ultrasonic welding, with step 1 representing the assembly, step 2 the welding process, and step 3 the obtention of the final, bonded composite layer. B-E, Properties of the PETE-TE membrane sealed with ultrasonic welding, from chamber overview to the analysis of the pores. J and K, Surface deflection for an energy transfer of 20 Ws and 160 Ws respectively. L, Plot of the surface waviness along the membrane diameter, as a function of the applied energy transfer. I-L, Properties of the PS-ES membrane bonded with ultrasonic welding, from chamber overview to the analysis of the fibrous network.

each processing condition, Figure 4.10 H, it is possible to observe the significant reduction of waviness obtained from increasing the welding energy. Whereas for E_{USW} = 20 Ws, the difference between the highest and lowest points of the membrane surface profile is equivalent to 80.7 ± 36.9 µm, for E_{USW} = 160 Ws, this value reduces to 22.8 ± 9.7 µm. Especially for OOC applications, where a flat membrane surface is preferred for the culture of cells and their respective analysis, as it facilitates microscopy-based approaches, the presented approach with ultrasonic welding becomes particularly advantageous.

Similar to the approach with the PETE-TE membranes, preliminary studies were conducted to evaluate the minimal process parameters for the successful welding of PS-ES membranes. Since both the device and the membrane are made of PS, a stronger bond was achieved for lower process conditions. In this case, the parameters E_{USW} = 10 Ws, P_{USW} = 3.6 [bar] and V_{USW} = 2.5, were sufficient to obtain a robust seal, as shown in Figure 4.10 I by the distinctive weld on the periphery of the membrane. An analysis via SEM, Figure 4.10 J, evidences the strength of the seal but also the violence of the process involved. This is indicated by the high material deformation at the outer edge of the bond, due to the ultrasonic vibrations. This deformation is particularly noticeable when comparing this seal with the one obtained via thermal fusion, in Figure 4.9 G, which is more uniform. A closer look in Figure 4.10 H, highlights the transition between the bonded and free-standing surface of the membrane. Finally, Figure 4.10 I demonstrates that the network of fibres within the free-standing surface of the membrane remains intact, despite the violent effect of the ultrasonic vibrations, suggesting the preservation of the permeability properties of the membrane.

Ultimately, ultrasonic welding presents greater potential to bond the PETE-TE membranes, as opposed to thermal fusion. Despite defining a strong seal with the PS-ES membranes, the violent effect characteristic to the procedure is more prone to compromising the structural properties of the membrane than bonding with thermal fusion, whose seal was more focused. However, when it comes to bonding the PETE-TE membranes, ultrasonic welding provides a more reliable seal, without requiring additional surface treatments such as oxygen plasma. More so, the ability to stretch the membrane and reduce surface deflection as a function of welding energy, provides a very attractive solution to various applications within microfluidics and in particular OOC.

4.2.4 Summary of Bonding Technologies and Fabrication of a Multi-Layered Microfluidic Device with Integrated Porous Membrane

Various bonding technologies and different strategies were investigated and employed to seal microfluidic channels, based on PS substrates, and porous membranes, consisting of both PETE-TE and PS-ES types. Table 4.1 and Table 4.2 provide an overview of the technologies respectively tested for channel and membrane bonding, detailing their optimal process parameters and additional strategies, as well as their key advantages, limitations and most suitable applications.

When it comes to channel bonding, the technology seen as most suitable for the PS microfluidic substrates was thermal fusion bonding. Not only does it provide a strong, reliable seal, but it also does not compromise on channel geometry, nor does it require the addition of extra features, such as energy directors. This ultimately enables the bonding of dense networks of channels. Importantly, it also generates a high surface finish and thus high optical transparency. Additionally, the process is extremely reproducible and highly scalable. Ultrasonic welding provides an even more rapid process. However, not only was the bonding quality less reproducible, but also, the optical qualities of the bonded devices were poorer in comparison to those presented by thermal fusion bonding. More so, not only do the energy directors compromise on channel density, but also, they difficult achieving an accurate seal with smaller channels. Finally, despite being a good approach to rapid prototyping and the testing of concepts, providing a reliable seal and reasonable fluidic confinement, the use of adhesive tapes is significantly limited by the manual labour involved, associated variability and its low scalability. Regarding sealing porous membranes, it was observed that, depending on the material and nature of the membrane involved, either thermal fusion or ultrasonic welding were the most suitable processes. For the PETE-TE membranes, ultrasonic welding provided the most promising approach. Not only was it capable of bonding the membranes without additional surface treatments, but also, it provided a strong reliable seal, with the particular ability of reducing surface waviness as a function of process parameters such as the amount of energy transfer. This defines a very attractive feature to various applications within microfluidics, particularly OOC, where a flat membrane surface is desired for the culture and analysis of cells, based on microscopy approaches. In turn, for the PS-

ES membranes, thermal fusion was seen as the most suitable bonding process. It provided a strong and uniform seal, without causing surface deformation and while preserving the fibrous network of the membranes, keeping their permeability properties. The usage of liquid optical adhesives was seen, however, as a less suitable approach, significantly compromising on the permeability properties of the membranes involved. This was due to the impregnation of the membrane prior to UV exposure and curing, a phenomena which was seen to provide greater implications for the PS-ES membranes, compromising the permeability of the membrane almost entirely. To provide a proof-of-concept for the developed bonding protocols, a three—layered microfluidic device, following a layout similar to that of Figure 4.6 A, was fabricated. The device is displayed in Figure 4.11 A, highlighting a channel network defined by two individual, parallel channels, one filled with blue-coloured medium and the other red, connected only via the porous barrier of a PS-ES membrane, in the centre chamber. Both the channels and membrane were bonded using thermal fusion, by employing the parameters defined in Table 4.1 and Table 4.2 respectively. Figure 4.11 B highlights the empty membrane chamber, as well as inlet and outlet channels, and Figure 4.11 C provides a similar frame but with the chamber and channels filled with media. Figure 4.11 D and E further provides a higher magnification view, highlighting the

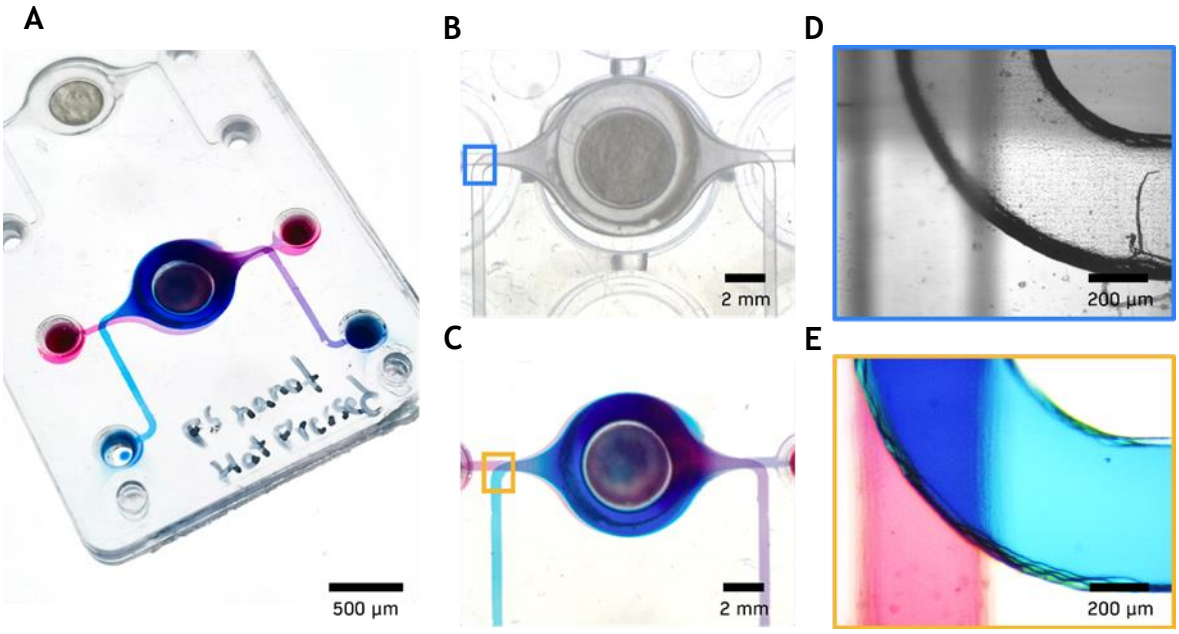

Figure 4.11: Fabrication of a multi-layered microfluidic device with integrated porous membrane as proof-of-concept. A, Microfluidic device integrating a PS-ES membrane, bonded via thermal fusion. B and C, Membrane chamber and inlet and outlet channels respectively empty and filled with red- (top) and blue-coloured media (bottom). D and E, overlapping top and bottom channels, respectively empty and filled with red- (bottom) and blue-coloured media (top).

overlapping, yet isolated, top and bottom channels, respectively empty and filled with media, and providing an appropriate seal.

Table 4.1: Technologies for microfluidic channel bonding with PS substrates, and their respective optimal parameters, additional strategies, general properties, advantages, disadvantages and suitable applications. Classification: "+" (good); "+/-" (moderate); "-" (poor).

Technology	Pressure Sensitive Double-Sided Tape	Ultrasonic Welding	Thermal Fusion
Optimal Process Parameters	• Pressure: 3.3 bar • Time: 1 min	Time and Energy Mode • E_{USW} = 50 Ws • t_{USW} = 300 ms • P_{USW} = 3.6 bar • V_{USW} = 5	• T_{TF} = 78 °C • P_{TF} = 35.7 bar • t_{TF} = 20 min
Additional Strategies	-	• Provide a secure and stable fitting between the channels and the anvil, to avoid the relative movement between layers and in regard to the welding horn, and optimize bonding quality	• Use carrier layers to enhance surface quality. Opt for materials with a higher *Tg* or different polarity to avoid bonding with devices
Bonding Quality	-	+/-	+
Scalability	-	+	+
Process Time	+/-	+	+/-
Design Freedom	-	+/-	+
Equipment Requirements	+	-	+/-
Advantages	• Cost-effective • Provides a strong reliable seal	• Extremely rapid bonding (~1 s) • Provides a strong seal	• Extremely reliable and high-quality seal • High geometric freedom • No additional process or elements are needed
Disadvantages	• Lack of accuracy when bonding fine channels • Air entrapment	• Energy directors compromise on channel geometry, minimum feature size and channel density	• Long bonding cycle (20 min) • Channels with low aspect ratio are prone to significant deformation
Suitable Applications	• Rapid prototyping	• Rapid bonding layers with mesoscale features (> 100 µm)	• Microfluidic devices involving fine channels and strict quality requirements

4.3 Fluidic Interfacing

As established in Section 2.2.2, microfluidic interfacing for thermoplastic devices is far from being standardized and it is, in most cases, application specific. Similarly, throughout this project, fluidic interfacing was explored and developed according to the varying fluidic requirements of different applications. These fluidic requirements encompassed both pressure- and gravity-driven flow, leading therefore to the exploration of both tubing interconnect and open well solutions.

Table 4.2: Technologies for bonding membranes to PS substrates, and their respective optimal parameters, additional strategies, general properties, advantages, disadvantages and suitable applications. Classification: "+" (good); "+/-" (moderate); "-" (poor).

Technology	Liquid Optical Adhesives	Ultrasonic Welding	Thermal Fusion
Optimal Process Parameters	• Adhesive: Norland Optical Adhesive 73 • Exposure: 50 s	Energy Mode • E_{USW} = 160 Ws (PETE-TE) / 10 Ws (PS-ES) • P_{USW} = 3.6 bar • V_{USW} = 5	• T_{TF} = 78 °C • P_{TF} = 242.6 bar • t_{TF} = 20 min
Additional Strategies	-	• Development of a fixture to focus the pressure and ultrasonic vibrations to the peripheral surface of the membrane in direct contact with the bonding area	• Use surface treatments, such as oxygen plasma, to increase surface energy and enhance adhesion (PETE-TE) • Use structures such as washers, to focalize the pressure and enhance bonding in the periphery of the membrane
Bonding Quality	-	+/-	+/-
Scalability	-	+	+
Process Time	+/-	+	+/-
Design Freedom	+/-	+/-	+
Equipment Requirements	+	-	+/-
Advantages	• Strong and rapid bond	• Does not require additional surface treatments to bond materials with opposing polarities such as PETE and PS • Capability of stretching membranes as a function of welding energy	• High quality seal between materials with similar surface polarities
Disadvantages	• Wetting prior to curing affects membrane permeability properties	• Violent procedure, with significant effect on fragile membrane matrices, such as obtained from electrospinning • Energy directors provide geometric limitations	• Poor bonding between materials with opposing molecular polarities, such as PS and PETE, even after surface treatments such as oxygen plasma
Suitable Applications	• Rapid prototyping and testing new device architectures	• Bonding track-etched membranes • Bonding materials with opposing molecular polarities • Regulating membrane deflection as a function of process parameters	• Bonding membranes to substrates with similar molecular polarities. • Bonding membranes with diverse structural matrices, electrospun or track-etched

4.3.1 Materials and Methods

The materials and methods involved in the investigation and development of approaches to microfluidic interfacing will be identified and described in the following section.

4.3.1.1 3D Printing with Elastomer Prepolymer Resins

The development of soft components, particularly inserts, plugs and gaskets for fluidic interfacing and sealing, was explored using 3D printing. The system employed was a Phrozen Sonic Mini 8K (Phrozen, Taiwan). Two different elastomer prepolymer resins were investigated, namely the Formfutura Flex 63A (FF63A) and 82A (FF82A) (Formfutura, Netherlands). The FF63A presents high flexibility and elongation up to 80%, being optimal for elastic components. In turn, the FF82A combines reasonable flexibility with a higher strength and hardness, being optimal for seals and gaskets. Both resins were printed using a layer exposure of 8 s, a layer height of 50 µm, a bottom layer exposure of 60 s and a bottom layer count of 10. The printed components were then washed and agitated in a bath of IPA for 5 min, using a Form Wash (Formlabs, US). After washing, the rinsed components were blown dry using an air gun. Finally, they were cured under UV exposure for 30 min at 60 ºC, using a Form Cure (Formlabs, US).

4.3.1.2 Injection Moulding of Well Plate with Polystyrene

Well plates were injection moulded using existing, machined, steel tooling. The design of the respective well plates followed the dimensions of the standard 96-well plate format. The distinguishing feature is that the well plate is adapted to fit the size of a standard lab slide, presenting an array of 3 x 8 (number of rows x number of columns) wells, and therefore a bottom surface of 32 mm x 77 mm (width x length). The respective tooling is then inserted and fixed to the injection moulding machine, a Victory 28 (Engel, Austria). The polymer selected for injection moulding was polystyrene (PS) (1810 crystal polystyrene, Total Petrochemical and Refining, Belgium), to match the material of the microfluidic chips. The granules of PS were fed into the barrel, where they were heated until 250 ºC, and then cooled at the nozzle to 240 ºC, to prevent stringing. The shot volume was defined to 16 cm^3 and the injection moulding speed to 25 cm^3s^{-1}. After injection, holding pressure was maintained at 450 bar for 4 s, after which the

polymer was allowed to cool for 30 s. Finally, the tool was opened and the part ejected, after which a new cycle began. Sprues were manually cut from all injection moulded parts.

4.3.1.3 Flow Analyses

The development of a microfluidic layout for gravity-driven, bi-directional flow, using a platform for mechanical tilting, involved the characterisation of flow. For such, a setup was developed, as shown in Figure 4.12 A, consisting of a laser cut acrylic base and structures, providing the support to an optical setup and a platform for the imaging of the microfluidic chips. This setup was further implemented on top of a shaker (Ohaus Corporation, US), enabling 3D rocking using the pitch, a_{3DR} [º] and revolutions per minute, ω_{3DR} [rpm] as the control parameters. Importantly, this setup allowed the static imaging of dynamic, 3D rocking microfluidics. The optical setup included a 3.3X Macro Zoom Lens (Edmund Optics, US), with 0.3X to 1X magnification, and a Basler Ace acA1300-200uc Color high speed camera (Basler AG GmbH, Germany), with 1.3 MP and a frame rate of 203 fps, being capable of recording up to 2270 fps with appropriate image cropping. Below the acrylic setup, a daylight lamp (ZhuZhou Xuehan Electronic, China) was installed to provide the required illumination of the samples, as it can be seen in Figure 4.12 B. Imaging was done using the Pylon Viewer software (Basler AG GmbH, Germany). For the measurement of flow, blue polystyrene microbeads (Merck KGaA, Germany), with a diameter of 10 µm, were dissolved into medium and perfused in the channels, as Figure 4.12 C demonstrates. This enabled fluidic tracing by analysing the top view of microfluidic channels with the optical setup described above. The analysis consisted of, first, capturing a time lapse over a cropped portion of the channels at 2270 fps for a set period of time. The generated sequence of images was then analysed using a motion vector software which, following pixel calibration, calculated displacement as a function of time for each frame, as shown in Figure 4.12 D. Preliminary testing was conducted to evaluate the optimal concentration of diluted microbeads for noise reduction, from which it was determined that, a microbead concentration of 20%, dissolved from stock in water, provided the optimal condition for noise reduction, Figure 4.12 E. Other parameters, such as the pitch, angular velocity, and the set exposure time of the camera were also tested.

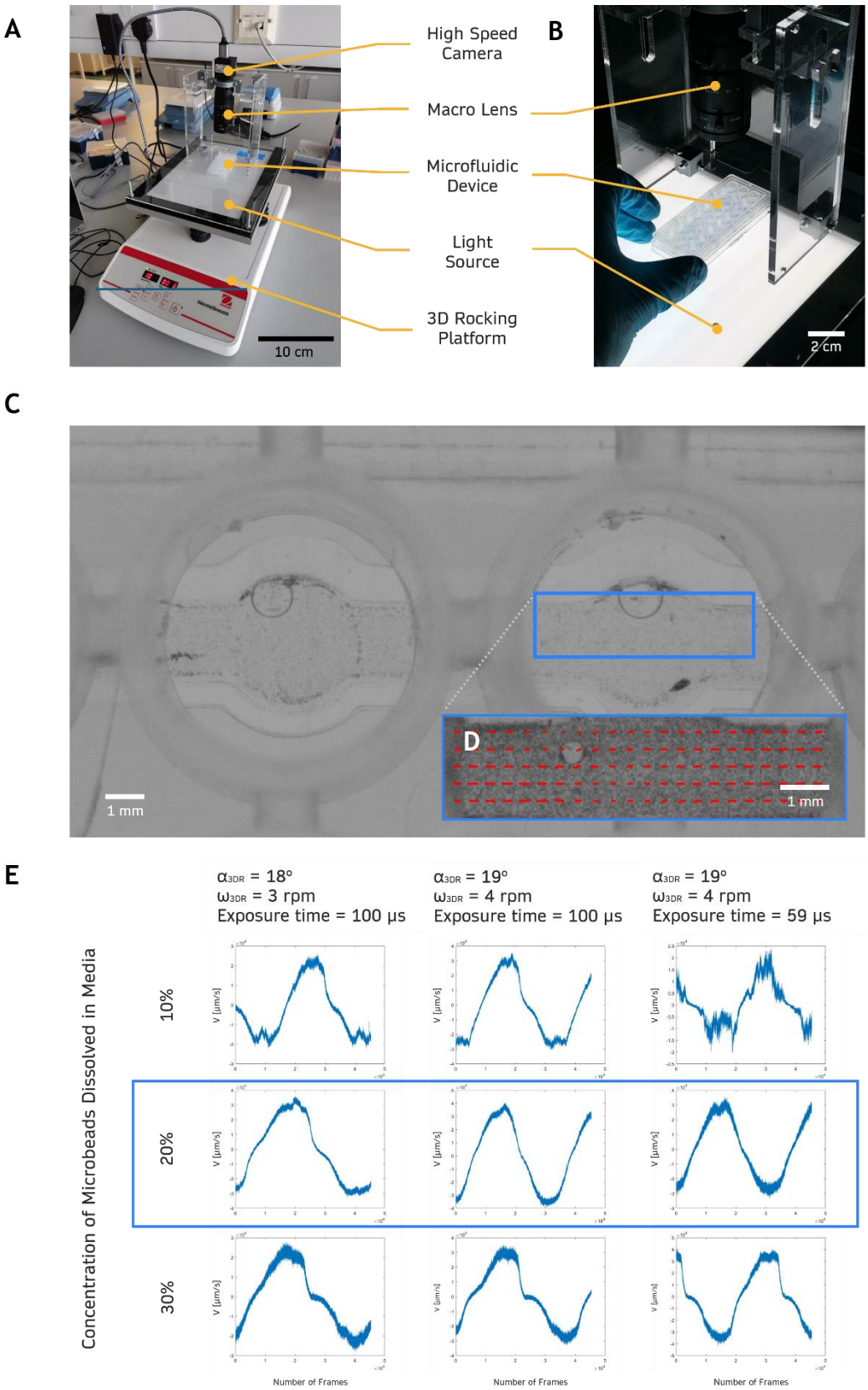

Figure 4.12: Method for fluidic analysis. A, Setup developed to measure fluid flow with gravity-driven microfluidic systems based on 2D and 3D rocking. B, Highlight of the respective system in operation, with the light source on. C, Top view of the respective microfluidic channels, filled with microbeads (black dots) dissolved in media. D, Cropped image of the channel, as recorded at high frame rates, displaying the generated velocity array of the dissolved microbeads. E, Noise reduction tests, evaluating the smoothness of data as a function of microbead concentration, as well as the pitch, revolutions per minute, and the exposure time of the camera.

4.3.2 Tubing Interconnects

To connect the developed microfluidic chips to peripherals such as external tubing and infusion pumps for pressure-driven fluidics, two different types of fluidic interconnects were tested. An initial approach consisted of permanently bonding commercial syringe tips to the I/Os of the developed microfluidic devices, as demonstrated in Figure 4.13 A. Figure 4.13 B provides a 3D illustration of the respective setup, whereas Figure 4.13 C highlights the associated cross section and fluidic path. As Figure 4.13 B and C show, the syringe tips were bonded to the microfluidic devices using liquid optical adhesives. The curing process consisted of exposing the liquid adhesive joints to UV radiation for 1 min. A key benefit of this approach is the ability to easily connect the microfluidic device to various different sizes of standardized fluidic tubing. However, the variability of the bonding procedure as well as the manual labour involved are significant downsides. Undesired wetting of channels with the liquid adhesive can further cause channel clogging, as well as become a source of contamination. Another downside of this approach is dead volume associated with each syringe which is significantly larger than the volume of the channels, as Figure 4.13 C demonstrates. The ratio is approximately five to one, with each syringe encompassing a volume of 137 µL and the channels a volume of 26.14 µL.

Another approach consisted of integrating acrylic components, laser cut to present a taper similar to that of a Luer Connector [289], complemented by push-fit soft interconnects to lock capillary tubing and enhance sealing, as it is demonstrated in Figure 4.13 D. Both these components were designed and developed by Euan McDonald, KTP Associate. A 3D view of the setup is illustrated in Figure 4.13 E, together with the cross-section of the respective fluidic path, Figure 4.13 F. As identified in the figure, pressure sensitive double-sided tape was used, complemented by cold pressing, to bond the laser cut Luer connector to the microfluidic substrate. The acrylic Luer connector is 5 [mm] in height and presents an outer diameter of 8 [mm]. The soft interconnect is made by 3D printing with the FF82A resin. This setup offers a more robust and versatile fluidic interconnect, capable of easily connecting tubing with different dimensions by adapting the inner diameter of the push fit soft interconnect. Moreover, it provides a convenient solution to reversible fluidic interconnects, being extremely easy to plug tubing in and out via simple push fit. It also presents a much smaller solution

to fluidic interfacing, with virtually null dead volume, providing the fluidic tubing is plugged all the way in until reaching the surface of the microfluidic device. Finally, the fabrication of the acrylic Luer connectors via laser cutting is automated and relatively scalable. The bonding procedure using the pressure sensitive double-sided tape and cold pressing is, as well, both reproducible and reliable.

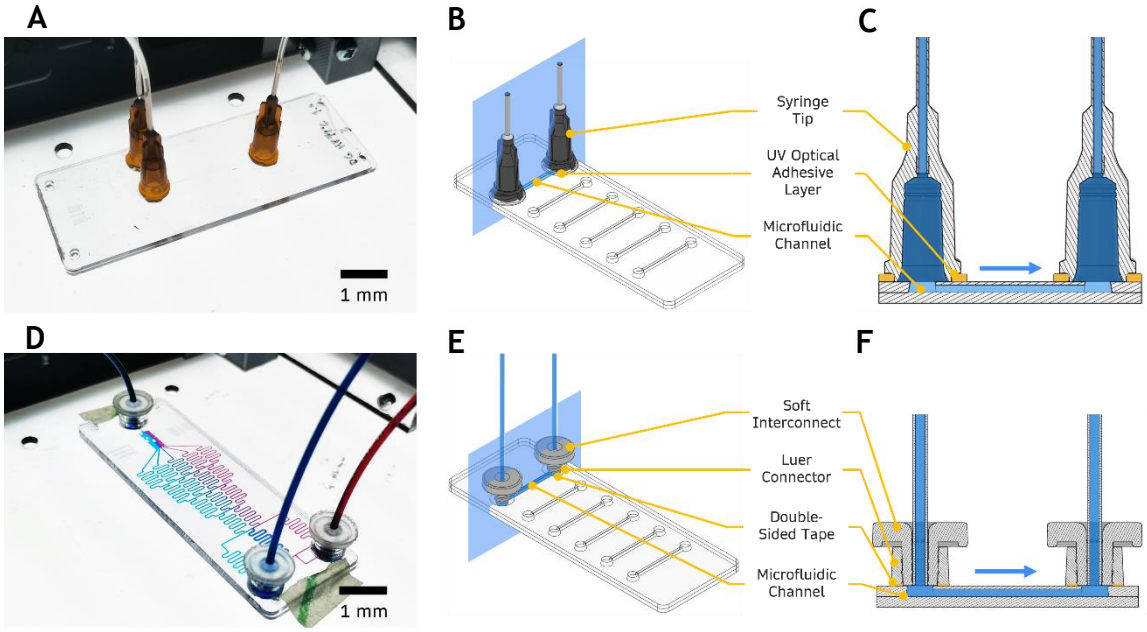

Figure 4.13: Strategies for microfluidic tubing interconnects. A, Dispense syringe tips as fluidic interconnects, using optical adhesive as the bonding strategy. B, 3D illustration of the fluidic interfacing strategy using fluidic dispense tips, identifying its key elements and further highlighting them on the cross-sectional view of the channel and fluidic path, C. D, Laser cut Luer connectors and soft inserts as fluidic interconnects, using tape as the method to bond the laser cut Luer connectors and simple push fit to connect the soft inserts and tubing. E, 3D illustration of the fluidic interfacing strategy using Luer connectors and soft inserts, identifying its key elements and further highlighting them on the cross-sectional view of the channel and fluidic path, F.

4.3.3 Open Well Connection

Searching to simplify fluidic interfacing, many microfluidic applications, particularly in the realm of OOC, as described in Section 2.2.2.2, are returning to open well solutions to reduce operation complexity, the footprint of peripherals, and increase usability. During the course of this degree, some of the applications developed for OOC purposes required similar strategies towards implementing gravity-driven flow and simplifying fluidic interfacing. For this reason, an approach to integrating open wells was investigated.

4.3.3.1 Well Plate Concept

Part of the challenge associated with the respective strategy lies in including reservoirs where a large volume of liquid can be stored and enable recirculating, bi-directional flow through hydrostatic pressure and cyclic rocking. The integration of such large reservoirs is particularly challenging with the current RT setup, given that due to tooling and process constrains, the thickness of the fabricated microfluidic chips is fixed to 1.1 mm. Increasing this thickness towards facilitating the integration of larger reservoirs would introduce significant instabilities to polymer cooling and ultimately lead to residual stress, distortion, and warpage [83]. Instead of modifying the present RT setup to contemplate the fabrication of a new component, an existing injection moulding tooling, developed for previous projects in the lab, was employed. This tool provided the mould for a standard 96-well plate adapted to the size of a standard lab slide, and therefore, the size of the current PS devices. This way not only did the well plate format define a standardized interface, well-known across every lab and field in life sciences research and industry, but also, its wells provided fitting reservoirs to enable gravity-driven flow. Therefore, this approach proposed injection moulding the respective well plate with the same PS material as the microfluidic chips, to be integrated as the top interfacing layer, as the exploded view on Figure 4.14 A illustrates. After bonding, each well would be connected to the I/Os of each respective microfluidic channel, allowing the storage of larger volumes of medium, as Figure 4.14 B demonstrates, and ultimately enabling gravity-driven flow using 2D or 3D rocking.

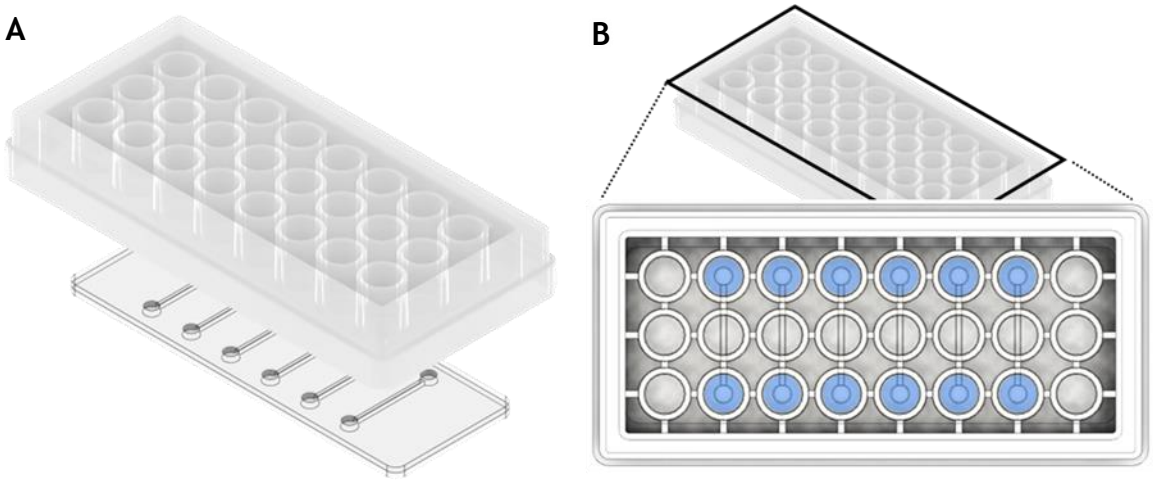

Figure 4.14: Well plate integration for open well microfluidic interfacing. A, Exploded view of the well plate and polymer device. B, Well plate bonded to the device, highlighting its top view, where the microfluidic channels are visible, as well as the wells filled with media for gravity-driven flow.

4.3.3.2 Well Plate Bonding and Gravity-Driven Fluidics

Bonding the well plate to the PS chips is particularly challenging. Due to its unique characteristics, such as its height (1 cm tall), hollow features and thin walls, achieving a successful bond without channel or well plate deformation is not trivial. The work on Section 4.2 lead to the selection of thermal fusion as the optimal process for bonding the microfluidic channels. This way, a first strategy to the integration of the well plate consisted of similarly employing thermal fusion as the bonding process to seal both channels and well plate together. Considering that the top surface of the well plate provides a smaller area to that of the PS microfluidic devices (1336.7 mm^3 < 2021.6 mm^3, respectively), a first approach consisted of reducing the cylinder pressure to P_c = 4 psi, and this way maintaining the process pressure at P_{TF} = 2.5 bar. Temperature and process time were maintained at T_{TF} = 78 °C and t_{TF} = 20 min, respectively. However, with these conditions, the components did not bond. A second approach consisted of increasing the pressure and temperature, to P_{TF} = 3.8 bar and t_{TF} = 79 °C respectively. However, as demonstrated in Figure 4.15 A and B, while the seal is apparently good immediately after filling the reservoirs, Figure 4.15 A, it is quickly broken after a few minutes, leading to the spreading of media, as shown in Figure 4.15 B. It is important to note that the leakages developed exclusively at the interface between the well plate and the microfluidic device, where delamination occurred. In contrast, the microfluidic channels presented a strong, reliable seal, similar to that described in Section 4.2. More so, an analysis to Figure 4.15 C and D further demonstrates the effects of the process parameters involved. In Figure 4.15 C it is possible to observe that strong surface deformation is observed due to the high temperature and pressure applied, hot embossing the bottom surface of the well plate to the top surface of the microfluidic device, without improving the seal. This translates further into channel distortion, as can be observed in Figure 4.15 D, with the channel presenting a slight curvature in the section between the two wells. Figure 4.15 D further highlights the appearance of rainbow patterns, which indicate a partially bonded surface. This way, the figure demonstrates the fragility of the bond established between the well plate and the microfluidic device which, upon fluidic pressure, such as in Figure 4.15 A, cause the seal to break and create leakages, such as in Figure 4.15 B.

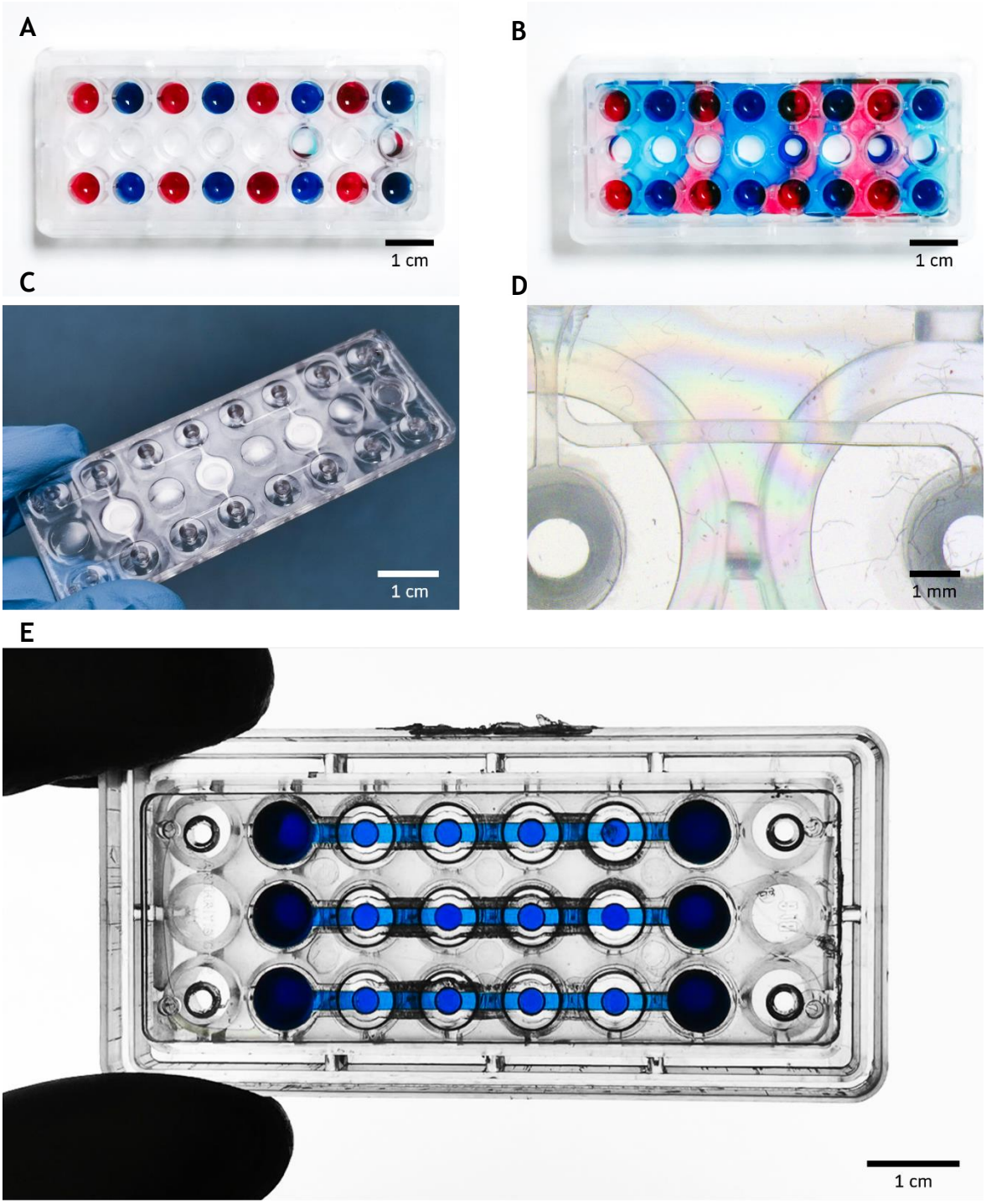

Figure 4.15: Well plate bonding. A, Microfluidic channels and well plate, bonded via thermal fusion and filled with media. B, The same microfluidic device, minutes later, evidencing a broken seal and media leakage. C, Delaminated device, evidencing surface deformation due to temperature and the pressure applied by the well plate against the device surface. D, Channel distortion and the appearance of rainbow patterns, evidencing a partial bond between the well plate and the microfluidic device. E, Microfluidic channels bonded to the well plate using double-sided tape, resulting in a strong, reliable bond, capable of suitably confine media.

Another approach consisted of bonding the well plate to the microfluidic channels using ultrasonic welding. For this strategy, a different tool was employed, contemplating well plates with energy directors around the perimeter of the wells. This tool had been similarly developed previously in the lab. However, it

was found that this approach was only viable when the channels were ultrasonic welded as well. When they were bonded using thermal fusion, it was observed that the ultrasonic vibrations would break the seal established between the channels. A more suitable and reliable approach was found by using pressure sensitive double-sided tape instead. While the microfluidic channels were bonded using thermal fusion, as previously proposed, the well plate was sealed afterwards with tape. Due to the wide diameter of the wells, bonding tape to the bottom surface of the well plate is less affected by lower-precision alignment, as opposed to when fine microfluidic channels are involved. This way, by laser cutting 3M tape with the parameters established in Section 4.2.2.1, attaching it to the bottom surface of the well plate, and bonding the component to the microfluidic devices using cold pressing, a strong, reliable seal was obtained, as shown in Figure 4.15 E. The appropriate confinement of the blue-medium to the channels and reservoirs demonstrates the successful seal.

To evaluate the ability of the presented setup in obtaining bi-directional flow induced by gravity and tilting, a device similar to the one presented in Figure 4.15 D was tested in a 3D rocking platform. As illustrated in Figure 4.16 A-F, the device was continuously tilted in both directions, according to $\alpha_{3DR} = 15^{\circ}$ and a cycle period of 14 s. The working principle behind this technique is that, by tilting the device, flow is forced downwards to equalize the liquid level between the top and bottom reservoirs, Figure 4.16 A-C, ultimately displacing the volume of media from one reservoir to the other via hydrostatic pressure. By cyclically tilting the device from one side to the other, Figure 4.16 D-F, it is possible to obtain recirculating, bi-directional flow. The fluidic profile that results from the respective motion, with fluid velocity plotted as a function of the cycle time, is observed in Figure 4.16 G. The same figure also demonstrates the effects of changing the volume of media contained in each reservoir to the resulting fluidic profile. For a volume of 400 µL (highlighted in yellow) it is observed that the fluidic profile is slightly discontinuous, suggesting that the medium is quickly transferred from one reservoir to the other and resulting in transition periods (such as observed between 9 s an 11 s) where the flow velocity is null. Instead, a volume of 1200 µL (highlighted in blue) provides a more continuous fluidic profile,

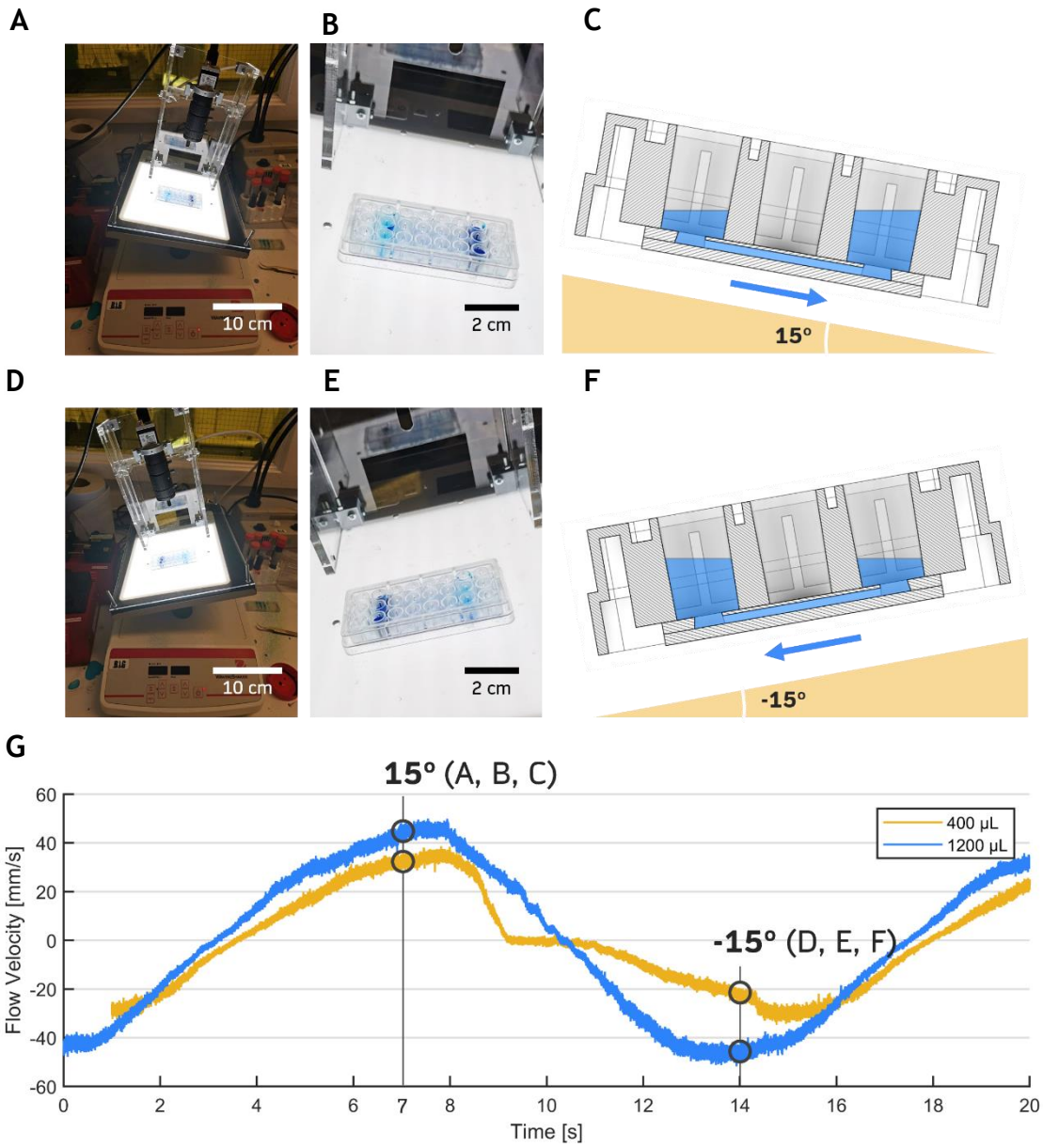

Figure 4.16: Gravity-driven flow with well plate interfacing and 2D tilting. A and B, Respectively a general view, highlighting the 3D rocking machine with integrated optical setup, and a close-up, demonstrating the microfluidic platform, both at a pitching angle of 15°. C, Illustration of the respective setup at the pitching angle of 15°, highlighting the flow of media from the left reservoir to the right. D and E, Respectively a general view, highlighting the 3D rocking machine with integrated optical setup, and a close-up, demonstrating the microfluidic platform, both at a pitching angle of -15°. F, Illustration of the respective setup at the pitching angle of -15°, highlighting the flow of media from the right reservoir to the left. G, Flow velocity plotted as a function of the cycle time and the volume of media in each reservoir.

resembling a sinusoidal curve. It suggests that with the respective conditions, the medium on the reservoirs is not completely depleted after each cycle, meaning that there is always medium flowing from one reservoir to the other, resulting in a smoother profile. More so, it is possible to observe that a larger volume of medium results in an increase of flow velocity as well. As Figure 4.16 G demonstrates, whereas for 400 µL, the top fluid velocity was approximately 35 mm/s, for 1200 µL, this value increased to approximately 45 mm/s. Furthermore, Figure 4.16 G identifies the time points of the plot which correspond to Figure

4.16 A-C, where a_{3DR} = 15°, and Figure 4.16 D-F, where a_{3DR} = -15°. Ultimately, not only does this data provide evidence to the ability of the current microfluidic setup and interfacing system in producing gravity-driven, recirculating, bi-directional flow, but also, it demonstrates the relevance of media volume in determining the fluidic profile and velocity magnitude.

4.3.3.3 Integration of Pressure-Driven Fluidics

Following the work with 3D printing using elastomer resins and aiming to define a versatile platform capable of integrating multiple modes of fluidic perfusion, the presented interfacing system was explored in the integration of pressure-driven fluidics. This way, by adopting a similar concept to that of the inserts described in Section 4.3.2, soft fluidic plugs were designed and printed using the FF82A resin to fit the tapered surfaces of the well plate. The respective fluidic plugs are illustrated in Figure 4.17 A, with their cross section demonstrated in Figure 4.17 B. An analysis of the cross section of the inserts highlights three important elements. First, a Luer connector, to house fluidic tubing, complemented by a female Luer lock format [290], to allow the connection to standardized syringe tips. Second, a fluidic channel traversing the insert from top to bottom, and therefore connecting the fluidic tubing to the inlet of the microfluidic device. And third, three sealing rings to press against the tapered wall of the wells and obtain conformal sealing. The cross section of a fully mounted system, incorporating a microfluidic channel, well plate, fluidic plugs and respective tubing is illustrated in Figure 4.17 C. The equivalent microfluidic device, with inserted tubing and fluidic plugs, is presented in Figure 4.17 D, highlighting the connected microfluidic channel, with orange-coloured medium, in the centre well. Furthermore, on the top left corner, a fluidic plug connected to a standard syringe tip by using the integrated Luer locking system is shown. This setup describes an extremely easy and simple solution to connecting the current microfluidic platform to peripherals such as external tubing and infusion pumps, for pressure-driven flow. Furthermore, not only does it facilitate plugging tubing in and out, through simple push-fit, but it also allows the connection to standard syringe tips of various different sizes. By doing so, tubing of various different diameters can be connected with one single plug. More so, by plugging the tubing directly into the plug, it is possible to obtain minimal dead volume, similar to the Luer interconnects defined in Section 4.3.2. And finally, through 3D printing, not only

can the plugs be easily redesigned to suit different fluidic tubing sizes, but they can be produced in high volume and good reproducibility as well.

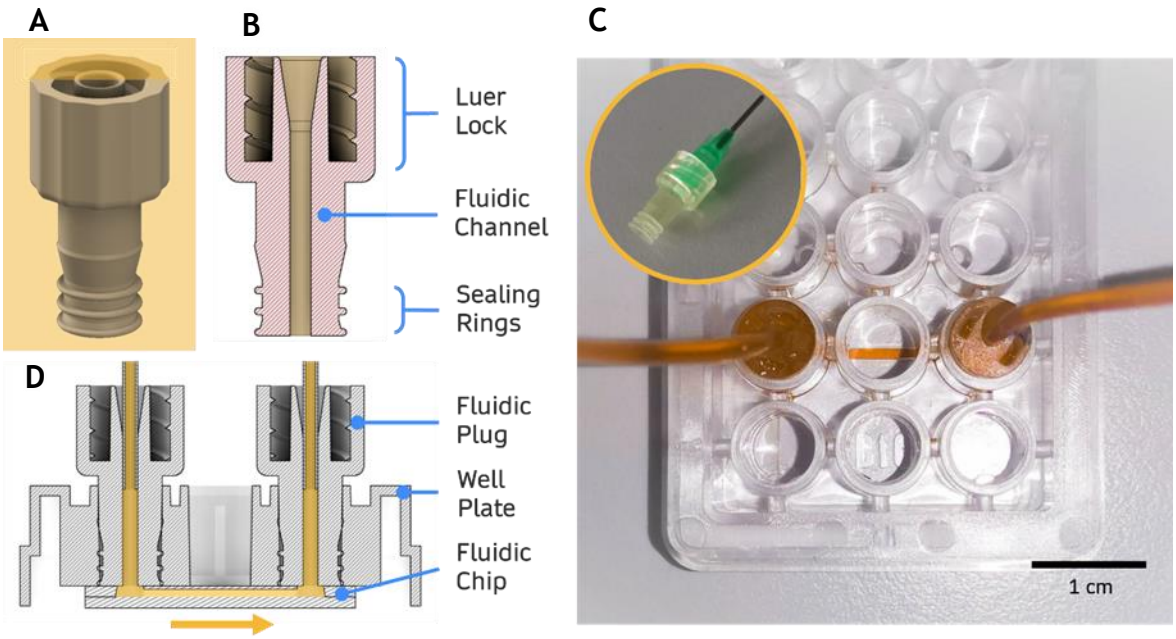

Figure 4.17: Pressure-driven fluidics with the well plate interfacing layer. A and B, Fluidic plug and its cross section, respectively, highlighting the various designed elements. C, Cross sectional view of a microfluidic device with a well plate, integrating the respective fluidic plugs for pressure-driven flow. D, The equivalent fabricated device, highlighting the tubing, connected to the plugs, and ultimately generated the flow of media in the microfluidic channels. The figure also highlights, in the top left corner, how the respective fluidic plugs can be integrated with standardized dispense syringe tips using the integrated Luer lock system.

4.3.3.4 Open Chamber Microfluidics and Temporary Sealing of Individual Chambers

A practical challenge to microfluidic systems, particularly in the context of OOC applications, is the limited accessibility to channels and the limitations it imposes to cell culture. Due to the confinement of channels in traditional microfluidic systems, it is not possible to directly access and seed cells in their respective microfluidic chambers. Instead, cells must be pipetted through the inlet of the device and pushed along the channels until eventually reaching their allocated chamber. Naturally, this procedure results in high variability in the precision and density of cell seeding in the desired chambers. For this reason, a significant amount of research within microfluidic literature is focusing on the development and investigation of open chamber microfluidic systems [291, 292].

The presented microfluidic devices and respective interfacing system are highly compatible with open chamber microfluidics. Such a devices is shown in Figure 4.18 A, highlighting three individual, linear channels, filled with red-coloured

medium, open to the wells above and, therefore, directly accessible. By combining this device with the developed 3D printed soft inserts, it is possible to expand the concept further and enable the temporary sealing of individual chambers. To achieve this purpose, simple, soft plugs were designed and printed, using the FF63A resin, as demonstrated in Figure 4.18 B. More so, a rigid cover with a rotating locking system and top access to the wells was designed and printed using the FC resin for the presented well plate format, as shown in Figure 4.18 C and D. What these two components achieve together is that, by inserting the soft plugs into the wells and using the rigid cover to lock and press them against the surface of the microfluidic chambers, it is possible to temporarily seal individual microfluidic chambers. As it is observed in Figure 4.18 E, while the bottom channel is entirely filled with medium, the chamber with the soft plug (third from the left) is not, and remains dry. The opposite is observed in Figure 4.18 F, where the chamber with the fluidic plug is filled with medium, while the rest of the channel is maintained dry. This simple feature opens the possibility to pathways of great potential, particularly in the separate culture of different cell types in the same common microfluidic channel. A brief proof-of-concept is provided in Figure 4.18 G and H, by culturing osteoblasts in the respective microfluidic chambers. It is observed that, when the plugs are inserted and locked in by the rigid cover, Figure 4.18 G, it is possible to directly access the culture chambers and separately seed and culture cells. The higher magnification view allows to observe the perimeter of the soft plug, isolating the osteoblasts in the centre chamber and keeping the channels, on the right, free of cells. Once the cells attach to the surface of their respective chambers, the plugs are removed, opening the fluidics across the channels and allowing the communication between the different cell types. The higher magnification view allows to observe that, despite the absence of the soft plug, the cells remain in culture on the centre of the chamber, whilst the channel on the right is kept cell-free.

Despite being a simple technique, this feature is extremely relevant in enabling the investigation of different communication pathways between multiple cell types and organ tissues. Ultimately, it provides an approach of great potential to explore the “human-on-chip” concept model, as briefly introduced in Section 1.1.4, and enable a better representation of the ADME processes [74].

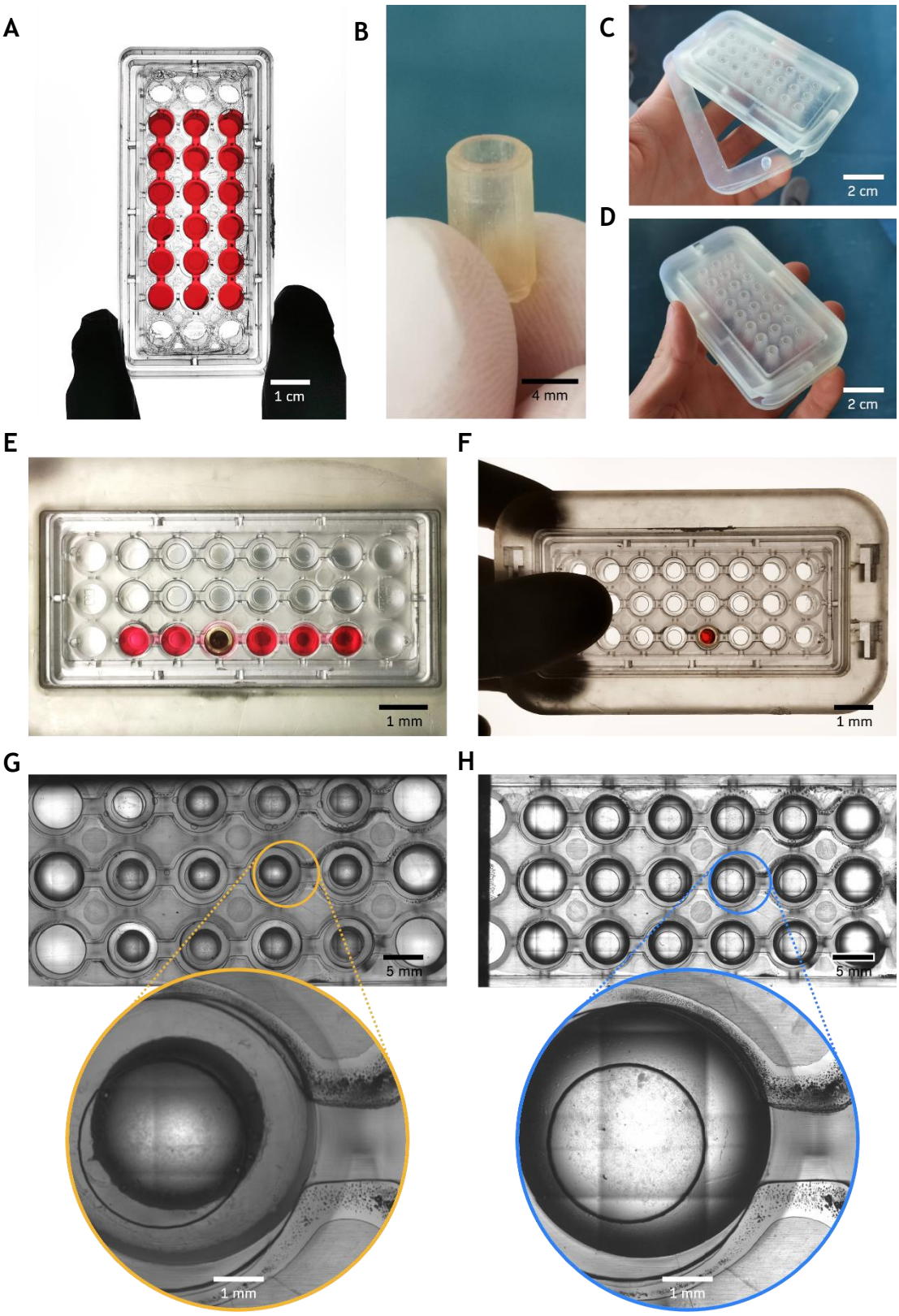

Figure 4.18: Open chamber microfluidic system and temporary sealing of individual chambers using the well plate layer and soft 3D printed plugs. A, Open chamber microfluidic system presenting three individual, linear channels. B, Soft plug printed using the FF63A resin. C and D, Rigid cover for the well plate, illustrating its rotational locking mechanism. E and D, Isolation of individual chambers due to the conformal contact created between the soft plug and the surface of the chambers, due to the pressure provided by the locked rigid cover. G, Usage of the soft plugs and rigid cover to separately culture osteoblasts in their individual chambers. H, Having removed the plugs, the osteoblast remain in culture in their respective chambers, while open flow is established across the channel, enabling the communication between the different culture sites.

4.4 Dynamic Valving Integration

The developed microfluidic platform, composed by the PS microfluidic layers and the well plate interface, presents unique characteristics. These characteristics, when complemented with 3D printed soft components, give rise to a wide range of applications and vast potential, some of which has already been explored in the previous chapter, in the development of fluidic interconnects and plugs to seal individual chambers. In this section, the work with elastomer prepolymer resins will be explored further in the development of elastic membranes for plug-and-play dynamic valving. The fabrication of the respective membranes involved exploring spin-coating and single layer masked UV exposure using the LEX resin. By further integrating the membranes into soft plugs, compatible for pneumatic delivery, an approach to plug-and-play microvalving was developed and characterized.

4.4.1 Materials and Methods

The processes for the fabrication and integration of the elastic membranes, as well as the measurement of their physical and mechanical properties, will be described in the following. This section will also characterize the electro-pneumatic system developed to pressurize and activate the elastic membranes for valving. These methods and technologies were developed by Rui Zhang, MSc Student, under my supervision. Finally, this section will also address the strategies implemented for the characterization of valving performance.

4.4.1.1 Fabrication of Elastic Membranes

The development of plug-and-play dynamic valving included the fabrication of elastic membranes. These membranes were produced using the Liqcreate Elastomer–X (Liqcreate, Netherlands) (LEX) elastomer prepolymer resin. Beyond being a very soft material, with a shore A of 43, it provides exceptional elasticity, with an elongation at break of 140 - 180%, making it particularly suitable in the fabrication of elastic components such as membranes. The fabrication of the elastic membranes entailed the development of a protocol based on spin coating and single layer masked UV exposure, to produce membranes with controllable thickness. This protocol explored two materials as the substrates for curing the

liquid resin. These were a standard microscope glass slide (Avantar, US) and an PFA film (Phrozen, Taiwan). For the glass slide, and to ensure the release of the membrane post-curing, its surface was first coated with a layer of poly(acrylic acid) (PAA) (Merck, Germany), afterwards baked at 100°C for 2 min, to this way obtain a sacrificial layer, dissolvable with water as described by Linder et al 2005 [293]. Spin coating was performed using an SPS Spin 150 (SPS, Netherlands) system, and parameters such as the spin rate, ω_{SC} [rpm] and the spin time, t_{SC} [s] were explored. In turn, single layer masked UV exposure was performed using the Elegoo Mars 4 Ultra (Elegoo, China) as the UV light source, providing a power output of 4.36 ± 0.0 mW/cm^2. UV exposure was done by performing single screen exposures, for a set period of time, t_{UV} [s].

4.4.1.2 Physical and Mechanical Properties of Elastic Membranes

Evaluating the properties of the fabricated elastic membranes involved the analysis of primarily three parameters, namely the membrane thickness, maximum deflection, and durability. Measuring membrane thickness was done using a Leica DM 750M (Leica Microsystems GmbH, Germany) optical microscope. Each membrane was marked with five different dots, as it is shown in Figure 4.19 A, using a permanent marker, and the height of each dot was measured using the focus drive unit of the microscope, with each division corresponding to 3 μm. This way, by recording the start and end position, a value for the height of a single point was obtained. By repeating the procedure for each of the five points, a rough topography of the membrane was reconstructed using MATLAB. This procedure was repeated for each of the fabricated membranes and tested conditions, obtaining a library similar to that in Figure 4.19 B. The values for the average and standard deviation associated with each condition were then retrieved.

Additionally, membrane deflection, δ_M [mm], was measured as a function of pneumatic pressure, P_{air} [mbar]. Dynamic pressure delivery was achieved using a World Precision Instruments AL-300 (World Precision Instruments, US) syringe pump. A standard 5 mL syringe (Becton, Dickinson and Company, US) was installed in the pump and connected via pneumatic tubing to the elastic membrane. This way, simple pressure loops were achieved by setting the pump to pump and withdraw according to a set volume, ultimately leading the membrane to inflate and deflate accordingly. To measure pressure as a function of the displaced

volume, and therefore time, the pneumatic system was further connected to an Adafruit MPRLS pressure sensor (Adafruit, US), calibrated to measure absolute pressure from 0 – 25 psi. The respective pressure sensor was connected to an Arduino microcontroller (Arduino, Italy), from which the pressure data was recorded with an associated time stamp. Data for P_{air} was recorded in parallel to δ_M data. The latter was obtained by recording membrane deflection as a function of the displaced volume, and time, using an Ossila Contact Angle Goniometer (Ossila Ltd, UK). For such, the Ossila Contact Angle native software was employed, enabling edge detection and the measurement of δ_M. By combining the data retrieved from the goniometer and the pressure sensor, it was possible to plot δ_M as a function of P_{air}. An illustration of the setup employed for the measurement of deflection as a function of pressure is presented in Figure 4.20, identifying each of the components described.

To measure long-term durability, only P_{air} data was retrieved. Therefore, the syringe pump was set to continuous operation, pumping and withdrawing according to a set volume, until reaching a predefined number of cycles. The volume displaced per cycle was defined according to the elastic properties of the membrane, to provide a maximum deflection, $\delta_{Mmax,}$ of 1 mm, which is sufficient to close any microfluidic channel produced with the present RT layout, as the maximum channel height is 0.8 mm.

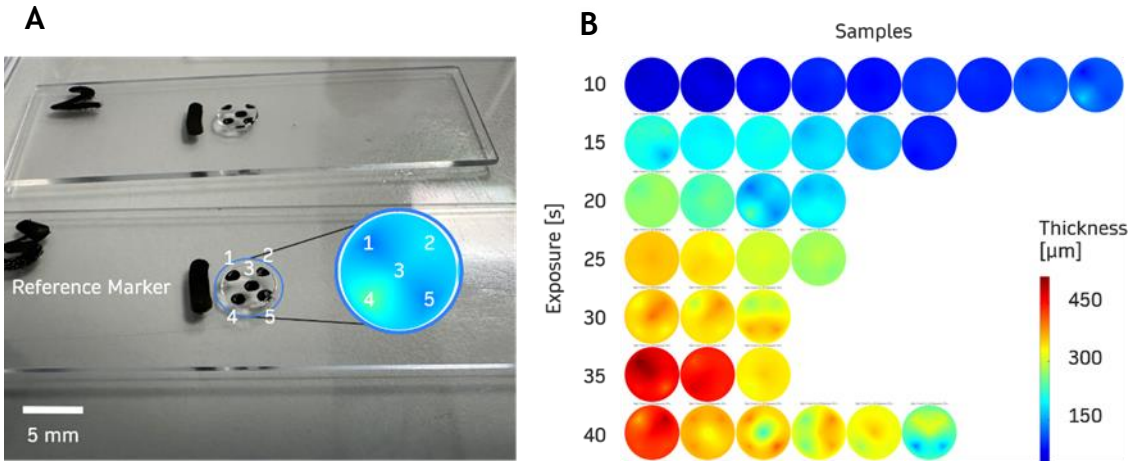

Figure 4.19: Thickness measurement of elastic membranes. A, Two glass slides, each with a cured membrane, marked with 5 dots for the measurement of height. It is further highlighted in the blue circle the corresponding reconstructed membrane topography, using MATLAB. B, Library of different samples, obtained for different exposures.

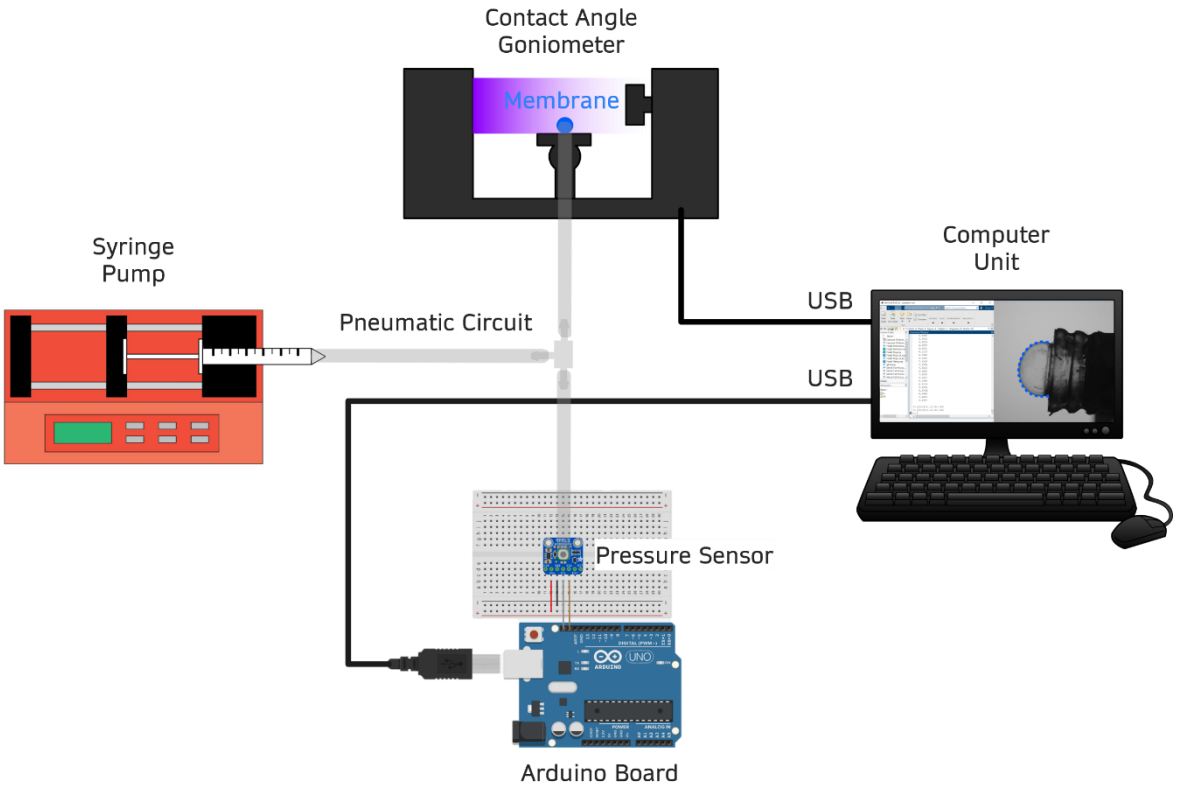

Figure 4.20: Illustration of setup employed for measurement of membrane deflection as a function of applied pneumatic pressure.

4.4.1.3 Pneumatic System for Valving

A pneumatic system was designed to test fluidic microvalving using the developed elastic membranes. The respective system is demonstrated in Figure 4.21 A, further complemented by its corresponding pneumatic circuit diagram, Figure 4.21 B, both identifying the various components involved. It integrated an air pump, P_{air}, and vacuum DC motor (Adafruit, US) (Figure 4.21, element P), set to a volume rate of 3 mL/min; an air tank, T_{air}, (Figure 4.21, element T), corresponding to a 60 mL Corning sterile container (Corning, US), to store the compressed air and reduce pressure fluctuations within the system; five three-port pneumatic valves (Adafruit, US) (Figure 4.21, elements PV0 to PV4), to direct the compressed air into the two different outlets, each meant to integrate an individual membrane valve (Figure 4.21, elements MV1 to MV2), and for general pressure release; and an MPRLS pressure sensor (Adafruit, US) (Figure 4.21, element S), to monitor and measure pressure within the respective system. It can be further observed that, while PV0, PV2 and PV3 are integrated as normally open valves, PV1 and PV4 are integrated as normally closed.

To provide automatic control over the respective pneumatic elements, an Arduino-based control system was developed, as shown in Figure 4.21 C and illustrated in Figure 4.21 D. The Arduino board was connected to the air pump, valves, and pressure sensor, S, providing individual control over each and enabling the readout of live pressure data. Additionally, the Arduino board was also connected to three LEDs, showing the status of both the pump and the individual outlet valves, and a screen, where the live pressure data was displayed. The pressure sensor and screen were connected to the Arduino board via inter-integrated circuit for serial communication. The complete electro-pneumatic system is observed in Figure 4.21 E, and its respective electric circuit diagram is displayed in Figure 4.21 F. Beyond the elements already mentioned, the respective circuit also highlights the existence of N-channel Metal-Oxide-Semiconductor Field-Effect Transistors (MOSFETS)(Figure 4.21 F, elements Q1 to Q6, highlighted in blue) and flyback diodes (Figure 4.21 F, elements FB1 to FB6, highlighted in blue), connected to both the pump and air valves, for current regulation and protection against electromagnetic fields respectively. The gate of each N-MOSFET is connected to the digital output pin on the Arduino board through current-regulating resistors (Figure 4.21 F, elements R1 to R6), and its source is connected to the ground. To automatically operate the whole system, a script was written in Python using the Arduino Integrated Development Environment (Arduino, Italy).

The respective script incorporated various functions for pressure control and dynamic valving. An overarching function consisted of providing automatic feedback pressure control, activating the pump when the pressure within the system dropped below 97% of a set value, and deactivating it for when the pressure reaches the respective set value. Regarding valving, different functions allowed switching the pneumatic connection from one outlet to the other, by individually controlling each air valve, according to a certain frequency, cycle time, and pressure.

4.4.1.4 Analyses of Valving Performance

The analysis of valving performance was achieved via microscopy. Two different coloured dyes (MOB Cosmetics, UK), blue and red, were diluted in water and pipetted into two distinct reservoirs placed at a height, *h* [mm], of 100 mm above

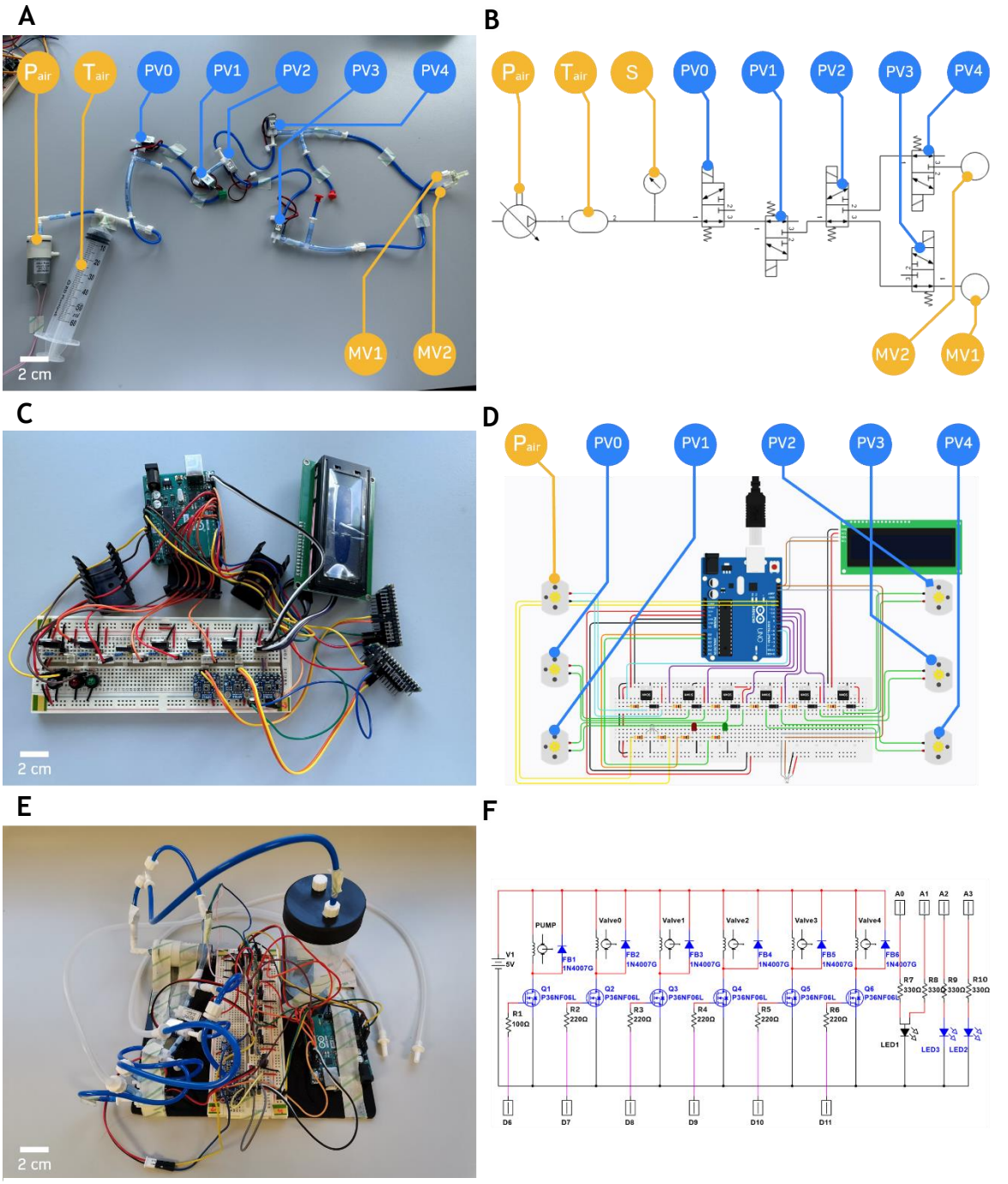

Figure 4.21: Electro-pneumatic system developed for fluidic switching. A, Pneumatic circuit and its constituting elements, namely an air pump, Pair, air tank, Tair (first integrated using a dispense syringe, but later, as shown in E, using a container), air valves, PV0 to PV4, and two outlets for valving with elastic membranes. The corresponding circuit diagram is shown in, B, further highlighting the existence of a pressure sensor, P. C, Electronic circuit, displaying the Arduino board, display screen, and the general bread board integrating the pressure sensor, N-MOSFETS, flyback diodes, resistors and LED lights. In D, an illustration of the corresponding circuit can be observed. E, Fully mounted electro-pneumatic system, and, F, its corresponding electric circuit.

the microfluidic channels. Each reservoir was then individually connected to the respective microfluidic inlet, using soft plugs for fluidic interfacing. Flow within the microfluidic channels was achieved as a product of the hydrostatic pressure resulting from the established column of water. Hydrostatic pressure, p_{HS}, is calculated by employing $p_{HS} = \rho \times g \times h + p_0$, where ρ [kg/m^3] is the fluid density,

g [m/s^2] is the gravitational acceleration, p_0 [Pa] the atmospheric pressure and h [m] the height of the column. By connecting the developed valving system to the pneumatic circuit described in Figure 4.21 A, and fitting the valve into its respective microfluidic chamber, it was possible to individually close, and open, the flow coming from either inlets. Switching performance was then evaluated by analysing the change in colour intensity between the blue- and red-coloured media. Imaging was done using the optical setup described in Section 4.3.1.3. Image analysis was performed using the Colour Deconvolution2 plugin on ImageJ. Ultimately, colour intensity was obtained as a percentual value, measured in comparison to the value provided by the inlet of each respective colour.

4.4.2 Integration and Preparation of Elastic Membranes

The concept behind the plug-and-play valve is presented in Figure 4.22. As Figure 4.22 A and B demonstrate, a soft plug was designed, similar to the one displayed in Figure 4.17, but specifically meant for the connection with pneumatic tubing. In addition to the sealing rings, the plug contains a levelling ring for systematic fitting into the well plate and a male Luer lock connector [290], to facilitate the connection with further Luer components and pneumatic tubing. The bottom surface is open and designed to integrate a thin elastic membrane (highlighted in blue) for valving, the fabrication process of which is described below. The mounted setup is illustrated in Figure 4.22 C, with the soft plug inserted into the well and connected to pneumatic tubing. In turn, the elastic membrane sits at the bottom, closing the microfluidic channel into a sealed volume, as shown in Figure 4.22 D. When pneumatic pressure is applied, the membrane expands and blocks the passage of media by sealing a fluidic inlet, as Figure 4.22 E illustrates.

The fabrication of the membrane and soft plug is carried out separately. The plug is obtained via 3D printing, using as previously described the FF82A resin. Instead, the membrane is fabricated using single layer masked UV exposure assisted with spin coating. This fabrication procedure was developed and explored towards obtaining finer membrane layers, otherwise not feasible with conventional 3D printing. The respective protocol is described, step-by-step, in Figure 4.23 A. The procedure begins by depositing a sacrificial layer, based on PAA, onto a glass substrate, and baking it for 2 min at 100°C, as described by Linder et al 2005 [293] (Figure 4.23 A, step 1). Then, a droplet of the LEX resin is placed on top of the

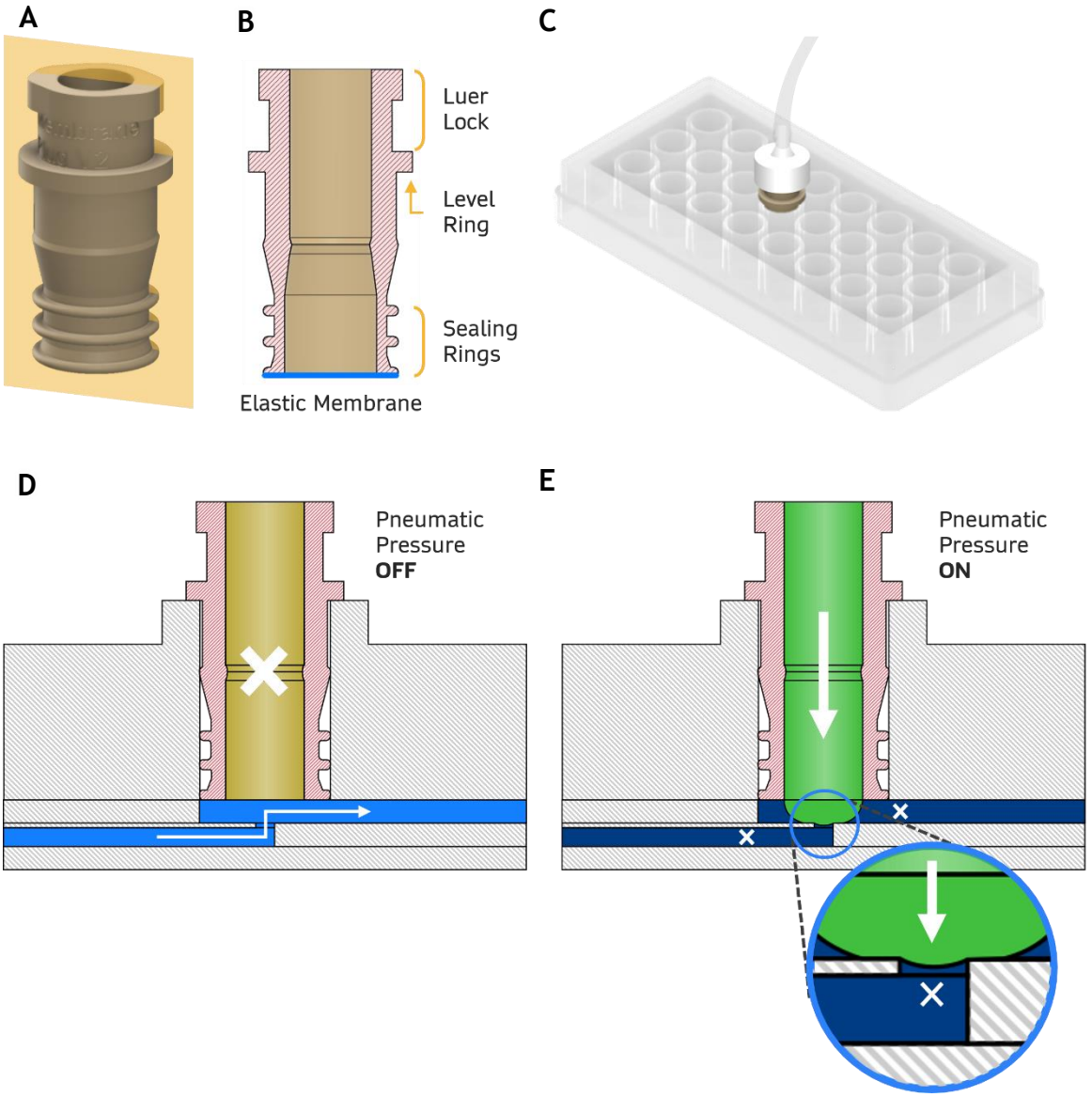

Figure 4.22: Integration and working principle of elastic membranes. A, 3D view of the pneumatic plug and, B, its respective 2D cross section, highlighting the main design elements. C, Plug and membrane inserted in the well plate layer and connected to external pneumatics. D and E, Working principle of the elastic membranes for micro valving, respectively illustrating the off and on status of the valves as a function of pneumatic pressure. Whereas the off status does not disturb flow, the on status blocks flow by pressurizing the system and expanding the elastic membrane until closing the microfluidic channel, as illustrated by the close-up image in E.

sacrificial layer and spin-coated according to the parameters ω_{SC} [rpm] and t_{SC} *[s]*, to obtain a fine membrane (Figure 4.23 A, step 2). It follows the curing of the resin, using single layer masked UV exposure, for a specific time, t_{UV} *[s]*, so that a fine membrane with the outer diameter of the plug is obtained (Figure 4.23 A, step 3). After exposure, the uncured excess of LEX resin is removed using IPA, until only a fine membrane is left on the substrate (Figure 4.23 A, step 4). The next step consists of stamping the plug with the LEX resin (Figure 4.23 A, step 5), so that the plug can then be placed on top of the membrane and sealed by performing a second and final exposure using UV light for 100 s, to ensure

appropriate bonding (Figure 4.23 A, step 6). Finally, the sacrificial layer is dissolved in water, as reported by Linder et al 2005 [293], and the soft plug is lifted off with the elastic membrane attached to its bottom surface (Figure 4.23 A, step 7). The final component is observed in greater detail in Figure 4.23 B. Alternatively, instead of glass, PFA film can be used as the substrate for the fabrication of the elastic membranes. Due to its low surface energy and resulting non-stick properties, the membrane can be easily peeled off after curing, without the need for a sacrificial layer. However, its high hydrophobicity also means that, after spin coating the resin retracts back into multiple, small droplets, distributed across the substrate, instead of forming a uniform film such as in the glass substrate. This way, when using PFA film as a substrate, step 1 and 2 do not apply.

The presented protocol and its respective control parameters were investigated as a function of the membrane thickness. The two most relevant parameters were t_{UV}, in step 3, and ω_{SC}, in step 2. Figure 4.23 C demonstrates the correlation between t_{UV} and the obtained membrane thickness, with a liner regression model highlighting that thinner membranes are generally obtained for lower exposure times. It is further possible to observe that, despite the systematic decrease, the minimum membrane thickness possible to obtain using exclusively layer exposure as the control parameter is 84.0 ± 21.2 µm, for t_{UV} = 10 s with the glass substrate, and 158.9 ± 21.6 µm, for t_{UV} = 13 s with the PFA film. Below the aforementioned exposures, it was not possible to cure the resin into a consistent film. The obtention of thinner membranes was only possible when using spin coating, which was only explored in the glass substrate, as previously explained. As Figure 4.23 D demonstrates, by increasing the spinning rate it is possible to reduce the thickness of the film according to an exponential fit. This way, while for ω_{SC} = 750 rpm and t_{SC} = 15s (highlighted in yellow) membrane thickness is equivalent to 61.2 ± 7.5 µm, for ω_{SC} = 2000 rpm and t_{SC} = 15s, membrane thickness reduces to 14.4 ± 0.6 µm. By increasing the spinning time to t_{SC} = 30s (highlighted in blue), a similar curve was obtained, however shifted to the left, meaning that, for similar spinning rates, a thinner membrane is obtained. The thinnest membranes were obtained for ω_{SC} = 1500 rpm and t_{SC} = 15 s, exhibiting a thickness of 8.6 ± 2.1 µm. These measurements were obtained post-curing, with t_{UV} = 45 s. Despite being a relatively high value, the exposure did not compromise on membrane thickness,

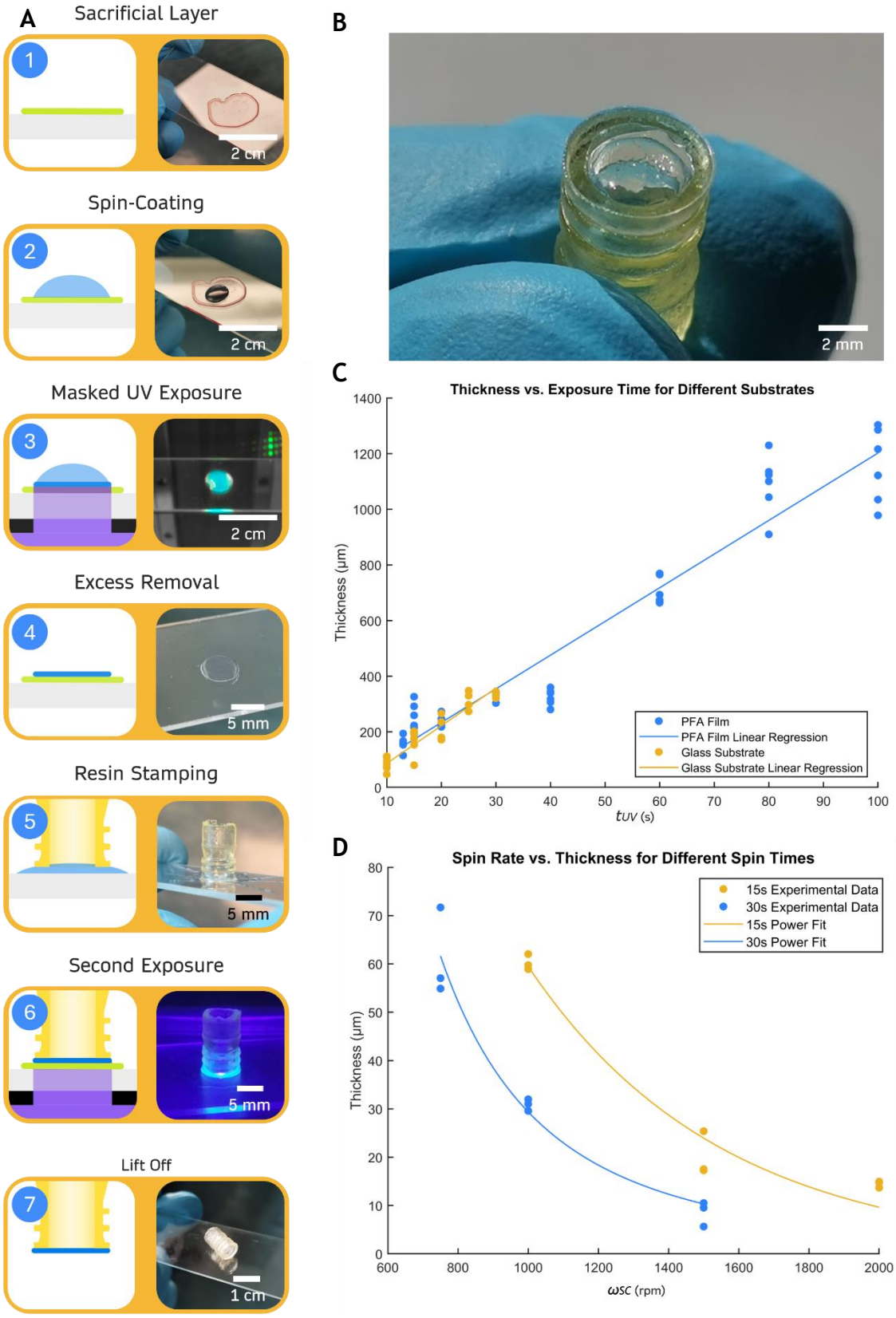

Figure 4.23: Elastic membrane fabrication and control of thickness. A, Step-by-step protocol based on spin-coating and single layer masked UV exposure for the fabrication of elastic membranes using LEX resin. B, Soft plug evidencing an elastic membrane produced according to the previously described procedure. C, Membrane thickness as a function of layer exposure and substrate material. D, Membrane thickness as a function of spin rate and spin time, for a layer exposure of 45 s. The data in C and D was collected and processed by Rui Zhang, MSc Student.

given that the thickness of the film post spinning is lower the minimal thickness obtained for the minimal exposure value.

Ultimately, it is demonstrated that by regulating ω_{SC} and t_{UV}, this protocol provides systematic control over membrane thickness, covering a wide range of values from 1156.8 ± 122.2 µm, for t_{UV} = 100 s in the PFA film substrate, to 8.6 ± 2.1 µm, in a glass substrate, for ω_{SC} = 1500 rpm, t_{SC} = 15 s, and t_{UV} = 45 s.

4.4.3 Membrane Deflection and Durability

After characterizing the fabrication procedure of the membrane and the relevant control parameters determining its thickness, the resulting elastic properties were investigated as a function of membrane size, thickness and the applied pressure. As it can be observed in Figure 4.24 A, the produced membranes present exceptional elastic properties, in this case for a membrane with a thickness of 187 µm and a diameter of 5 mm. By regulating P_{air}, δ_M is highly tuneable, from a null deflection and flat surface for P_{air} = 0 mbar, to an expanded membrane with δ_M = 3.8 mm for P_{air} = 400.0 mbar. A single inflation/deflation cycle, for a similar membrane, can be observed in the plot presented in Figure 4.24 B, superimposing the pressure loop (highlighted in yellow) and the resulting membrane deflection (highlighted in blue) as a function of the cycle time. It is observed that not only δ_M accurately follow P_{air}, but also, the membrane returns to its initial state of no deflection when the pressure returns to P_{air} = 0 mbar. This suggests that for the single cycle in analysis the membrane operated within its elastic behaviour, evidencing little to no plastic deformation despite the obtained deflection. Nevertheless, the ability of the membrane to operate within in its elastic regime for multiple cycles and longer periods of time will be briefly investigated next.

As demonstrated in Figure 4.23, the presented fabrication procedure enables systematic control over membrane thickness by regulating ω_{SC}, in step 2, and t_{UV} in step 3. Additionally, the diameter of the membrane is another parameter which is easily tuneable by changing the diameter of the area exposed to UV light during the single layer masked UV exposure step. The diameter of the membrane is, however, limited by the size of the soft plug and the diameter of the well.

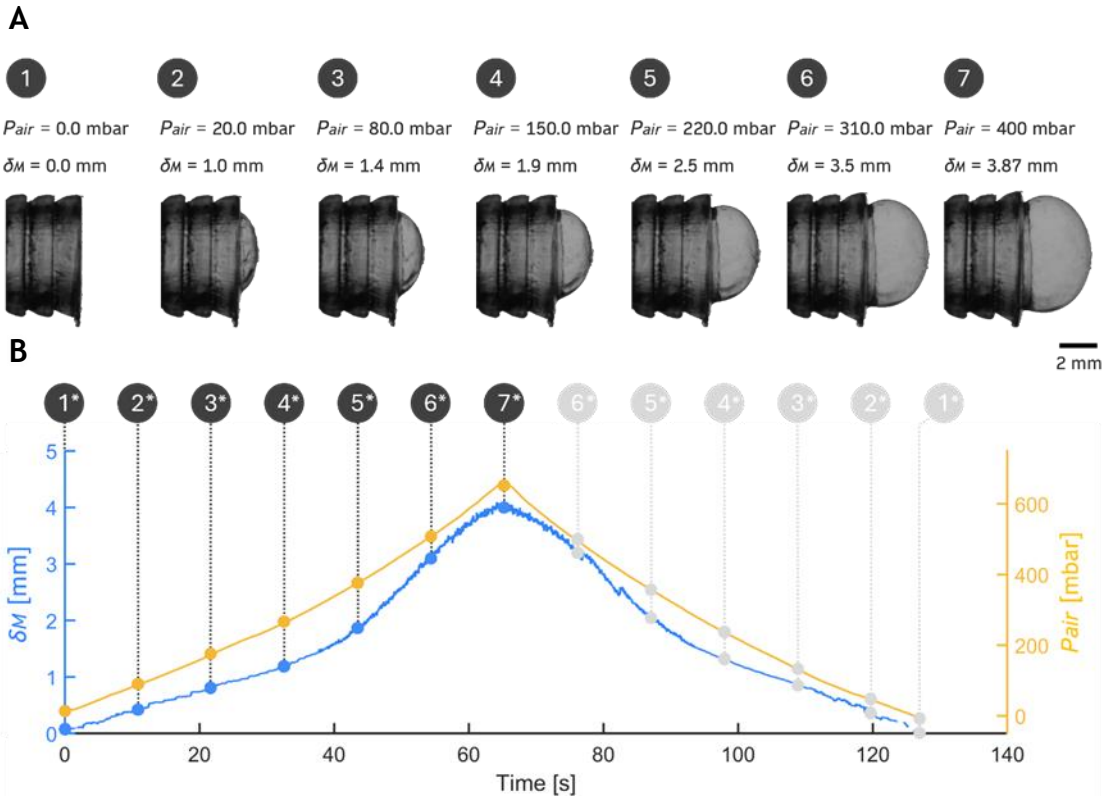

Figure 4.24: Elastic membrane deflection as a function of pneumatic pressure. A, Side view of membrane deflection as a function of pneumatic pressure, for a membrane with a thickness of 187 µm and a diameter of 5 mm. B, Plot of δ_M (in blue) overlapped by P_{air} (in yellow) both as a function of the cycle time, representing a single inflation/deflection loop, for a membrane with a thickness of 187 µm and a diameter of 5 mm. Despite having been obtained for membranes with similar properties, the images in A do not correspond to the same test as the one which originated the plot in B, reason which the numbers are marked with an "*". The data in B was collected and processed by Rui Zhang, MSc Student.

Membranes were therefore fabricated according to five different diameters, from 1 mm to 5 mm, as demonstrated in Figure 4.25 A. This way, the maximum membrane deflection, δ_{Mmax}, was investigated not only as a function of the membrane thickness but also of the membrane diameter. Prior to this analysis, preliminary testing was performed to assess the burst pressure, BP_{air} [mbar], for each of the conditions in analysis. The results are displayed in Figure 4.25 B. It can be observed that, predictably, the bursting pressure reduces with the membrane diameter and with the decrease of thickness. It should be noticed that, to avoid reaching the limit pressure of the sensor (723.7 mbar above atmospheric pressure (1013.25 mbar)) and prevent unnecessary damage, the maximum tested pressure was capped to BP_{air} = 650 mbar.

To investigate δ_{Mmax}, a pressure loop similar to the one presented in Figure 4.24 B was applied to each condition. The limit pressure, LP_{air}, applied to each condition was determined by applying a safety factor, sf, of 10 %, and therefore calculating

$LP_{air} = BP_{air}$ x (1 – sf). This way, it was possible to determine δ_{Mmax} as a function of both membrane thickness and membrane diameter, as shown in Figure 4.25 C. It is possible to observe that there is a systematic increase to δ_{Mmax} as the membrane diameter increases. An inverse relationship is observed, as expected, for the effect of membrane thickness, with deflection generally increasing as the thickness decreases. It is observed that this relationship is, however, not fully systematic, with some conditions presenting unexpected results and significant inter sample variation, therefore suggesting deeper investigation. These variations are greater for wider membranes, particularly at 5 mm of diameter (highlighted in blue). It is possible to observe that, while the maximum deflection increases predictably with the decrease of membrane thickness until the value of 187 µm, where the maximum deflection was measured as δ_{Mmax} = 3.19 ± 0.79 mm, after this value the maximum deflection presents a less predictable evolution. It is observed that, for a thickness of 71 µm, δ_{Mmax} = 1.56 ± 0.52 mm, whereas for a thickness of 49 µm, this value increases to δ_{Mmax} = 4.16 ± 0.77 mm. These results suggest that, with such wide diameters and thin films, the properties of the membrane may be less consistent across samples, this way presenting varying mechanical properties and justifying the variability of the collected data for δ_{Mmax}. More so, this hypothesis also justifies the fact that, as the membrane diameter decreases, so does the variability of the data for δ_{Mmax}. It is observed that, while for a diameter of 4 mm, there is still some significant variability, particularly for thicknesses lower than 127 µm, for diameters below 3 mm, the variation of maximum deflection as a function of thickness follows a more predictable evolution.

To analyse the elastic resilience and long-term durability of elastic membranes during on and off switching, a membrane with a 5 mm diameter and 20 µm thickness, representing the most fragile condition, was tested for a period of 15.5 h. The test was designed to cyclically displace a volume of 0.1625 mL, corresponding to δ_M = 1 mm. This value was selected because it provides sufficient deflection to close any microfluidic channels produced with the current RT procedure, as the maximum channel height is 0.8 mm. The cyclic switching of P_{air} is plotted as a function of time in Figure 4.26 for the entire 15.5 h period. An analysis of the first 10 min of testing, Figure 4.26 A, reveals a reduction in pressure amplitude from 8.8 mbar between the two initial on and off states to 4.9 mbar.

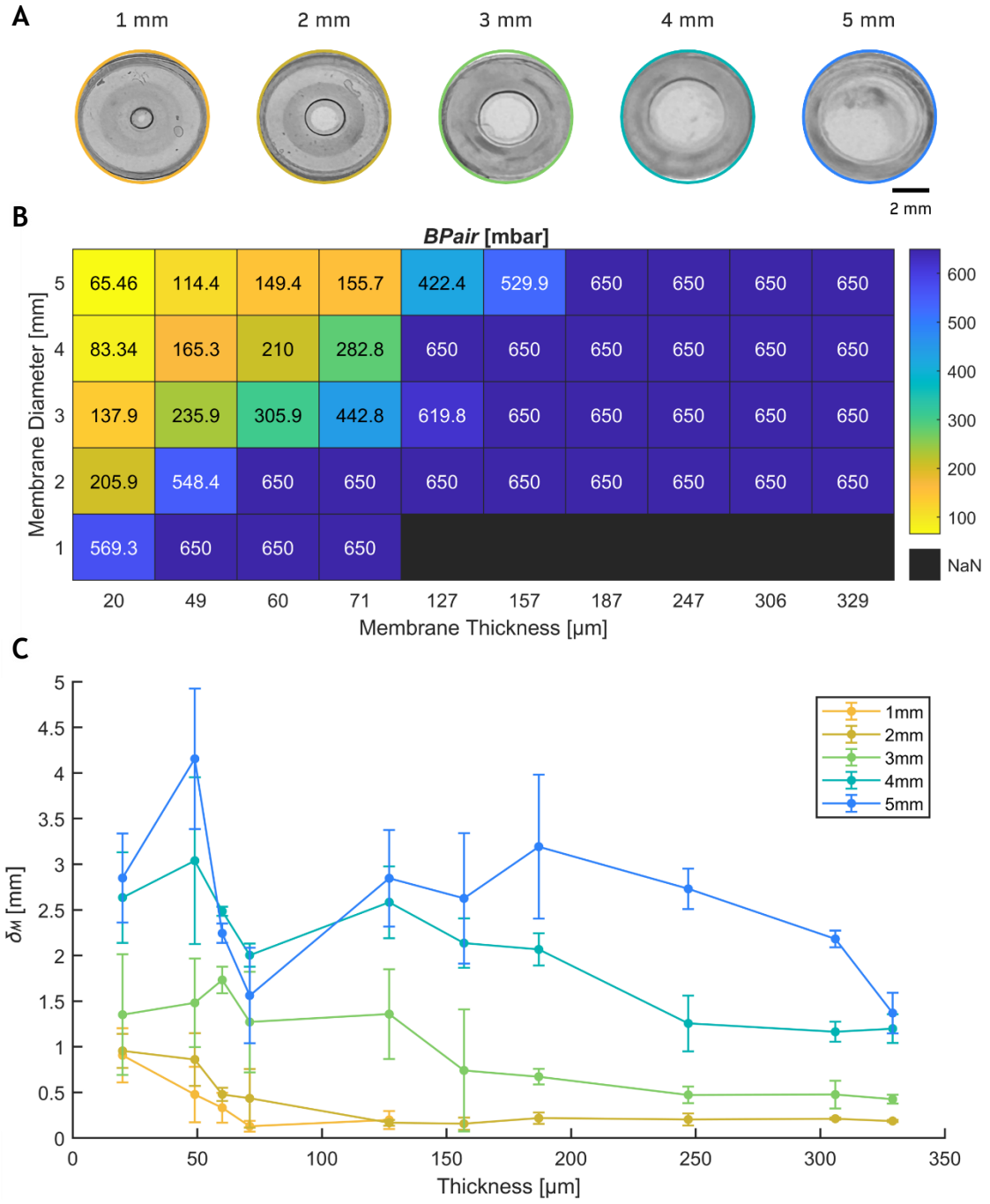

Figure 4.25: Maximum elastic membrane deflection as a function of thickness and diameter. A, Bottom surface of soft pneumatic plugs, evidencing the different diameters, from 1 mm to 5 mm, tested for the elastic membranes. B, Heatmap displaying the values for BP_{air} as measured for each condition of membrane thickness and diameter. C, Maximum membrane deflection as function of membrane thickness and diameter, by applying $LP_{air} = BP_{air}$ x (1 – *sf*). The data in this figure was collected and processed by Rui Zhang, MSc Student.

This indicates the onset of plastic deformation, which deteriorates over time, as the material fatigues due to the cyclic loading. During the first hour of testing, amplitude gradually decreases, until stabilizing at approximately 4.0 mbar, as it is observed in Figure 4.26 B between instances t = 60 min and t = 70 min. This suggests that, despite significant plastic deformation, the membrane retains its elastic properties and can operate between the on an off states. This elastic

behaviour persisted for the remaining test period, until 15.5 h as shown in Figure 4.26 C, with the pressure amplitude remaining relatively stable.

However, Figure 4.26 C also highlights a decrease in average pressure, which occurs more rapidly until t = 2 h, before stabilizing into a slow but steady pressure release. This suggests the presence of a slow air leakage within the pneumatic system.

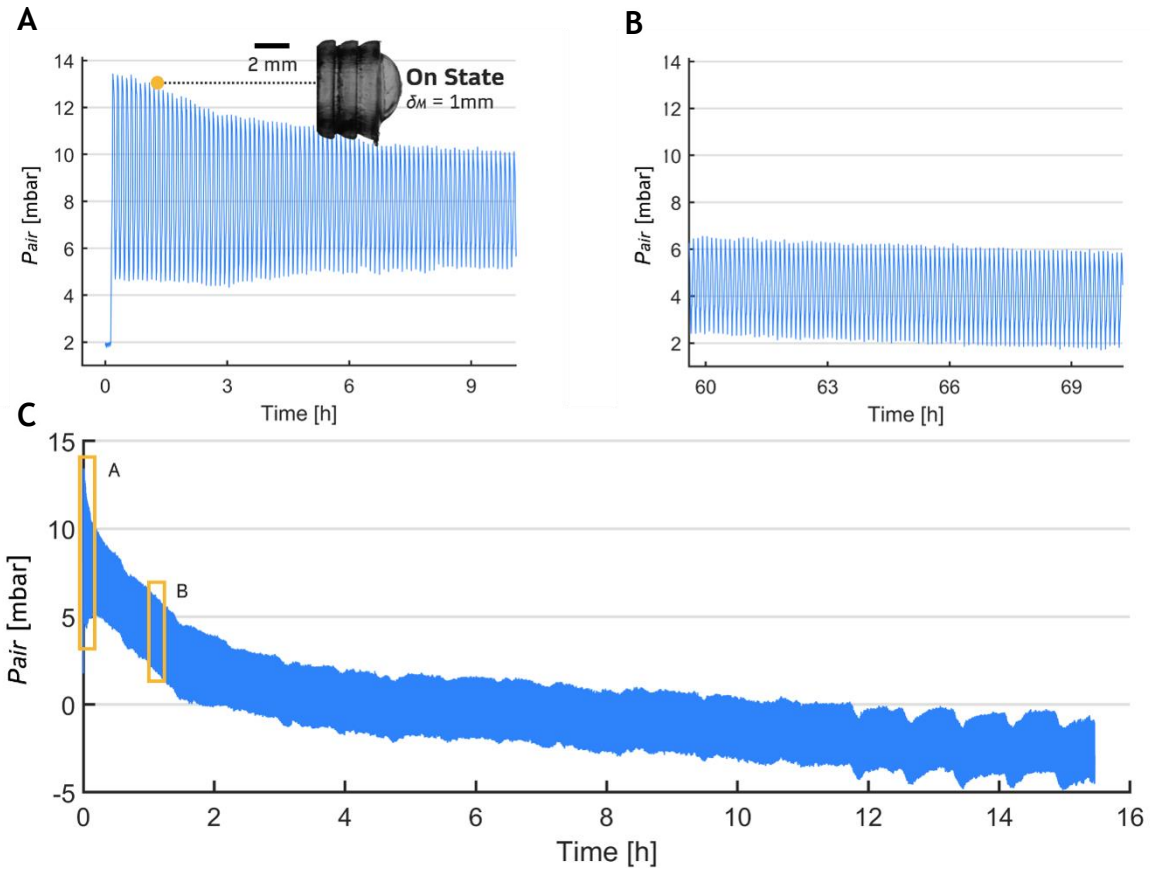

Figure 4.26: Elastic resilience and durability during long-term switching. A, Initial 10 min of the switching test, highlighting the plastic deformation undergone by the membrane as observed by the reduction in pressure amplitude. It is also denoted that the volume displaced at each cycle is corresponds to a membrane deflection of 1 mm. B, Pressure amplitude as measured further along the test, between instances t = 60 h and t = 70 h, evidencing the preservation of the elastic properties, despite the cyclic loading. C, Overview of the entire 15.5 h of testing, highlighting the long-term preservation of the membrane's elastic properties, but also evidencing the existence of a slow, steady leakage in the pneumatic system. The data in C and D was collected and processed by Rui Zhang, MSc Student.

4.4.4 Applications of Microfluidic Valving

To test the elastic membranes for microfluidic valving, a new pneumatic valve was specifically designed for fluidic switching, as shown in Figure 4.27 A. The valve features two male Luer lock connectors, connecting it to the two outlets of the pneumatic system described in Section 4.4.1.3 and shown in Figure 4.27 B. Each connector is then linked via separate pneumatic channels within the soft plug to two membrane valves, MV1 and MV2, Figure 4.27 B. The membrane-integrated plug is shown in Figure 4.27 C, while a closer look at the membrane layer demonstrates its activation via pneumatic pressure, individually controlling MV1, Figure 4.27 D, and MV2, Figure 4.27 E. To evaluate microfluidic switching, a dedicated microfluidic device was developed, shown in Figure 4.27 F. This device includes two separate fluidic ports, each connected via distinct microfluidic channels and 0.5 mm wide inlets to a common valving chamber, Figure 4.27 G, where the plug is inserted and valving takes place. The levelling ring, Figure 4.27 A, ensures a precise 300 µm gap between the membranes and the chamber's bottom surface. Valving efficiency is then assessed in the mixing channel, Figure 4.27H, where the colour of media changes as a function of valving.

As observed in Figure 4.28 A, the device was fitted with soft plugs to integrate the fluidics (top elements) and the pneumatic switch valve (bottom elements), which were connected to the pneumatic system described in Figure 4.27 B. Figure 4.28 A shows the device under fluidic perfusion, where each inlet supplies different-coloured media (colour blue from inlet 1, and red from inlet 2). This results in two separate laminar interfaces, easily identifiable in the mixing channel, as demonstrated in Figure 4.28 B, image 1. The fluidic state in the respective figure is achieved when both MV1 and MV2 are closed, keeping the inlets open and allowing blue- and red-coloured to flow in equal proportions. The plot in Figure 4.28 C shows P_{air} as measured by the sensor over time. The fluidic state in Figure 4.28 B, image 1, corresponds to instance 1 in Figure 4.28 C, where the pneumatic circuit connecting the air pump to the sensor is pressurized. However, neither membrane is pressurized, as PV1 remains off, thereby disconnecting the pneumatic loop from the pressure source. By activating PV1, MV1 will be connected to the source and quickly (in $\approx$ 0.2 s) pressurized to the set value of P_{air} = 250 mbar, Figure 4.28 C instance 2. This pressure change enables the calculation of the displaced volume for membrane activation, which is

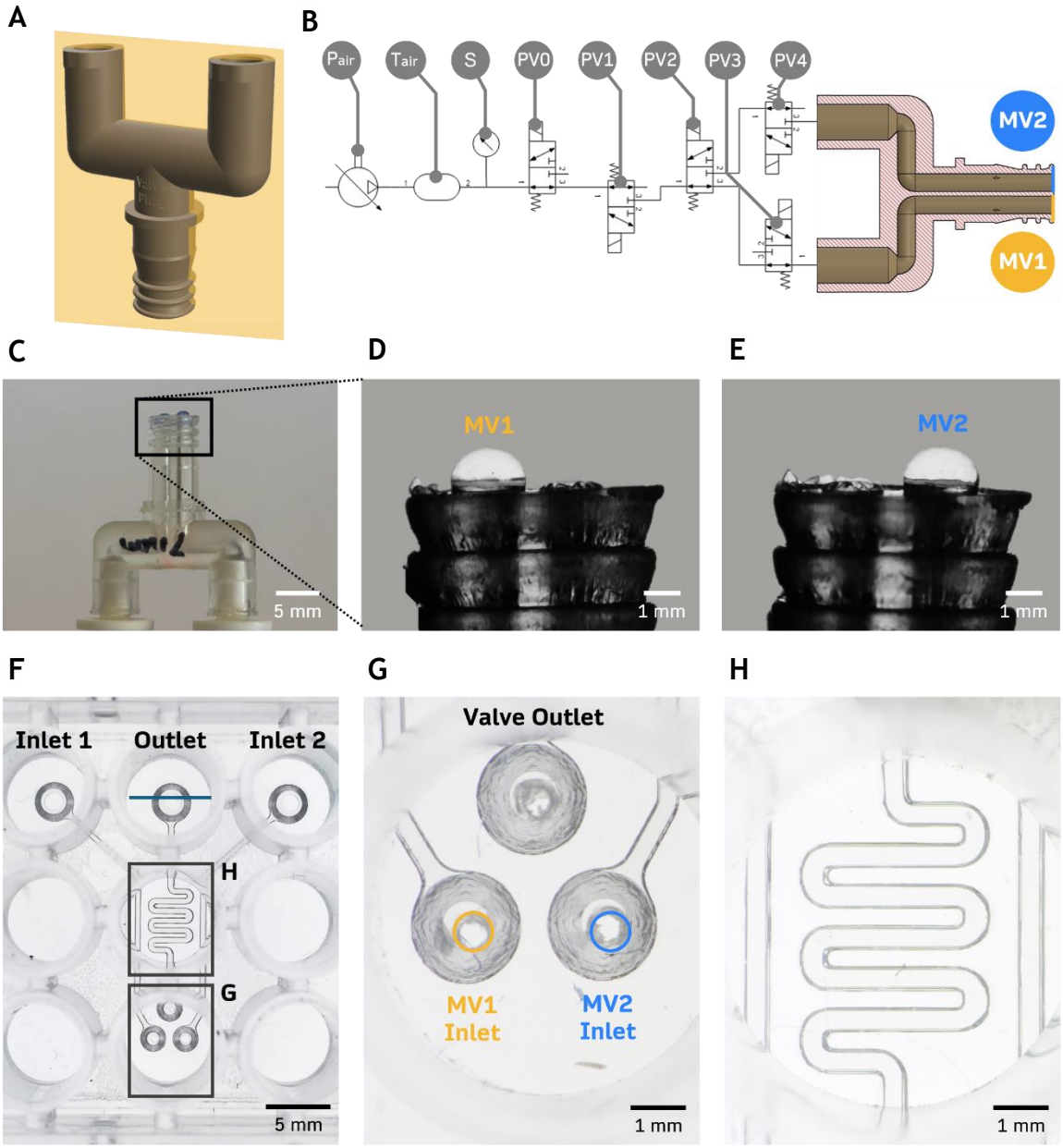

Figure 4.27: Dual-membrane pneumatic switch valve and microfluidic setup for switching analysis. A, 3D view of the pneumatic switch valve, containing two connecting ports for separate pneumatic action. B, Pneumatic circuit used for valve switching, respectively connected to the pneumatic switch valve and accessing its respective membrane valves, MV1, highlighted in yellow, and MV2, highlighted in blue. C, Printed pneumatic switch valve connected to the respective pneumatic system. D and E, Close-up of the membrane layer, respectively highlighting MV1 and MV2 open. F, Layout of new microfluidic device specifically designed to test fluidic switching. G, Valving section, highlighting the inlet for MV1, in yellow, and for MV2, in blue, as well as the valve outlet, at the top. H, Mixing channel, accessed by the valve outlet, where the analysis on the performance of fluidic switching will be done.

approximately 10 µL. As the membrane expands, it closes the respective inlet and blocks the blue-coloured medium from entering the valving chamber. Consequently, only the red-coloured medium flows into the mixing channel, as shown in Figure 4.28 B, image 2. By maintaining PV1 open while simultaneously activating PV2 and PV4 (Figure 4.28 C instance 3) the opposite occurs: MV2 activates, blocking the red-coloured medium. At the same time, PV3 is activated

to release the pressure in MV1, allowing the membrane to contract and restoring the flow of blue-coloured medium into the mixing channel (Figure 4.28 B, image 3).

The previous example provides proof-of-concept for fluidic switching, demonstrating the ability to activate and deactivate valves based on a set pressure. However, as shown in Figure 4.24, the system also enables accurate control over membrane deflection through the precise delivery of pneumatic pressure. This capability extends beyond simple binary on and off switching and opens the possibility for more advanced functions. This was demonstrated by using the current setup to achieve dynamic control over concentration gradient generation, as observed in Figure 4.28 D. In this figure it is shown that by independently pressurizing MV1 and MV2 at different levels, the relative volume of the two liquids in theμ mixing channel can be controlled, thereby changing the colour balance. The correlation between applied pressure and colour balance was quantified through colour deconvolution, which measured the relative intensity of each individual colour in the mixing channel as a function of pressure. As shown in Figure 4.28 D, when MV1 is pressurized to P_{air} = 275 mbar, the blue channel is fully closed, preventing any flow. As a result, the mixing channel is almost entirely filled with red-coloured medium, which reaches a colour intensity of 97.6%. However, when the pressure is reduced to P_{air} = 150 mbar, MV1 is relaxes slightly, allowing a small volume of blue-coloured medium to enter the mixing channel, increasing its relative intensity to 18.9%, while the red decreases to 94.5%. A further reduction of pressure results in a more pronounced change until both colours are equalized at P_{air} = 0 mbar. The opposite effect is observed when MV2 is pressurized. At P_{air} = 150 mbar, MV2 expands, restricting the red channel's flow, reducing its colour intensity to 34.9%, while the blue increases to 82.49%. Increasing the pressure in MV2 to P_{air} = 275 mbar fully closes the red channel, raising the blue intensity to 96.6%.

Ultimately, these results demonstrate that the developed valves are not only capable of performing on and off switching but also providing dynamic control over concentration gradient generation, significantly expanding their functional capabilities.

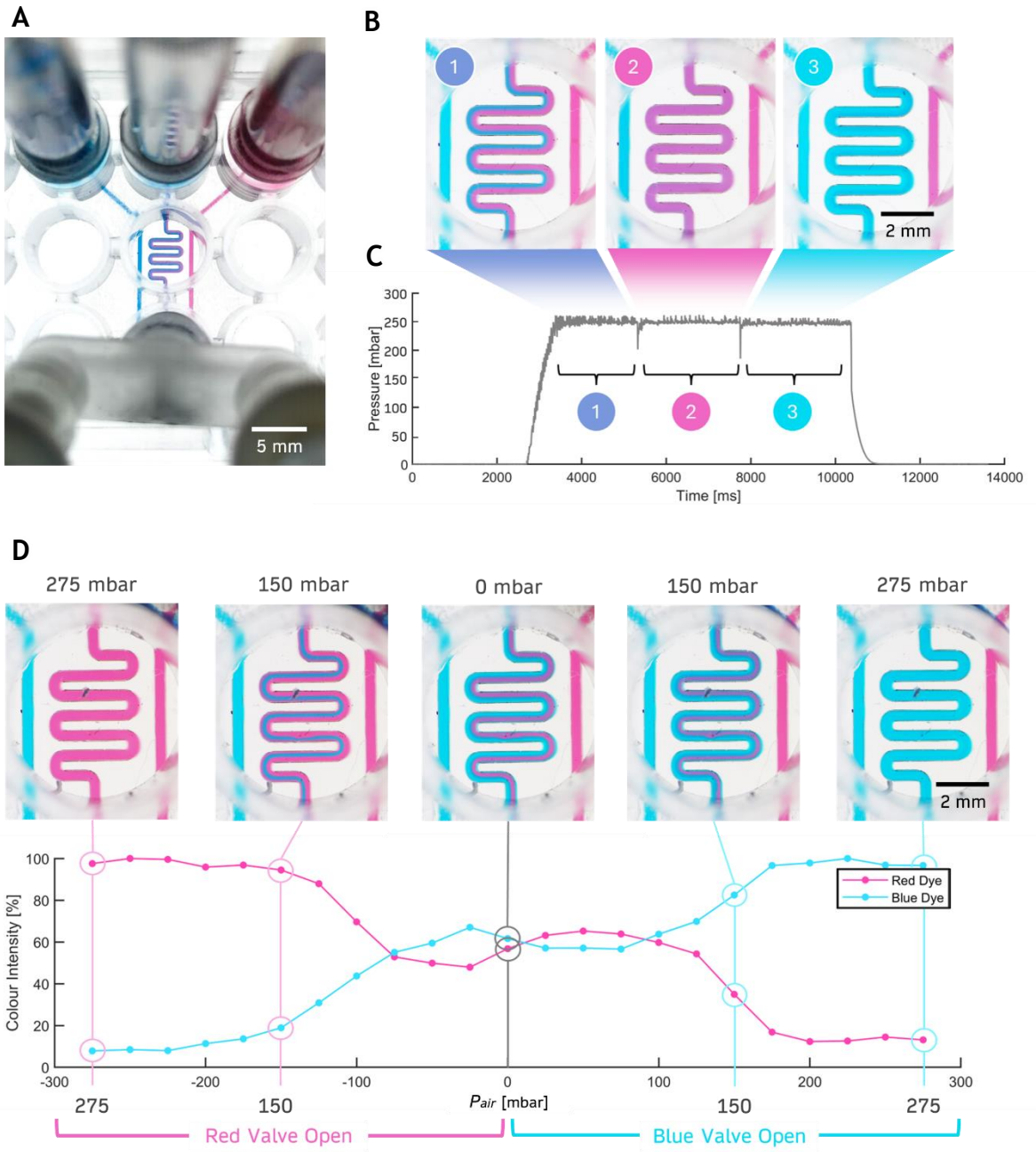

Figure 4.28: Microfluidic switching and dynamic control of gradient generation with the dual-membrane pneumatic valve. A, Microfluidic platform with integrated fluidics (elements at the top) and pneumatics (elements at the bottom), presenting evenly distributed flow of blue- and red-coloured media due to both MV1 and MV2 being closed. B, Three different fluidic states achieved with on and off switching, with figure 1 representing A, figure 2 MV1 open, and figure 3 MV2 open. C, System's pressure as a function of time, highlighting the different instances corresponding to the figures in B. D, Dynamic control over concentration gradient generation resulting from the controlled deflection of the MVs achieved as a function of precise pneumatic delivery.

4.5 Conclusions

This chapter addressed various aspects of microfluidic integration, specifically aimed at supporting the presented RT-based PS devices. The work consisted of exploring existing back-end processes, as well as developing new strategies, to

achieve and characterize channel bonding, porous membrane integration, fluidic interfacing and dynamic valving.

4.5.1 Channel Bonding Strategies - Key Findings and Suggested Future Work

The work addressing channel bonding involved exploring pressure sensitive double-sided tape, ultrasonic welding and thermal fusion, as viable technologies to seal the PS microfluidic substrates. From this work, it was determined that thermal fusion bonding provided the highest quality seal and most reproducible results, with little to no channel deformation and high scalability. By integrating carrier layers made from PC and acrylic, it was further possible to enhance the optical quality of the final bonded devices. More so, given that the procedure does not require additional features to achieve bonding, such as energy directors in ultrasonic welding, it allows sealing layers with much greater channel density and resolution. Optimal bonding parameters were defined according to T_{TF} = 78 °C, P_{TF} = 35.7 bar, and t_{TF} = 20 min. Alternatively, ultrasonic welding proved to be an extremely scalable and rapid bonding procedure, representing a highly attractive sealing strategy for microfluidics. Perhaps its greatest downside is, however, the dependency on energy directors which, not only compromise channel density and resolution, but also pose a significant challenge in the obtention of precise channel dimensions and geometry. It is important to note that some strategies, such as described by Luo et al 2010 [191], have been reported to employ solvent and thermally assisted ultrasonic welding to reduce the reliance on energy directors. However, considering the modifications they would imply to the ultrasonic welding setup, and conversely, the success thermal fusion bonding was providing in sealing channels, the present work did not explore such techniques.

4.5.2 Porous Membrane Integration - Key Findings and Suggested Future Work

Similar technologies were explored in the bonding of porous membranes, with adhesive layer bonding being investigated using liquid optical adhesives instead. Firstly, a new microfluidic layout was developed, to address some of the issues found with the typical bilayer architecture, which requires sandwiching the membrane in between the channels, compromising both the structural integrity of the membrane and the reliability of the channel seal. The new layout consisted

of integrating a chamber specifically designed to house and seal the membrane. This way, it allowed to not only seal the membrane prior to bonding the channels, enabling the direct analysis of the obtained seal, but it also did not interfere with the subsequent bonding of the channels, as the membranes was allocated to its own, individual chamber. With this layout, both ultrasonic welding and thermal fusion presented extremely effective solutions to bond porous membranes. Ultrasonic welding was observed to be particularly relevant and efficient in bonding PETE-TE membranes, evidencing the ability to mechanically stretch their surface and reduce deflection as a function of the welding energy. It also proved a reliable procedure to seal PS-ES membranes. Nevertheless, for these membranes, thermal fusion provided the highest quality bond, achieving a uniform seal with little to no substrate deformation. The procedure was, however, less efficient in bonding PETE-TE membranes, due to their opposing molecular polarity in relation to the PS layers. Oxygen plasma treatment was necessary to introduce polar functional groups and increase the adhesion between the membrane and channel substrates. Nevertheless, the bond was observed to be more fragile. Liquid adhesives presented the least promising approach. One of the issues is the manual labour involved, which comes at the expense of time and reproducibility. To this aspect, it is important to note methods allowing the automation of liquid adhesive dispensing. One such method is enabled by direct ink write (DIW) printers. These are particularly common in the integration of microelectronics, capable of automatically dispensing conductive inks, and ultimately enabling printed circuit board (PCB) design and prototyping directly on the microfluidic substrate [294]. Instead of conductive inks, the respective printers can be adapted to write with liquid adhesives instead, this way providing a pathway to the automation of liquid adhesive bonding. This work briefly addressed this concept, by using a Voltera V-One (Voltera, Canada) printer to write with the NOA 68 liquid optical adhesive and, this way, provide a new bonding strategy. However, further work is required to fully assess and explore this option. More so, beyond the manual labour involved, the challenge identified to compromise membrane integration with liquid adhesives to a greater extent, was the impregnation of the membrane surface and fibres prior to curing. With PETE-TE membranes, this resulted in the partial blocking of the pores. While with the PS-ES membranes, this compromised the permeability of the membrane almost entirely due to quick capillary action, by wetting and unifying the fibres into a single, solid surface. To

this effect, liquid adhesive dispensing with DIW printers for membrane bonding would likely present no significant improvement.

4.5.3 Pressure-Driven Fluidic Interconnects - Key Findings and Suggested Future Work

Searching to interface the developed PS microfluidic devices with various methods of fluidic perfusion, several approaches were explored in the course of this chapter. To integrate pressure-driven microfluidics and therefore connect the devices to external peripherals, such as fluidic tubing and syringe pumps, two types of fluidic interconnects were implemented. One was based on permanently fixing dispense syringe tips to the microfluidic substrates by using liquid optical adhesives. Part of the advantage of this procedure is allowing the integration of standardized components, namely the dispense tips, which ultimately allow the connection to fluidic tubing of different dimensions. However, not only does it potentially result in channel clogging and source of contamination, but also, it involves a significantly high dead volume. The integration of laser cut Luer connectors with fitted soft insert provided a more promising approach, with a standardized interface and a significant reduction of dead volume. More so, it not only allowed the connection to standardized tubing, but it also greatly facilitated reversible interfacing, by allowing the integration of tubing via simple push fit. Given the potential of this approach, and towards providing a more quantifiable analysis regarding the obtained sealing strength, it would be beneficial to characterize its maximum tolerated bursting pressure. Furthermore, its applicability would be greatly enhanced by directly integrating the Luer shaped connectors directly into the injection moulding tooling, an approach which is suggested for future work.

4.5.4 Integration of Gravity-Driven Flow - Key Findings and Suggested Future Work

Searching to integrate gravity-driven microfluidics instead, this chapter addressed the integration of a 96 well plate format adapted to fit the size of a single microfluidic chip. By using the wells as reservoirs for media and a 3D rocking machine to provide cyclic tilting, the ability of the developed microfluidic setup to carry out recirculating, bi-directional flow was demonstrated. Furthermore, the influence of media volume in defining the resulting fluidic profile in respect to

continuity and velocity magnitude was briefly shown. Beyond providing the setup to gravity-driven microfluidics, the current platform was also developed to integrate pressure-driven flow, by employing soft 3D printed plugs to connect the device to external tubing and pumps. This way, a standardized interface was defined, presenting extremely high versatility to integrate different modes of fluidic perfusion. Finally, the platform was also shown to be compatible with open chamber microfluidics, and particularly isolating specific chambers using a purposefully developed rigid cover and soft insert. Such an approach is especially interesting to culture multiple organ tissues on the same microfluidic channel, and enable the study of communication pathways and ADME processes.

However, significant issues were faced when thermally bonding the well plate to the microfluidic devices, characterized by channel deformation and a poor seal. This challenge was solved by using adhesive tape, which provided a suitable approach and a reliable seal. Nevertheless, solvent-assisted thermal bonding presents another alternative of high potential to facilitate the bonding between the well plate and the microfluidic device. By partially dissolving and softening the polymer interfaces, it increases chain mobility and enhances adhesion. This way, it allows the reduction of process temperature and pressure, while increasing the bonding strength and reducing channel deformation [295]. This approach was briefly addressed in this project to attempt bonding between the well plate and the microfluidic devices. However, further work is required, and suggested, to systematize the deposition of the solvent layer and optimize bonding without compromising on the structural integrity of the channels due to the action of the solvent.

4.5.5 Plug-and-Play Dynamic Valving Integration - Key Findings and Suggested Future Work

The work on 3D printing soft components was further extended to the development of components for dynamic valving. These defined an approach to plug-and-play integration, specifically fitting the microfluidic platform and interfacing system with the well plate format developed in this thesis. While the soft plugs were fabricated via 3D printing, using the FF82A resin, elastic membranes were manufactured based on a spin-coating assisted, single layer masked UV exposure, using the LEX resin. The respective protocol and associated

process parameters were characterized and explored towards providing systematic control over membrane thickness. Ultimately, by controlling t_{UV}, ω_{SC}, and the supporting substrate, it was possible to regulate membrane thickness from 1156.8 ± 122.2 µm, for t_{UV} = 100 s in the nFEP film substrate, to 8.6 ± 2.1 µm, in a glass substrate, for ω_{SC} = 1500 rpm, t_{SC} = 15 s, and t_{UV} = 45 s. In turn, the performance of the developed membranes was characterized based on δ_M as a function of membrane thickness and diameter. It was observed that, by precisely tuning the properties of the membrane, it was possible to obtain values for δ_{Mmax} up to 4.2 mm, for a thickness 49 µm, a diameter of 5 mm and P_{air} = 116.2 mbar. More so, a measure for long-term durability was obtained by testing a membrane with a thickness of 20 µm and a diameter of 5 mm for a period of 16 h. It was observed that, despite initial plastic deformation, the membrane maintained its elastic properties, and was capable of performing on and off switching for the entirety of the test, without bursting or presenting disabling changes in its behaviour. Ultimately, this established a well-characterized procedure, capable of fabricating elastic membranes with proven performance on fluidic switching, observed to efficiently block the passage of flow upon appropriate pneumatic pressure and resulting membrane expansion. More so, it was shown that, by precisely regulating pressure delivery, it was possible to generate dynamic control over concentration gradient generation, this way demonstrating the ability of these valves to carry functions beyond binary.

Despite the achieved body of work, further investigation is suggested. An important point is to address the variability observed in the δ_{Mmax} data, as shown in Figure 4.25 C, which requires further investigation to understand the causes and mitigate the existing variability. Also, evaluating the long-term elastic durability of membranes across a wider range of conditions would be valuable. Finally, performing continuous, rapid fluidic switching and characterizing the minimum switching time between two fluidic states would be a relevant study to benchmark the developed system against existing strategies.

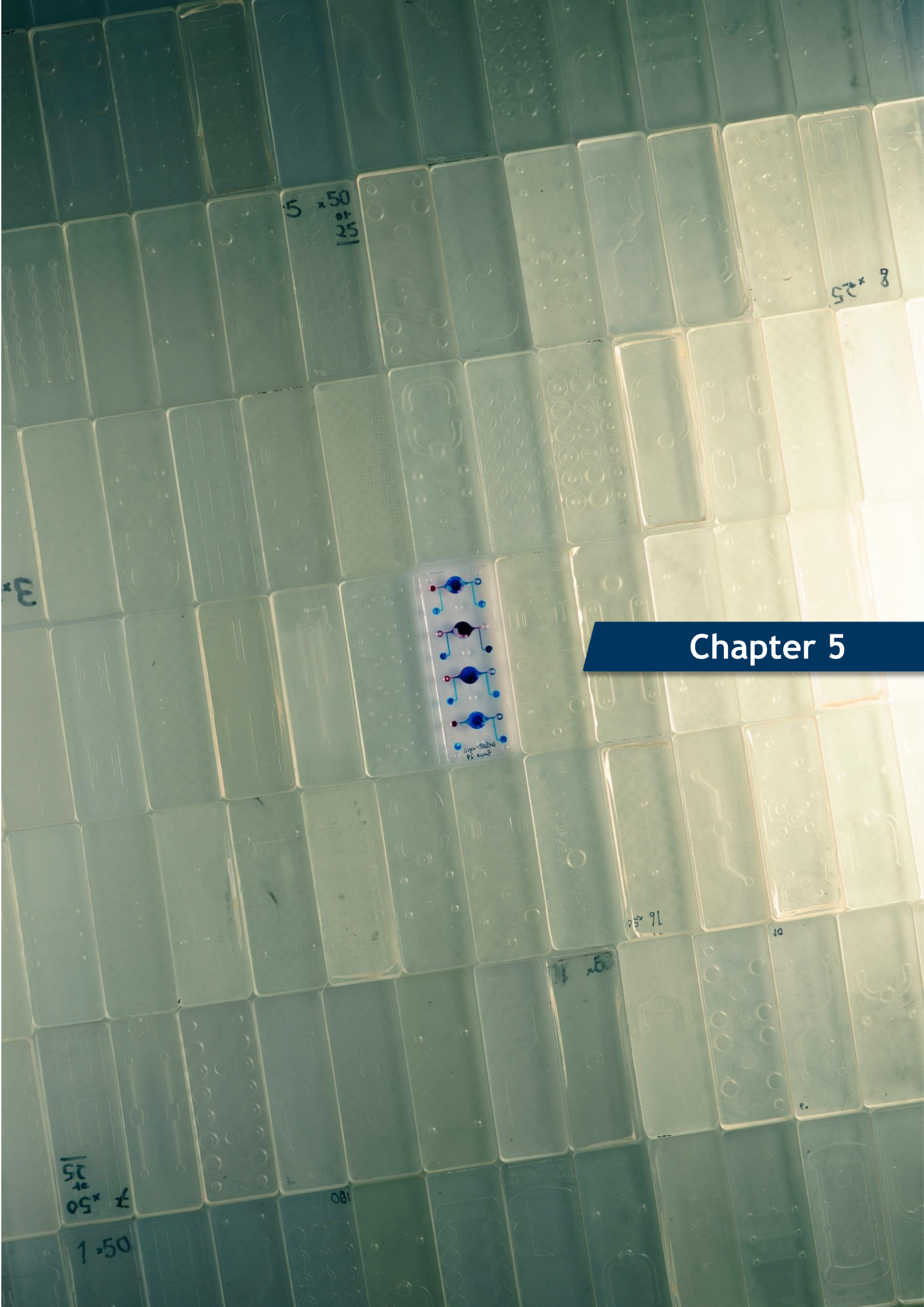

Chapter 5

5 Finite Element Simulation of Flow and Transport Kinetics in Microfluidic Systems with Integrated Porous Membranes

The following Chapter, with the exception of Section 5.7, is adapted from Menezes et al, *Chemical Engineering Journal*, **2024**, 481 [296].

Section 5.7 is adapted from Aizenshtadt et al, Advanced Healthcare Materials, **2024**, 13 [297].

5.1 Introduction

FEM is a tool of great potential and relevance within the field of microfluidics. Its value lies in the ability to investigate not only flow, but the entire multi physical nature of microfluidic devices, from mass transport to chemical reactions, thermodynamics, electromagnetics, acoustics, and solid mechanics [231]. More importantly, it does so in a cost- and time-effective manner, reducing waste, and enhancing the analysis to a level of detail impossible to achieve via experimental methods [231, 237]. For this reason, FEM is extremely relevant in the design and optimization of microfluidic devices, being capable of tailoring functionality to a much greater extent. Furthermore, the existence of a wide range of commercially available FEM software, such as COMSOL Multiphysics, specialised in the simulation of multiphysics phenomena, further contributes to the dissemination of the technology across the microfluidic field.

The kinetics of fluid flow and mass transport are well-described at the microscale, and can therefore be easily modelled using FEM. Nevertheless, and as highlighted in Section 2.3.2, there are design challenges involving flow and mass transport within microfluidic systems, to which an optimal solution is not yet obvious. FEM is therefore often employed to accelerate the investigation on challenges such as microfluidic mixing, gradient generation, shear stress delivery and droplet generation, and optimize channel design accordingly. The integration of porous membranes within microfluidic environments poses, as well, several implications to fluid flow and mass transport which have been often investigated using FEM. However, literature is clear in indicating the necessity to provide a more systematic investigation addressing the different control parameters and

respective output variables, and this way provide clearer guidelines on membrane selection and chip design [259].

5.1.1 Limitations in the characterisation of Porous Membrane Parameters

As described in Section 2.3.2.2, porous membranes have become an essential element to a wide variety of microfluidic applications, from sample filtration to gas separation, energy generation and, of more relevance to this work, OOC technology [164]. By acting as scaffolds for the culture of cells, porous membranes provide a permeable barrier capable of not only protecting cells against direct shear by regulating its effect [252], but also controlling the delivery and extraction of soluble compounds, such as nutrients, metabolites and proteins, which play a role in the long-term maintenance of cells in culture [253]. This way, it is imperative that the effect of control parameters involved in the integration of membranes in microfluidic devices is well characterized and identified. In Section 2.3.2.2, the analytical work addressing the characterization of porous membranes and their respective regulatory parameters was introduced and described. But another approach, and perhaps more comprehensive and promising, to the investigation of porous membranes is FEM.

Significant work has been done using numerical methods in the identification and characterization of parameters regulating the fluidic and mass transport kinetics of microfluidic devices with integrated porous membranes. Despite not employing FEM, but rather the finite difference method coupled with immersed boundary conditions, the work of Chen et al 2020 provides a comprehensive characterization of membrane parameters in regulating the fluid dynamics in a bilayer microfluidic device [259]. This way, the dependence of flow and shear on channel geometry, membrane permeability and fluid viscosity were systematically studied and characterized. In turn, Frost et al 2019 provides an extensive investigation using FEM on the convective-diffusive molecular transport characteristic to microfluidic bilayer devices with integrated porous membranes [263]. In this work, parameters such as flow rate, flow direction, membrane porosity, membrane pore size, channel height and molecular size were systematically studied, both *in silico*, using FEM, and experimentally, to complement and validate the numerical results. This way, a comprehensive study is provided on the effects of control parameters

in regulating transport and exchange through porous membranes. The work of Khosravikia et al 2022 reports, instead, the study of membrane porosity and thickness, together with drug concentration, applied voltage and phase pH, in determining the performance of electro membrane extraction by analysing the transfer of acidic and basic drugs [264]. More advanced membrane parameters, such as the morphology of pores, have also been analysed using FEM to quantify their effect on electroosmotic flow and transport [256, 257]. Beyond its physical properties, the permeability of porous membranes has also been quantified according to different diluted molecules. Glucose [265, 266], oxygen [267] and carbon dioxide [268] are some of the molecules whose diffusive properties have been numerically investigated according to different microfluidic applications and porous barriers. The concentration distribution of cell-secreted analytes [269] and electroactive tracers [270] was likewise studied using FEM to improve on-chip detection and the physiological relevance of microfluidic bilayer devices with *in vitro* tissue barriers.

Despite the substantial amount of published research and reviews [192, 254], literature is clear in identifying a subsisting 'lack of criteria for membrane porosity selection and channel size design' [259]. Particularly in the realm of flow and transport kinetics, there is no single study addressing both aspects simultaneously in a systematic way. Therefore, important interdependencies between control parameters, induced fluidic properties and resulting transport dynamics are this way neglected and uncharacterized. Furthermore, whereas membrane, flow, and molecular properties are regularly addressed, the influence of channel geometry and different fluidic setups is often overlooked. Therefore, a key aspect in microfluidic design, whose relevance is expressed by both the *Re* and *Pe* numbers, is neglected. This way, a broader and more systematic investigation is called for in literature [163, 254, 263], aiming at addressing these gaps and providing a more comprehensive characterization of control parameters in defining flow and transport within microfluidic bilayer devices with integrated porous membranes.

5.1.2 Aims

The aims of this chapter are the following:

- Use COMSOL Multiphysics to develop an FEM model of a microfluidic bilayer device with an integrated porous membrane, capable of systematically studying control parameters and output variables.

- Validate the model against data present in literature addressing both the dynamics of flow and mass transport.

- Use the model to develop a systematic characterization of the interdependencies existing between different fluidic setups, control parameters, involving membrane, channel, flow and diffusion properties, and output variables related to the kinetics of flow and mass transport in microfluidic bilayer devices with integrated porous membranes.

- Demonstrate the validity of the obtained numerical results in the context of microfluidic and organ-on-a-chip technology.

5.2 Methods

This chapter focuses on the development of a FEM strategy to the simulation and characterization of microfluidic bilayer devices with integrated porous membranes. COMSOL Multiphysics v6.0 was used as the FEM solver to predict both the flow and transport kinetics, as well as identifying and investigating the effect of the relevant control parameters. The implemented FEM approach is therefore described in the following. Beyond the implemented physics, the geometric model, design parameters and variables of analysis are also expressed in detail. Finally, two examples are provided validating the model's ability in predicting both flow and transport kinetics.

5.2.1 Geometric Model

This study focuses on simulating a generalized model of a microfluidic bilayer device with an integrated porous membrane, as illustrated in Figure 5.1 A. Its design contemplates the basic elements of most common OOC devices for tissue barrier simulation, hence including two adjacent channels separated by a porous membrane [65, 298-301]. At the bottom, the flow channel (*FC*) takes on the role similar to that of blood vessels, allowing for independent flow of oxygen, nutrients

and drugs. On the top, the cell channel (*CC*) provides the site for culture of cells. At the same time the porous membrane (*PM*) acts as an artificial *in vitro* endothelial barrier [302], confining convective transport to perfused channels, whilst enabling diffusive transport between compartments and providing mechanical support for cell growth.

Simulations were carried out in COMSOL Multiphysics v6.0, using a 2D FEM model, as illustrated in Figure 5.1 B, to avoid unnecessary computational expenses associated with 3D modelling. The model was parametrically defined. This way, all initial conditions and design parameters are fully adjustable, enabling their impact on fluid flow, *Q* [µL/h], and the molecular concentration, *C* [mol/m^3].

5.2.2 Numerical Model

Two fundamental modules, available in COMSOL, were implemented to solve the fluid dynamics along the channels and through the membrane, as well as the transport of diluted molecules by the effect of both advective and diffusive mechanisms. The modules are respectively designated as *Porous Media Flow* and *Transport of Diluted Species*.

The *Porous Media Flow* module solves fluid flow in both free and porous media, which in the case of the presented device, is represented by the flow along the channels and across the porous membrane respectively. First, to ensure both the conservation of momentum and mass, the Navier-Stokes and the Continuity

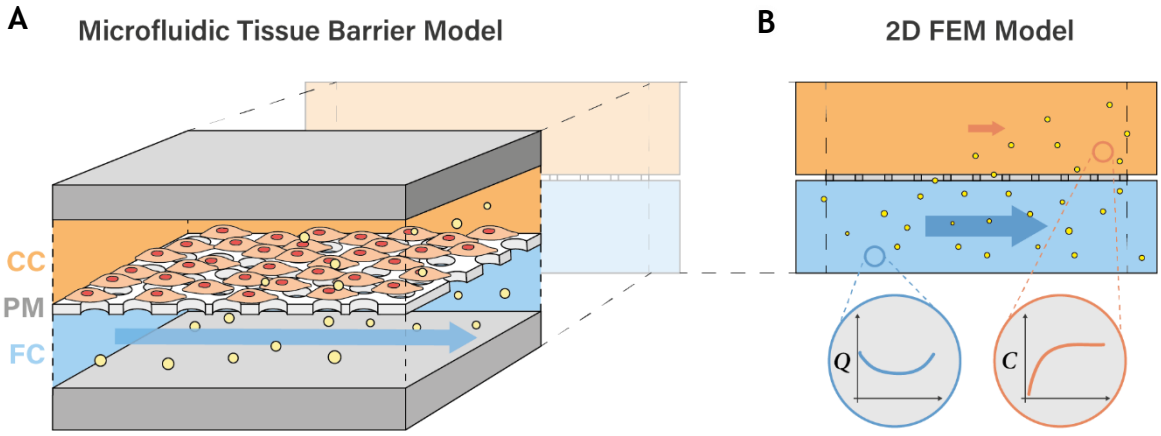

Figure 5.1: Illustration of the simulated microfluidic environment. A, 3D vie of the simulated microfluidic bilayer device with an integrated porous membrane subdividing the domain into the CC (cell channel) and FC (flow channel). B, 2D representation of the same device, illustrative of the geometry employed for FEM, from where data on *Q* (flow rate) and C (concentration) will be measured, analysed, and investigated.

equations [303] are respectively engaged. The Navier-Stokes equation is defined as follows:

$$\rho(\mathbf{u}\cdot\nabla\mathbf{u}) = -\nabla\cdot p\mathbf{I} + \nabla\cdot\left[\mu(\nabla\mathbf{u} + (\nabla\mathbf{u})^T) - \frac{2}{3}\mu(\nabla\mathbf{u})\mathbf{I}\right] + \rho\mathbf{F} \quad (5)$$

Where ρ [kg/m^3] is the fluid density, **u** [m/s] is the velocity vector, **I** is the identity matrix, and **F** [N/kg] are the volume forces per unit mass of fluid. On the other hand, the Continuity equation is defined as follows:

$$\nabla\cdot(\rho\mathbf{u}) = 0 \quad (6)$$

Both equations are coupled together to solve for the free-flowing laminar motion of media being perfused into the microchannels of the device.

To calculate the flow of media across the membrane, described as slow flow through the interstices of a fully saturated medium, Darcy's Law must be engaged, as expressed in Equation 3, Section 2.3.2.2. Similarly, permeability and pore resistance were also defined as expressed in Equations 2 and 1 respectively, Section 2.3.2.2.

The *Transport of Diluted Species* module solves the motion of diluted particles flowing within the bulk media, by activating and coupling the transport mechanisms of advection and diffusion, expressed by the Advection-Diffusion equation. This equation derives from Brownian motion and Fick's law [6], and is expressed as follows:

$$\mathbf{u}\nabla C - D\nabla C = s(x,t) \quad (7)$$

Where D [m^2/s] the diffusion coefficient and $s(x,t)$ [mol/(m^{2}s)] a source or sink of the respective diluted species for a specific x [m] position along the channel and at a certain time, t [s]. Whereas the first term of the equation, $\mathbf{u}\nabla C$, represents the advection component, the second, $D\Delta C$, represents the diffusion. However, the presence of a porous medium, such as a membrane, imposes constraints to diffusion, which must be considered. These constraints can be translated by applying the Millington and Quirk model, which correlates porosity with tortuosity, τ, the latter defined as the ratio between the effective path length of the pore

and the straight distance across the porous medium. This way, the notion of effective diffusivity, D_{eff} [m^2/s], is formulated, and can be expressed by the following expression:

$$D_{eff} = \frac{P}{\tau} D \tag{8}$$

5.2.3 Design Parameters

The focus of this study is to characterize the intricate interdependencies existing between the kinetics of flow and mass transport, and the relevant control parameters. To do so, a comprehensive list of parameters, including membrane features, channel geometry parameters, flow and diffusion properties, and different fluidic setups, will be investigated and characterized. In this subsection, each specific control parameter will be therefore identified.

5.2.3.1 Control Parameters

Eight distinct control parameters, namely porosity, P, pore radius, r [µm], membrane thickness, t_M [µm], membrane length, L_M [mm], cell channel height, H_{CC} [µm], flow channel height, H_{FC} [µm], inlet flow rate, Q_{in} [µL/h], and diffusion coefficient rate, D [m^2/s], identified in Figure 5.2, were individually studied over a defined interval of values. These intervals were defined based on literature references and commercial examples. To facilitate the analysis of results, parameters were grouped into three distinct categories, namely the membrane properties, channel geometry, and flow and diffusion parameters. Each parameter was studied across a defined range, and given an initial value (bold font), as

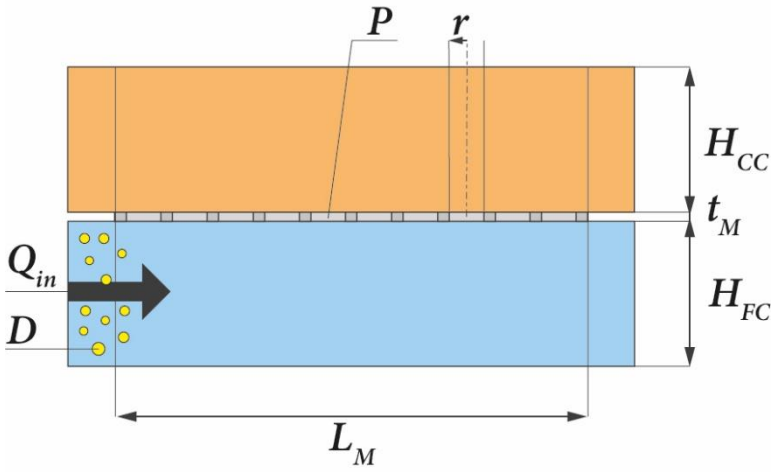

Figure 5.2: Illustration of the control parameters in analysis.

detailed in Table 5.1. When a parameter is being investigated over its respective range of values, all other parameters are fixed at their initial values.

Table 5.1: Investigated control parameters (CP), with their respective intervals of study and default values, highlighted in bold face. The values highlighted in bold with a * represent a default value which are not part of the interval of study.

CP	Designation	Interval of Study
P	Porosity	[0.001; 0.01; **0.1**; 0.2; 0.3; 0.4; 0.5; 0.6; 0.7; 0.8; 0.9]
R [µm]	Pore Radius	[0.001; 0.005; 0.01; 0.05; 0.1; 0.5; **1**; 5; 10; 50; 100]
t_M [µm]	Thickness of Membrane	[1; 5; **10**; 50; 100; 500; 1000]
L_M [mm]	Length of Membrane	[0.1; 0.25; 0.5; 0.75; 1; 2.5; **5**; 7.5; 10; 25; 50; 75; 100]
H_{CC} [µm]	Height of Cell Channel	[10; 50; 100; **300***; 500; 1000; 5000; 10000]
H_{FC} [µm]	Height of Flow Channel	[10; 50; 100; **300***; 500; 1000; 5000; 10000]
Q_{in} [µL/h]	Inlet Flow Rate	[0.1 0.5 1 5 10 **50** 100 500 1000]
D [m^2/s]	Diffusion Coefficient Rate	[1×10^{-13}; 1×10^{-12}; 1×10^{-11}; 1×10^{-10}; 1×10^{-9}; **3.39×10^{-9}***;1×10^{-8}; 1×10^{-7}]

5.2.3.2 Fluidic Setup

To contemplate the multitude of fluidic architectures common to OOC technology, four distinct fluidic conditions were analysed, as demonstrated in Figure 5.3. These can be divided first into single channel perfusion, *SCP* (Figure 5.3 A and B), and parallel perfusion, *PP* (Figure 5.3 C and D). Within *SCP*, the cell channel was either treated as a reservoir, SCP_R (Figure 5.3 A), for media flow and molecule transport, or as an outlet, SCP_O (Figure 5.3 B). It means that, for both conditions, flow in the *CC* is always a function of both K_M and volumetric flow in the flow channel, Q_{FC}. On the other hand, in *PP*, both the *CC* and the *FC* have independent media perfusion. Two conditions were similarly modelled within *PP*, which can be differentiated by the direction in which media perfusion is done. Either in the same direction, for PP_{SD} (Figure 5.3 C), or in the opposite direction, for PP_{OD} (Figure 5.3 D).

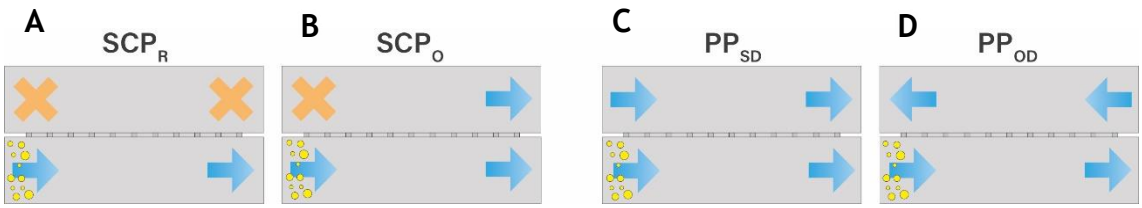

Figure 5.3: Schematic representation of the fluidic conditions tested, illustrating the boundary conditions for fluid flow and molecular transport, where A, represents *SCP$_R$*, B, *SC$_{PO}$*, C, *PP$_{SD}$*, and D, *PP$_{OD}$*.

5.2.4 Variables of Analysis

Aiming to provide a comprehensive characterization regarding the kinetics of flow and transport, as a function of the above-mentioned control parameters, various aspects are relevant to address. These include an analysis of the flow rate, shear stress, concentration distribution and the settling time. Each of these variables will be in the following appropriately described.

5.2.4.1 Flow Field

Q is a crucial factor in many biological processes, such as accelerating phenotypic change of cells [304] or altering gene expression and biosynthesis of endothelial cells [305]. It is calculated as follows:

$$Q = v(H \cdot W) \tag{9}$$

Where *H* and *W* are respectively the height and width of the channel with media flow. *Q* is further normalised in relation to the inlet flow rate, $Q_n = Q/Q_{in}$, and analysed along the channels parallel to the direction of perfusion, in both the *CC* and the *FF*, respectively Q_{nCC} and Q_{nFC}, as illustrated in Figure 5.4 A. Representing, perhaps, one of the most critical manifestations of fluid flow in biological applications [306], responsible for promoting vasculature growth in embryonic cardiovascular development [307], changing hepatocyte morphology and function [308, 309] and even resulting in the direct destruction of cells [310], wall shear stress, *WSS* [Pa], was also analysed. By considering the media as being a Newtonian fluid, *WSS* was calculated as follows:

$$WSS = \gamma\mu \tag{10}$$

Where γ represents the shear rate [s^{-1}]. *WSS* was analysed in data sets placed at cell height, defined as 10 µm [311], in the membrane surface of both the *FC* and *CC*, and in the upper surface of the *CC*, as illustrated in Figure 5.4 B and respectively identified as WSS_{MFC}, WSS_{MCC} and WSS_{UCC}.

Finally, as introduced in Section 1.1.2, *Re* is an important dimensionless number for fluidic analysis. It is defined by the ratio between inertial and viscous forces, and it is commonly employed to determine the fluidic regime of a certain environment. It is expressed as follows:

$$Re = \frac{\rho v D h}{\mu} \tag{11}$$

Where D_h represents the hydraulic diameter. Given the nature of microfluidics, *Re* is usually of very low magnitude, characterizing highly laminar systems [3, 14]. For this reason, both *Q* and *WSS* were analysed for their steady response alone.

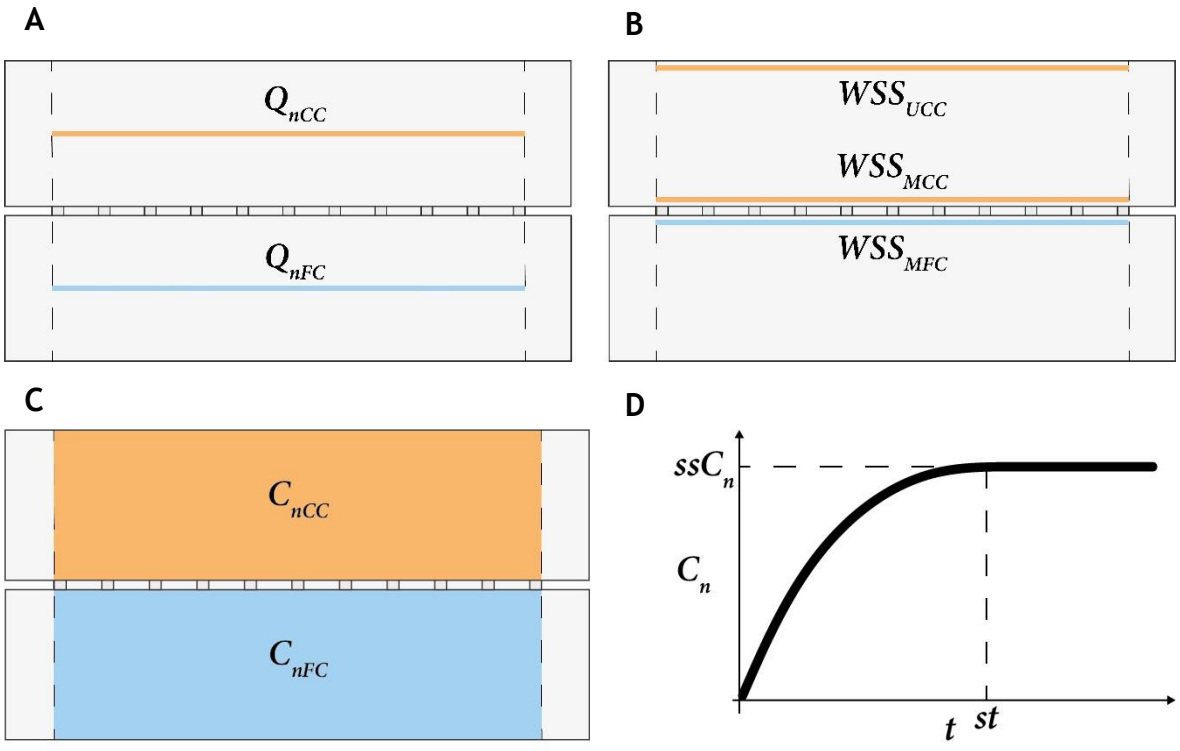

Figure 5.4: Location and geometry of data sets, employed to measure, A, the normalized flow in both channels, respectively *QnCC* and *QnFC*, B, the shear in both the membrane surface of the *FC*, WSS_{MFC}, and the *CC*, WSS_{MCC}, and in the upper surface of the *CC*, WSS_{UCC}, and C, the transient and steady state molecular concentration distribution in the *CC*, C_nCC, and the *FC*, C_nFC. D, Illustration of a time-dependant concentration measurement, from which it is calculated both the steady state normalized concentration, ssC_n, and the settling time, st.

5.2.4.2 Mass Transport

High resolution control over the delivery of soluble factors is a key advantage of OOC technology [312]. Providing accurate biochemical cues, such as concentration gradients [313], continuous nutrient exchange, waste removal and hormonal flux [314], and delivery of soluble factors, such as growth factors and peptides [315], is critical for the establishment of relevant physiological environments. Therefore, data on molecular concentration, C, was normalized, C_n ($=C/C_{in}$), in relation to the inlet concentration, C_{in}, and measured as an average for both the *CC* and *FC*, identified respectively by C_{nCC} and C_{nFC}, as shown in Figure 5.4 C.

Considering the time-dependency of molecular transport, highlighted by Equation 7, C_n was studied for both its transient and steady state behaviours. For the transient response, the time it takes for molecular transport to occur before stabilizing into a steady state, known as settling time, *st* [s], was analysed, as illustrated in Figure 5.4 D, for both the *CC* and the *FC*, represented by st_{CC} and st_{FC} respectively. For the steady state, the normalized concentration at which molecular transport stabilizes, ssC_n, was also measured, as illustrated in Figure 5.4 D. Measurements were done for both the *CC*, ssC_{nCC}, and the *FC*, ssC_{nFC}.

Finally, as introduced in Section 1.1.2, *Pe* is a dimensionless number of great interest in the analysis of transport phenomena. It is defined by the ratio between advective and diffusive rates of transport, and can be expressed as follows:

$$Pe = \frac{vDh}{D} \tag{12}$$

A system displaying $Pe > 1$, is characterized by the dominant influence of advection, as the main mode of transport. In turn, $Pe < 1$ characterizes diffusion as being the predominant transport phenomena.

5.2.5 Model Validation

To verify the predicative capabilities of the developed model, two distinct literature experiments were replicated, each aiming to address a different component of simulation. Therefore, the works of Chen et al 2020 [259] and Frost et al 2019 [263] were simulated to validate the model's capability on predicting both the fluid field and molecular transport respectively.

Chen et al 2020 [259] performed Immersed Boundary Methods (IBM) simulations towards characterizing the relationship between flow features and the design properties of a microfluidic bilayer device with an integrated membrane. Beyond many other experiments, the relationship of L_m with both Q_{jn}, fluid velocity, V and WSS_n were studied and plotted. The geometric structure and fluidic conditions of the respective experiment were simulated by this model, and the obtained results can be observed in continuous line in Figure 5.5 A, for Q_{jn}, the normalized fluid velocity, V_n, and WSS_n, superimposed over the original data, identified with markers. It can be analysed that there is a very clear affinity between the data provided by this model and that reported by Chen et al, where the relationship between L_m and the various response variables match accurately. More so, Figure 5.5 B demonstrates that the flow velocity profile, V_x, measured vertically along the channels for different values of L_m, is also well matched between the present model, in continuous line, and the data provided by Chen et al, in dashed lines.

Frost et al 2019 [263] researches the transient response of the molecular concentration distribution of a microfluidic bilayer device with an integrated membrane. The experimental data characterizing the relationship between Q_{jn} and C_{nCC} is shown in Figure 5.5 C in point markers (triangles, squares and circles), fitted with an exponential regression model in dashed lines. This data is based on the transport of fluorescein, D = 5.4x10^{-10} m^2/s through a membrane with P = 0.1. The continuous lines represent instead the numerical data provided by the present

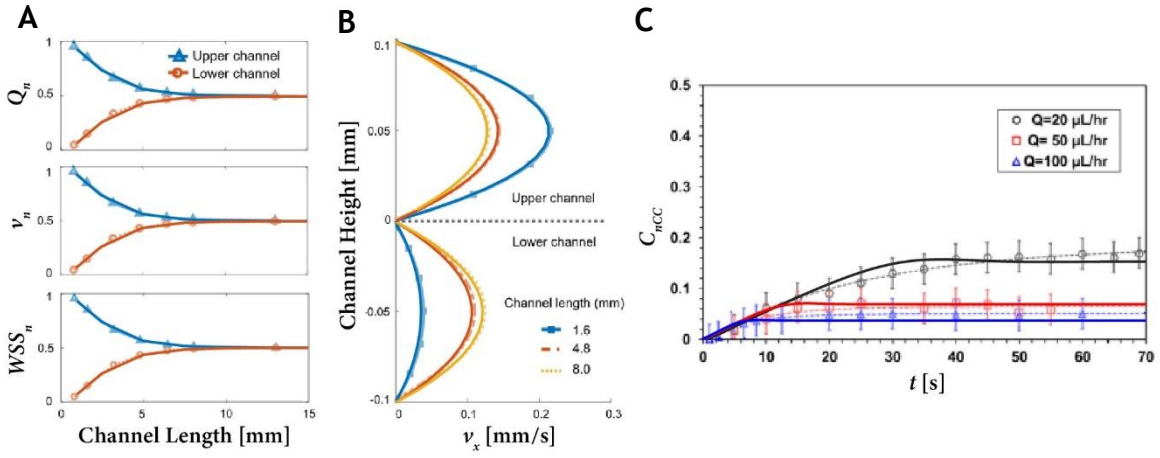

Figure 5.5: Model validation for fluid flow and molecular transport. A, Q_n, V_n and WSS_n, as calculated by the present model, in continuous line, and as provided by Chen et al, in markers. B, V_x calculated by the present model, in continuous line, and as provided by Chen et al, in dashed line. C, Experimental data provided by Frost et al 2019, identified by coloured markers, characterizing the transient concentration of fluorescein for a membrane with P = 0.1 and different Q, and in dashed lines, the respective exponential fit. Overlapping the respective results is presented the data simulated by the present model, identified in continuous lines.

model. It is possible to observe that for all three tested Q_{in}, C_n follows a similar trend, characterized by a steeper initial increase, settling afterwards into a fixed, steady state value. Despite some differences between the shape of the exponential fit, as described by Frost et al, and the numerical data, provided by this model, the latter presents, nonetheless, a great affinity with the experimental results, always remaining within the standard deviation intervals provided. Furthermore, it is possible to see that the steady state values for all three functions present a good match between experimental, exponential and numerical fit. The highest deviation was found for the condition of Q = 100 µl/h (Figure 5.5 E, black line) and equivalent to a difference of C_{nCC} = 0.02.

5.3 Fluidic Field

Control parameters will be first investigated on their effect on fluid dynamics. Initially, the analysis will focus on the fluidic implications characteristic to each setup, highlighting the fluidic distribution as a function of the boundary conditions and the permeability of the membrane. It follows an analysis addressing each of the control parameters individually and their respective effect in defining Q and WSS. The analysis will be further subdivided into membrane parameters, channel geometry, and flow and diffusion properties.

5.3.1 Single Channel versus Parallel Perfusion

The boundary conditions defining *SCP* imply that flow in the *CC* is always a function of both the properties of the membrane and Q_{FC}. Figure 5.6 demonstrates that, if for SCP_R (Figure 5.6 A), the *CC* experiences a pressure similar to the outlet, in this case 0 Pa, for SCP_O (Figure 5.6 B), the pressure will be equivalent to the average value of the gradient established in the *FC*. It results that the *CC* experiences peak volumetric flow halfway along the length of the membrane for SCP_R, as demonstrated in Figure 5.6 C, and a continuously growing flow for SCP_O, as shown in Figure 5.6 D. More importantly, Figure 5.6 C and D demonstrate the important role played by passive parameters, such as P, in controlling flow in the *CC* for SCP_R and SCP_O, respectively.

On the other hand, the boundary conditions characterizing *PP* imply that both channels are perfused with independent perfusion of media. For PP_{SD}, a null

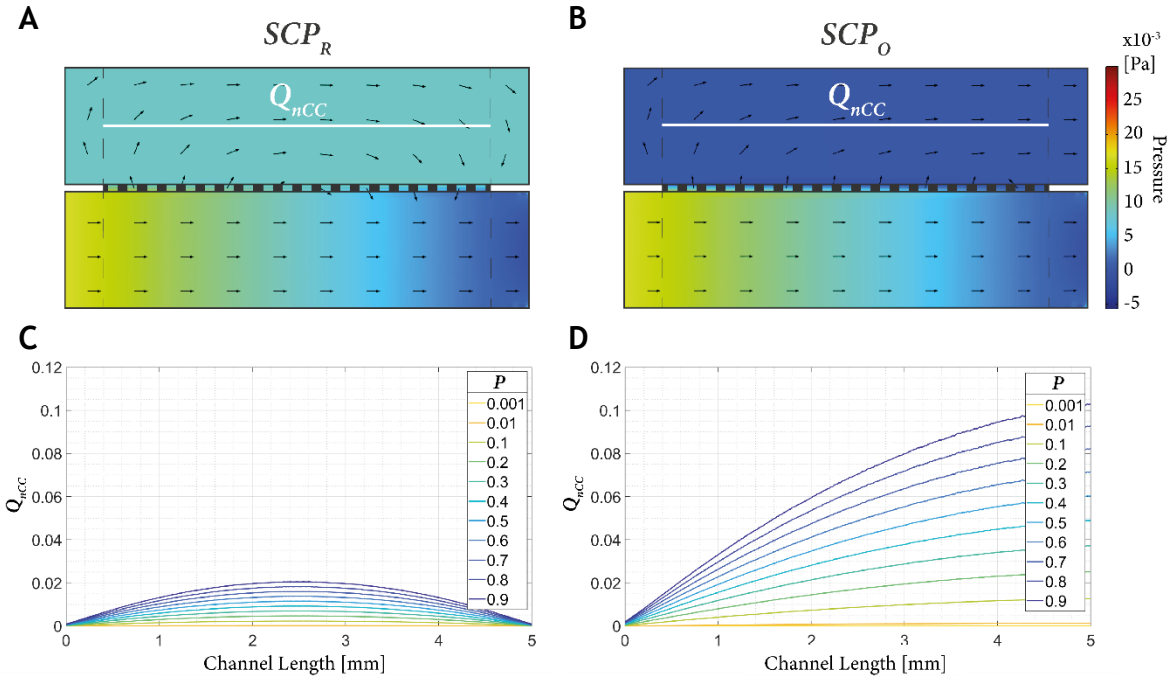

Figure 5.6: Pressure distribution and fluidic profile for *SCP*. A and B, Pressure distribution and fluidic field, in black arrows, for SCP_R and SCP_O respectively. C and D, Fluidic profile in the *CC*, for SCP_R and SCP_O respectively, measured for different values of *P*.

pressure gradient is defined between the *CC* and *FC* due to their equal pressure profiles, as shown in Figure 5.7 A. In the absence of a driving pressure potential, media is hindered from crossing the membrane, resulting in a constant fluidic profile along the channels. This balance is strongly imposed by the perfused media, meaning that changes to passive parameters, such as *P*, will often result in negligible effects to the microfluidic environment, as Figure 5.7 C demonstrates. However, the symmetry between the pressure gradients of both the *CC* and *FC* for PP_{OD} promotes a small exchange of media across the membrane, as demonstrated in Figure 5.7 B. Ultimately, it results in a faint curvature of the fluidic profile. This exchange means the fluidic profile in both channels is significantly more dependent on the membrane properties, as demonstrated in Figure 5.7 D for the case of *P*.

Here forth, Q_n and *WSS* will be studied as a direct function of control parameters, by analysing their average value, Q^A_n and WSS^A, along the respective data sets. The analysis will primarily focus on SCP_R, where results were found to be more meaningful. Otherwise, the reader is referred to Figure 5.19, Figure 5.20 and Appendix A, where the results and discussion for all conditions are present. Finally, an analysis to *Re* is included in Appendix A. It is possible to, first, verify

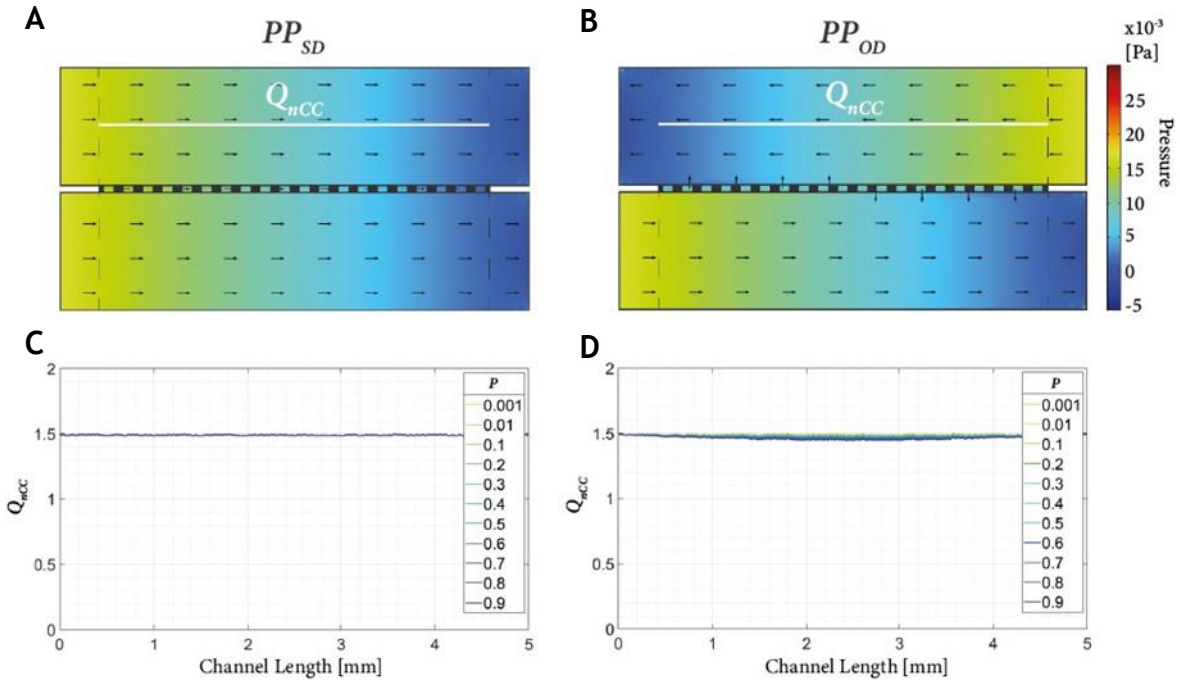

Figure 5.7: Pressure distribution and fluidic profile for *PP*. A and B, Pressure distribution and fluidic field, in black arrows, for PP_{SD} and PP_{OD} respectively. C and D, Fluidic profile in the *CC*, for PP_{SD} and PP_{OD} respectively, measured for different values of *P*.

the highly laminar nature of flow, generally with $Re<<1$, and second, the differences between *SCP* and *PP*, where *Re* in the *CC* is significantly larger for the latter due to the independent perfusion.

Box 1

Design guidelines for modelling fluid dynamics with different fluidic setups.

- **Single Channel Perfusion, *SCP*:** Extremely relevant for modelling flow in the *CC* with passive parameters. A change from SCP_R to SCP_O increases fluidic exchange and flow in the *CC*.

- **Parallel Perfusion, *PP*:** Firmly governed by the imposed Qin and generally unaffected by changes in passive parameters. The symmetric pressure gradients in *PP* provide a slight increase to fluidic exchange.

5.3.2 Membrane Parameters

The effects of P on the Q^A_n and WSS^A are displayed in Figure 5.8 A and D, respectively. It is observed in the yellow-dotted line that for P < 0.2, Q^A_{nCC} experiences an exponential decrease, reaching a value on the order of -5 for P = 0.01 (Q^A_{nCC} (P=0.01) = 1.55x10^{-5}, Appendix A), which corresponds to a 2.5-fold reduction. On the other hand, for P > 0.2, it is observed that the function gradually levels out, with Q^A_{nCC} only increasing 0.5-fold until P = 0.9. The correlations are similar for WSS, as shown in Figure 5.8 D. It is analysed that higher control over WSS^A_{CC} is obtained for P < 0.2, where an exponential decrease leads to a value on the order of -7 dyn/cm^2 for a P = 0.01 (WSS^A_{CC} (P=0.01) = 2.10x10^{-7} dyn/cm^2, Appendix A). Given the nature of SCP_R, the changes of WSS^A_{FC} in relation to P are negligible, regarding both Q^A_n and WSS^A.

Changing r results in a response of greater magnitude and a more linear behaviour within the CC, as seen in yellow in Figure 5.8 B and E for Q^A_{nCC} and WSS^A_{CC}, respectively. It is seen that, if for nanopores, with r = 0.001 µm, Q^A_{nCC} has an order of magnitude of -9 (Q^A_{nCC} (r=0.001) = 1.73x10^{-9}, Appendix A), this value increases to an order of magnitude of 0 for an r = 100 µm (Q^A_{nCC} (r=100) = 0.42, Appendix A), almost reaching a balance with the Q^A_{nFC}. A similar relationship is observed for WSS^A, where the usage of nanopores results in a virtually shear-free environment, with WSS^A on the order of -10 dyn/cm^2 (WSS^A_{CC} (r=0.001) = 1.06x10^{-10}dyn/cm^2, Appendix A). Conversely, the flow dynamics in the FC are virtually unaffected by parametric changes, with the exception of values for r above 10 µm, which show a gentle decrease for both Q^A_n and WSS^A.

An increase of t_M will enhance pore resistance and hinder porous flow, which justifies the inversely proportional relationship with Q^A_{nCC} and WSS^A_{CC}, shown in Figure 5.8 C and F in yellow-dotted lines. It is observed that for t_M = 1 µm, Q^A_{nCC} is on the order of -2 and WSS^A_{CC} of -4 dyn/cm^2 (Q^A_{nCC} (t_M =1) = 7.80 x10^{-3} and WSS^A_{CC} (t_M =1) = 1.06x10^{-4} dyn/cm^2, Table A.1). On the other hand, increasing t_M to 1000 µm will result on a decrease of Q^A_{nCC} and WSS^A_{CC} by approximately 3-fold (Q^A_{nCC} (t_M =1000) = 1.45x10^{-5} and WSS^A_{CC} (t_M =1000) = 1.48x10^{-7} dyn/cm^2, Table A.1). Finally, the blue lines in Figure 5.8 C and F demonstrate that Q^A_{nFC} and WSS^A_{FC} experience virtually no change with t_M.

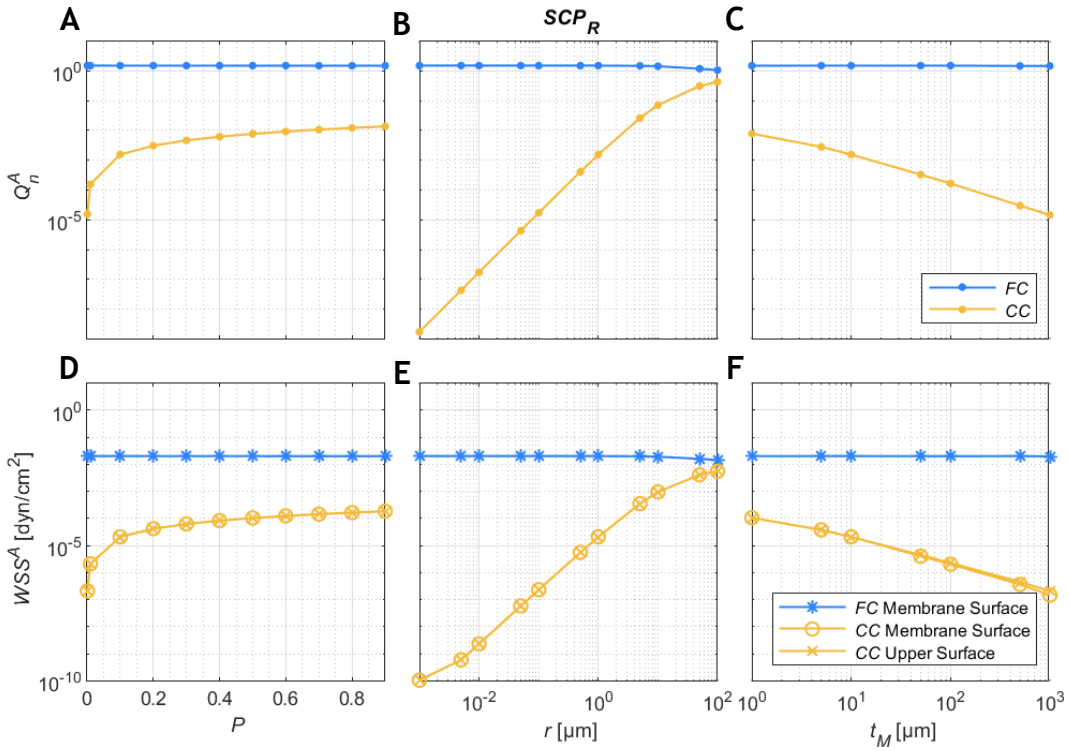

Figure 5.8: Membrane properties and their effect on Q^A_n and WSS^A for SCP_R.

Box 2

Design guidelines for modelling fluid dynamics in *SCP* using membrane parameters.

- **Porosity, *P*:** Especially influential for values below 0.2, where both Q^A_{nCC} and WSS^A_{CC} present an exponential decrease.

- **Pore Radius, *r*:** Extremely relevant in controlling both Q^A_{nCC} and WSS^A_{CC}, being able to define virtually shear-free microenvironments for nanopores.

- **Membrane Thickness, t_M:** Provides a moderate, linear, inversely proportional relationship with both Q^A_{nCC} and WSS^A_{CC}.

5.3.3 Channel Geometry

L_M directly regulates the surface area available for fluidic exchange. Figure 5.9 A demonstrates that a change to L_M corresponds to a linear variation of Q^A_{nCC}. For the interval tested, delimited by L_M = 0.1 mm and L_M = 100 mm, Q^A_{nCC} increased from a magnitude of -6.3 to -0.5, nearly reaching a balance with Q^A_{nFC}. A similar profile characterizes WSS^A_{CC}, as shown in Figure 5.9 C. At L_M = 100 mm, the maximum WSS^A_{CC} was recorded with a value on the order of -2.3 dyn/cm^2 (WSS^A_{CC} (L_M =100) = 4.23x10^{-3} dyn/cm^2, Appendix A). For smaller membranes, Figure 5.9 C highlights a critical length, equivalent to L_M = 1 mm, where the shear in the *CC* is experienced differently, depending on the surface of analysis. This feature can amount to a difference of 1.7 dyn/cm^2 orders of magnitude, for L_M = 0.1 mm, where $WSS_{MCC} > WSS_{UCC}$.

H_{CC} is directly responsible for controlling the cross-sectional area of the *CC*, and hence influences Q_{CC} as well. The displayed relationship proves nevertheless complex, as shown in Figure 5.9 B. For H_{CC} = 10 µm, Q^A_{nCC} is at its lowest, with a value on the order of -4.3 (Q^A_{nCC} (H_{CC} =10) = 4.24x10^{-5}, Appendix A). An initial increase to H_{CC} also increases Q^A_{nCC}, until this value stabilizes in the order of -2.8. However, for H_{CC} > 5000 µm it is observed that Q^A_{nCC} drops again, suggesting that the increase in chamber volume is no longer followed by a proportional increase of fluidic exchange, ultimately decreasing Q^A_{nCC}. In turn, Figure 5.9 E demonstrates that an increase of H_{CC} corresponds to a continuous decrease of WSS^A_{CC}. And similar to L_M, it is observed that for H_{CC} > 1000 µm, shear is experienced differently in the *CC* depending on the surface of analysis. The difference between WSS_{MCC} and WSS_{UCC} was measured to amount to 3.2 dyn/cm^2 orders of magnitude, for H_{CC} = 10000 µm.

Figure 5.9 C demonstrates the relationship between H_{FC} and *Q*. It is observed that for shallower channels, with H_{FC} = 10 µm, high pressure enhances fluidic exchange across the membrane, and determines $Q^A_{nCC} > Q^A_{nFC}$. By increasing H_{FC}, Q^A_{nFC} increases as well, and stabilises above the inlet rate (Q^A_{nFC} (H_{FC}=100) = 1.43, Appendix A). Conversely, Q^A_{nCC} decreases continuously, getting as low as -7.26 orders of magnitude for H_{FC} = 10000 µm (Q^A_{nFC} (H_{FC}=10000) = 5.53x10^{-8}, Appendix A). This reduction is equally felt on WSS^A_{CC}, as observed in Figure 5.9 D, where the latter variable drops from a magnitude of -1.8 dyn/cm^2, for H_{FC} = 10

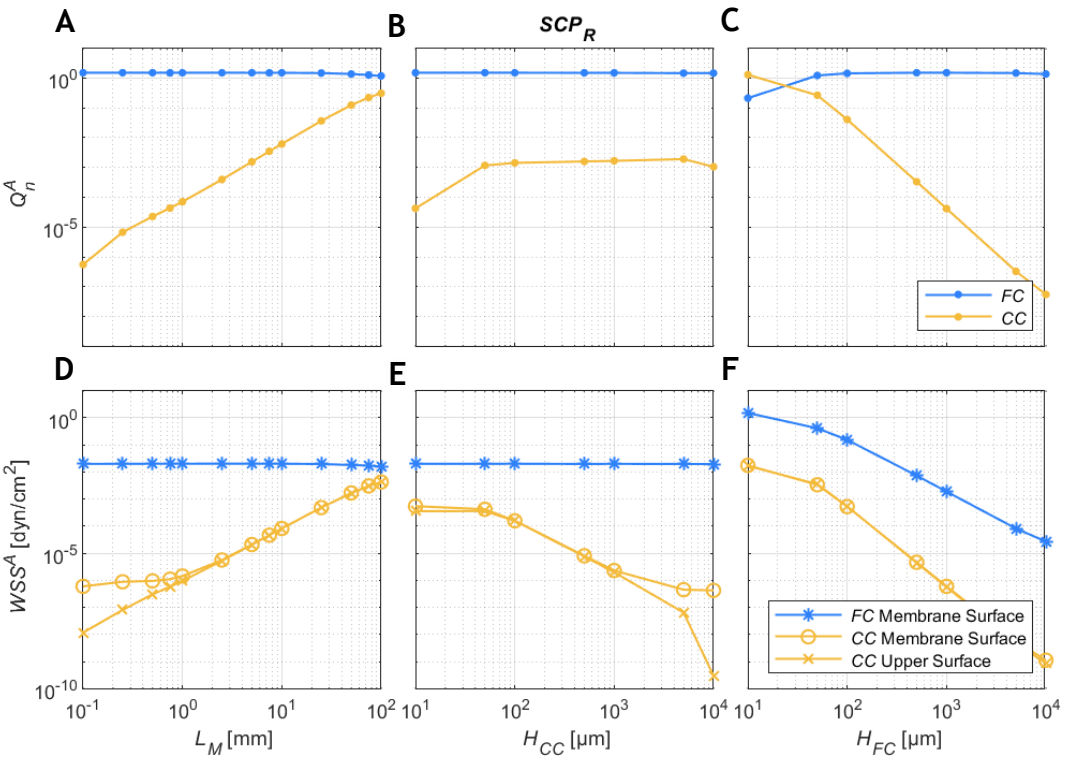

Figure 5.9: Channel geometry and their effect on Q^A_n and WSS^A for SCP_R.

µm, to -9.0, for H_{FC} = 10000 µm. Additionally, this decrease is also accompanied by a decrease in WSS^A_{FC}, from the order of 0.17 dyn/cm^2, for H_{FC} = 10 µm, to -4.7, for H_{FC} = 10000 µm.

Box 3

Design guidelines for modelling fluid dynamics in *SCP* using channel geometry.

- **Length of Membrane, L_M:** Linearly controls Q^A_{nCC} and WSS^A_{CC} and enables the differentiation of WSS^A_{MCC} and WSS^A_{UCC} for L_M < 1 mm.

- **Height of Cell Channel, H_{CC}:** Differentiates the magnitude of WSS^A_{MCC} and WSS^A_{UCC} for H_{CC} > 1000 µm.

- **Height of Flow Channel, H_{FC}:** Provides control over both WSS^A_{CC} and WSS^A_{FC} and uniquely enables $Q^A_{nCC} > Q^A_{nFC}$ for $H_{FC} \leq 10$ µm.

5.3.4 Flow and Diffusion Properties

The analysis of Q^A was done in relation to its normalized values, Q^A_n, which explains the horizontal functions seen in Figure 5.10 A. However, it is worth noting that the ratio between Q^A_{nCC} and Q^A_{nFC} is unaffected by Q_{in}, given that both variables are kept at the same fixed values (Q^A_{nCC} = 1.55x10^{-3} and Q^A_{nFC} = 1.49, Appendix A). When it comes to WSS^A, Figure 5.10 C shows how increasing Q_{in} results in a likewise linear and proportionate increase of WSS^A in both channels. If in the *FC*, WSS^A ranges from a magnitude of -4.39 to -0.39 dyn/cm^2, for the studied interval of Q_{in}, in the *CC*, it ranges between -8.37 and -4.37 dyn/cm^2.

On the other hand, it comes naturally that the effects of D on the established fluidic field are null, as the respective feature concerns the properties of diluted molecules alone. This way, the functions obtained describing Q^A_n and WSS^A are steady and horizontal, as seen in Figure 5.10 B and D respectively.

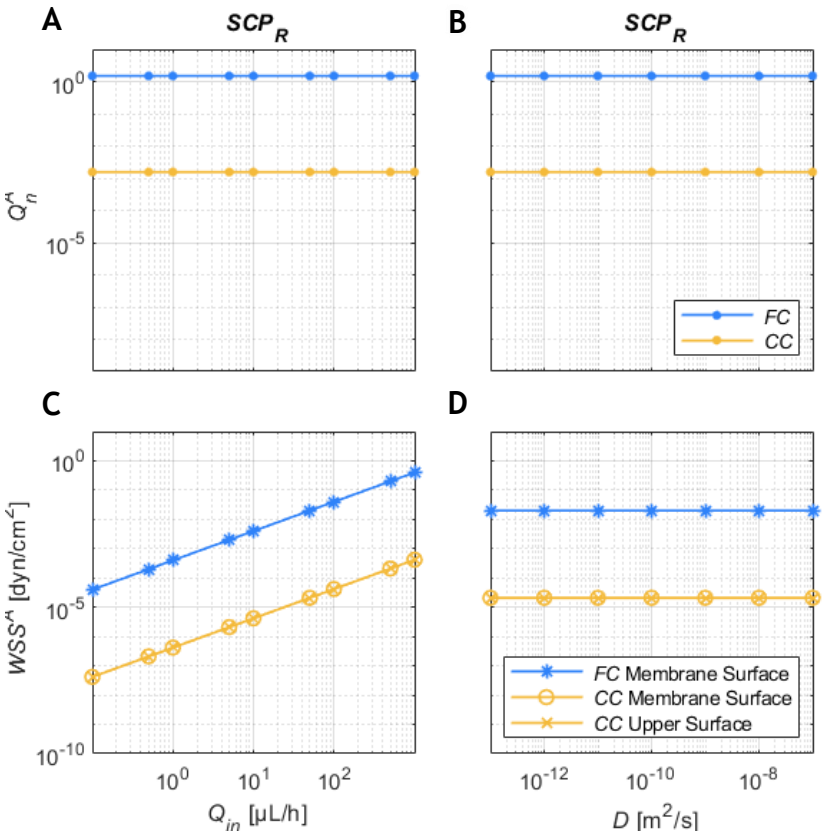

Figure 5.10: Flow and diffusion parameters and their effect on Q^A_n and WSS^A for SCP_R.

Box 4

Design guidelines for modelling fluid dynamics in *SCP* using flow and diffusion parameters.

- **Inlet Flow Rate, Q_{in}:** Widely controls Q^A_n without changing the ratio between Q^A_{nCC} and Q^A_{nFC}, a feature exclusive for membrane and geometry parameters.

- **Diffusion Coefficient Rate, *D*:** Being exclusively a property of the diluted molecule, it does not influence the established fluidic field.

5.4 Mass Transport

After identifying and characterizing the influence of control parameters on flow dynamics, the next step is to examine their impact on mass transport kinetics. Similar to the structure in Section 5.3, a first analysis will focus on the transport kinetics associated with each setup. Thereby, the settling time to reach steady state is highlighted, as well as the concentration distribution, both as a function of the boundary conditions and the diffusive properties of dissolved molecules. This is followed by an analysis addressing each control parameter and their respective effect in defining *st* and ssC_n. The analysis will be subdivided into membrane parameters, channel geometry, and flow and diffusion properties.

5.4.1 Single Channel versus Parallel Perfusion

Given that the *CC* is simulated as a reservoir for *SCP*, Fick's Law determines that the flux of molecules from the *FC* to the *CC* only stabilizes when the concentration gradient between the domains is null. To satisfy this condition, a steady state is reached only when $C_{nCC} = 1$, as demonstrated in Figure 5.11 A and B for SCP_R or SCP_O, respectively. Figure 5.11 C and D further highlight that the tendency to reach $C_{nCC} = 1$ is independent of molecule size. The same figures also demonstrate that the increased porous flow in SCP_O contributes to higher molecular transport

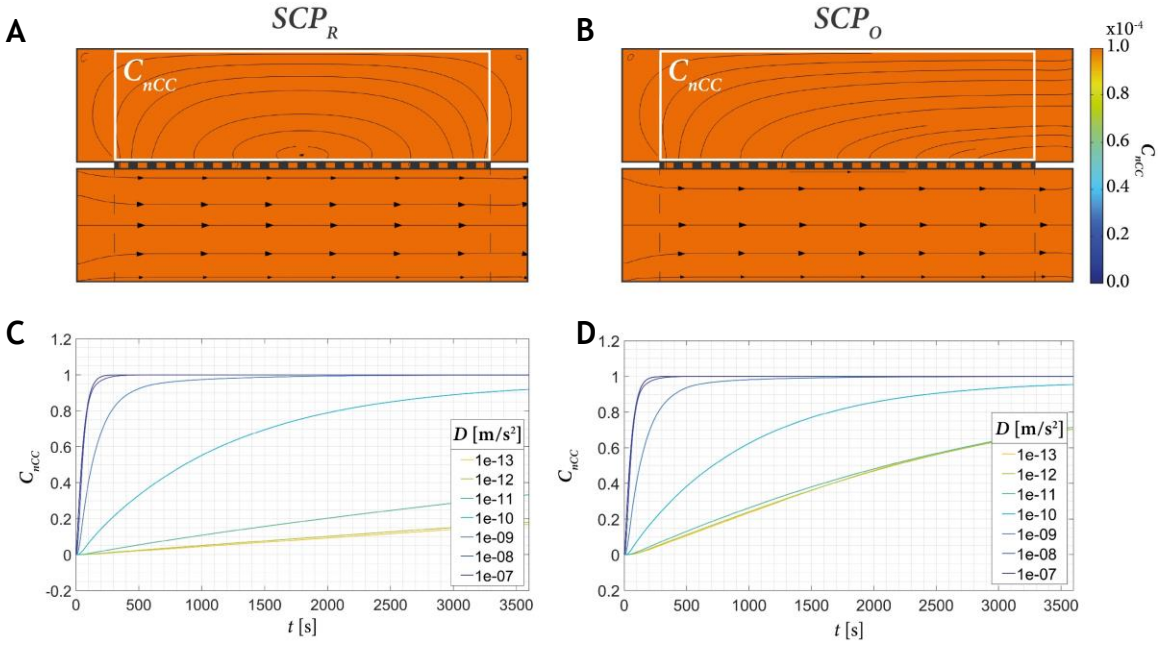

Figure 5.11: Steady state concentration distribution and transient evolution for *SCP*. A and B, Steady state concentration distribution and molecular flux, in black arrows, for SCP_R and SCP_O respectively. C and D, Transient concentration evolution in the *CC*, for SCP_R and SCP_O respectively, measured for different values of *D*.

across the membrane. This is particularly noticeable for heavier molecules, with a lower *D* (such as represented in yellow and green lines in Figure 5.11 C and D), whose higher reliance on convective transport defines faster exchange rates across the membrane for SCP_O than for SCP_R.

Due to the perfusion of media in both channels, during *PP* the normalized inlet concentration values are fixed at $C_{inFC} = 1$ and $C_{inCC} = 0$. Therefore, Fick's Law determines that molecular exchange reaches a steady state when $C_{nCC} = C_{inFC}$. This implies an heterogenous steady state distribution of concentration, as shown in Figure 5.12 A and B. The transient permeability curves in Figure 5.12 C and D demonstrate that a steady state is achieved for an intermediate concentration value which generally satisfies the condition $ssC_{nCC} + ssC_{nFC} = 1$. Figure 5.12 A and B also show the differences between PP_{SD} and PP_{OD}, respectively, where the polarity of the concentration distributions reflects the convective patters associated with each setup. Figure 5.12 C and D demonstrate as well that PP_{SD} contributes to faster molecular transport then PP_{OD}, as observed by the steeper increase to concentration in the first instances of the test.

Given that for *PP*, *st* is relatively low (as observed in both Figure 5.12 C and D) and often unresponsive to parametric changes, and that for *SCP*, ssC_n is always

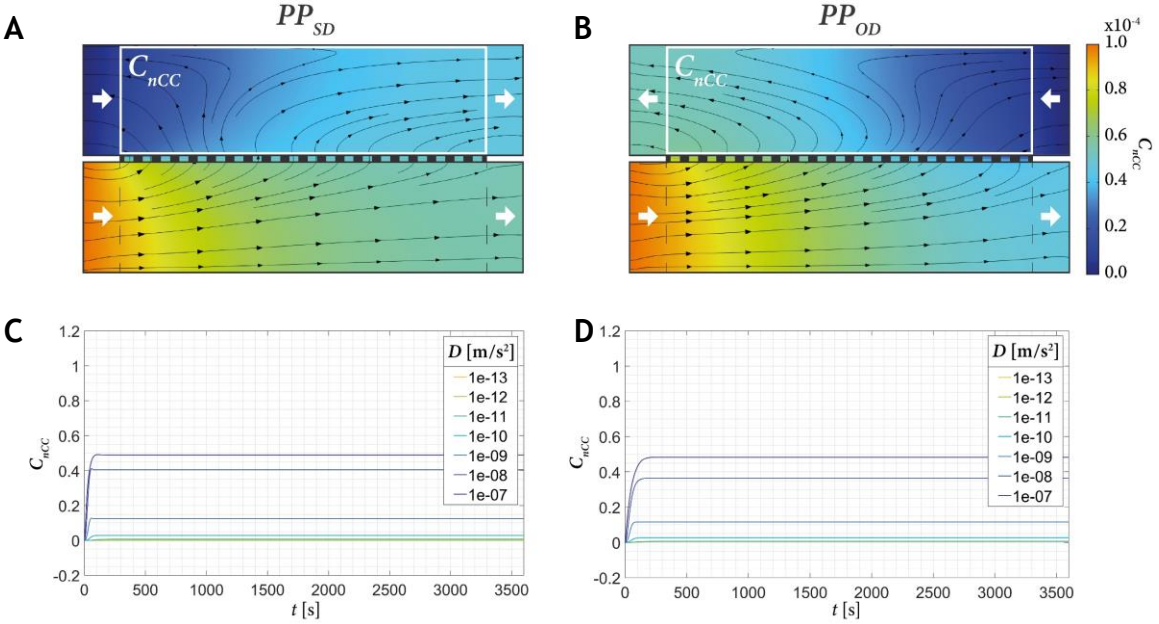

Figure 5.12: Steady state concentration distribution and transient evolution for *PP*. A and B, Steady state concentration distribution and molecular flux, in black arrows, for PP_{SD} and PP_{OD} respectively. C and D, Transient concentration evolution in the *CC*, for PP_{SD} and PP_{OD} respectively, measured for different values of *D*.

equal to 1, the analysis that follows will primarily focus on studying *st* for SCP_R, and ssC_n for PP_{SD}. Nonetheless, the reader is referred to Figure 5.19, Figure 5.20 and Appendix A, where all results and respective discussion can be found. Finally, an analysis of the Péclet number is included in Appendix A. In general, it is observed that for *SCP*, transport in the *CC* is more subject to variations induced by a different choice of parameters, with Pe_{CC} fluctuating above and below the

Box 5

Design guidelines for modelling molecular transport with different fluidic setups.

- **Single Channel Perfusion, *SCP*:** Determines a uniform concentration distribution equal to the inlet value, regardless of the selected passive parameters, but provides wide control over the rate of transient transport. The increase of convective flow in SCP_O provides slightly faster transport over SCP_R.

- **Parallel Perfusion, *PP*:** Capable of widely modelling the steady state concentration distribution based on the selected passive parameters. PP_{SD} provides a slight increase to the exchange rate, and therefore, decrease to *st*, when compared to PP_{OD}.

value of 1. On the other hand, it is observed that Pe_{CC}, for *PP*, and Pe_{FC}, for both *SCP* and *PP*, are generally maintained above the value of 1, suggesting that advection is the predominant mode of transport.

5.4.2 Membrane Parameters

The changes induced by a variation of *P* to *st* in SCP_R are presented Figure 5.13 A and demonstrate the existence of a critical value at $P = 0.1$. For $P < 0.1$, it is observed that not only does st_{FC} decrease from $st_{FC} = 155$ s to $st_{FC} = 50$ s, for $P = 0.01$, but also st_{CC} sharply increases from $st_{CC} = 285$ s to $st_{CC} > 3600$ s. In turn, for $P > 0.1$, both functions stabilize and settle on the values of $st_{FC} = 135$ s and $st_{CC} = 185$ s. Figure 5.13 D demonstrates another critical value at $P = 0.2$ for the correlation between *P* and ssC_n in PP_{SD}. For $P < 0.2$, the functions for ssC_{nCC} and ssC_{nFC} respectively decrease and increase symmetrically, with a magnitude of approximately $ssC_n = 0.32$. For $P > 0.2$, both functions stabilize at the respective values of $ssC_{nCC} = 0.36$ s and $ssC_{nFC} = 0.64$ s.

A change to *r* displays instead a very negligible effect. Figure 5.13 B shows that *st*, in *SCP*, is maintained stable for a vast range of *r*. Only for $r > 10$ µm, *st* is marginally reduced, ultimately reaching $st_{CC} = 1755$ s and $st_{FC} = 95$ s, for $r = 100$ µm. Figure 5.13 E further demonstrates that the influence of *r* over ssC_n in *PP* is virtually null.

The relationship between t_M and *st* in SCP_R is shown in Figure 5.13 C. It is observed that an increase of t_M results as well in an increase to st_{CC}, from the value of $st_{CC} = 190$ s, for $t_M = 1$ µm, to $st_{CC} > 3600$ s, for $t_M = 1000$ µm. Regarding st_{FC} it is observed a steadier profile, with st_{FC} being contained within the interval from 135 s to 150 s for the majority of the tested values, and decreasing to $st_{FC} = 55$ s only for $t_M < 500$ µm. On the other hand, Figure 5.13 F demonstrates that t_M produces a gradual change to ssC_n in PP_{SD}. Values for ssC_n steadily increase and decrease, in the *FC* and *CC* respectively, with an increase of t_M. It was analysed that an increase from $t_M = 1$ µm to $t_M = 1000$ µm corresponds to an absolute change equivalent to $ssC_n = 0.34$.

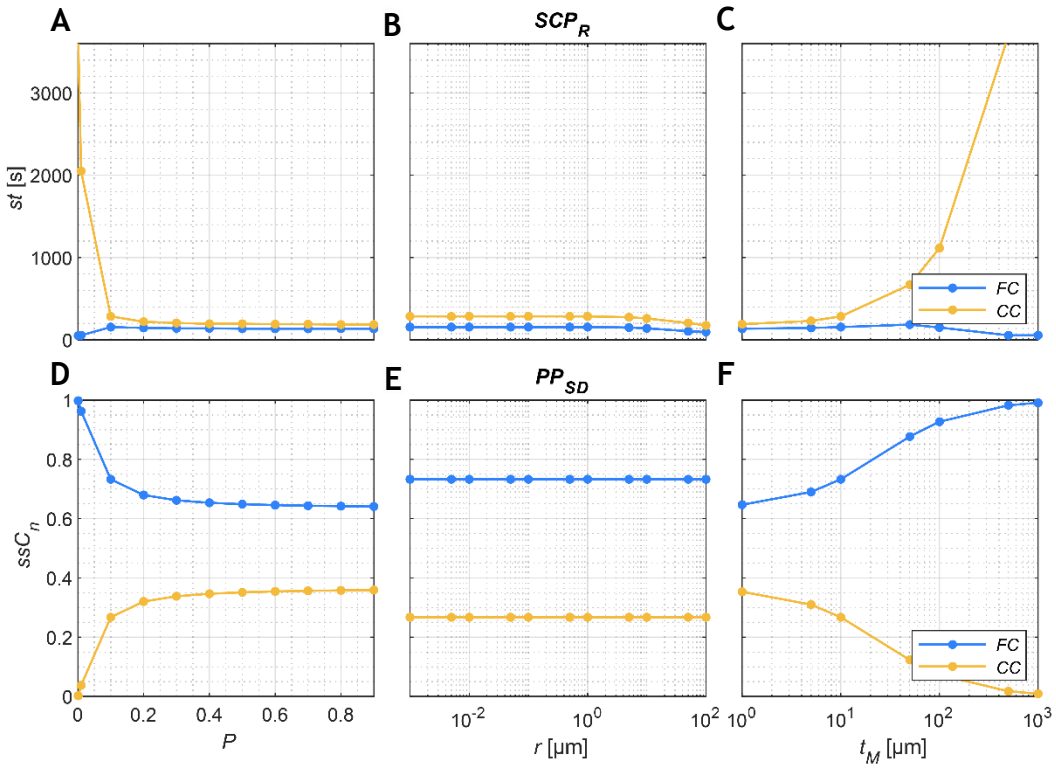

Figure 5.13: Membrane properties and their effect on *st*, in SCP_R, and ssC_n for PP_{SD}.

Box 6

Design guidelines for transient transport in *SCP* and molecular concentration in *PP* using membrane parameters.

- **Porosity, *P*:** For $P < 0.1$ and $P < 0.2$ it is possible to widely control *st* and ssC_n respectively.

- **Pore Radius, *r*:** Provides very modest control over *st*, for $r > 10$ µm, but no measured influence over ssC_n.

- **Membrane Thickness, t_M:** Increasing t_M provides a steep increase to st_{CC} and reduce membrane transport, characterized by an increase of ssC_{nFC} and decrease of ssC_{nCC}.

5.4.3 Channel Geometry

A change in L_M affects both the surface area for porous exchange and the volume of channels. Each of these contributions will have a unique effect on molecular transport. In Figure 5.14 A shows that st_{CC} in SCP_R is described by a quadratic function, with a lower limit at st_{CC} = 285 s, for L_M = 5 mm and L_M = 7.5 mm. For L_M < 5 mm, the decreasing exchange area reduces molecular transport and increases st_{CC}. For L_M > 7.5 mm, the increasing exchange area is outweighed by the increasing volume of channels, ultimately increasing st_{CC}. Figure 5.14 A further demonstrates that augmenting L_M results in the continuous increase of st_{FC}. Regarding the influence over ssC_n in PP_{SD}, Figure 5.14 D demonstrates that increasing L_M results in the increase of molecular transport across the membrane as well. For the tested interval of values, it is seen that ssC_{nCC} and ssC_{nFC} nearly reach a balance, with ssC_{nCC} = 0.46.

A change to H_{CC} results in a change of the *CC* volume. This way, by increasing H_{CC}, and thus increasing volume, *st* in SCP_R also increases, as Figure 5.14 B demonstrates. This increase follows approximately an exponential fit. Whereas for H_{CC} = 10 µm, st_{CC} = st_{FC} = 50 s, for H_{CC} = 10000 µm, st_{CC} > 3600 s and st_{FC} = 2770 s. Figure 5.14 B also demonstrates that, as H_{CC} increases, so does the gap between st_{CC} and st_{FC}, benefiting the prior. When it comes to ssC_n in PP_{SD}, the correlation is inversely proportional, with an increase to H_{CC} resulting in a decrease of molecular transport, as shown in Figure 5.14 E. In turn, this increases ssC_{nFC} and decreases ssC_{nCC}.

Very similar relationships are observed for the changes induced by H_{FC} in both the *st* in SCP_R and the ssC_n in PP_{SD}, as Figure 5.14 C and F respectively demonstrate. An increase of H_{FC} will correspond to an exponential increase of both st_{CC} and st_{FC}, even though generally, st_{CC} > st_{FC}. And regarding molecular transport, it is verified a generally linear decrease. If for H_{FC} = 10 µm, ssC_{nFC} = 0.60 and ssC_{nCC} = 0.47, for H_{CC} = 10000 µm, ssC_{nFC} = 0.87 s and ssC_{nCC} = 0.10 s. H_{FC} and H_{CC} are the only cases where the condition ssC_{nCC} + ssC_{nFC} = 1 does not necessarily apply, due to the imposed geometric asymmetries.

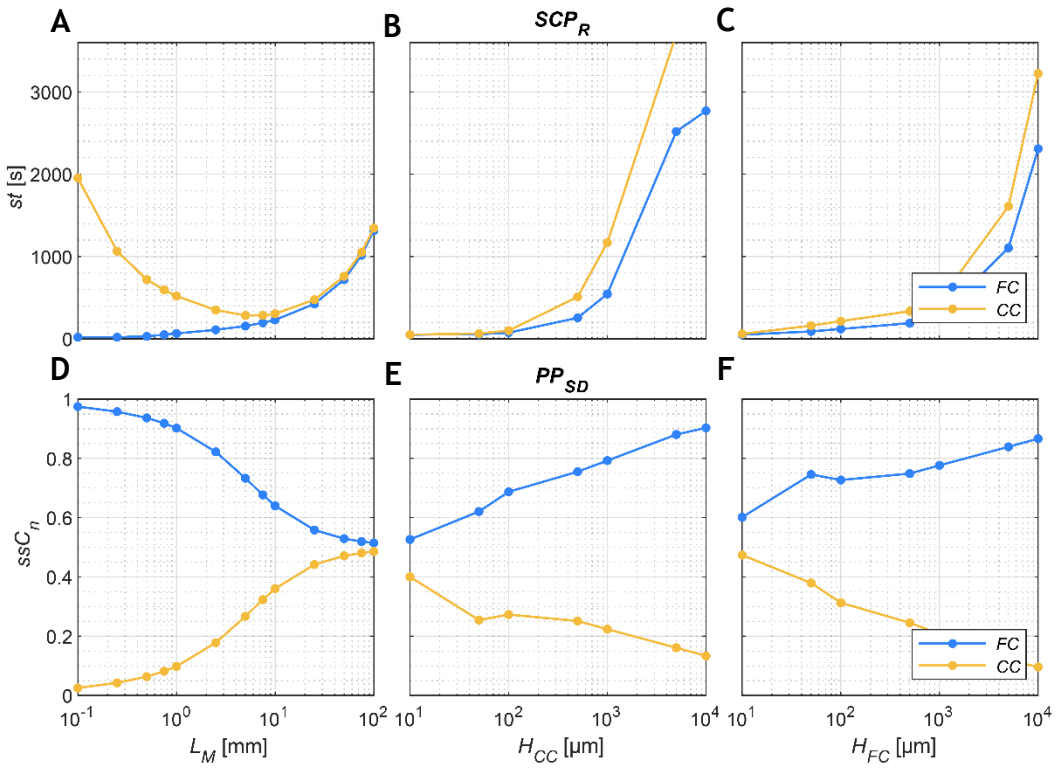

Figure 5.14: Channel geometry and their effect on *st* and ssC_n for SCP_R and *PP* respectively.

Box 7

Design guidelines for transient transport in *SCP* and molecular concentration in *PP* using channel geometry.

- **Length of Membrane, L_M:** Provides full control over ssC_n and a quadratic function modelling st_{CC}, with a lower limit at st_{CC} = 285 s, for L_M = 5 mm and L_M = 7.5mm.

- **Height of Cell Channel, H_{CC}:** Exponential control over *st* and inversely linear over ssCn, while creating asymmetries between *CC* and *FC*, being the exception to $ssC_{nCC} + ssC_{nFC} = 1$.

- **Height of Flow Channel, H_{FC}:** Exponential control over *st* and inversely linear over ssC_n, while creating asymmetries between CC and FC, being the exception to $ssC_{nCC} + ssC_{nFC} = 1$.

5.4.4 Flow and Diffusion Properties

The relationship between Q_{in} and st in SCP_R is displayed in Figure 5.15 A. It can be observed that an increase of Q_{in} accelerates the rate of transport, and therefore, reduces st. If for $Q_{in} \leq 1$ µL/h, st_{CC} and st_{FC} are superior to 3600 s, for $Q_{in} \geq 100$ µL/h, both are inferior to 300 s, evidencing a very steep reduction of the transient interval. Regarding the parameter's influence over ssC_n in PP_{SD}, it can be seen that the relationship is inversely proportional, where an increase of Q_{in} corresponds to a decrease of molecular transport. As Figure 5.15 C demonstrates, whereas for $Q_{in} = 0.1$ µL/h a concentration balance between both channels is observed, with $ssC_{nCC} = 0.49$ and $ssC_{nFC} = 0.51$, for $Q_{in} = 1000$ µL/h, $ssC_{nCC} = 0.04$ and $ssC_{nFC} = 0.96$, evidencing instead very little signs of molecular exchange.

It comes naturally that a change in D will likewise impose changes in st in SCP_R and ssC_n in PP_{SD}, which Figure 5.15 B and D respectively identify. It is observed in Figure 5.15 B that a heavier molecule results in a long transient interval in the *CC*, with $st_{CC} > 3600$ s for $D \leq 1 \times 10^{-10}$ m^2/s. On the contrary, a smaller molecule travels faster through the membrane and reaches a steady state quicker. This way, for $D \geq 1 \times 10^{-8}$ m^2/s, $st_{CC} \leq 200$ s. Interestingly, st_{FC} remains steady within the interval between 70 – 185 s regardless of the molecule size. This is justified by the role convection plays in the *FC*, which outweighs diffusion and outright defines the steady state. Figure 5.15 D demonstrates the relationship between D and ssC_n in PP_{SD}. It is observed that an increase of D corresponds to an increase of molecular exchange, thus increasing ssC_{nCC} and decreasing ssC_{nFC}.

Box 8

Design guidelines for transient transport in *SCP* and molecular concentration in *PP* using flow and diffusion parameters.

- **Inlet Flow Rate, Q_{in}:** An increase to Q_{in} decreases molecular transport across the membrane but accelerates the exchange.

- **Diffusion Coefficient Rate, D:** An increase to D greatly decreases st_{CC}, without disrupting st_{FC}, and increases molecular transport across the membrane.

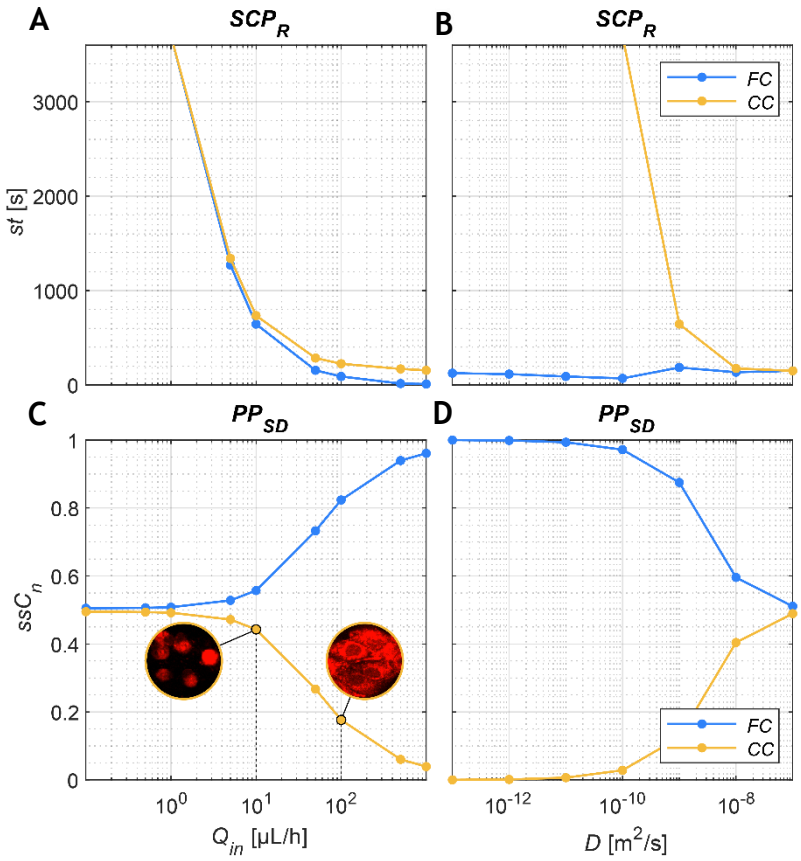

Figure 5.15: Flow and diffusion parameters and their effect on *st* and ssC_n for SCP_R and *PP* respectively. C, Observation that a decrease in Q_{in}, which results in an increase of the ssC_nCC, will increase the transport of Cytochalasin D across the membrane, disrupting actin filaments and providing greater cell retraction. The respective experiment is described in further detail in the following section.

5.5 Experimental Validation and Biological Significance

To illustrate the reported numerical findings, a simple experimental setup was established, as shown in Figure 5.16. It consisted of a microfluidic bi-layer device, hence with two individual channels on parallel planes, separated by a porous membrane. Both channels were perfused with media, but only in one the media was mixed with a given diluted molecule (channel in yellow, Figure 5.16). This way, the PP_{SD} setup was experimentally replicated, not only allowing the experimental validation of the numerical results, particularly in determining ssC_{nCC}, but also allowing the demonstration of their relevance to applications involving cell culture. To do so, two different control parameters were explored, r and Q_{in}. To investigate the influence of r, two different membranes were tested, with a pore diameter of respectively 0.4 µm (P = 0.01) and 3.0 µm (P = 0.17). Similarly, to explore Q_{in}, both membranes were tested at the flow rates of 10 and

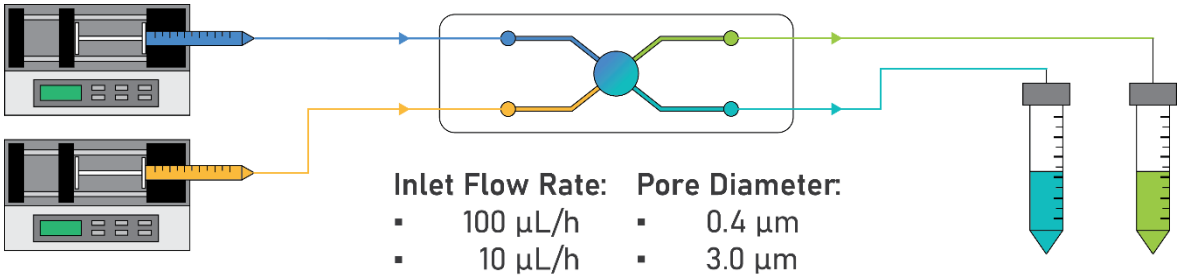

Figure 5.16: Experimental setup for fluidic perfusion. The fluidic pumps, on the left, provide media with (in yellow) and without (in blue) a diluted molecule to both channels of the microfluidic device, in the middle, whose outlets are connected to reservoirs, on the right.

100 µL/h. To validate the numerical results, two experiments were performed, with and without cells. This way, it was possible to obtain not only a direct measurement of the membrane's permeability as a function of the control parameters, but also describe their effect on cell culture. Permeability experiments without cells were performed using fluorescein (0.332 [KDa], 5.4×10^{-10} m^2/s), to describe it as a function of both r and Q_{in}. In parallel, Madin-Darby canine kidney (MDCK) cells were cultured *on-chip*, and their morphological behaviour was studied as a function of the transport of Cytochalasin D across the membrane. Fluorescein was intentionally selected to establish an approximation model for the transport of Cytochalasin D, given that both molecules have comparable molecular weight ($M_{fluorescein}$ = 332.3 g/mol; $M_{cytochalasin\ D}$ = 507.6 g/mol) and hence similar diffusion properties [316]. Both experiments provide experimental and biological evidence to support the obtained numerical data.

5.5.1 Membrane Permeability with Fluorescein

The permeability experiments with fluorescein are illustrated in Figure 5.17 A, highlighting the membrane interface and the transport of fluorescein from the *FC* to the *CC*. The experimental results are shown in Figure 5.17 B. Using GraphPad Prism, a two-way ANOVA test with a significance level of 0.05 was performed to evaluate the statistical variance between pore diameter and Q_{in} on regulating the ssC_{nCC}. The data was presented as mean ± standard deviation. Statistical notation was defined as non-significant (ns) for $p > 0.05$; "*", or significant with * $p \leq 0.05$. There are two key takeaways. First, that a change in pore size provides non-significant changes in the ssC_{nCC}, with a difference of only 0.03 when changing the pore diameter from 0.4 to 3.0 µm. And second, that a change in Q_{in} provides instead significant control over transport and the resulting steady state concentration, with an increase up to 0.17 in ssC_{nCC} when decreasing Q_{in} from 100 to 10 µL/h. Both results are in great conformity with those obtained numerically.

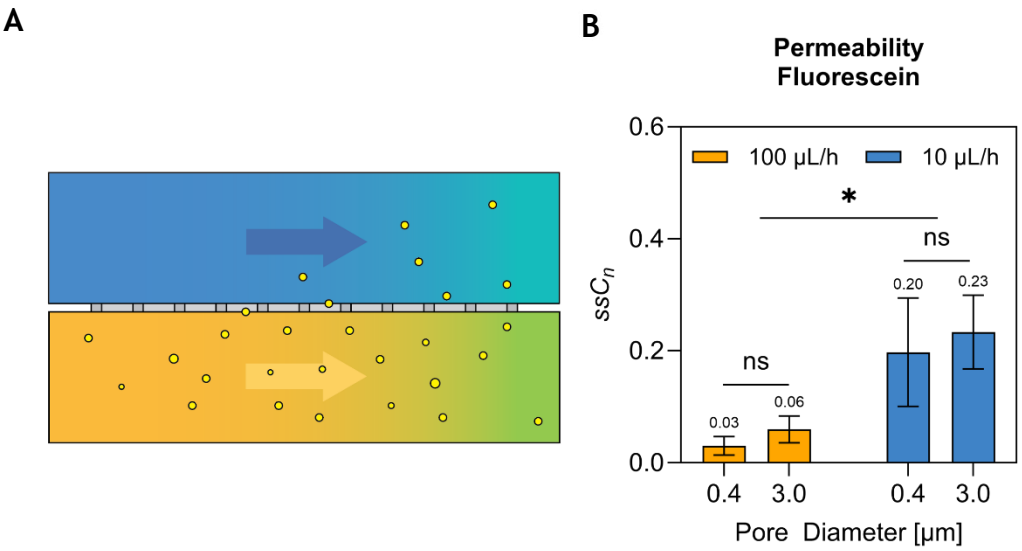

Figure 5.17: Membrane permeability testing. A, Illustration of the membrane interface, highlighting the exchange of fluorescein from the *FC* to the *CC*. B, Steady state concentration ratio of fluorescein for 100 µL/h (in yellow) and 10 µL/h (in blue), as well as a pore diameter of 0.4 and 3.0 µm.

As observed in Figure 5.13 B and E, numerical data predicts a negligible influence of r in controlling transport, but on the contrary, it evidences in A and D a significant effect induced by a change in porosity. However, given the diffusion coefficient of fluorescein is lower than the one modelled (specified in Table 5.2), Figure 5.15 D predicts that the diffusive component of transport will play a lesser role, and hence, membrane properties will provide a smaller influence in manipulating ssC_{nCC}, as observed experimentally. On the other hand, Figure 5.15 C verifies the dominant influence of Q_{in} in controlling ssC_{nCC}. Numerical data goes further in predicting an increase of approximately 0.26, when changing from Q_{in} = 100 to 10 µL/h, a value which provides a good approximation to that obtained experimentally.

The nature of this phenomenon can be better understood by taking into consideration two key factors. First, the length scales involved. The diameter of a single molecule of fluorescein ranges around a nanometre. Instead, the changes in pore diameter varied in the micrometre scale, which explains why no significant changes did occur to the magnitude of molecular transport across the membrane. And second, the time scales involved. While diffusion governs the rate at which molecules move from regions of high to low concentration - typically perpendicular to the channels in microfluidics - the flow rate controls how quickly molecules are transported by convection along the channel. Therefore, if diffusion remains constant, it results that a decrease in flow rate will benefit the transport

of molecules across the membrane by allowing more time for their diffusion to occur in the direction perpendicular to the channel. Ultimately, this explains why the resulting ssC_{nCC} is greater for the condition at 10 µL/h than at 100 µL/h.

5.5.2 Impact of Membrane Parameters on the Transport of Cytochalasin D and respective impact on Cells

For the biological assays, chips were perfused with media (Gibco CO_2 independent media, Thermofisher) in both channels, and the *FC* supplied with Cytochalasin D at a fixed concentration of 20 µM. Using a confocal microscope (LSM800, Zeiss), the behaviour of the MDCK cells, cultured on the *CC*, was observed over a period of 90 minutes of perfusion and analysed as a function of the concentration of Cytochalasin D, transported from the *FC* to the *CC* via the porous membrane. Cytochalasin D is a well-known actin-disruptive toxin [317, 318], whose inhibiting effect results in drastic changes in cell shape by reducing actin filament length. Its effect on MDCK is well-reported [319, 320], and provides a good correlation to the concentration of the respective toxin in the surrounding microenvironment.

An illustration of the setup is shown in Figure 5.18 A, highlighting the transport of Cytochalasin D as well as its effect on cells as a function of time. Based on the respective measurement, *on*-chip experiments verified a similar trend to both numerical and fluorescent data, with conditions at lower Q_{in} contributing to a higher transport of Cytochalasin D across the membrane and into the *CC*, ultimately resulting in higher morphological change and greater cell retraction. In Figure 5.18 B, a brief overview of the time-lapse performed is presented, highlighting the morphological changes of cells at time points t = 0 min, t = 45 min and t = 90 min, for all the tested setups. Fluorescence was obtained by labelling MDCK cells with CellTracker Red CMTPX. It is observed that, despite their dynamic behaviour, the cells do not evidence signs of retraction for both conditions at 100 µL/h, this way indicating low concentration of Cytochalasin D. On the other hand, cells undergo much greater morphological change, becoming round and decreasing in size, for 10 µL/h, manifesting the higher concentration of Cytochalasin D for both the 0.4 and 3.0 µm membranes. A measurement to these observations is provided in Figure 5.18 C, where the changes in cell morphology are quantified as a function of the angular second moment. This parameter measures image homogeneity and has been used to detect morphological changes [321, 322].

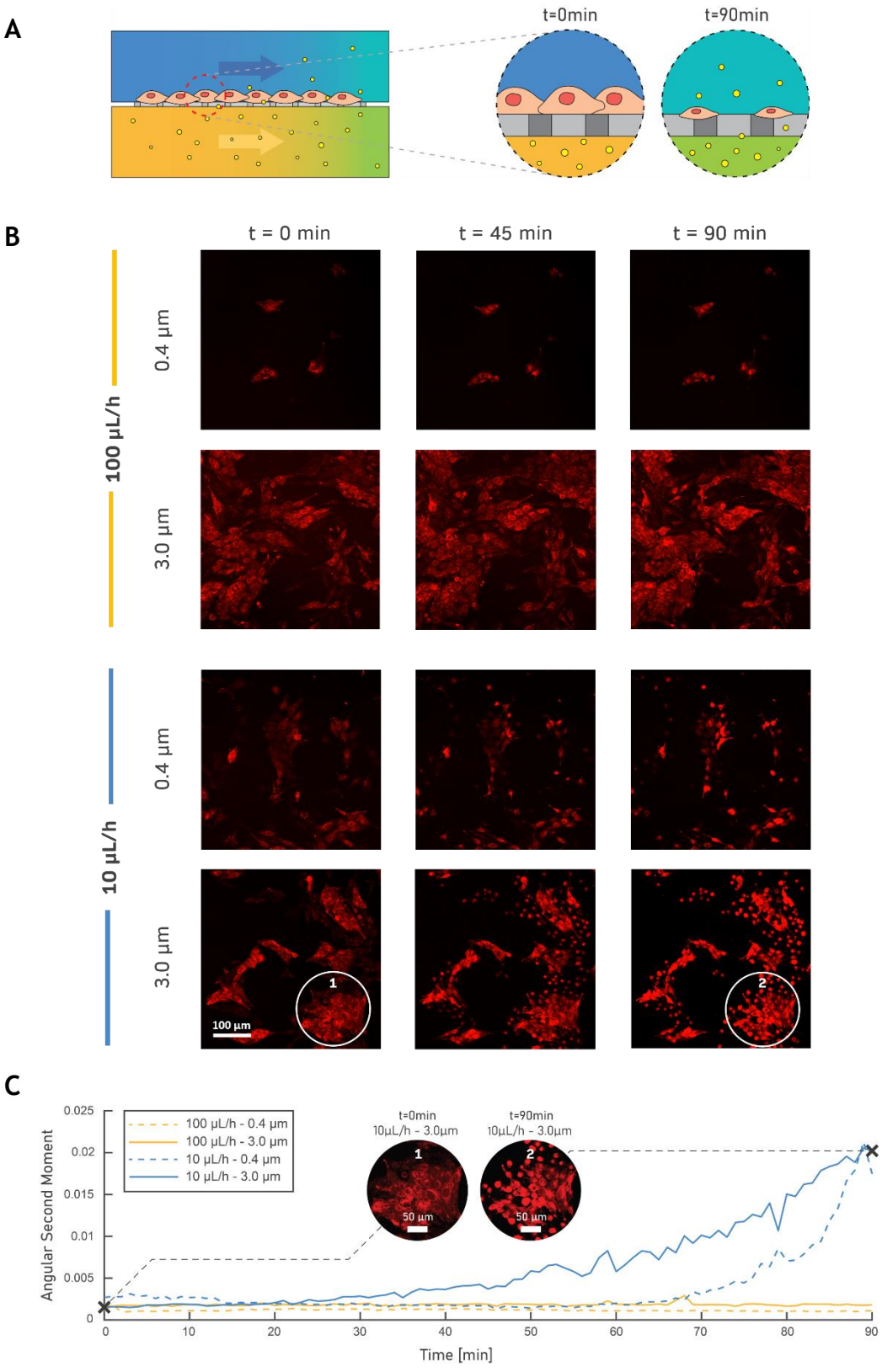

Figure 5.18: Effect of membrane permeability with Cytochalasin D on MDCK cells. A, Illustration of the membrane interface, with cells cultured on the CC and evidencing the effect of the increasing concentration of Cytochalasin D along the duration of experiments. B, Time-lapse series performed with confocal microscopy for the permeability experiments with MDCK cells cultured on-chip according to the four different set of conditions in analysis. Cells are labelled with CellTracker Red. C, The effect of Cytochalasin D is measured as a function of the angular second moment for the four conditions tested, with lines in yellow representing the conditions tested at 100 µL/h, in blue those at 10 µL/h, in continuous lines those performed with the 3.0 µm membrane, and in discontinuous lines with the 0.4 µm. Finally, similar fluorescent images as those numbered with 1 and 2 in B are presented and connected to their respective time point within the plot, respectively corresponding to t = 0 min and t = 90 min for the 3.0 µm membrane at 10 µL/h condition.

Plotting the angular second moment as a function of time evidences a steeper increase for the conditions at 10 µL/h, as highlighted in blue, than for those at 100 µL/h, highlighted in yellow, which remain rather constant and horizontal. This manifests greater morphological change, and specifically stronger cell retraction for the conditions at 10 µL/h then for those at 100 µL/h. On the other hand, the variation between membrane properties demonstrates, once again, a relatively passive role in controlling the transport of molecules across the membrane. This is visible in Figure 5.18 C by the small differences between the same-coloured curves, plotted with continuous and discontinuous lines for the 3.0 and 0.4 µm membranes respectively, manifesting minor morphological changes as a result of the different pore sizes tested.

Crucially, both experiments demonstrate the biological impact of permeability mechanisms and, more importantly, the significance of the developed numerical guidelines in predicting the most relevant permeability parameters in regard to specific devices and biological applications.

5.6 Overview of All Tested Setups and Summary of Results

As described in Section 5.2.3.2, the work reported in this chapter simulated and covered four different microfluidic environments, namely SCP_R, SCP_O, PP_{SD}, and PP_{OD}. Even though the majority of the analysis focused on SCP_R and PP_{SD}, all four setups were simulated. Therefore, to provide a complete overview of the results, all data was gathered and composed together, as displayed in Figure 5.19 and Figure 5.20. In these figures, beyond the plots already presented and discussed, the remaining conditions and results can be observed, analysed, and compared. Each column is associated with a control parameter, with the respective scale bars presented at the bottom. Similarly, response variables are displayed into rows, and their respective units are presented at the right-hand side of both figures. Figure 5.19 and Figure 5.20 are respectively representative of the *SCP* and *PP* conditions, and are further subdivided into two halves, to account for SCP_R and SCP_O (Half A and B), in Figure 5.19, and PP_{SD} and PP_{OD} (Half C and D), in Figure 5.20. Moreover, and as previously described, each plot displays multiple markers, each one illustrative of the different data sets tested, with the associated labels present at the bottom of each figure. Each individual plot is labelled with a unique

code which can be used to read Appendix A, where the original data for each plot of Figure 5.19 and Figure 5.20 can be seen and analysed. Altogether, both figures provide an extensive overview of all the parameters and setups tested, ultimately contributing to a more systematic analysis of the collective whole. In the following, the unexplored sections of Figure 5.19 and Figure 5.20 will be discussed, analysed and summarized.

5.6.1 Fluidic Field

5.6.1.1 Single Channel Perfusion with Cell Channel as an Outlet (SCP_O)

As it is possible to observe in Figure 5.19, the functions correlating control parameters to response variables for SCP_O are very similar to those presented for SCP_R. The main difference is that the amount of Q^A_n, and WSS^A, experienced in the *CC* is on average higher for SCP_O than for SCP_R, as can be observed in Figure 5.19, by comparing half B and A respectively. This phenomena results from the increase in porous flow between SCP_O and SCP_R. Another effect of this phenomena is that the increase in Q^A_{nCC} also results in the increase of WSS^A in the upper surface of the *CC*. Ultimately, the difference between WSS^A_{UCC} and WSS^A_{MCC} for the L_M and H_{CC} parametric sweeps is smaller than measured for SCP_R.

5.6.1.2 Parallel Perfusion with Same Direction Flow (PP_{SD})

As explained in Section 5.3, parallel flow creates symmetrical pressure profiles in the top and bottom channels, which ultimately hinders flow exchange across the membrane. Therefore, it results in the flow and shear properties measured in both the *CC* and *FC* being predominantly a function of the Q_{in}. This explains why changes to most membrane and some geometry parameters result in virtually no effect to the established fluidic field and shear stress, as observed in half C of Figure 5.20.

The only exceptions are the parametric sweeps for the H_{CC} and H_{FC}, where the geometric asymmetries created, especially for H_{CC} and H_{FC} < 100 μm, generate fluidic asymmetries between the channels, where increased pressure on the shallower channel, leads to increased Q^A_n in the opposing channel. Another effect is the decrease of WSS^A_{CC} and WSS^A_{FC} for increasing H_{CC} and H_{FC} respectively. Taking the parametric sweep over H_{CC} as an example, whereas WSS^A_{FC} is

maintained steady at -2.71 dyn/cm^2, WSS^A_{CC} continuously decreases from the relatively high order of 0.1 dyn/cm^2, for H_{CC} = 10 μm ($WSS^A_{MCC}(H_{CC}=10)$ = 1.26 dyn/cm^2, Appendix A), to -4.6 dyn/cm^2, for H_{CC} = 10000 μm ($WSS^A_{MCC}(H_{CC}=10000)$ = 2.71x10^{-5} dyn/cm^2, Table A.1). A similar but inverse relationship is observed for H_{FC}, as it is shown in Figure 5.20 C26.

5.6.1.3 Parallel Perfusion with Opposite Direction Flow (PP_{OD})

The results obtained for PP_{OD} are generally similar to those for PP_{SD}. The key differences are: first, the slight decrease in Q^A_{nCC} and Q^A_{nFC} for the parametric sweeps of H_{FC} and H_{CC}, respectively, when compared to the values obtained for PP_{SD}; and second, the gentle decrease of both the Q^A_n and WSS^A for r > 10 μm, resulting from the phenomena described in Figure 5.7 B and D.

5.6.2 Mass Transport

5.6.2.1 Single Channel Perfusion with Cell Channel as a Reservoir (SCP_R)

Half A, row 4 of Figure 5.19 demonstrates that concentration always reaches a value of ssC_n = 1 for SCP_R, regardless of changes to control parameters. This is due to the existence of only one concentration source, which implies that, according to Fick's Law, a steady state is only achieved when the concentration of the domain equals the concentration of the source.

5.6.2.2 Single Channel Perfusion with Cell Channel as an Outlet (SCP_O)

Figure 5.11 shows that molecular transport occurs at a faster rate for SCP_O than for SCP_R. This means that SCP_O achieves a steady state faster than SCP_R, a difference which can be as high as 70 s. However, the profile of the functions remains similar, as can be observed in Figure 5.19 B31, B32 and B33. Half B, row 4 of Figure 5.19 also demonstrates that ssC_n = 1 for all tested parameters due to the existence of a single concentration source.

5.6.2.3 Parallel Perfusion with Same Direction Flow (PP_{SD})

Half C, row 3 of Figure 5.20 demonstrates that *st* in PP_{SD} is low and almost instantaneous for the majority of the parametric values tested. Membrane parameters provide little to no influence in controlling *st*. Channel geometry

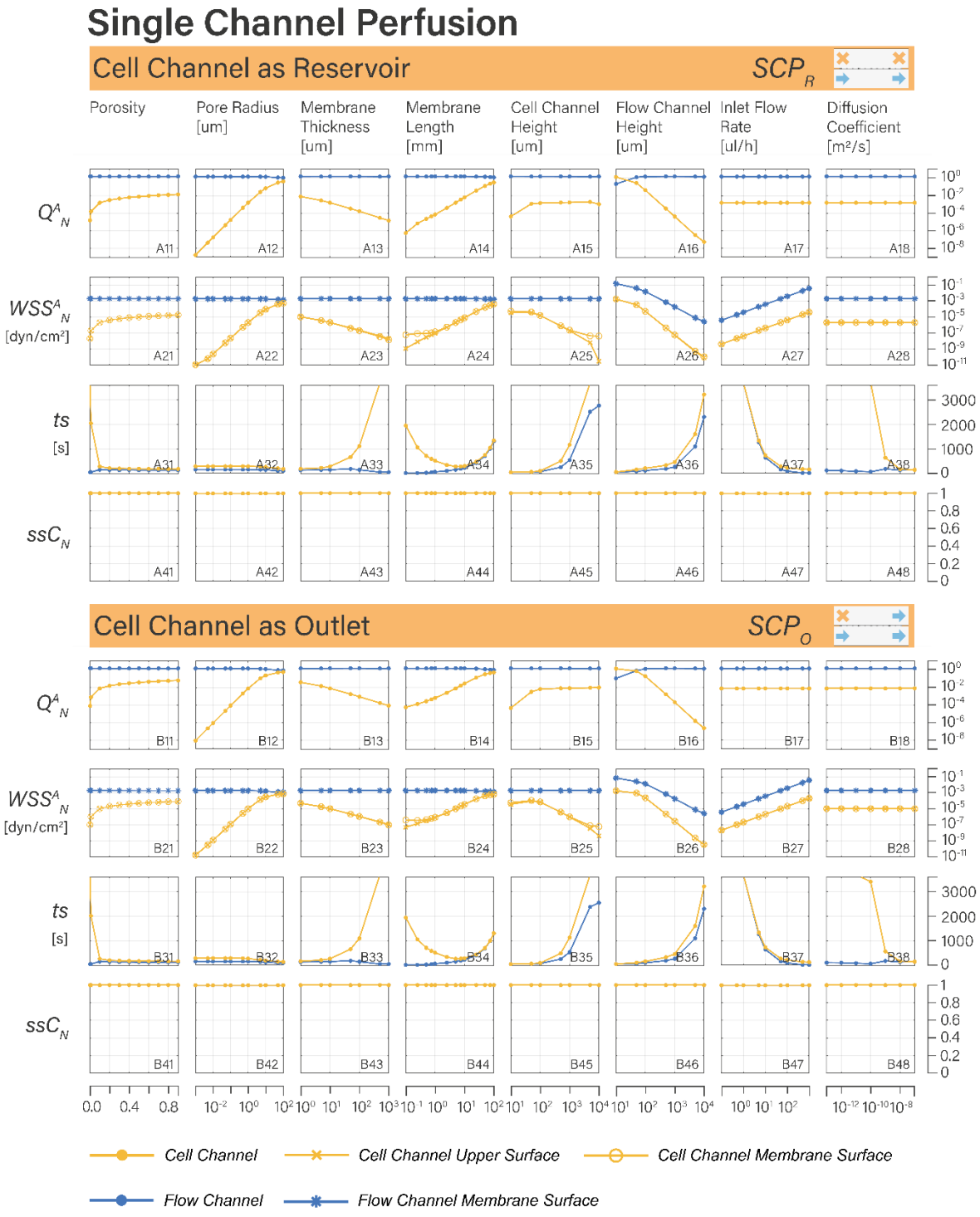

Figure 5.19: Compilation of numerical results for the *SCP* condition, obtained for the different control parameters and response variables analysed, as well as the various data sets involved in the process.

parameters evidence some control, where high parametric values (L_M > 10 mm, H_{CC} > 1 mm, H_{FC} > 1 mm) slow down transport and increase *st*. Finally, it is observed that Q_{in} plays a crucial role in modelling *st*. As Figure 5.20 C37 demonstrates, whereas $st(Q_{in}$ = 1 µL/h) > 3600 s, $st(Q_{in}$ = 50 µL/h) = 50 s, evidencing the big influence Q_{in} plays, especially for Q_{in} < 50 µL/h, in controlling molecular exchange.

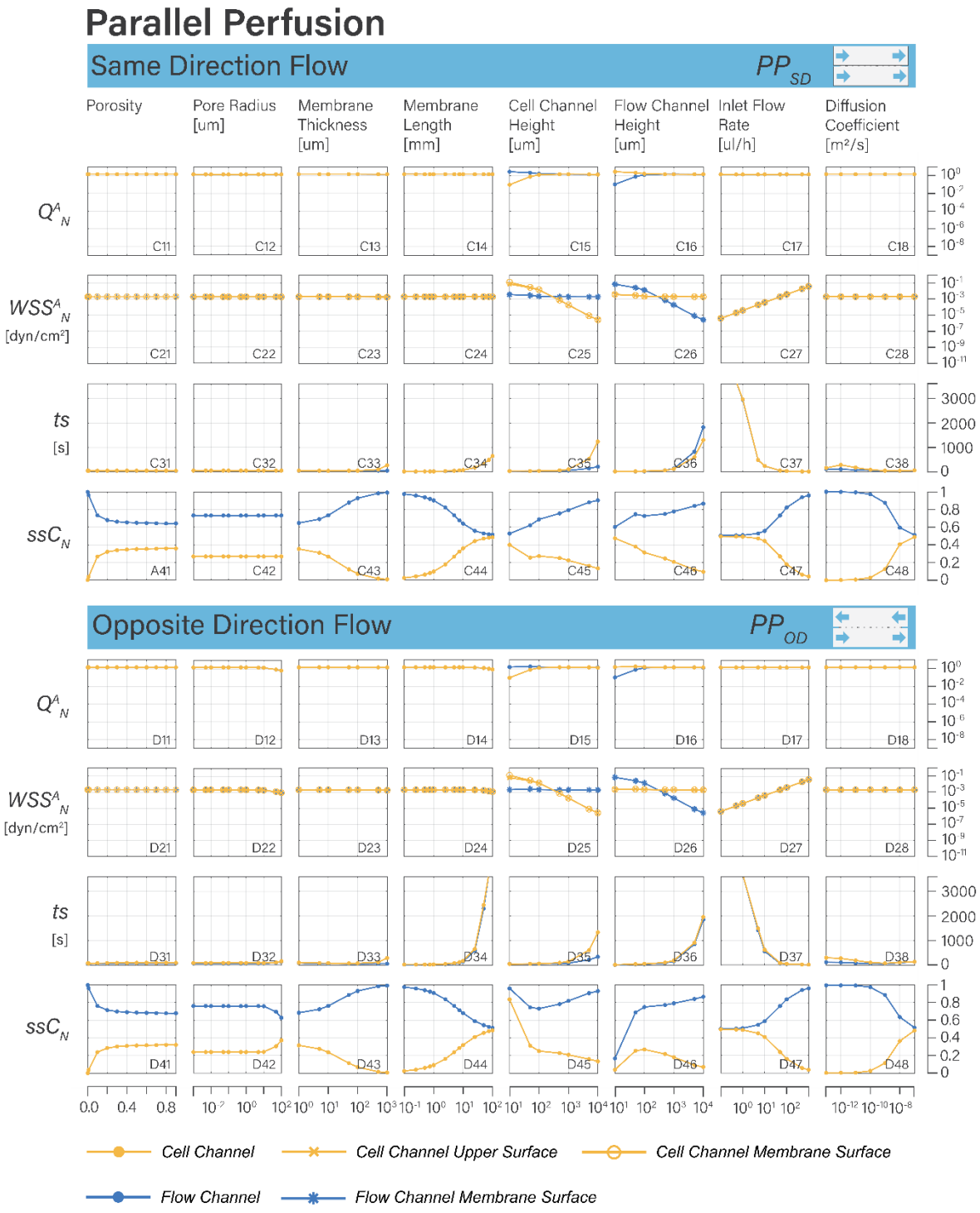

Figure 5.20: Compilation of numerical results for the *PP* condition, obtained for the different control parameters and response variables analysed, as well as the various data sets involved in the process.

5.6.2.4 Parallel Perfusion with Opposite Direction Flow (PP_{OD})

A change from PP_{SD} to PP_{OD} results in lower molecular transport, and therefore, lower ssC_{nCC}. However, more changes are observed for the parametric sweeps over r, H_{CC} and H_{FC}. First, Figure 5.20 D42 demonstrates that for r > 5 µm, molecular transport is substantially increased, ultimately yielding higher values than for the

same conditions in PP_{SD}. This phenomenon is justified by the increase in porous flow, resulting from the wider pores. Second, it is observed that, whereas for H_{CC} < 100 µm, ssC_n seems to reverse its tendency and increase until both channels are nearly saturated with solute, for H_{FC} < 100 µm, the opposite happens, and ssC_n decreases until both channels are nearly depleted of diluted molecules. This phenomenon arises from the opposite relative flow established between the *CC* and *FC*. For low values of H_{FC}, a higher pressure builds due to the small volume of the channel, which pushes the perfused molecules across the membrane and onto the *CC*. However, due to the opposite direction of flow, as soon as the molecules cross the membrane into the *CC*, they are pushed backwards into the outlet of the respective channel. This way, a loop is created where the molecules travel from the inlet of the *FC* to the outlet of the *CC* without accumulating in neither of the channels, which justifies the low ssC_n values shown in Figure 5.20 D45. The opposite happens for low values of H_{CC}, where due to the small volume the channel, it quickly becomes saturated, justifying the high ssC_n values shown in Figure 5.20 D46. Finally, it is observed that the correlations with *st* are similar to those presented for PP_{SD}, even though usually higher for PP_{OD} than for PP_{SD} for the same parametric values.

5.6.3 Summary of Results

Finally, appreciating the volume of data encompassed by Figure 5.19 and Figure 5.20, and aiming to summarize results and provide a more qualitative overview, Figure 5.21 is provided. In this sunburst chart, every tested fluidic setup and control parameter is displayed radially, with the *SCP* condition being shown in yellow and the *PP* in blue. The relative influence of each individual condition in regard to the output variables of analysis is then hierarchized according to a qualitative colouring scheme on the four outer rims. This way, whereas white identifies the conditions that have a negligible influence on a certain desired output, grey identifies those that provide a moderate control, and yellow and blue those that were shown to present the most effective influence.

In this figure, the following observations can be made:

- **Passive control over flow rate:** primarily relevant in *SCP*, with membrane properties and channel design parameters playing fundamental roles in

modelling fluid flow in the *CC*. Thereby *r*, capable of modelling flow in the *CC* across 9 orders of magnitude, and H_{FC}, with the ability of reversing the flow ratio between channels must be highlighted. Otherwise, in *PP*, the flow dynamics are predominantly governed by Q_{in}, which influence hinders the effects the remaining parameters potentially trigger.

- **Passive control over shear stress:** primarily relevant in *SCP*, where both membrane properties and channel geometry play crucial roles. More significantly, *r* is capable of modelling shear stress from high levels, for large pores, to virtually shear-free conditions, for nano pores, ranging a total of 7 orders of magnitude. The influence of L_M and H_{CC} is also of great interest, both capable of uniquely establishing different levels of shear on opposing surfaces of the same channel. On the other hand, in *PP*, *WSS* is primarily dominated by the influence of Q_{in}. The only exceptions are H_{CC} and H_{FC}, which influence enables modelling the shear stress whilst keeping flow at a constant rate.

- **Passive control over transient transport:** significantly modelled by the majority of passive parameters across both *SCP* and *PP*. While *r* provided

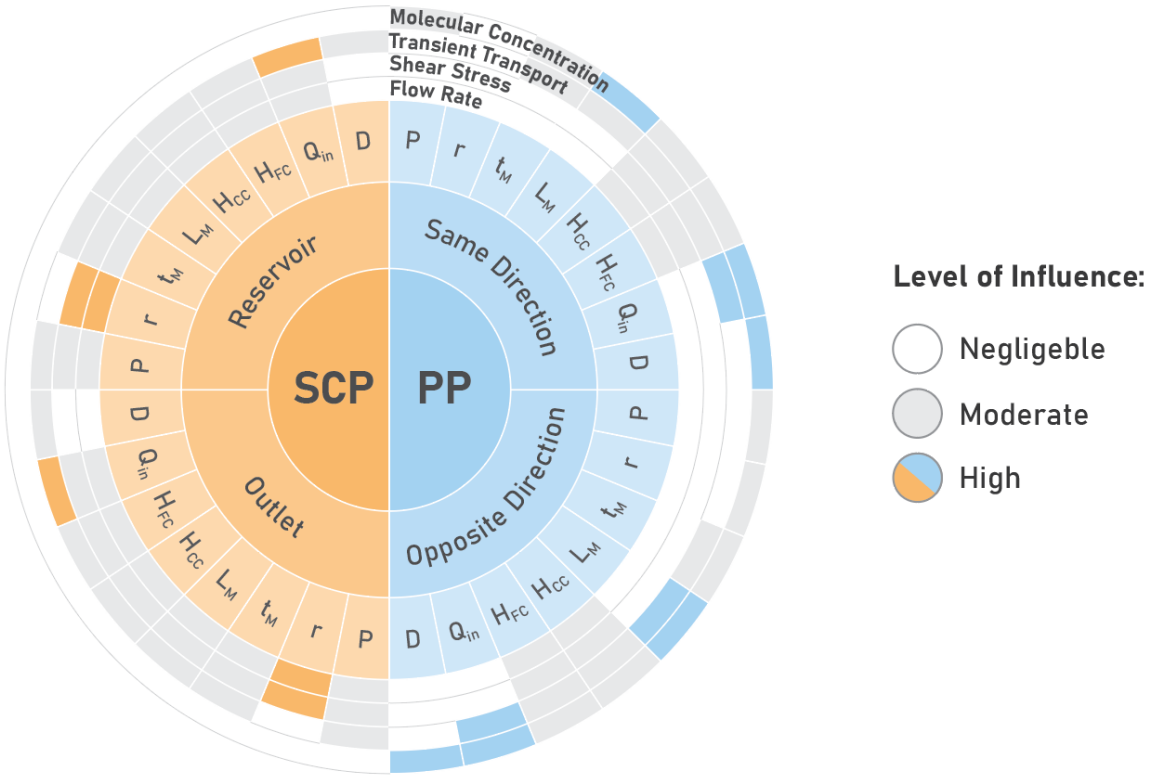

Figure 5.21: Qualitative overview of the obtained numerical results, displaying radially the different tested fluidic setups and control parameters, and hierarchizing the influence associated with each. In white, the influence in characterized as negligible, in grey moderate, and in blue or orange, high.

virtually no influence, a very sharp change was measured for $P < 0.1$. H_{CC}, H_{FC} and t_M demonstrated instead a more gradual control over the transient transport. On the other hand, L_M displayed a quadratic relationship in SCP, suggesting the existence of an optimal value for increasing the exchange rate, and providing better performance for PP_{OD} when compared with PP_{SD}. Finally, it was verified that an increase to Q_{in} widely contributes to increasing the exchange rate and reduce the transient interval.

- **Passive control over molecular concentration and distribution:** only possible in *PP*. Whereas for *SCP*, Fick's Law determines the molecular concentration distribution is necessarily equal to the inlet value, for *PP*, this balance can be modelled by the design parameters. Membrane properties, in particular P, for $P < 0.1$, and t_M, play influential roles. H_{CC} and H_{FC} evidence a linear correlation, and present a unique behaviour for PP_{OD}, with the ability of respectively saturating or depleting the microenvironment. The more significant contributions are, however, provided by L_M and Q_{in}, capable of modelling the concentration from a uniform distribution to an extreme heterogeneity between the channels, the *CC* and the *FC* becoming respectively depleted and saturated.

5.7 Simulating the Transport Kinetics of Recirculating Flow: A Case Study on the Dual-rOOC Platform

The membrane model developed in this thesis has been proved to provide a valuable asset in the study of fluid and transport kinetics in microfluidic systems. Despite the various tested fluidic architectures, as described in the previous sections, all are based on continuous and directional fluid flow. Nevertheless, and as described in Section 2.2.2.2, a growing part of microfluidic research is opting for open well solutions, which generally describe architectures where fluid flow recirculates. These microfluidic solutions have very particular kinetics which, despite not having been contemplated in the study presented previously, can be similarly incorporated and explored using the same model. Therefore, to extend the applicability of the presented model and demonstrate its validity in simulating recirculating flow, a case study is presented, where the particular transport kinetics of a pumpless, recirculating organ-on-chip platform are studied.

The microfluidic system proposed by Busek et al 2023, illustrated in Figure 5.22 A and designated as rOOC [212], is based on connecting two large reservoirs with microfluidic channels, forming a closed loop which allows the cyclic filling and emptying of the reservoirs. This motion relies on pitching the platform to a certain degree, and rolling it continuously, this way generating unidirectional, pulsatile, gravity-driven flow, as observed in Figure 5.22 B. By then including two separate loops interconnected via an ECM channel, this platforms opens the possibility for simultaneous organ and tissue culture and interaction, as it was shown by culturing both endothelial cells and stem-cell (sc) derived liver organoids. Another variation to this concept surged later, in a work which is also now published and to which this thesis also contributed. Aizenshtadt et al 2024 [297] described a new microfluidic design, based on the same concept of pitching and rolling to obtain pumpless, recirculating, gravity-driven flow. The variation to this design, however, is that instead of an ECM, the two separate loops are interconnected by a porous membrane, therefore enabling the co-culture of multiple organs and the study of their respective crosstalk and exchange of factors. This device was termed dual, pumpless, recirculating organ-on-chip (dual-rOOC), and its geometry and layer distribution is presented and detailed in Figure 5.22 C. Beyond the various unique factors describing this platform, perhaps one is less obvious, but nevertheless extremely important to characterize, as it actively benefitted the biological application reported. This factor is the directionality of transport, which is enhanced from the top (purple layer, housing the sc derived islet organoids, Figure 5.22 C) to the bottom loop (green loop, housing the sc derived liver organoids, Figure 5.22 C) rather than from the bottom to the top, or symmetrical. This way, the platform provides asymmetrical, bi-directional crosstalk. This detail is particularly important to the biological application involved, which involves studying the crosstalk between sc derived liver and islet organoids. Most platforms performing similar studies, establish directionality in transport by implementing directed flow-through perfusion, for instance, from the islet to the liver organoid. However, such approaches do not contemplate the return feedback, from the liver to the islet, which is critical in the regulation of energy homeostasis. However, the dual-rOOC platform allows for both, the bi-directional crosstalk between both organs, and the enhanced transport from one organ to the other. This way, it establishes a platform with unique characteristics and benefits to the study of transport kinetics.

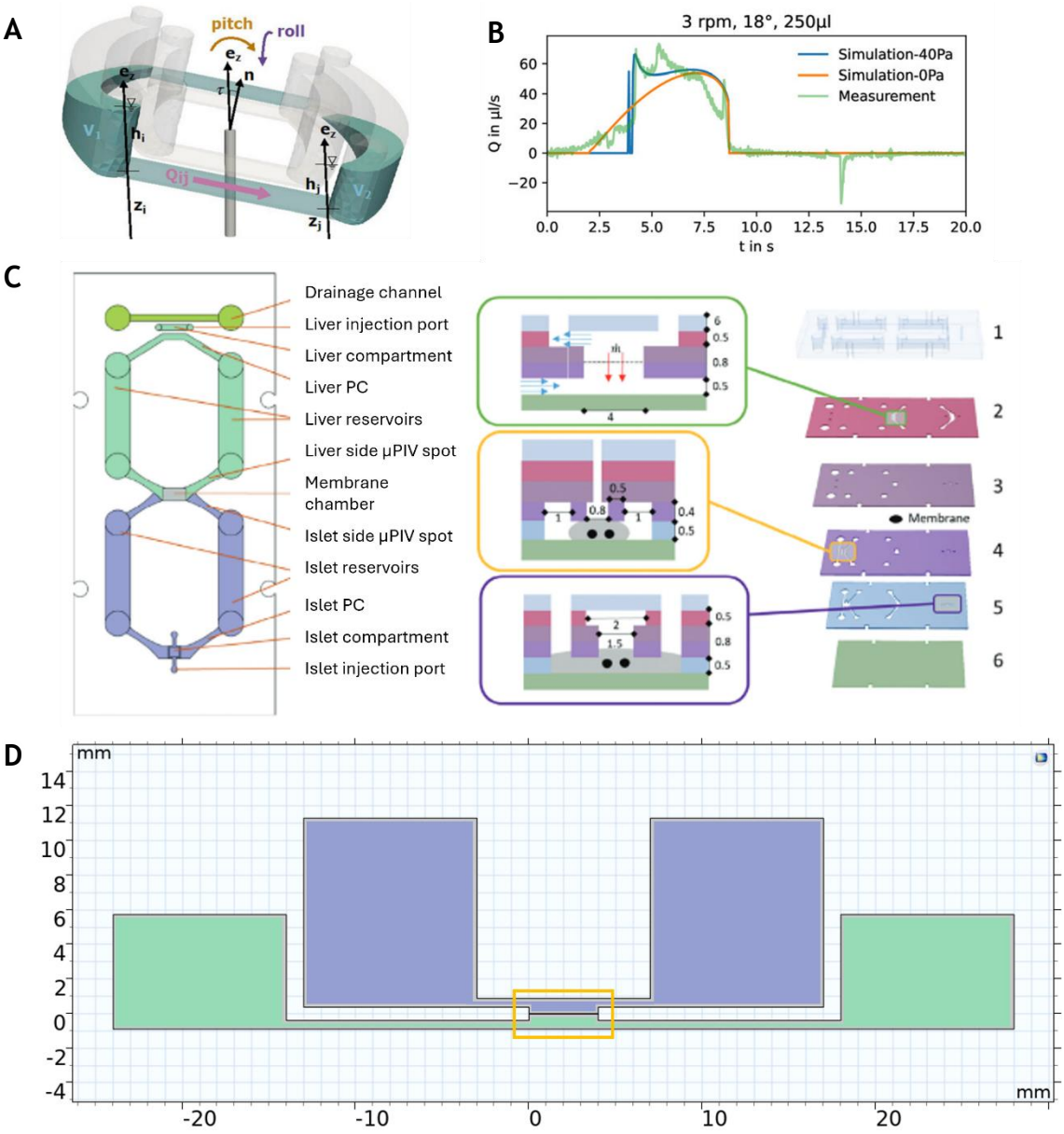

Figure 5.22: Fluidic concept of the rOOC platform and FEM simulation. A, Graphical explanation of the pitching and rolling movement involved in the rOOC platform. B, The characteristic unidirectional, pulsatile flow generated by the rOOC platform, as measured experimentally and simulated. C, The structural layout of the dual-rOOC platform. D, The 2D geometric model employed to numerically simulate the dual-rOOC fluidic and transport dynamics, with the original membrane module highlighted by the yellow box, and both the islet and liver loops highlighted in purple and green respectively. Figures A to B reproduced with permission from Busek et al [210], and C with permission from Aizenshtadt et al [295].

To investigate and explain the enhanced directionality from the top to the bottom loop, tools beyond experimental are advantageous. For this reason, this model was employed and extended to study the particular fluid and transport kinetics of the dual-rOOC platform, and this way explain the transport direction bias. The geometry of the model was therefore extended to simulate the volume of the channels and reservoirs characteristic to the dual-rOOC, as demonstrated in Figure 5.22 D, and expanded to simulate its recirculating, pulsatile fluidic pattern.

5.7.1 Asymmetric, Pulsatile, Phase Shifted Flow

As previously indicated, the pumpless, pulsatile, recirculating flow, characteristic to the rOOC platform, is inherently connected to pitching and rolling, achieved by using a 3D tilting platform. Pitching is the main factor inducing directional gravity-driven flow. By pitching the platform, as illustrated in Figure 5.23 A, flow will be forced downwards to equalize the liquid level between the reservoirs, ultimately displacing the volume of media from one reservoir to the other. This aspect of the concept is similar to that of most platforms employing 2D tilting towards achieving gravity-driven flow. Rolling, however, is what sets the rOOC concept apart, introducing circulating flow. Through continuous rotation, using a 3D tilting platform, flow is perpetually forced into a circular motion, to equalize the liquid height between the unlevelled reservoirs. Additionally, there is a third important component to the rOOC concept, which ensures unidirectionality and prevents backflow. This is the total liquid volume present in each loop. Busek et al 2023 highlights that, to ensure the respective fluidic properties, the total liquid volume present in each loop should be approximately equivalent to the total volume of a single reservoir [212]. This way, as the platform tilts, reservoirs are cyclically, and sequentially, filled and emptied. By doing so, capillary forces, established between the air-liquid interface as the reservoirs empty, prevent backflow and ensure the unidirectionality of flow.

To this set of particular features, the dual-rOOC introduces yet another one. By presenting two individual loops on opposing sides of the device, each with their respective pair of reservoirs, the flow generated at the membrane interface (the only intersecting point between the loops) is not only parallel, resembling this way the *PP* condition, but also asynchronous. As it is possible to see in Figure 5.23 A and B, the flow profiles of respectively the top and bottom loops are significantly different. One of these differences is that the peak maximum flow rate occurs at opposing phases of the rotational cycle which, in this case, is 20 s long. Whereas Figure 5.23 A demonstrates that the flow profile in the top loop peaks at the start

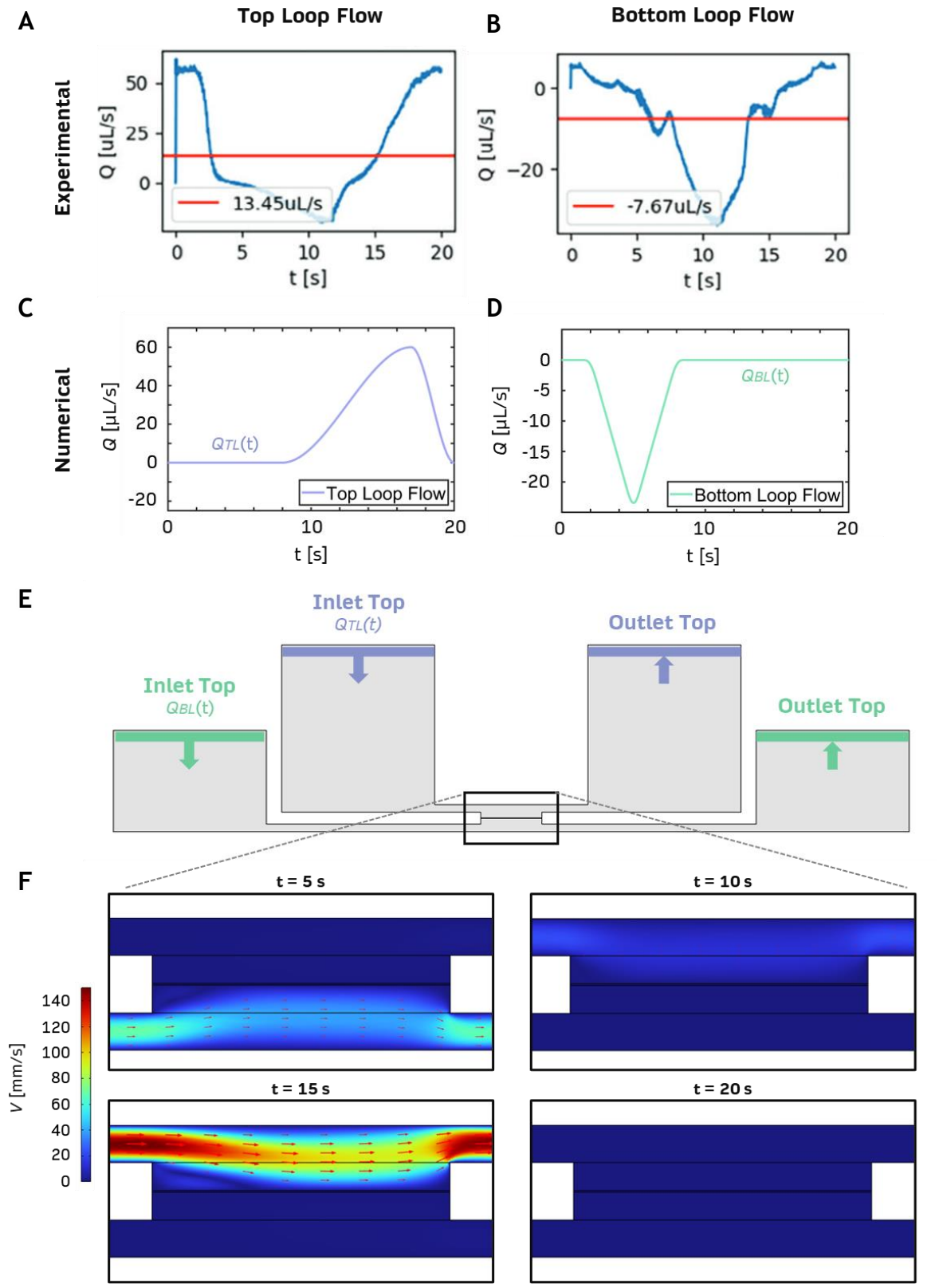

Figure 5.23: Simulation of the asymmetric, pulsatile, phase shifted flow of the rOOC platform. A and B, Flow profile for the top and bottom loops respectively, as measured experimentally. C and D, Single pulse, periodic functions implemented in the COMSOL model to simulate the top and bottom fluidic profiles respectively. E, Geometric model, highlighting the inlets and outlets for both loops, as well as the implemented fluidic functions. F, Discrete time points of an entire tilting cycle, highlighting the simulated fluidic pattern as expressed in the membrane interface. interface.

(t ≈ 0 s) and end (t ≈ 20 s) of the cycle, in the bottom loop this peak occurs at the middle (t ≈ 10 s), as seen in Figure 5.23 B. This is due to the fact that the loops are positioned on opposite sides of the device, which ultimately shifts their phase by approximately 180 degrees. More so, It is also possible to see that the peaks themselves have different magnitudes, the highest intensity being in the top loop. This is in great effect due to the fact that loop volumes are different, being slightly larger at the top (450 µL) than at the bottom (375 µL), which ultimately results in a higher volume displacement per cycle [297]. Finally, It can also be seen that, despite being primarily unidirectional, both fluidic profiles present, nonetheless, some backflow.

To simulate the presented system and respective kinetics using the developed model, several concepts must be implemented. The first one is already contemplated by the model, as the dual-rOOC platform can be effectively described by the *PP* fluidic setup. Therefore, this was the selected fluidic model. Then, the fluidic profiles associated with each channel were individually implemented. As can be observed in Figure 5.23 C and D, periodic, pulsatile functions were manually implemented into the COMSOL model, and respectively attributed to the inlet boundary conditions of each channel, as highlighted in Figure 5.23 E. Higher degree functions, contemplating backflow and the more particular variances of each fluidic profile were explored. However, they consistently prevented the convergence of the model. Instead, simpler functions such as those presented in Figure 5.23 C and D, enabled the model to converge and provided a suitable approximation, by preserving features such as the phase shift and magnitude of the fluidic peak. The time position of the fluidic peaks was, however, phase shifted in their numerical counterparts by 5 s, to ensure that both at the start and end of each cycle the flow rate is equivalent to Q = 0 [uL/s]. Finally, the geometric model was expanded to contemplate the individual volume of each loop, as seen in Figure 5.23 E, therefore presenting a volume equivalent to 450 µL and 375 µL for the top and bottom loops respectively. The resulting fluidic cycle can be observed in Figure 5.23 F, highlighting the phase shift between the two loops, where at t = 5 s flow is highest in the bottom loop, and in turn at t = 15 s in the top loop. Finally, the parameters used to describe the presented system can be found in Table 5.2.

Table 5.2: Geometric parameters used in the dual-rOOC COMSOL model.

Parameter Family	Parameter	Value
Membrane	*P* [%]	11.3
	r [μm]	3
	t_m [μm]	22
Channels	Channel Height [mm]	0.5
	Membrane Chamber Height [mm]	0.9
Loops	Islet (top) Volume [μL]	450
	Liver (Bottom) Volume [μL]	375

5.7.2 Recirculation of Mass and Investigation of Transport Directional Bias

The recirculation of flow is one of the key characteristics of the dual-rOOC platform. This naturally yields that mass recirculates too, which for the presented model implies the redefinition of boundary conditions, particularly those concerning the balance of mass. The continuity equation, as expressed in Equation 6, imposes the conservation of mass. In turn, the advection-diffusion equation, as expressed in Equation 7, asserts the balance between advective and diffusive transport and imposes the existence of a source/sink element, which ensures the conservation of mass whilst allowing its continuous movement. To model the recirculation of mass, however, a third condition must be additionally engaged that satisfies both the advection-diffusion and continuity equations. Therefore, continuous boundary conditions were introduced at the inlets and outlets of the model, as highlighted in Figure 5.24 A, to ensure the continuity of mass from one boundary to the other. These boundaries impose that, any given amount of mass C_2 and C_4, at any given time *t*, crossing the top and bottom outlet boundaries, will be equally compensated at the top and bottom inlet boundaries, where the local

inflow of mass is C_1 and C_3. This way, and as indicated in Figure 5.24 A, it yields that $C_1(t) = C_2(t)$ and $C_3(t) = C_4(t)$.

Maintaining both these conditions together, however, yielded a highly unstable model that was uncappable of converging. To therefore simplify the model and relax its boundary conditions, the model was subdivided into two separate ones, each respectively designated to address the top to bottom and bottom to top transports individually. To do so, the loops were divided into the categories of donor and acceptor. The donor loop acts as the source, providing a fixed concentration, C_0, of a certain diluted molecule. For this loop, the boundary conditions are fixed and relaxed, by not contemplating the recirculation of mass. In turn, the acceptor loop acts as the sink, to which the transport of mass is conducted and, via the continuous boundaries at the inlet and outlet, mass recirculates and accumulates. This ultimately defines that, the model studying the bottom to top transport, assumes the bottom loop as being the donor and the top the acceptor, and therefore $C_1(t) = C_2(t)$ (boundaries and conditions highlighted in blue in Figure 5.24 A). On the other hand, the model studying the top to bottom transport assumes, instead, the top loop as being the donor and the bottom the acceptor, and therefore $C_3(t) = C_4(t)$ (boundaries and conditions highlighted in red in Figure 5.24 A).

Figure 5.24 B presents the finite element generated cross-sectional view of the mass transport dynamics across the membrane interface for each of the models, and therefore, the bottom to top and top to bottom directions respectively. This analysis is extended beyond a single cycle and until a mass equilibrium is found between both channels, as the mass concentration in the acceptor channel reaches $C_n = 1$. This way, beyond demonstrating the mass concentration distribution at $t = 5$ s and $t = 15$ s, it is also possible to observe its evolution as concentration approximates an equilibrium, at $t = 2015$ s for cycle 301. Whereas the top row of panels in Figure 5.24 B illustrates the evolution for the bottom to top transport, the bottom row illustrates the top to bottom direction. Finally, Figure 5.24 C allows to compare the mass concentration distribution panels with their respective fluidic phase. The presented panels are important to fundament the direction bias experienced in the dual-rOOC platform. As it is possible to observe, at $t = 5$ s, the bottom channel is experiencing peak pulse flow, which therefore results in the transport of mass (top, left panel Figure 5.24 B), or the

repelling of it (bottom, left panel Figure 5.24 B), from the bottom channel to the top. A similar but opposite reaction will occur at t = 15 s, as the top channel experiences peak pulse flow and therefore forces the transport of mass (top, middle panel Figure 5.24 B), or repels it (bottom, middle panel Figure 5.24 B), from the top channel to the bottom. However, this reaction happens with greater magnitude, induced by the higher flow rate (middle panel Figure 5.24 C) and pressure of the top channel, and therefore resulting in a bigger mass displacement. Ultimately, this profile provides the transport bias, as it is seen in the right panels of Figure 5.24 B, as the concentration in the acceptor channel is highest and closer to the equilibrium at t = 2015 s for the top to bottom direction. This defines a system where mass transport is primarily convection driven. The *Pe* number identifies this aspect well. The *Pe* value measured for the dual-rOOC platform is considerably high, at *Pe* = 210 000, especially when compared to traditional microfluidic platforms (*Pe* $\approx$ 100), this way evidencing the dominant influence of convection for mass transport. A similarly high *Re*, at *Re* = 181.04, denotes a higher influence of inertial forces. However, its value is still well within the laminar range (*Re* $\ll$ 4000), this way discarding any possibility of forces such as gravity of contributing to the top to bottom transport directional bias.

The *in silico* experiments presented in Figure 5.24 B and C were performed by simulating the diluted molecule as being glucose, with $D = 6x10^{-10}$ [m^2/s] [323]. These experiments were performed for a total simulated duration of 60 [min] (3600 [s]). Similar *in-silico* experiments were also performed by simulating insulin instead of glucose, and therefore, changing the diffusion coefficient to $D = 1.5x\ 10^{-10}$ [m^2/s] [323]. Both these simulations intended to support and fundament experimental data obtained for the same conditions, using the dual-rOOC chip with both glucose and insulin for the period of 60 [min], and by sampling data every 5 [min]. The evolution of C_n is displayed as a function of time for both glucose and insulin in Figure 5.24 D and E respectively. Additionally, a regression model was also plotted, based on the ordinary differential equation for the mass flow defined in equation 6 of Aizenshtadt et al 2024 [297]. Ultimately it is possible to observe a great affinity between the numerical data, in dashed lines, the regression model, in continuous line, and the experimental results, in discrete crosses, characterizing both top to bottom, in red, and bottom to top transport, in blue, using the dual-rOOC platform.

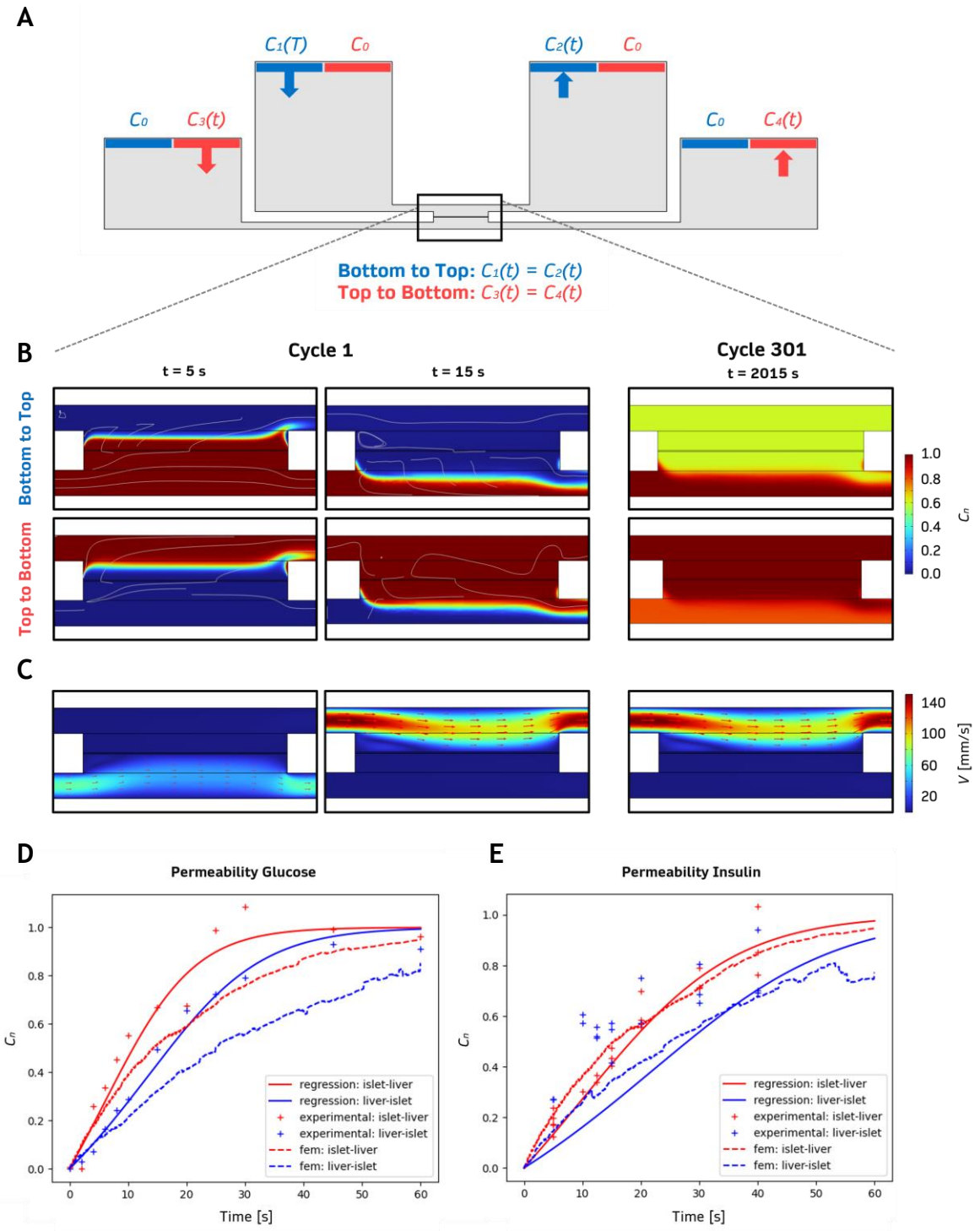

Figure 5.24: Simulation of mass recirculation and investigation of the directionality bias in the rOOC platform. A, Geometric model, highlighting the continuous boundary conditions for mass recirculation, *C(t)*, and the fixed conditions, C_0, for both bottom to top, in blue, and top to bottom, in red, transport. B, Panels demonstrating the mass concentration distribution at the membrane interface, as a function of time, for t = 5 s, t = 15 s and t = 2015 s, and as a function of transport direction, the top row being for the bottom to top and the bottom row for the top to bottom transport. C, Panels illustrating the fluidic phase associated with each of the previous time frames. D and E, *Cn* plotted as a function of time, for a duration of 60 [min], displaying good affinity between the data obtained via experimental testing, discrete crosses, regression model, continuous line, and numerical model, dashed line, for both the top to bottom, in red, and bottom to top, in blue, direction.

5.8 Conclusions

A finite element model of a microfluidic bilayer device with integrated porous membrane has been established, providing extensive knowledge on the correlation between membrane integration parameters and resulting fluid dynamics and mass transport. The respective model enabled the development of a large-scale, systematic study, where eight distinct parameters, related to membrane, geometry, flow, and diffusion properties were individually analysed. At the same time, four different fluidic conditions were, in parallel, tested, this way addressing a wider range of microfluidic architectures. All these parameters were then studied in relation to four distinct response variables, characterizing the steady state fluid flow, wall shear stress, and concentration distribution, as well as the transient convective-diffusive mass transport. The obtained results provide a comprehensive analysis, with design guidelines for membrane integration in OOC and microfluidic applications.

On-chip experiments were further carried out, providing fluorescent and biological evidence in support of the obtained numerical data. An experimental platform and protocol were developed to replicate PP_{SD} and analyse the transport of molecules across the membrane as a function of both membrane parameters, namely r and P, and flow properties, Q_{in}. Experiments with fluorescein evidenced a mainly convection-driven permeability, with Q_{in} displaying a dominant role over both r and P, whose control over ssC_{nCC} was limited. A similar trend was seen with the transport of Cytochalasin D, whose actin-disruptive effect, quantified by the angular second moment as a measure of cell retraction, manifested the dominant role of Q_{in} in controlling porous transport of Cytochalasin D and defining ssC_{nCC}. By verifying the same trends as numerically predicted, both experiments, fluorescent and biological, ultimately demonstrated the experimental significance of the provided numerical data.

The model was furthermore used to simulate a novel platform with a unique fluidic concept, to explain and characterize the similarly distinct kinetics of transport it generates. This system, designated as dual-rOOC, employs large reservoirs, closed in a microfluidic loop with an integrated porous membrane, and 3D tilting to obtain gravity-driven, recirculating, pulsatile flow. Not only does it display a unique fluidic behaviour, but also, it leads to bidirectional mass transport across

the membrane, with a bias from the top to the bottom loop. By extending the developed model to integrate and simulate the unique features of the dual-rOOC platform, such as its particular fluidic profile and recirculation of both media and mass, it was possible to investigate the respective kinetics influencing the mass transport bias across the membrane. It was observed that the increased volume of the top loop generated higher magnitude pulsed flows, which ultimately contributed to the greater transport of mass in the top to bottom direction, in a platform presenting convection-driven mixing, as expressed by high *Pe* and *Re* numbers. More so, permeability characterization using both glucose and insulin were performed numerically and provided data in great agreement with both a regression model and experimental data.

As a concluding reflection, it is crucial to realise the influence played by confluent tissue barriers in further shaping both the fluidic and mass transport dynamics within microfluidic bilayer devices with integrated porous membranes. By adopting an electrical circuit analogy, it is possible to defer that the permeability of a tissue barrier formed on a membrane, K, is the combined result of both the diffusive permeability of the tissue barrier, K_{tb}, and of the membrane, K_m [254]. The respective relationship can be expressed by the following expression:

$$\frac{1}{K} = \frac{1}{K_{tb}} + \frac{1}{K_m} \tag{13}$$

The implications of Equation 13 can be further appreciated through the work of Frost et al. 2019 [324], where the permeability of a microfluidic bilayer device was measured, using several different molecules, for a membrane with and without a confluent tissue barrier model. Not only does this work demonstrates the similarities between the permeability behaviours of each model, but also, the necessity of knowing the individual contributions of both the membrane and the tissue barrier. It highlights that the design of a specific membrane platform should contemplate the contributions of each, towards ensuring accurate biochemical outputs. Membrane properties should also be considered regarding the cell behaviour and migration patterns they might induce and should be selected appropriately.

Finally, it is important to highlight the usage of hydrogel matrices which, combined with microfluidics, has generated wide interest. It is appreciated that, when it comes to replicating biological tissue constructs, the elasticity and 3D porous networks of hydrogels prove desirable for tissue emulation [325]. However, contrary to porous membranes, whose physics are extensively characterized and well established, hydrogel matrices can be notoriously unpredictable, due to their dynamic, irregular properties. Nonetheless, tortuosity models, and more noticeably, the Millington and Quark and Bruggeman models, have been growing as accurate models to predict hydrogel dynamics. Therefore, an effective diffusivity, such as the one described in Equation 8, can be calculated to describe the motion of a specific molecule more accurately within a certain hydrogel. Ultimately, it follows that the data here presented can be translated into hydrogels, by applying a tortuosity model and resulting diffusion factor.

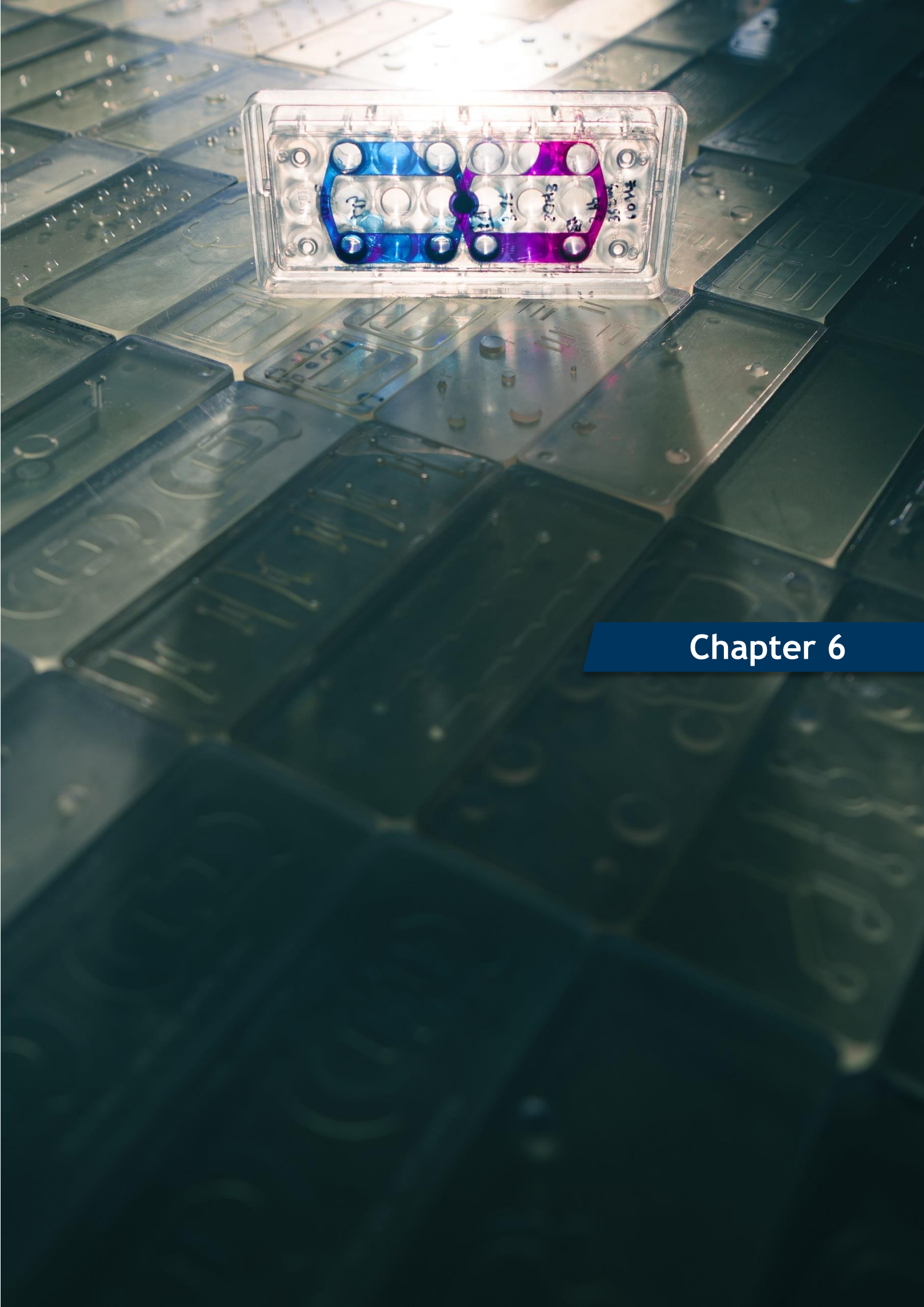

Chapter 6

6 Conclusions and Future Work

6.1 Summary and Concluding Remarks

This thesis set out to develop a novel design cycle for polystyrene-based microfluidic devices, using injection moulding and 3D printing as the two overarching technologies. To do so, the project encompassed the fabrication, integration and simulation of the respective devices, according to which, three primary research goals were set, as stated in Section 1.2.1 To evaluate the success of this thesis in meeting its research objectives, each statement will here be recapitulated and discussed, according to the work achieved.

6.1.1 Success in Meeting the Goals of Research Statement One

The first research statement was:

> *"Explore 3D printing and injection moulding towards defining a protocol capable of fabricating polystyrene-based microfluidic devices of high optical quality and feature resolution, with high cost-efficiency, short lead production times and high scalability."*

Chapter 3 addressed this topic by reporting the development of a novel RT protocol. It first consisted of exploring state-of-the-art RT setups, based on traditional SLA technology, and comparing their performance with LCD 3D printing. The latter were observed to provide higher feature resolution, greater geometric accuracy, and improved surface quality in the fabrication of microfluidic tooling. Further investigation on LCD 3D printing uncovered important parameters. First, the influence of material selection in determining the side wall waviness, interlocking angle and deflection properties of the printed tooling, ultimately defining mould release and tool life during injection moulding. Second, the impact of layer exposure in regulating, not only feature resolution and dimensional accuracy, but also the surface properties of the tooling and resulting optical transparency of the injection moulded devices. And third, the effect of post-processing parameters in determining the mechanical properties of 3D printed tooling, and the influence of design parameters, such as orientation and draft, in determining feature reproducibility and durability.

The developed protocol enabled fabricating microfluidic polystyrene devices with 50 µm features and optical transparency close to that of glass, as measured by a line amplitude and contrast of 47.6 ± 5.3 grey scale/mm and 169.0 ± 1.6 grey scale respectively. These results answer the first goal of the research statement above. Then, three different microfluidic devices, a maze, a mixer and a droplet generator were fabricated. By presenting different levels of geometrical complexity, with a turnaround time from CAD to a fully functional device of only 159 min (2 h 39 min), and from CAD to 500 replicas of 504 min (8 h 04 min), the unique potential of the current RT procedure to achieve rapid prototyping and scalable manufacturing is highlighted. More so, with each mould coming at a value of just £1, the low fabrication costs associated with the RT procedure are demonstrated. Therefore, the goals encompassed by the research statement expressed above were shown to be successfully met.

6.1.2 Success in Meeting the Goals of Research Statement Two

The second research statement was:

> *"Investigate and optimize bonding strategies to define scalable, high-quality seals for microfluidic channels and porous membranes. Develop easy to use fluidic interfacing approaches, compatible with scalable manufacturing and different modes of fluidic perfusion. Develop dynamic fluidic valving technology, capable of seamless integration into rigid, polystyrene-based microfluidic substrates, and with proven performance."*

Chapter 4 addressed microfluidic integration, which began by investigating adhesive layer strategies, ultrasonic welding and thermal fusion in bonding microfluidic channels and porous membranes. Regarding channel bonding, thermal fusion was observed to be the most promising technology, delivering high quality seals, with little to no channel deformation, highly reliable results and great surface quality, in a scalable manner. These results were obtained after process optimization, defining T_{TF} = 78 ºC, P_{TF} = 35.7 bar, and t_{TF} = 20 min, and by integrating carrier layers, made of PC and acrylic, to protect the microfluidic surfaces from direct contact with the heat plates. In turn, for porous membrane bonding, both thermal fusion and ultrasonic welding were observed as highly promising approaches. Ultrasonic welding was most suited to bond PETE-TE

membranes, requiring no additional surface treatments, and being capable of stretching the surface of the membrane to a surface deflection of only 22.8 ± 9.7 µm, for E_{USW} = 160 Ws. Instead, thermal fusion provided better results for the PS-ES membranes, delivering reliable, high-quality seals, with little to no surface deformation, and while preserving the structural integrity of the fibrous network of the membrane. By providing two scalable technologies, capable of bonding a range of different substrates and materials, the first goal of the research statement expressed above was met.

Furthermore, pressure-driven microfluidics was achieved in the presented platform by using laser cut Luer connectors complemented by 3D printed soft inserts. This solution was capable of establishing a tight, reversible seal with fluidic tubing, via push-fit, being this way extremely easy to use. It is also possible to batch fabricate the connectors and soft inserts which, by using double-sided tape, are equally easy to attach to the microfluidic devices. While these interconnects solved pressure-driven flow, the integration of an injection moulded 96-well plate, adapted to the size of the microfluidic chips, provided a solution to gravity-driven flow. By using the wells as reservoirs, it was possible to obtain bi-directional flow and briefly study the properties of the resulting fluidic profile. By using 3D printed soft fluidic plugs, the well plate interface was further shown to be capable of integrating both gravity- and pressure-driven fluidics. This way, this work answers the second goal of the research statement. It lacks, however, in providing a more quantitative analysis to benchmark the developed approaches against existing technologies through, for instance, parameters such as bursting pressure.

Finally, an approach to plug-and-play dynamic valving was developed by exploring elastomer prepolymer resins. A new protocol based on spin-coating and single layer masked UV exposure was developed and characterized in the fabrication of elastic membranes with controlled thickness. Soft pneumatic plugs, manufactured via 3D printing, then provided the supporting structure to the membranes, and enable their easy integration into the microfluidic environment. By connecting the plugs and membrane to an electro-pneumatic system, it was possible to investigate membrane deflection and long-term durability as a function of pneumatic pressure and physical properties, such as membrane diameter and thickness. Using the presented protocol, it was possible to achieve extremely thin

membranes, with a thickness of 8.6 ± 2.1 μm, capable of high elastic properties, with δ_{Mmax} = 4.16 ± 0.77 mm, and proven long-term durability. The functionality of the respective elastic membranes for fluidic switching was also experimentally verified. More so, their ability to perform functions beyond binary switching, such as dynamic control over concentration gradient generation, was demonstrated by regulating the applied P_{air}. By characterizing both the mechanical properties and valving performance of the developed membranes, the presented work meets the criteria expressed by the research statement above.

Nevertheless, data variability, particularly on the maximum deflection as a function of membrane properties, suggest the necessity of deeper investigation towards normalizing the results. More so, a more comprehensive study over membrane durability according to different physical properties could prove essential for applications involving long-term mechanical loading. Finally, regarding valving performance, it would be relevant to test fast fluidic switching and benchmark the minimum switching time between the on and off states, as a function of changes in the flow of media, against state-of-the-art technologies.

6.1.3 Success in Meeting the Goals of Research Statement Three

The third research statement was:

> *"Use FEM software to simulate and characterize the kinetics of flow and transport across porous membranes in microfluidic bilayer devices, and highlight the experimental relevance of the developed numerical model in the context of microfluidic and OOC applications."*

Chapter 5 addressed this subject by establishing an FEM model based on COMSOL Multiphysics software to simulate the fluid and transport kinetics of microfluidic bilayer devices with integrated porous membranes. By making the model parametric, relevant process parameters associated to membrane properties, channel geometry, microfluidic layout, fluidic and diffusive properties, were systematically studied in relation to flow rate, shear stress, transient transport and steady state concentration. To do so, extensive data was collected and further organized according to their hierarchical influence, providing comprehensive

design guidelines for porous membrane integration in microfluidic and OOC applications.

From the various described regulatory pathways, the predominant influence of Q_{in} in determining the steady state molecular concentration, ssC_{nCC}, in bilayer microfluidic devices with parallel flow, which is the most common microfluidic setup, was highlighted. Surprisingly, membrane permeability properties, such as *P* and *r*, presented, by comparison, a much lesser role in regulating the kinetics of molecular transport. This presents one of the many guidelines provided by the developed study, whose implications to molecular transport and cell culture were further verified experimentally. First, permeability tests with fluorescein supported the numerical data, by verifying the limited effect of *r* in regulating molecular transport which, in turn, was approximately multiplied by a factor of 5 when changing from Q_{in} = 100 to Q_{in} = 10 µL/h. The biological implications of this phenomenon were further demonstrated by investigating the transport of Cytochalasin D, whose disruptive effect on cells evidenced the predominant effect of Q_{in} in determining molecular transport across the membrane. Not only did these results provide validation to the developed FEM model, but also, they evidenced the experimental significance of the obtained numerical data, for both microfluidic and OOC applications. This way, the goals encompassed by the research statement expressed above were shown to be successfully met.

The presented membrane model was applied to simulate and characterize further microfluidic concepts. This involved the investigation of the unique transport kinetics originating from recirculating, gravity-driven flow. This way, the model was expanded to contemplate the integration of media reservoirs, and mimic the unique fluidic profile of the rOOC platform. This meant implementing recirculating, asymmetric, phase shifted flow. The recirculation of media further involves the recirculation of mass which meant adding continuous boundary conditions that satisfy the balance of mass to the existing model. The upgraded model allowed the investigation of flow and transport characteristic to the rOOC platform, and helped characterizing its kinetics as being highly driven by convection. The numerical data obtained for the permeability with both glucose and insulin supported experimental results and helped explaining the observed bias in molecular transport in the rOOC platform. Ultimately, it was the respective bias, explained by the FEM model, defining enhanced transport from top to bottom

while still enabling bi-directional crosstalk across the membrane, that helped defining a platform capable of reproducing key aspects of the metabolic crosstalk between sc derived liver and islet organoids. By undertaking this project, the described work provides further evidence to support the relevance of the developed FEM-based membrane model in contributing to the design and development of microfluidic and OOC applications.

6.2 Limitations and Future Work

Despite meeting the overall criteria and overarching research goals set at the start of the thesis, the presented body of work has some limitations which will be briefly discussed in the following and further connected to future suggested work.

It is first highlighted that the achieved performance with the RT procedure developed in Chapter 3 on feature resolution, surface quality, and overall durability, are tightly connected to, and limited by, the 3D printing machine employed for mould fabrication. Therefore, it is suggested that novel 3D printing systems and resin materials, that might become available in the future, may be integrated and explored with the presented RT protocol, to continuously upgrade its properties and progressively increase the quality of the developed microfluidic tooling. This is particularly relevant given the rapidly evolving market of 3D printing technology, which encompasses, as well, LCD systems.

In Chapter 4, a limitation of the presented work is the absence of a more quantitative analysis benchmarking the strategies for fluidic interfacing and channel bonding. As highlighted by the literature review in Section 2.2.2, most approaches to fluidic interfacing are described using bursting pressure as an important parameter to benchmark the performance of the seal and its ability to retain pressure. Therefore, in the interest of defining a reliable fluidic interconnect with an identified range of operating pressures, the characterization of bursting pressure presents an important parameter. However, in the presented thesis, fluidic interfacing was primarily investigated as the means to serve different developed microfluidic applications, and not as the main end goal of research. For this reason, deeper characterization of fluidic interconnects was not seen as a productive nor relevant aspect.

Given the value of the developed Luer interconnects in providing an easy, reliable, and reversible connection to tubing, a further suggestion is their integration directly into the injection moulding tooling. This way, chips could be manufactured with standardized fluidic interconnects from the start. Not only would this reduce the amount of procedures involved in the integration of microfluidic devices, but also, it would systematize fluidic interfacing and potentially provide a stronger and more secure fit. Therefore, the investigation of this approach is suggested for future work.

Despite the robust body of work present in Chapter 4 in characterizing channel bonding, the analysis is primarily qualitative. In turn, literature commonly employs bonding strength as a popular parameter to benchmark different sealing technologies and protocols. Therefore, in the interest of providing a more quantitative analysis on the strategies and technologies implemented for bonding, the analysis of parameters such as the bonding strength are suggested for future work. Beyond benchmarking, this parameter is also very useful for microfluidic applications and in particular OOC, where the analysis of cells directly on their substrate of culture is often a desired feature. For this reason, characterizing bonding strength and investigating the compatibility of the bonded devices to being delaminated post culture of cells, is a parameter of great interest for potential applications.

Chapter 5 provided extensive work on the characterization of microfluidic bilayer devices with integrated porous membranes. The obtained data was further explored and evaluated through various different angles, having been further corroborated with experimental data. As part of the concluding remarks, in Section 0, it was mentioned that the presented results can be similarly translated to hydrogel matrices by applying a tortuosity model and resulting diffusion factor. For this reason, it would also be valuable to apply the developed model in the simulation of the transport kinetics of devices containing hydrogel and, this way, corroborate the proposed approach with experimental data and extend the functionality of the model.

Ultimately, while leaving room for further research, the work performed during this PhD enabled the upscaling of microfluidic and OOC technology to small production series, with compatible solutions for integration and well-described

microfluidic environments. This progress is already sparking interest amongst research and industry partners. In the long term, the procedures and protocols developed are expected to support the broader dissemination of microfluidic technology across science and industry, and advance research in the biomedical field, particularly in OOC.

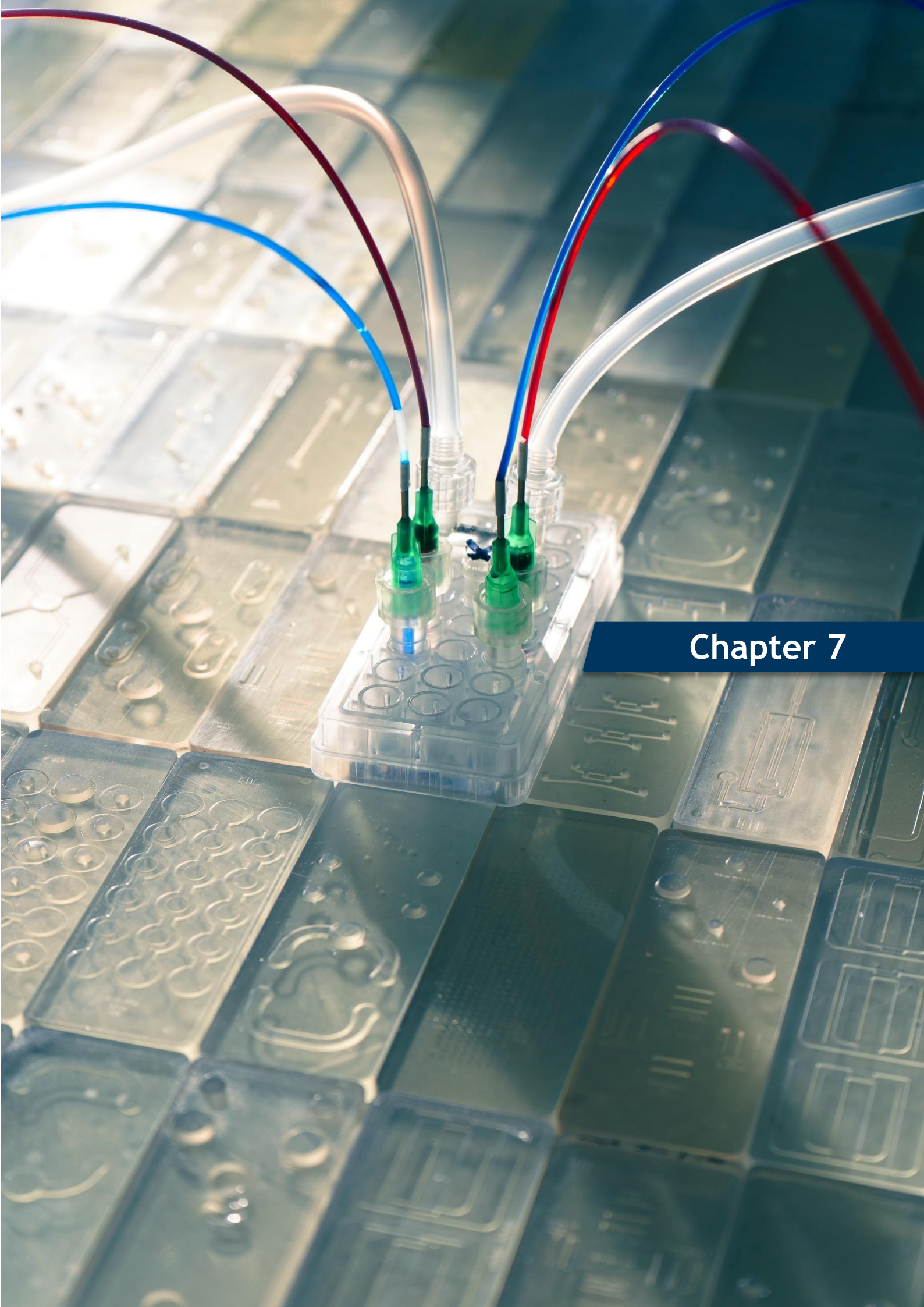
Chapter 7

References

1. Gravesen, P., J. Branebjerg, and O.S. Jensen, *Microfluidics-a review.* Journal of Micromechanics and Microengineering, 1993. **3**(4): p. 168.
2. Niculescu, A.-G., et al., *Fabrication and Applications of Microfluidic Devices: A Review.* International Journal of Molecular Sciences, 2021. **22**(4): p. 2011.
3. Whitesides, G.M., *The origins and the future of microfluidics.* Nature, 2006. **442**(7101): p. 368-73.
4. Nguyen, N.-T., S.T. Wereley, and S.A.M. Shaegh, *Fundamentals and applications of microfluidics*. 2019: Artech house.
5. Sackmann, E.K., A.L. Fulton, and D.J. Beebe, *The present and future role of microfluidics in biomedical research.* Nature, 2014. **507**(7491): p. 181-9.
6. Tabeling, P., *Introduction to microfluidics*. 2023: Oxford university press.
7. Research, G.V. *GVR Report cover Microfluidics Market Size, Share & Trends Analysis Report By Application (Medical/Healthcare, Non-Medical), By Material (Silicon, Glass), By Technology, By Region, And Segment Forecasts, 2024 - 2030.* [cited 2024 19/10]; Available from: https://www.grandviewresearch.com/industry-analysis/microfluidics-market.
8. Hajam, M.I. and M.M. Khan, *Microfluidics: a concise review of the history, principles, design, applications, and future outlook.* Biomaterials Science, 2024. **12**(2): p. 218-251.
9. Feynman, R., *There's plenty of room at the bottom.* Resonance: Journal of Science Education, 2011. **16**(9).
10. Kilby, J.S., *Miniaturized electronic circuits [US Patent no. 3,138, 743].* IEEE Solid-State Circuits Society Newsletter, 2007. **12**(2): p. 44-54.
11. Algamili, A.S., et al., *A Review of Actuation and Sensing Mechanisms in MEMS-Based Sensor Devices.* Nanoscale Research Letters, 2021. **16**(1): p. 16.
12. Bogue, R., *Recent developments in MEMS sensors: a review of applications, markets and technologies.* Sensor Review, 2013. **33**(4): p. 300-304.
13. Terry, S.C., J.H. Jerman, and J.B. Angell, *A gas chromatographic air analyzer fabricated on a silicon wafer.* IEEE transactions on electron devices, 1979. **26**(12): p. 1880-1886.
14. Convery, N. and N. Gadegaard, *30 years of microfluidics.* Micro and Nano Engineering, 2019. **2**: p. 76-91.
15. Harrison, D.J., et al., *Capillary electrophoresis and sample injection systems integrated on a planar glass chip.* Analytical chemistry, 1992. **64**(17): p. 1926-1932.
16. Vowell, S., *Microfluidics Effects of Surface Tension.* Recovered from, 2009.
17. Chakraborty, D. and S. Chakraborty, *Microfluidic Transport and Micro-scale Flow Physics: An Overview*, in *Microfluidics and Microfabrication*, S. Chakraborty, Editor. 2010, Springer US: Boston, MA. p. 1-85.
18. Folch, A. *Microfluidics: The tiny, beautiful tech hidden all around you*. 2021 [cited 2025 27/01]; Available from: https://theconversation.com/microfluidics-the-tiny-beautiful-tech-hidden-all-around-you-160436.

19. Wu, L., Z. Guo, and W. Liu, *Surface behaviors of droplet manipulation in microfluidics devices.* Advances in Colloid and Interface Science, 2022. **308**: p. 102770.
20. Mazutis, L., et al., *Single-cell analysis and sorting using droplet-based microfluidics.* Nature protocols, 2013. **8**(5): p. 870-891.
21. Kaushik, A.M., K. Hsieh, and T.H. Wang, *Droplet microfluidics for high-sensitivity and high-throughput detection and screening of disease biomarkers.* Wiley Interdiscip Rev Nanomed Nanobiotechnol, 2018. **10**(6): p. e1522.
22. Kim, Y.G., S. Park, and S.-H. Kim, *Designing photonic microparticles with droplet microfluidics.* Chemical Communications, 2022. **58**(74): p. 10303-10328.
23. Filatov, N.A., et al., *Open-Source Pressure Controller Based on Compact Electro-Pneumatic Regulators for Droplet Microfluidics Applications.* IEEE Transactions on Instrumentation and Measurement, 2022. **71**: p. 1-10.
24. Sachdeva, S., R.W. Davis, and A.K. Saha, *Microfluidic Point-of-Care Testing: Commercial Landscape and Future Directions.* Frontiers in Bioengineering and Biotechnology, 2021. **8**.
25. Yum, S.I. and J. Roe, *Capillary blood sampling for self-monitoring of blood glucose.* Diabetes Technology & Therapeutics, 1999. **1**(1): p. 29-37.
26. Tayyab, M., et al., *Potential Microfluidic Devices for COVID-19 Antibody Detection at Point-of-Care (POC): A Review.* IEEE Sensors Journal, 2021. **21**(4): p. 4007-4017.
27. Cate, D.M., et al., *Recent Developments in Paper-Based Microfluidic Devices.* Analytical Chemistry, 2015. **87**(1): p. 19-41.
28. Madou, M. and C. Wang, *Photolithography*, in *Encyclopedia of Nanotechnology*, B. Bhushan, Editor. 2012, Springer Netherlands: Dordrecht. p. 2051-2060.
29. Nishimura, Y., et al., *Photolithography*, in *Flat Panel Display Manufacturing*. 2018. p. 287-310.
30. Lorenz, H., et al., *High-aspect-ratio, ultrathick, negative-tone near-UV photoresist and its applications for MEMS.* Sensors and Actuators A: Physical, 1998. **64**(1): p. 33-39.
31. Sato, H., et al., *An all SU-8 microfluidic chip with built-in 3D fine microstructures.* Journal of Micromechanics and Microengineering, 2006. **16**(11): p. 2318.
32. Nielsen, J.B., et al., *Microfluidics: Innovations in Materials and Their Fabrication and Functionalization.* Analytical Chemistry, 2020. **92**(1): p. 150-168.
33. Ahrberg, C., et al., *Plasmonic heating-based portable digital PCR system.* Lab on a Chip, 2020. **20**: p. 3560-3568.
34. Bakhshpour-Yucel, M., et al., *Highly-Sensitive, Label-Free Detection of Microorganisms and Viruses via Interferometric Reflectance Imaging Sensor.* Micromachines (Basel), 2023. **14**(2).
35. Ocvirk, G., et al., *High-performance liquid-chromatography partially integrated onto a silicon chip.* Analytical Methods and Instrumentation, 1995. **2**(2): p. 74-82.
36. Sackmann, E.K., A.L. Fulton, and D.J. Beebe, *The present and future role of microfluidics in biomedical research.* Nature, 2014. **507**(7491): p. 181-189.
37. Martins, J.P., G. Torrieri, and H.A. Santos, *The importance of microfluidics for the preparation of nanoparticles as advanced drug*

delivery systems. Expert Opinion on Drug Delivery, 2018. **15**(5): p. 469-479.
38. Ren, K., J. Zhou, and H. Wu, *Materials for microfluidic chip fabrication.* Acc Chem Res, 2013. **46**(11): p. 2396-406.
39. Shakeri, A., et al., *Biofunctionalization of Glass- and Paper-Based Microfluidic Devices: A Review.* Advanced Materials Interfaces, 2019. **6**(19): p. 1900940.
40. McDonald, J.C., et al., *Fabrication of microfluidic systems in poly(dimethylsiloxane).* ELECTROPHORESIS, 2000. **21**(1): p. 27-40.
41. Xia, Y. and G.M. Whitesides, *SOFT LITHOGRAPHY.* Annual Review of Materials Science, 1998. **28**(1): p. 153-184.
42. Lin, L. and C.-K. Chung, *PDMS microfabrication and design for microfluidics and sustainable energy application.* Micromachines, 2021. **12**(11): p. 1350.
43. Thorsen, T., S.J. Maerkl, and S.R. Quake, *Microfluidic large-scale integration.* Science, 2002. **298**(5593): p. 580-584.
44. Borók, A., K. Laboda, and A. Bonyár, *PDMS bonding technologies for microfluidic applications: A review.* Biosensors, 2021. **11**(8): p. 292.
45. Zhou, J., et al., *Surface modification for PDMS-based microfluidic devices.* Electrophoresis, 2012. **33**(1): p. 89-104.
46. Banik, S., et al., *The revolution of PDMS microfluidics in cellular biology.* Critical Reviews in Biotechnology, 2023. **43**(3): p. 465-483.
47. McDonald, J.C. and G.M. Whitesides, *Poly(dimethylsiloxane) as a Material for Fabricating Microfluidic Devices.* Accounts of Chemical Research, 2002. **35**(7): p. 491-499.
48. McDonald, J.C., et al., *Fabrication of microfluidic systems in poly (dimethylsiloxane).* ELECTROPHORESIS: An International Journal, 2000. **21**(1): p. 27-40.
49. de Visser, S. and H. Truebel, *Chapter 18 - The pharmaceutical research and development productivity crisis: can exploratory clinical studies be of any help?*, in *Principles of Translational Science in Medicine (Third Edition)*, M. Wehling, Editor. 2021, Academic Press: Boston. p. 239-245.
50. Plenge, R.M., *Disciplined approach to drug discovery and early development.* Sci Transl Med, 2016. **8**(349): p. 349ps15.
51. Scannell, J.W., et al., *Diagnosing the decline in pharmaceutical R&D efficiency.* Nature Reviews Drug Discovery, 2012. **11**(3): p. 191-200.
52. Laermann-Nguyen, U. and M. Backfisch, *Innovation crisis in the pharmaceutical industry? A survey.* SN Business & Economics, 2021. **1**(12): p. 164.
53. DiMasi, J.A., et al., *Trends in risks associated with new drug development: success rates for investigational drugs.* Clin Pharmacol Ther, 2010. **87**(3): p. 272-7.
54. Yan, J., et al., *Organ-on-a-chip: A new tool for in vitro research.* Biosensors and Bioelectronics, 2022. **216**: p. 114626.
55. Ronaldson-Bouchard, K. and G. Vunjak-Novakovic, *Organs-on-a-Chip: A Fast Track for Engineered Human Tissues in Drug Development.* Cell Stem Cell, 2018. **22**(3): p. 310-324.
56. Delon, L.C., et al., *Hele Shaw microfluidic device: A new tool for systematic investigation into the effect of the fluid shear stress for organs-on-chips.* MethodsX, 2020. **7**: p. 100980.
57. Zhang, J., et al., *Stem cell culture and differentiation in microfluidic devices toward organ-on-a-chip.* Future science OA, 2017. **3**(2): p. FSO187.

58. Ergir, E., et al., *Small force, big impact: Next generation organ-on-a-chip systems incorporating biomechanical cues.* Frontiers in physiology, 2018. **9**: p. 1417.
59. Sala, F., et al., *Microfluidic lab-on-a-chip for studies of cell migration under spatial confinement.* Biosensors, 2022. **12**(8): p. 604.
60. Corral-Nájera, K., et al., *Polymeric and biological membranes for organ-on-a-chip devices.* Microsystems & Nanoengineering, 2023. **9**(1): p. 107.
61. Francis, I., et al., *Recent advances in lung-on-a-chip models.* Drug Discovery Today, 2022. **27**(9): p. 2593-2602.
62. Onal, S., M.M. Alkaisi, and V. Nock, *A Flexible Microdevice for Mechanical Cell Stimulation and Compression in Microfluidic Settings.* Frontiers in Physics, 2021. **9**.
63. Ni, L., et al., *A microfluidic device for noninvasive cell electrical stimulation and extracellular field potential analysis.* Biomedical Microdevices, 2019. **21**: p. 1-12.
64. Ferrari, E., et al., *Integrating biosensors in organs-on-chip devices: A perspective on current strategies to monitor microphysiological systems.* Biosensors, 2020. **10**(9): p. 110.
65. Huh, D., et al., *Reconstituting organ-level lung functions on a chip.* Science, 2010. **328**(5986): p. 1662-8.
66. Fernández-Costa, J.M., et al., *Training-on-a-chip: a multi-organ device to study the effect of muscle exercise on insulin secretion in vitro.* Advanced Materials Technologies, 2023. **8**(7): p. 2200873.
67. Mansoorifar, A., et al., *Bone-on-a-chip: microfluidic technologies and microphysiologic models of bone tissue.* Advanced functional materials, 2021. **31**(6): p. 2006796.
68. Rogal, J., et al., *WAT-on-a-chip integrating human mature white adipocytes for mechanistic research and pharmaceutical applications.* Scientific Reports, 2020. **10**(1): p. 6666.
69. Moradi, E., S. Jalili-Firoozinezhad, and M. Solati-Hashjin, *Microfluidic organ-on-a-chip models of human liver tissue.* Acta biomaterialia, 2020. **116**: p. 67-83.
70. Liu, Y., L. Lin, and L. Qiao, *Recent developments in organ-on-a-chip technology for cardiovascular disease research.* Analytical and Bioanalytical Chemistry, 2023. **415**(18): p. 3911-3925.
71. Raimondi, I., et al., *Organ-on-a-chip in vitro models of the brain and the blood-brain barrier and their value to study the microbiota-gut-brain axis in neurodegeneration.* Frontiers in bioengineering and biotechnology, 2020. **7**: p. 435.
72. Ashammakhi, N., et al., *Gut-on-a-chip: Current progress and future opportunities.* Biomaterials, 2020. **255**: p. 120196.
73. Mandrycky, C.J., et al., *Organ-on-a-chip systems for vascular biology.* Journal of molecular and cellular cardiology, 2021. **159**: p. 1-13.
74. Loskill, P., et al., *µOrgano: A Lego®-Like Plug & Play System for Modular Multi-Organ-Chips.* PLoS One, 2015. **10**(10): p. e0139587.
75. Toepke, M.W. and D.J. Beebe, *PDMS absorption of small molecules and consequences in microfluidic applications.* Lab on a Chip, 2006. **6**(12): p. 1484-1486.
76. Mukhopadhyay, R., *When PDMS isn't the best*. 2007, ACS Publications.
77. Regehr, K.J., et al., *Biological implications of polydimethylsiloxane-based microfluidic cell culture.* Lab on a Chip, 2009. **9**(15): p. 2132-2139.

78. Eddington, D.T., J.P. Puccinelli, and D.J. Beebe, *Thermal aging and reduced hydrophobic recovery of polydimethylsiloxane*. Sensors and Actuators B: Chemical, 2006. **114**(1): p. 170-172.
79. Gervais, T., et al., *Flow-induced deformation of shallow microfluidic channels*. Lab on a Chip, 2006. **6**(4): p. 500-507.
80. Battat, S., D.A. Weitz, and G.M. Whitesides, *An outlook on microfluidics: the promise and the challenge*. Lab on a Chip, 2022. **22**(3): p. 530-536.
81. Mastrangeli, M., et al., *Organ-on-chip in development: Towards a roadmap for organs-on-chip*. ALTEX, 2019. **36**(4): p. 650-668.
82. Scott, S.M. and Z. Ali, *Fabrication Methods for Microfluidic Devices: An Overview*. Micromachines, 2021. **12**(3): p. 319.
83. Attia, U.M., S. Marson, and J.R. Alcock, *Micro-injection moulding of polymer microfluidic devices*. Microfluidics and Nanofluidics, 2009. **7**(1): p. 1-28.
84. Naderi, A., N. Bhattacharjee, and A. Folch, *Digital Manufacturing for Microfluidics*. Annu Rev Biomed Eng, 2019. **21**: p. 325-364.
85. Catoen, B. and H. Rees, *1 - Introduction*, in *Injection Mold Design Handbook*, B. Catoen and H. Rees, Editors. 2021, Hanser. p. 1-16.
86. Olatunji, O., *A History of Plastics*, in *Re-envisioning Plastics Role in the Global Society: Perspectives on Food, Urbanization, and Environment*, O. Olatunji, Editor. 2024, Springer Nature Switzerland: Cham. p. 11-26.
87. Merrill, A.M., *Plastics Technology*. 1955: Gardner Publications.
88. Advisory, M.I.R. *Plastics Injection Molding Market Size - Industry Report on Share, Growth Trends & Forecasts Analysis (2024 - 2029)*.
89. Goodship, V., *Injection Moulding: A Practical Guide*. 2020: Walter de Gruyter GmbH & Co KG.
90. Wegner, G., *Functional polymers*. Acta Materialia, 2000. **48**(1): p. 253-262.
91. Huang, C.K., *Polymeric nanofeatures of 100 nm using injection moulding for replication*. Journal of Micromechanics and Microengineering, 2007. **17**(8): p. 1518.
92. Catoen, B. and H. Rees, *2 - Overview of Plastics for Mold Design*, in *Injection Mold Design Handbook*, B. Catoen and H. Rees, Editors. 2021, Hanser. p. 17-32.
93. Engel. [cited 2025 10/01]; Available from: https://www.engel-injection.co.nz/wp-content/uploads/2014/11/ENGEL_Plast_Eurasia_2014_ENGEL_e-victory_120.
94. Damiati, L.A., et al., *Role of Polymers in Microfluidic Devices*. Polymers, 2022. **14**(23): p. 5132.
95. Giri, K. and C.-W. Tsao, *Recent Advances in Thermoplastic Microfluidic Bonding*. Micromachines, 2022. **13**(3): p. 486.
96. Berthier, E., E.W.K. Young, and D. Beebe, *Engineers are from PDMS-land, Biologists are from Polystyrenia*. Lab on a Chip, 2012. **12**(7): p. 1224-1237.
97. Lerman, M.J., et al., *The Evolution of Polystyrene as a Cell Culture Material*. Tissue Engineering Part B: Reviews, 2018. **24**(5): p. 359-372.
98. Sastri, V.R. *Chapter 6 - Commodity Thermoplastics: Polyvinyl Chloride, Polyolefins, and Polystyrene*. 2010.
99. Johnston, I.D., et al., *Mechanical characterization of bulk Sylgard 184 for microfluidics and microengineering*. Journal of Micromechanics and Microengineering, 2014. **24**(3): p. 035017.

100. Larsson, A. and H. Dérand, *Stability of Polycarbonate and Polystyrene Surfaces after Hydrophilization with High Intensity Oxygen RF Plasma.* Journal of Colloid and Interface Science, 2002. **246**(1): p. 214-221.
101. Bodas, D. and C. Khan-Malek, *Hydrophilization and hydrophobic recovery of PDMS by oxygen plasma and chemical treatment—An SEM investigation.* Sensors and Actuators B: Chemical, 2007. **123**(1): p. 368-373.
102. Catoen, B. and H. Rees, *15 - Selection of Mold Materials*, in *Injection Mold Design Handbook*, B. Catoen and H. Rees, Editors. 2021, Hanser. p. 549-563.
103. Zhang, N., et al., *Manufacturing microstructured tool inserts for the production of polymeric microfluidic devices.* Journal of Micromechanics and Microengineering, 2015. **25**(9): p. 095005.
104. Fu, G., et al., *Fabrication of robust tooling for mass production of polymeric microfluidic devices.* Journal of Micromechanics and Microengineering, 2010. **20**(8): p. 085019.
105. Ardila, L.K.R., et al. *Micro-milling process for manufacturing of microfluidic moulds.* in *Proceedings of the 23rd ABCM International Congress of Mechanical Engineering*. 2015.
106. Gadegaard, N., S. Mosler, and N.B. Larsen, *Biomimetic Polymer Nanostructures by Injection Molding.* Macromolecular Materials and Engineering, 2003. **288**(1): p. 76-83.
107. Yoon, S.-H., et al. *Comparison of Tooling Materials in Injection Molding of Microscale Features*. 2009.
108. Hansen, T.S., D. Selmeczi, and N.B. Larsen, *Fast prototyping of injection molded polymer microfluidic chips.* Journal of Micromechanics and Microengineering, 2010. **20**(1): p. 015020.
109. Stormonth-Darling, J.M. and N. Gadegaard, *Injection Moulding Difficult Nanopatterns with Hybrid Polymer Inlays.* Macromolecular Materials and Engineering, 2012. **297**(11): p. 1075-1080.
110. Zhao, J., et al. *Development of Rapid Manufacturing Technology of Polymer Microfluidic Devices by Micro Moulding Using Silicon Mould Inserts*. in *ASME 2008 6th International Conference on Nanochannels, Microchannels, and Minichannels*. 2008.
111. Macintyre, D. and S. Thoms, *The fabrication of high resolution features by mould injection.* Microelectronic Engineering, 1998. **41-42**: p. 211-214.
112. Park, S., et al., *Injection molding micro patterns with high aspect ratio using a polymeric flexible stamper.* Express Polymer Letters, 2011. **5**: p. 950-958.
113. Srivastava, M. and S. Rathee, *Additive manufacturing: recent trends, applications and future outlooks.* Progress in Additive Manufacturing, 2022. **7**(2): p. 261-287.
114. Prashar, G., H. Vasudev, and D. Bhuddhi, *Additive manufacturing: expanding 3D printing horizon in industry 4.0.* International Journal on Interactive Design and Manufacturing (IJIDeM), 2023. **17**(5): p. 2221-2235.
115. Bourell, D.L., et al., *Rapid prototyping.* ASM Handbook, 2001. **21**: p. 383-7.
116. Hull, C.W., *The Birth of 3D Printing.* Research-Technology Management, 2015. **58**(6): p. 25-30.
117. Gao, W., et al., *The status, challenges, and future of additive manufacturing in engineering.* Computer-Aided Design, 2015. **69**: p. 65-89.

118. Faraji Rad, Z., P.D. Prewett, and G.J. Davies, *High-resolution two-photon polymerization: the most versatile technique for the fabrication of microneedle arrays*. Microsystems & Nanoengineering, 2021. **7**(1): p. 71.
119. El-Tamer, A., U. Hinze, and B.N. Chichkov, *Two-Photon Polymerization in Optics, Microfluidics, and Biomedicine*, in *Handbook of Laser Micro- and Nano-Engineering*, K. Sugioka, Editor. 2020, Springer International Publishing: Cham. p. 1-44.
120. Quan, H., et al., *Photo-curing 3D printing technique and its challenges*. Bioactive Materials, 2020. **5**(1): p. 110-115.
121. Kushwaha, A.K., et al., *3 - Fundamentals of stereolithography: techniques, properties, and applications*, in *Tribology of Additively Manufactured Materials*, P. Kumar, M. Misra, and P.L. Menezes, Editors. 2022, Elsevier. p. 87-106.
122. Anycubic. [cited 2025 28/05]; Available from: https://wiki.anycubic.com/en/resin-3d-printer/photon-m3-premium.
123. Printer, T.B.a.D. [cited 2025 28/05]; Available from: https://tobuya3dprinter.com/types-of-3d-printing-fdm-sla-and-dlp/.
124. Al Rashid, A., et al., *Vat photopolymerization of polymers and polymer composites: Processes and applications*. Additive Manufacturing, 2021. **47**: p. 102279.
125. Yang, W., et al., *1 - Introduction to vat polymerization 3D printing technologies*, in *Vat Photopolymerization Additive Manufacturing*, X. Wang, Editor. 2024, Elsevier. p. 1-28.
126. Watters, M.P. and M.L. Bernhardt, *Curing parameters to improve the mechanical properties of stereolithographic printed specimens*. Rapid Prototyping Journal, 2018. **24**(1): p. 46-51.
127. Zguris, Z., *How mechanical properties of stereolithography 3D prints are affected by UV curing*. Formlabs White Paper, 2016: p. 1-11.
128. Bhattacharjee, N., et al., *The upcoming 3D-printing revolution in microfluidics*. Lab on a Chip, 2016. **16**(10): p. 1720-1742.
129. Science, W.o. *Analyze Results: 3d print microfluidic (Topic) and Preprint Citation Index (Exclude Database)*. [cited 2024 19/10]; Available from: https://www.webofscience.com/wos/alldb/analyze-results/0e65be6d-c980-4f17-a66e-e72240dc417b-011409fc3d.
130. Ho, C.M.B., et al., *3D printed microfluidics for biological applications*. Lab on a Chip, 2015. **15**(18): p. 3627-3637.
131. Su, R., F. Wang, and M.C. McAlpine, *3D printed microfluidics: advances in strategies, integration, and applications*. Lab on a Chip, 2023. **23**(5): p. 1279-1299.
132. Prabhakar, P., et al., *3D-Printed Microfluidics and Potential Biomedical Applications*. Frontiers in Nanotechnology, 2021. **3**.
133. Fernandes Quero, R., D.P.d. Jesus, and J.A. Fracassi da Silva, *Simple modification to allow high-efficiency and high-resolution multi-material 3D-printing fabrication of microfluidic devices*. Lab on a Chip, 2023. **23**(16): p. 3694-3703.
134. Au, A.K., et al., *3D-Printed Microfluidics*. Angewandte Chemie International Edition, 2016. **55**(12): p. 3862-3881.
135. Bertsch, A., et al., *Static micromixers based on large-scale industrial mixer geometry*. Lab on a Chip, 2001. **1**(1): p. 56-60.
136. Gittard, S.D., et al., *Multiphoton microscopy of transdermal quantum dot delivery using two photon polymerization-fabricated polymer microneedles*. Faraday Discuss, 2011. **149**: p. 171-85; discussion 227-45.

137. Warr, C.A., et al., *3d-printed microfluidic droplet generator with hydrophilic and hydrophobic polymers*. Micromachines, 2021. **12**(1): p. 91.
138. Sanchez Noriega, J.L., et al., *Spatially and optically tailored 3D printing for highly miniaturized and integrated microfluidics*. Nat Commun, 2021. **12**(1): p. 5509.
139. Cabaleiro, J.M., *Flowrate independent 3D printed microfluidic concentration gradient generator*. Chemical Engineering Journal, 2020. **382**: p. 122742.
140. Lee, W., et al., *3D-Printed Microfluidic Device for the Detection of Pathogenic Bacteria Using Size-based Separation in Helical Channel with Trapezoid Cross-Section*. Scientific Reports, 2015. **5**(1): p. 7717.
141. Lee, W., et al., *Ultrarapid detection of pathogenic bacteria using a 3D immunomagnetic flow assay*. Analytical chemistry, 2014. **86**(13): p. 6683-6688.
142. Patrick, W.G., et al., *DNA Assembly in 3D Printed Fluidics*. PLOS ONE, 2016. **10**(12): p. e0143636.
143. Milton, L.A., et al., *Vat photopolymerization 3D printed microfluidic devices for organ-on-a-chip applications*. Lab on a Chip, 2023. **23**(16): p. 3537-3560.
144. Waheed, S., et al., *3D printed microfluidic devices: enablers and barriers*. Lab Chip, 2016. **16**(11): p. 1993-2013.
145. Guttridge, C., et al., *Biocompatible 3D printing resins for medical applications: A review of marketed intended use, biocompatibility certification, and post-processing guidance*. Annals of 3D Printed Medicine, 2022. **5**: p. 100044.
146. Vedhanayagam, A., et al., *Rapid Micromolding of Sub-100 µm Microfluidic Channels Using an 8K Stereolithographic Resin 3D Printer*. Micromachines, 2023. **14**(8): p. 1519.
147. Tosello, G., et al., *Value chain and production cost optimization by integrating additive manufacturing in injection molding process chain*. The International Journal of Advanced Manufacturing Technology, 2019. **100**(1): p. 783-795.
148. Rahmati, S. and P. Dickens, *Stereolithography for injection mould tooling*. Rapid Prototyping Journal, 1997. **3**(2): p. 53-60.
149. Moving, S., E. Montgomery, and D. Somos, *Rapid Tooling via Stereolithography*. RTE Journal, 2006.
150. Whelan, C., *Rapid tooling: A model and methodology for the development of additive manufacturing based tooling for injection moulding*. 2022, University of Limerick.
151. Hopkinson, N. and P. Dickens, *A comparison between stereolithography and aluminium injection moulding tooling*. Rapid Prototyping Journal, 2000. **6**(4): p. 253-258.
152. Harris, R.A., R.J.M. Hague, and P.M. Dickens, *The structure of parts produced by stereolithography injection mould tools and the effect on part shrinkage*. International Journal of Machine Tools and Manufacture, 2004. **44**(1): p. 59-64.
153. Hopkins, M., et al., *Stereolithography (SLA) utilised to print injection mould tooling in order to evaluate thermal and mechanical properties of commercial polypropylene*. Procedia Manufacturing, 2021. **55**: p. 205-212.
154. Rosochowski, A. and A. Matuszak, *Rapid tooling: the state of the art*. Journal of Materials Processing Technology, 2000. **106**(1): p. 191-198.

155. Equbal, A., A.K. Sood, and M. Shamim, *Rapid tooling: A major shift in tooling practice*. Manufacturing and Industrial Engineering, 2015. **14**(3-4).
156. Convery, N., et al., *3D Printed Tooling for Injection Molded Microfluidics*. Macromolecular Materials and Engineering, 2021. **306**(11).
157. Becker, H. and C. Gärtner, *Polymer microfabrication technologies for microfluidic systems*. Analytical and Bioanalytical Chemistry, 2008. **390**(1): p. 89-111.
158. Becker, H., *It's the economy….* Lab on a Chip, 2009. **9**(19): p. 2759-2762.
159. Temiz, Y., et al., *Lab-on-a-chip devices: How to close and plug the lab?* Microelectronic Engineering, 2015. **132**: p. 156-175.
160. Kim, E., Y. Xia, and G.M. Whitesides, *Micromolding in capillaries: Applications in materials science*. Journal of the American Chemical Society, 1996. **118**(24): p. 5722-5731.
161. Zhou, J., A.V. Ellis, and N.H. Voelcker, *Recent developments in PDMS surface modification for microfluidic devices*. ELECTROPHORESIS, 2010. **31**(1): p. 2-16.
162. Christensen, A.M., D.A. Chang-Yen, and B.K. Gale, *Characterization of interconnects used in PDMS microfluidic systems*. Journal of Micromechanics and Microengineering, 2005. **15**(5): p. 928.
163. Chen, X., et al., *Manufacturing methods and applications of membranes in microfluidics*. Biomedical Microdevices, 2016. **18**(6): p. 104.
164. de Jong, J., R.G.H. Lammertink, and M. Wessling, *Membranes and microfluidics: a review*. Lab on a Chip, 2006. **6**(9): p. 1125-1139.
165. Wang, Y., et al., *An integrated microfluidic device for large-scale in situ click chemistry screening*. Lab Chip, 2009. **9**(16): p. 2281-5.
166. Shakeri, A., et al., *The Fabrication and Bonding of Thermoplastic Microfluidics: A Review*. Materials, 2022. **15**(18): p. 6478.
167. Guevara-Pantoja, P.E., et al., *Pressure-actuated monolithic acrylic microfluidic valves and pumps*. Lab on a Chip, 2018. **18**(4): p. 662-669.
168. Gu, P., et al., *Chemical-Assisted Bonding of Thermoplastics/Elastomer for Fabricating Microfluidic Valves*. Analytical Chemistry, 2011. **83**(1): p. 446-452.
169. Roy, E., J.-C. Galas, and T. Veres, *Thermoplastic elastomers for microfluidics: Towards a high-throughput fabrication method of multilayered microfluidic devices*. Lab on a Chip, 2011. **11**(18): p. 3193-3196.
170. Smith, S., M. Sypabekova, and S. Kim, *Double-Sided Tape in Microfluidics: A Cost-Effective Method in Device Fabrication*. Biosensors, 2024. **14**(5): p. 249.
171. Barrios, C.A., *Pressure Sensitive Adhesive Tape: A Versatile Material Platform for Optical Sensors*. Sensors, 2020. **20**(18): p. 5303.
172. Dabaghi, M., et al., *Adhesive-Based Fabrication Technique for Culture of Lung Airway Epithelial Cells with Applications in Cell Patterning and Microfluidics*. ACS Biomaterials Science & Engineering, 2021. **7**(11): p. 5301-5314.
173. Kratz, S.R.A., et al., *Characterization of four functional biocompatible pressure-sensitive adhesives for rapid prototyping of cell-based lab-on-a-chip and organ-on-a-chip systems*. Scientific Reports, 2019. **9**(1): p. 9287.
174. Tsao, C.-W. and D.L. DeVoe, *Bonding of thermoplastic polymer microfluidics*. Microfluidics and Nanofluidics, 2008. **6**(1): p. 1-16.
175. Arayanarakool, R., S. Le Gac, and A. van den Berg, *Low-temperature, simple and fast integration technique of microfluidic chips by using a UV-curable adhesive*. Lab on a Chip, 2010. **10**(16): p. 2115-2121.

176. Yao, Y., et al., *Reversible bonding for microfluidic devices with UV release tape*. Microfluidics and Nanofluidics, 2022. **26**(3): p. 23.
177. Liu, K., et al., *PMMA microfluidic chip fabrication using laser ablation and low temperature bonding with OCA film and LOCA*. Microsystem Technologies, 2017. **23**(6): p. 1937-1942.
178. Le, N.X.T., K.T.L. Trinh, and N.Y. Lee, *Poly(acrylic acid) as an adhesion promoter for UV-assisted thermoplastic bonding: Application for the in vitro construction of human blood vessels*. Materials Science and Engineering: C, 2021. **122**: p. 111874.
179. Serra, M., et al., *A simple and low-cost chip bonding solution for high pressure, high temperature and biological applications*. Lab on a Chip, 2017. **17**(4): p. 629-634.
180. Chai, M., et al., *Polyformaldehyde-based microfluidics and application in enhanced oil recovery*. Microsystem Technologies, 2022. **28**(4): p. 947-954.
181. Yuen, P.K. and V.N. Goral, *Low-cost rapid prototyping of flexible microfluidic devices using a desktop digital craft cutter*. Lab on a Chip, 2010. **10**(3): p. 384-387.
182. Sui, C., J. Zilberberg, and W. Lee, *Microfluidic device engineered to study the trafficking of multiple myeloma cancer cells through the sinusoidal niche of bone marrow*. Scientific Reports, 2022. **12**(1): p. 1439.
183. Flachsbart, B.R., et al., *Design and fabrication of a multilayered polymer microfluidic chip with nanofluidic interconnects via adhesive contact printing*. Lab on a Chip, 2006. **6**(5): p. 667-674.
184. Vendan, S.A., et al., *Ultrasonic welding of polymers*. Confluence of multidisciplinary sciences for polymer joining, 2019: p. 73-101.
185. Benatar, A., *27 - Plastics Joining*, in *Applied Plastics Engineering Handbook (Third Edition)*, M. Kutz, Editor. 2024, William Andrew Publishing. p. 619-635.
186. Ng, S.H., Z.F. Wang, and N.F. de Rooij, *Microfluidic connectors by ultrasonic welding*. Microelectronic Engineering, 2009. **86**(4): p. 1354-1357.
187. Kistrup, K., et al., *Ultrasonic welding for fast bonding of self-aligned structures in lab-on-a-chip systems*. Lab on a Chip, 2015. **15**(9): p. 1998-2001.
188. Stokes, V.K., *Joining methods for plastics and plastic composites: an overview*. Polymer Engineering & Science, 1989. **29**(19): p. 1310-1324.
189. Sackmann, J., et al., *Review on ultrasonic fabrication of polymer micro devices*. Ultrasonics, 2015. **56**: p. 189-200.
190. Truckenmüller, R., et al., *Micro ultrasonic welding: joining of chemically inert polymer microparts for single material fluidic components and systems*. Microsystem Technologies, 2006. **12**(10): p. 1027-1029.
191. Zhang, Z., et al., *A low temperature ultrasonic bonding method for PMMA microfluidic chips*. Microsystem Technologies, 2010. **16**(4): p. 533-541.
192. Schneider, S., et al., *Membrane integration into PDMS-free microfluidic platforms for organ-on-chip and analytical chemistry applications*. Lab Chip, 2021. **21**(10): p. 1866-1885.
193. Runge, T., et al., *Ultrasonically manufactured microfluidic device for yeast analysis*. Microsystem Technologies, 2017. **23**: p. 2139-2144.
194. Ye, M.-Y., X.-F. Yin, and Z.-L. Fang, *DNA separation with low-viscosity sieving matrix on microfabricated polycarbonate microfluidic chips*. Analytical and Bioanalytical Chemistry, 2005. **381**(4): p. 820-827.

195. Busek, M., et al., *Thermoplastic Elastomer (TPE)-Poly(Methyl Methacrylate) (PMMA) Hybrid Devices for Active Pumping PDMS-Free Organ-on-a-Chip Systems.* Biosensors, 2021. **11**(5): p. 162.
196. Ongaro, A.E., et al., *Polylactic is a Sustainable, Low Absorption, Low Autofluorescence Alternative to Other Plastics for Microfluidic and Organ-on-Chip Applications.* Analytical Chemistry, 2020. **92**(9): p. 6693-6701.
197. Jena, R.K. and C.Y. Yue, *Cyclic olefin copolymer based microfluidic devices for biochip applications: Ultraviolet surface grafting using 2-methacryloyloxyethyl phosphorylcholine.* Biomicrofluidics, 2012. **6**(1).
198. Young, E.W.K., et al., *Rapid Prototyping of Arrayed Microfluidic Systems in Polystyrene for Cell-Based Assays.* Analytical Chemistry, 2011. **83**(4): p. 1408-1417.
199. Gleichweit, E., et al., *UV/Ozone Surface Treatment for Bonding of Elastomeric COC-Based Microfluidic Devices.* Proceedings, 2018. **2**(13): p. 943.
200. Uba, F.I., et al., *High process yield rates of thermoplastic nanofluidic devices using a hybrid thermal assembly technique.* Lab on a Chip, 2015. **15**(4): p. 1038-1049.
201. Wang, Z.F., Y.P. Seah, and Z.P. Wang, *Seamless joining of porous membrane with thermoplastic microfluidic devices.* Microelectronic Engineering, 2013. **110**: p. 386-391.
202. Kappings, V., et al., *vasQchip: a novel microfluidic, artificial blood vessel scaffold for vascularized 3D tissues.* Advanced Materials Technologies, 2018. **3**(4): p. 1700246.
203. Bings, N.H., et al., *Microfluidic devices connected to fused-silica capillaries with minimal dead volume.* Analytical chemistry, 1999. **71**(15): p. 3292-3296.
204. Li, S. and S. Chen, *Polydimethylsioxane Fluidic Interconnects for Microfluidic Systems.* IEEE Transactions on Advanced Packaging, 2003. **26**(3): p. 242-247.
205. Etxeberria, L., et al., *Critical Study on the Tube-to-Chip Luer Slip Connectors.* Frontiers in Medical Technology, 2022. **4**.
206. Finkbeiner, T., et al., *Ultrasonic welding for the rapid integration of fluidic connectors into microfluidic chips.* Journal of Micromechanics and Microengineering, 2019. **29**(6): p. 065011.
207. Nie, M. and S. Takeuchi, *Luer-lock valve: A pre-fabricated pneumatic valve for 3D printed microfluidic automation.* Biomicrofluidics, 2020. **14**(4).
208. Fredrickson, C.K. and Z.H. Fan, *Macro-to-micro interfaces for microfluidic devices.* Lab on a Chip, 2004. **4**(6): p. 526-533.
209. Science, W.o. *Analyze Results: pumpless organ on chip*. [cited 2024 18/10]; Available from: https://www.webofscience.com/wos/alldb/analyze-results/8141021b-d1fa-42dd-8b2b-a89ee32cfa18-0113781207.
210. Busek, M., et al., *Academic User View: Organ-on-a-Chip Technology.* Biosensors (Basel), 2022. **12**(2).
211. Mimetas. *OrganoPlate family*. [cited 2024 18/10]; Available from: https://www.mimetas.com/files/products/MIM_OrganoPlate_Family_chart.pdf.
212. Busek, M., et al., *Pump-less, recirculating organ-on-a-chip (rOoC) platform.* Lab on a Chip, 2023. **23**(4): p. 591-608.

213. Wang, S., et al., *A Review of Capillary Pressure Control Valves in Microfluidics*. Biosensors, 2021. **11**(10): p. 405.
214. Li, B., et al., *A brief overview of passive microvalves in microfluidics: Mechanism, manufacturing, and applications*. Biomicrofluidics, 2024. **18**(2).
215. Ju, T., *Working Principle and Applications of Active and Passive Microfluidic Valves*. Journal of Physics: Conference Series, 2022. **2230**(1): p. 012013.
216. Hansen, C. and S.R. Quake, *Microfluidics in structural biology: smaller, faster… better*. Current Opinion in Structural Biology, 2003. **13**(5): p. 538-544.
217. Araci, I.E. and P. Brisk, *Recent developments in microfluidic large scale integration*. Current Opinion in Biotechnology, 2014. **25**: p. 60-68.
218. Zhou, P., L. Young, and Z. Chen, *Weak solvent based chip lamination and characterization of on-chip valve and pump*. Biomedical Microdevices, 2010. **12**(5): p. 821-832.
219. Lee, K.S. and R.J. Ram, *Plastic–PDMS bonding for high pressure hydrolytically stable active microfluidics*. Lab on a Chip, 2009. **9**(11): p. 1618-1624.
220. Pitchaimani, K., et al., *Manufacturable plastic microfluidic valves using thermal actuation*. Lab on a Chip, 2009. **9**(21): p. 3082-3087.
221. Ogilvie, I., et al., *Chemically resistant microfluidic valves from Viton® membranes bonded to COC and PMMA*. Lab on a Chip, 2011. **11**(14): p. 2455-2459.
222. Shaegh, S.A.M., et al., *Plug-and-play microvalve and micropump for rapid integration with microfluidic chips*. Microfluidics and Nanofluidics, 2015. **19**: p. 557-564.
223. Grover, W.H., M.G. von Muhlen, and S.R. Manalis, *Teflon films for chemically-inert microfluidic valves and pumps*. Lab on a Chip, 2008. **8**(6): p. 913-918.
224. Cortese, B., M.C. Mowlem, and H. Morgan, *Characterisation of an irreversible bonding process for COC–COC and COC–PDMS–COC sandwich structures and application to microvalves*. Sensors and Actuators B: Chemical, 2011. **160**(1): p. 1473-1480.
225. Au, A.K., et al., *3D-printed microfluidic automation*. Lab on a Chip, 2015. **15**(8): p. 1934-1941.
226. Steinhauser, M.O., *Fundamentals of Numerical Simulation*, in *Computational Multiscale Modeling of Fluids and Solids: Theory and Applications*, M.O. Steinhauser, Editor. 2022, Springer International Publishing: Cham. p. 185-225.
227. Sheidaei, Z., P. Akbarzadeh, and N. Kashaninejad, *Advances in numerical approaches for microfluidic cell analysis platforms*. Journal of Science: Advanced Materials and Devices, 2020. **5**(3): p. 295-307.
228. Hrennikoff, A., *Solution of problems of elasticity by the framework method*. 1941.
229. Courant, R., *Variational methods for the solution of problems of equilibrium and vibrations. B Am Math Soc 49: 1–23. doi: 10.1090*. 1943, S0002-9904-1943-07818-4.
230. Kajishima, T. and K. Taira, *Computational fluid dynamics: incompressible turbulent flows*. 2016: Springer.
231. Carvalho, V., et al., *Computational Simulations in Advanced Microfluidic Devices: A Review*. Micromachines, 2021. **12**(10): p. 1149.

232. Donea, J. and A. Huerta, *Finite element methods for flow problems*. 2003: John Wiley & Sons.
233. Dick, E., *Introduction to finite element methods in computational fluid dynamics*, in *Computational fluid dynamics*. 2009, Springer. p. 235-274.
234. Schieche, B. *The Strength of the Weak Form*. 2014 [cited 2024 30/09]; Available from: https://www.comsol.com/blogs/strength-weak-form.
235. COMSOL. *The Finite Element Method (FEM)*. 2017 [cited 2024 30/09]; Available from: https://www.comsol.com/multiphysics/finite-element-method.
236. Okereke, M. and S. Keates, *Finite element applications*. A Practical Guide to the FEMA Process. TextBook. Publisher: Springer, 2018.
237. Ferreira, M., et al., *Advances in Microfluidic Systems and Numerical Modeling in Biomedical Applications: A Review*. Micromachines, 2024. **15**(7): p. 873.
238. Erickson, D., *Towards numerical prototyping of labs-on-chip: modeling for integrated microfluidic devices*. Microfluidics and Nanofluidics, 2005. **1**(4): p. 301-318.
239. Bohm, S., et al., *Highly efficient passive Tesla valves for microfluidic applications*. Microsystems & Nanoengineering, 2022. **8**(1): p. 97.
240. Zheng, L., et al., *Design, Implementation, and Optimization of a Novel Chaotic Micromixer*. Industrial & Engineering Chemistry Research, 2024. **63**(32): p. 14444-14457.
241. Kheirkhah Barzoki, A., *Optimization of passive micromixers: effects of pillar configuration and gaps on mixing efficiency*. Scientific Reports, 2024. **14**(1): p. 16245.
242. Menezes, P.D., et al., *Modelling human liver microphysiology on a chip through a finite element based design approach*. International Journal for Numerical Methods in Biomedical Engineering, 2021. **37**(5): p. e3445.
243. Jaberi, A., et al., *Microfluidic Systems with Embedded Cell Culture Chambers for High-Throughput Biological Assays*. ACS Applied Bio Materials, 2020. **3**(10): p. 6661-6671.
244. Sweet, E., et al., *3D microfluidic gradient generator for combination antimicrobial susceptibility testing*. Microsystems & Nanoengineering, 2020. **6**(1): p. 92.
245. Suh, Y.K. and S. Kang, *A Review on Mixing in Microfluidics*. Micromachines, 2010. **1**(3): p. 82-111.
246. Jeong, G.S., et al., *Applications of micromixing technology*. Analyst, 2010. **135**(3): p. 460-473.
247. Kheirkhah Barzoki, A., *Enhanced mixing efficiency and reduced droplet size with novel droplet generators*. Scientific Reports, 2024. **14**(1): p. 4711.
248. Delon, L.C., et al., *A systematic investigation of the effect of the fluid shear stress on Caco-2 cells towards the optimization of epithelial organ-on-chip models*. Biomaterials, 2019. **225**: p. 119521.
249. Delon, L.C., et al., *Hele Shaw microfluidic device: A new tool for systematic investigation into the effect of the fluid shear stress for organs-on-chips*. MethodsX, 2020. **7**: p. 100980.
250. Spigarelli, L., et al., *A passive two-way microfluidic device for low volume blood-plasma separation*. Microelectronic Engineering, 2019. **209**: p. 28-34.
251. Rahimnejad, M., et al., *Engineered Biomimetic Membranes for Organ-on-a-Chip*. ACS Biomaterials Science & Engineering, 2022. **8**(12): p. 5038-5059.

252. Chung, H.H., et al., *Highly permeable silicon membranes for shear free chemotaxis and rapid cell labeling.* Lab on a Chip, 2014. **14**(14): p. 2456-2468.
253. Chen, L.-J., et al., *Microfluidic co-cultures of retinal pigment epithelial cells and vascular endothelial cells to investigate choroidal angiogenesis.* Scientific Reports, 2017. **7**(1): p. 3538.
254. Chung, H.H., et al., *Use of porous membranes in tissue barrier and co-culture models.* Lab Chip, 2018. **18**(12): p. 1671-1689.
255. VanDersarl, J.J., A.M. Xu, and N.A. Melosh, *Rapid spatial and temporal controlled signal delivery over large cell culture areas.* Lab Chip, 2011. **11**(18): p. 3057-63.
256. Fakhraee, M. and O. Akhavan, *Ultrahigh Permeable C2N-Inspired Graphene Nanomesh Membranes versus Highly Strained C2N for Reverse Osmosis Desalination.* The Journal of Physical Chemistry B, 2019. **123**(41): p. 8740-8752.
257. Khosravikia, M., *Quantitative model for predicting the electroosmotic flow in dual-pole nanochannels.* ELECTROPHORESIS, 2023. **44**(7-8): p. 733-743.
258. Gillet, A., et al., *Liposome surface charge influence on skin penetration behaviour.* International Journal of Pharmaceutics, 2011. **411**(1): p. 223-231.
259. Chen, S., et al., *Flow field analyses of a porous membrane-separated, double-layered microfluidic chip for cell co-culture.* Acta Mechanica Sinica, 2020. **36**(3): p. 754-767.
260. Andreev, O.A., D.M. Engelman, and Y.K. Reshetnyak, *pH-sensitive membrane peptides (pHLIPs) as a novel class of delivery agents.* Mol Membr Biol, 2010. **27**(7): p. 341-52.
261. Inamdar, N.K., L.G. Griffith, and J.T. Borenstein, *Transport and shear in a microfluidic membrane bilayer device for cell culture.* Biomicrofluidics, 2011. **5**(2): p. 22213.
262. Chung, H.H., et al., *Highly permeable silicon membranes for shear free chemotaxis and rapid cell labeling.* Lab Chip, 2014. **14**(14): p. 2456-68.
263. Frost, T.S., et al., *Convection–diffusion molecular transport in a microfluidic bilayer device with a porous membrane.* Microfluidics and Nanofluidics, 2019. **23**(10).
264. Khosravikia, M. and A. Rahbar-Kelishami, *A simulation study of an applied approach to enhance drug recovery through electromembrane extraction.* Journal of Molecular Liquids, 2022. **358**: p. 119210.
265. Mosavati, B., A.V. Oleinikov, and E. Du, *Development of an Organ-on-a-Chip-Device for Study of Placental Pathologies.* International Journal of Molecular Sciences, 2020. **21**(22): p. 8755.
266. Banaeiyan, A.A., et al., *Design and fabrication of a scalable liver-lobule-on-a-chip microphysiological platform.* Biofabrication, 2017. **9**(1): p. 015014.
267. Zahorodny-Burke, M., B. Nearingburg, and A.L. Elias, *Finite element analysis of oxygen transport in microfluidic cell culture devices with varying channel architectures, perfusion rates, and materials.* Chemical Engineering Science, 2011. **66**(23): p. 6244-6253.
268. Mäki, A.J., et al., *Modeling carbon dioxide transport in PDMS-based microfluidic cell culture devices.* Chemical Engineering Science, 2015. **137**: p. 515-524.

269. Wong, J.F., E.W.K. Young, and C.A. Simmons, *Computational analysis of integrated biosensing and shear flow in a microfluidic vascular model*. AIP Advances, 2017. **7**(11).
270. Wong, J.F. and C.A. Simmons, *Microfluidic assay for the on-chip electrochemical measurement of cell monolayer permeability*. Lab on a Chip, 2019. **19**(6): p. 1060-1070.
271. Menezes, P.D., et al., *Scalable, Transparent, and Micro: 3D-Printed Rapid Tooling for Injection Molded Microfluidics*. Advanced Engineering Materials, 2024. **26**(20): p. 2400276.
272. Griffiths, C.A., et al., *Prototype tooling for producing small series of polymer microparts*. Proceedings of the Institution of Mechanical Engineers, Part B: Journal of Engineering Manufacture, 2011. **225**(12): p. 2189-2205.
273. Griffiths, C.A., et al., *Micro-stereolithography tools for small-batch manufacture of polymer micro-parts*. Proceedings of the Institution of Mechanical Engineers, Part B: Journal of Engineering Manufacture, 2012. **226**(4): p. 708-721.
274. Zhang, Y., et al., *A Soft Tooling process chain employing Additive Manufacturing for injection molding of a 3D component with micro pillars*. Journal of Manufacturing Processes, 2017. **27**: p. 138-144.
275. Research, G.V. *3D Printing Market Size, Share & Trends Analysis Report By Component (Hardware, Software, Services), By Printer Type, By Technology, By Software, By Application, By Vertical, By Region, And Segment Forecasts, 2024 - 2030*. [cited 2024 31/10]; Available from: https://www.grandviewresearch.com/industry-analysis/3d-printing-industry-analysis.
276. Walsh, E., J.H. ter Horst, and D. Markl, *Development of 3D printed rapid tooling for micro-injection moulding*. Chemical Engineering Science, 2021. **235**: p. 116498.
277. Pritchard, Z.D., et al., *Modeling and Correcting Cure-Through in Continuous Stereolithographic 3D Printing*. Advanced Materials Technologies, 2019. **4**(12): p. 1900700.
278. Ahn, D., et al., *Rapid High-Resolution Visible Light 3D Printing*. ACS Central Science, 2020. **6**(9): p. 1555-1563.
279. Majewski, C. and N. Hopkinson, *Reducing ejection forces for parts moulded into direct metal laser sintered tools*. The International Journal of Advanced Manufacturing Technology, 2004. **24**: p. 16-23.
280. Weng, Z. and L. Wu, *2 - Foundation chemistry of vat photopolymerization*, in *Vat Photopolymerization Additive Manufacturing*, X. Wang, Editor. 2024, Elsevier. p. 29-48.
281. Shah, M., et al., *Vat photopolymerization-based 3D printing of polymer nanocomposites: current trends and applications*. RSC advances, 2023. **13**(2): p. 1456-1496.
282. Pham, Q.L., et al., *Cell Sequence and Mitosis Affect Fibroblast Directional Decision-Making During Chemotaxis in Microfluidic Mazes*. Cellular and Molecular Bioengineering, 2018. **11**(6): p. 483-494.
283. Salek, M.M., et al., *Bacterial chemotaxis in a microfluidic T-maze reveals strong phenotypic heterogeneity in chemotactic sensitivity*. Nature Communications, 2019. **10**(1): p. 1877.
284. Squires, T.M. and S.R. Quake, *Microfluidics: Fluid physics at the nanoliter scale*. Reviews of Modern Physics, 2005. **77**(3): p. 977-1026.
285. Stroock, A.D., et al., *Chaotic mixer for microchannels*. Science, 2002. **295**(5555): p. 647-651.

286. Han, W. and X. Chen, *A review on microdroplet generation in microfluidics.* Journal of the Brazilian Society of Mechanical Sciences and Engineering, 2021. **43**(5): p. 247.
287. McKeen, L.W., *Chapter 1 - Introduction to Plastics and Polymers*, in *Film Properties of Plastics and Elastomers (Third Edition)*, L.W. McKeen, Editor. 2012, William Andrew Publishing: Boston. p. 1-18.
288. Jacobs, T., et al., *Plasma Surface Modification of Biomedical Polymers: Influence on Cell-Material Interaction.* Plasma Chemistry and Plasma Processing, 2012. **32**(5): p. 1039-1073.
289. Gilson, R.W. and E.F. Windischman, *Luer connector*. 1983, Google Patents.
290. Werschmidt, G.S., R.P. Feith, and D.R. Kipp, *Luer lock system*. 1997, Google Patents.
291. Valle, N.M.E., et al., *Advances in Concentration Gradient Generation Approaches in a Microfluidic Device for Toxicity Analysis.* Cells, 2022. **11**(19): p. 3101.
292. Hsu, C.H., C. Chen, and A. Folch, *"Microcanals" for micropipette access to single cells in microfluidic environments.* Lab on a Chip, 2004. **4**(5): p. 420-424.
293. Linder, V., et al., *Water-soluble sacrificial layers for surface micromachining.* small, 2005. **1**(7): p. 730-736.
294. Sochol, R.D., et al., *3D printed microfluidics and microelectronics.* Microelectronic Engineering, 2018. **189**: p. 52-68.
295. Madadi, M., et al., *A simple solvent-assisted method for thermal bonding of large-surface, multilayer PMMA microfluidic devices.* Sensors and Actuators A: Physical, 2023. **349**: p. 114077.
296. Menezes, P.D., et al., *A membrane's blueprint: In silico investigation of fluid flow and molecular transport as a function of membrane design parameters in organ-on-a-chip.* Chemical Engineering Journal, 2024. **481**: p. 148189.
297. Aizenshtadt, A., et al., *Pump-Less, Recirculating Organ-on-Chip (rOoC) Platform to Model the Metabolic Crosstalk between Islets and Liver.* Advanced Healthcare Materials, 2024. **13**(13): p. 2303785.
298. Du, Y., et al., *Mimicking liver sinusoidal structures and functions using a 3D-configured microfluidic chip.* Lab Chip, 2017. **17**(5): p. 782-794.
299. Yang, X., et al., *Nanofiber membrane supported lung-on-a-chip microdevice for anti-cancer drug testing.* Lab Chip, 2018. **18**(3): p. 486-495.
300. Loskill, P., et al., *WAT-on-a-chip: a physiologically relevant microfluidic system incorporating white adipose tissue.* Lab Chip, 2017. **17**(9): p. 1645-1654.
301. Lee, J.S., et al., *Placenta-on-a-chip: a novel platform to study the biology of the human placenta.* J Matern Fetal Neonatal Med, 2016. **29**(7): p. 1046-54.
302. Carraro, A., et al., *In vitro analysis of a hepatic device with intrinsic microvascular-based channels.* Biomedical Microdevices, 2008. **10**(6): p. 795-805.
303. Batchelor, G.K., *An Introduction to Fluid Dynamics*. Cambridge Mathematical Library. 2000, Cambridge: Cambridge University Press.
304. Kawata, K., et al., *Mesenchymal cells and fluid flow stimulation synergistically regulate the kinetics of corneal epithelial cells at the air-liquid interface.* Graefe's Archive for Clinical and Experimental Ophthalmology, 2019. **257**(9): p. 1915-1924.

305. Humphrey, J.D., *Vascular Adaptation and Mechanical Homeostasis at Tissue, Cellular, and Sub-cellular Levels.* Cell Biochemistry and Biophysics, 2008. **50**(2): p. 53-78.
306. Song, J.W., et al., *Computer-Controlled Microcirculatory Support System for Endothelial Cell Culture and Shearing.* Analytical Chemistry, 2005. **77**(13): p. 3993-3999.
307. Zhong, M., et al., *Mechanosensing Piezo channels in tissue homeostasis including their role in lungs.* Pulm Circ, 2018. **8**(2): p. 2045894018767393.
308. Tanaka, Y., et al., *Evaluation of effects of shear stress on hepatocytes by a microchip-based system.* Measurement Science and Technology, 2006. **17**(12): p. 3167-3170.
309. Rashidi, H., et al., *Fluid shear stress modulation of hepatocyte-like cell function.* Arch Toxicol, 2016. **90**(7): p. 1757-61.
310. Torii, T., M. Miyazawa, and I. Koyama, *Effect of continuous application of shear stress on liver tissue: continuous application of appropriate shear stress has advantage in protection of liver tissue.* Transplant Proc, 2005. **37**(10): p. 4575-8.
311. Uroz, M., et al., *Regulation of cell cycle progression by cell–cell and cell–matrix forces.* Nature Cell Biology, 2018. **20**(6): p. 646-654.
312. Azizipour, N., et al., *Evolution of Biochip Technology: A Review from Lab-on-a-Chip to Organ-on-a-Chip.* Micromachines (Basel), 2020. **11**(6).
313. Keenan, T.M. and A. Folch, *Biomolecular gradients in cell culture systems.* Lab Chip, 2008. **8**(1): p. 34-57.
314. Ahadian, S., et al., *Organ-On-A-Chip Platforms: A Convergence of Advanced Materials, Cells, and Microscale Technologies.* Adv Healthc Mater, 2018. **7**(2).
315. Lee, K., E.A. Silva, and D.J. Mooney, *Growth factor delivery-based tissue engineering: general approaches and a review of recent developments.* J R Soc Interface, 2011. **8**(55): p. 153-70.
316. Grushka, E. and E.J. Kikta Jr, *Diffusion in liquids. II. The dependence of the diffusion coefficients on molecular weight and on temperature.* Journal of the American Chemical Society, 1976. **98**(3): p. 643-648.
317. Schliwa, M., *Action of cytochalasin D on cytoskeletal networks.* J Cell Biol, 1982. **92**(1): p. 79-91.
318. Casella, J.F., M.D. Flanagan, and S. Lin, *Cytochalasin D inhibits actin polymerization and induces depolymerization of actin filaments formed during platelet shape change.* Nature, 1981. **293**(5830): p. 302-305.
319. Stevenson, B.R. and D.A. Begg, *Concentration-dependent effects of cytochalasin D on tight junctions and actin filaments in MDCK epithelial cells.* Journal of Cell Science, 1994. **107**(3): p. 367-375.
320. Bricker, J.L., S. Chu, and S.A. Kempson, *Disruption of F-actin stimulates hypertonic activation of the BGT1 transporter in MDCK cells.* American Journal of Physiology-Renal Physiology, 2003. **284**(5): p. F930-F937.
321. STANKOVIC, M., et al., *Quantification of structural changes in acute inflammation by fractal dimension, angular second moment and correlation.* Journal of Microscopy, 2016. **261**(3): p. 277-284.
322. Pantic, I., et al., *Nuclear entropy, angular second moment, variance and texture correlation of thymus cortical and medullar lymphocytes: Grey level co-occurrence matrix analysis.* Anais da Academia Brasileira de Ciências, 2013. **85**.
323. Harvard. *Some Diffusion Coefficients*. [cited 2024 23/11]; Available from: https://bionumbers.hms.harvard.edu/files/Diffusion%20coefficients%20of%20various%20substances%20in%20Water.pdf.

324. Frost, T.S., et al., *Permeability of Epithelial/Endothelial Barriers in Transwells and Microfluidic Bilayer Devices.* Micromachines, 2019. **10**(8): p. 533.
325. Goy, C.B., R.E. Chaile, and R.E. Madrid, *Microfluidics and hydrogel: A powerful combination.* Reactive and Functional Polymers, 2019. **145**.

Appendix

A Numerical data from finite element modelling of flow and transport kinetics in microfluidic systems with integrated porous membranes

This appendix contains the complete data which was used to generate the figures present along Chapter 5, as well as in Figure 5.19 and Figure 5.20. The table subheadings provide references to the appropriate figures in Chapter 5 and the respective sub panels in Figure 5.19 and Figure 5.20.

Fluidic Setup	Boundary Condition Cell Channel	Parameter Sweep	Control Parameters								Variables of Analysis									Dimensionless Numbers			
			P	r [µm]	t_M [µm]	L_M [mm]	H_{CC} [µm]	H_{PC} [µm]	Q_{in} [µl/h]	D [m^2/s]	Q^A_{ACC}	Q^A_{APC}	WSS^A_{UCC} [dyn/cm^2]	WSS^A_{MCC} [dyn/cm^2]	WSS^A_{MPC} [dyn/cm^2]	st_{CC} [s]	st_{PC} [s]	ssC_{ACC}	ssC_{APC}	Pe_{CC}	Re_{CC}	Pe_{PC}	Re_{PC}
Single Channel Perfusion (SCP)	Reservoir (SCPP)	Porosity									Figure 5.8 A			Figure 5.8 D		Figure 5.13 A							
											Figure 5.19, A21			Figure 5.19, A21		Figure 5.19, A31		Figure 5.19, A41					
			0.001	1	10	5	300	300	50	1.0E-09	1.55E-05	1.49E+00	2.08E-08	2.10E-08	2.00E-03	3.70E+03	5.00E+01	1.00E+00	1.00E+00	7.20E-04	1.00E-09	6.91E+01	1.00E-04
			0.01	1	10	5	300	300	50	1.0E-09	1.55E-04	1.49E+00	2.08E-07	2.10E-07	2.00E-03	2.05E+03	5.50E+01	1.00E+00	1.00E+00	7.18E-03	1.00E-08	6.91E+01	1.00E-04
			0.1	1	10	5	300	300	50	1.0E-09	1.55E-03	1.49E+00	2.07E-06	2.10E-06	2.00E-03	2.85E+02	1.55E+02	1.00E+00	1.00E+00	7.16E-02	1.00E-07	6.90E+01	1.00E-04
			0.2	1	10	5	300	300	50	1.0E-09	3.09E-03	1.49E+00	4.14E-06	4.19E-06	2.00E-03	2.20E+02	1.45E+02	1.00E+00	1.00E+00	1.43E-01	2.10E-07	6.89E+01	1.00E-04
			0.3	1	10	5	300	300	50	1.0E-09	4.62E-03	1.49E+00	6.19E-06	6.26E-06	1.99E-03	2.05E+02	1.40E+02	1.00E+00	1.00E+00	2.14E-01	3.10E-07	6.89E+01	9.90E-05
			0.4	1	10	5	300	300	50	1.0E-09	6.14E-03	1.49E+00	8.23E-06	8.33E-06	1.99E-03	1.95E+02	1.40E+02	1.00E+00	1.00E+00	2.84E-01	4.10E-07	6.88E+01	9.90E-05
			0.5	1	10	5	300	300	50	1.0E-09	7.66E-03	1.48E+00	1.03E-05	1.04E-05	1.99E-03	1.95E+02	1.35E+02	1.00E+00	1.00E+00	3.54E-01	5.10E-07	6.87E+01	9.90E-05
			0.6	1	10	5	300	300	50	1.0E-09	9.16E-03	1.48E+00	1.23E-05	1.24E-05	1.99E-03	1.90E+02	1.35E+02	1.00E+00	1.00E+00	4.24E-01	6.10E-07	6.86E+01	9.90E-05
			0.7	1	10	5	300	300	50	1.0E-09	1.07E-02	1.48E+00	1.43E-05	1.45E-05	1.99E-03	1.90E+02	1.35E+02	1.00E+00	1.00E+00	4.94E-01	7.10E-07	6.86E+01	9.90E-05
			0.8	1	10	5	300	300	50	1.0E-09	1.22E-02	1.48E+00	1.63E-05	1.65E-05	1.98E-03	1.85E+02	1.35E+02	1.00E+00	1.00E+00	5.63E-01	8.10E-07	6.85E+01	9.90E-05
			0.9	1	10	5	300	300	50	1.0E-09	1.36E-02	1.48E+00	1.83E-05	1.85E-05	1.98E-03	1.85E+02	1.35E+02	1.00E+00	1.00E+00	6.32E-01	9.10E-07	6.84E+01	9.90E-05
		Pore Radius									Figure 5.8 B			Figure 5.8 E		Figure 5.13 B							
											Figure 5.19, A12			Figure 5.19, A22		Figure 5.19, A28		Figure 5.19, A24					
			0.1	0.001	10	5	300	300	50	1.0E-09	1.73E-09	1.49E+00	1.06E-11	1.06E-11	2.00E-03	2.85E+02	1.55E+02	1.00E+00	1.00E+00	8.03E-08	1.16E-13	6.91E+01	9.98E-05
			0.1	0.005	10	5	300	300	50	1.0E-09	4.33E-08	1.49E+00	5.95E-11	6.02E-11	2.00E-03	2.85E+02	1.55E+02	1.00E+00	1.00E+00	2.01E-06	2.90E-12	6.91E+01	9.98E-05
			0.1	0.01	10	5	300	300	50	1.0E-09	1.73E-07	1.49E+00	2.33E-10	2.35E-10	2.00E-03	2.85E+02	1.55E+02	1.00E+00	1.00E+00	8.02E-06	1.16E-11	6.91E+01	9.98E-05
			0.1	0.05	10	5	300	300	50	1.0E-09	4.31E-06	1.49E+00	5.78E-09	5.85E-09	2.00E-03	2.85E+02	1.55E+02	1.00E+00	1.00E+00	1.99E-04	2.88E-10	6.91E+01	9.98E-05
			0.1	0.1	10	5	300	300	50	1.0E-09	1.71E-05	1.49E+00	2.30E-08	2.33E-08	2.00E-03	2.85E+02	1.55E+02	1.00E+00	1.00E+00	7.93E-04	1.15E-09	6.91E+01	9.98E-05
			0.1	0.5	10	5	300	300	50	1.0E-09	4.09E-04	1.49E+00	5.48E-07	5.55E-07	2.00E-03	2.85E+02	1.55E+02	1.00E+00	1.00E+00	1.89E-02	2.74E-08	6.91E+01	9.98E-05
			0.1	1	10	5	300	300	50	1.0E-09	1.55E-03	1.49E+00	2.07E-06	2.10E-06	2.00E-03	2.85E+02	1.55E+02	1.00E+00	1.00E+00	7.16E-02	1.03E-07	6.90E+01	9.97E-05
			0.1	5	10	5	300	300	50	1.0E-09	2.60E-02	1.47E+00	3.49E-05	3.53E-05	1.96E-03	2.75E+02	1.50E+02	1.00E+00	1.00E+00	1.21E+00	1.74E-06	6.79E+01	9.80E-05
			0.1	10	10	5	300	300	50	1.0E-09	7.01E-02	1.42E+00	9.38E-05	9.46E-05	1.90E-03	2.60E+02	1.40E+02	1.00E+00	1.00E+00	3.25E+00	4.69E-06	6.58E+01	9.50E-05
			0.1	50	10	5	300	300	50	1.0E-09	3.08E-01	1.18E+00	4.10E-04	4.08E-04	1.58E-03	2.05E+02	1.05E+02	1.00E+00	1.00E+00	1.43E+01	2.06E-05	5.45E+01	7.88E-05
			0.1	100	10	5	300	300	50	1.0E-09	4.22E-01	1.06E+00	5.57E-04	5.50E-04	1.42E-03	1.75E+02	9.50E+01	1.00E+00	1.00E+00	1.95E+01	2.82E-05	4.90E+01	7.08E-05
		Membrane Thickness									Figure 5.8 C			Figure 5.8 F		Figure 5.13 C							
											Figure 5.19, A13			Figure 5.19, A29		Figure 5.19, A38		Figure 5.19, A43					
			0.1	1	1	5	300	300	50	1.0E-09	7.80E-03	1.48E+00	1.05E-05	1.06E-05	1.99E-03	1.90E+02	1.35E+02	1.00E+00	1.00E+00	3.61E-01	5.22E-07	6.87E+01	9.92E-05
			0.1	1	5	5	300	300	50	1.0E-09	2.80E-03	1.49E+00	3.75E-06	3.78E-06	2.00E-03	2.30E+02	1.45E+02	1.00E+00	1.00E+00	1.30E-01	1.88E-07	6.89E+01	9.95E-05
			0.1	1	10	5	300	300	50	1.0E-09	1.55E-03	1.49E+00	2.07E-06	2.10E-06	2.00E-03	2.85E+02	1.55E+02	1.00E+00	1.00E+00	7.16E-02	1.03E-07	6.90E+01	9.97E-05
			0.1	1	50	5	300	300	50	1.0E-09	3.29E-04	1.49E+00	4.48E-07	4.03E-07	1.99E-03	6.70E+02	1.85E+02	1.00E+00	1.00E+00	1.52E-02	2.20E-08	6.89E+01	9.96E-05
			0.1	1	100	5	300	300	50	1.0E-09	1.65E-04	1.49E+00	2.26E-07	2.05E-07	1.98E-03	1.12E+03	1.50E+02	1.00E+00	1.00E+00	7.65E-03	1.11E-08	6.89E+01	9.96E-05
			0.1	1	500	5	300	300	50	1.0E-09	2.99E-05	1.45E+00	4.53E-08	3.64E-08	2.00E-03	3.70E+03	5.50E+01	1.00E+00	1.00E+00	1.38E-03	2.00E-09	6.74E+01	9.73E-05
			0.1	1	1000	5	300	300	50	1.0E-09	1.45E-05	1.45E+00	2.08E-08	1.48E-08	1.99E-03	3.70E+03	5.50E+01	1.00E+00	1.00E+00	6.72E-04	9.71E-10	6.73E+01	9.73E-05
		Membrane Length									Figure 5.9 A			Figure 5.9 D		Figure 5.14 A							
											Figure 5.19, A14			Figure 5.19, A24		Figure 5.19, A34		Figure 5.19, A44					
			0.1	1	10	0.1	300	300	50	1.0E-09	5.57E-07	1.49E+00	1.19E-09	6.02E-08	1.97E-03	1.96E+03	2.00E+01	1.00E+00	1.00E+00	2.58E-05	3.73E-11	6.92E+01	1.00E-04
			0.1	1	10	0.25	300	300	50	1.0E-09	6.75E-06	1.49E+00	8.15E-09	8.88E-08	1.98E-03	1.07E+03	2.00E+01	1.00E+00	1.00E+00	3.13E-04	4.52E-10	6.91E+01	9.99E-05
			0.1	1	10	0.5	300	300	50	1.0E-09	2.27E-05	1.49E+00	3.06E-08	9.56E-08	1.99E-03	7.20E+02	3.00E+01	1.00E+00	1.00E+00	1.05E-03	1.52E-09	6.91E+01	9.98E-05
			0.1	1	10	0.75	300	300	50	1.0E-09	4.36E-05	1.49E+00	5.82E-08	1.11E-07	1.99E-03	5.95E+02	5.00E+01	1.00E+00	1.00E+00	2.02E-03	2.92E-09	6.91E+01	9.98E-05
			0.1	1	10	1	300	300	50	1.0E-09	7.10E-05	1.49E+00	9.52E-08	1.44E-07	2.00E-03	5.20E+02	6.50E+01	1.00E+00	1.00E+00	3.29E-03	4.75E-09	6.91E+01	9.98E-05
			0.1	1	10	2.5	300	300	50	1.0E-09	3.94E-04	1.49E+00	5.29E-07	5.64E-07	2.00E-03	3.50E+02	1.10E+02	1.00E+00	1.00E+00	1.82E-02	2.64E-08	6.91E+01	9.98E-05
			0.1	1	10	5	300	300	50	1.0E-09	1.55E-03	1.49E+00	2.07E-06	2.10E-06	2.00E-03	2.85E+02	1.55E+02	1.00E+00	1.00E+00	7.16E-02	1.03E-07	6.90E+01	9.97E-05
			0.1	1	10	7.5	300	300	50	1.0E-09	3.49E-03	1.49E+00	4.64E-06	4.64E-06	2.00E-03	2.85E+02	1.95E+02	1.00E+00	1.00E+00	1.62E-01	2.34E-07	6.89E+01	9.96E-05
			0.1	1	10	10	300	300	50	1.0E-09	6.13E-03	1.49E+00	8.21E-06	8.16E-06	1.99E-03	3.05E+02	2.35E+02	1.00E+00	1.00E+00	2.84E-01	4.10E-07	6.88E+01	9.94E-05
			0.1	1	10	25	300	300	50	1.0E-09	3.64E-02	1.46E+00	4.88E-05	4.83E-05	1.95E-03	4.75E+02	4.25E+02	1.00E+00	1.00E+00	1.68E+00	2.43E-06	6.74E+01	9.73E-05
			0.1	1	10	50	300	300	50	1.0E-09	1.23E-01	1.35E+00	1.62E-04	1.67E-04	1.79E-03	7.60E+02	7.20E+02	1.00E+00	1.00E+00	5.70E+00	8.23E-06	6.25E+01	9.08E-05
			0.1	1	10	75	300	300	50	1.0E-09	2.20E-01	1.25E+00	3.01E-04	3.03E-04	1.71E-03	1.05E+03	1.02E+03	1.00E+00	1.00E+00	1.02E+01	1.47E-05	5.80E+01	8.38E-05
			0.1	1	10	100	300	300	50	1.0E-09	3.08E-01	1.17E+00	4.15E-04	4.23E-04	1.57E-03	1.35E+03	1.32E+03	1.00E+00	1.00E+00	1.42E+01	2.06E-05	5.41E+01	7.81E-05
		Cell Channel Height									Figure 5.9 B			Figure 5.9 E		Figure 5.14 B							
											Figure 5.19, A15			Figure 5.19, A25		Figure 5.19, A35		Figure 5.19, A45					
			0.1	1	10	5	10	300	50	1.0E-09	4.24E-05	1.50E+00	3.56E-05	5.44E-05	1.97E-03	5.00E+01	5.00E+01	1.00E+00	1.00E+00	3.80E-03	5.49E-09	6.93E+01	1.00E-04
			0.1	1	10	5	50	300	50	1.0E-09	1.17E-03	1.49E+00	3.58E-05	4.19E-05	1.98E-03	6.50E+01	5.50E+01	1.00E+00	1.00E+00	9.28E-02	1.34E-07	6.92E+01	9.99E-05
			0.1	1	10	5	100	300	50	1.0E-09	1.43E-03	1.49E+00	1.56E-05	1.58E-05	1.99E-03	1.00E+02	7.50E+01	1.00E+00	1.00E+00	9.90E-02	1.43E-07	6.91E+01	9.98E-05
			0.1	1	10	5	500	300	50	1.0E-09	1.59E-03	1.48E+00	7.65E-07	8.06E-07	1.96E-03	5.10E+02	2.55E+02	1.00E+00	1.00E+00	5.52E-02	7.97E-08	6.86E+01	9.91E-05
			0.1	1	10	5	1000	300	50	1.0E-09	1.66E-03	1.48E+00	1.99E-07	2.30E-07	1.97E-03	1.17E+03	5.45E+02	1.00E+00	1.00E+00	3.56E-02	5.14E-08	6.85E+01	9.89E-05
			0.1	1	10	5	5000	300	50	1.0E-09	1.91E-03	1.45E+00	6.49E-09	4.54E-08	1.95E-03	3.70E+03	2.52E+03	1.00E+00	1.00E+00	1.00E-02	1.44E-08	6.70E+01	9.67E-05
			0.1	1	10	5	10000	300	50	1.0E-09	1.05E-03	1.45E+00	3.04E-11	4.28E-08	1.94E-03	3.70E+03	2.77E+03	1.00E+00	1.00E+00	2.83E-03	4.09E-09	6.70E+01	9.68E-05
		Flow Channel Height									Figure 5.9 C			Figure 5.9 F		Figure 5.14 C							
											Figure 5.19, A16			Figure 5.19, A26		Figure 5.19, A36		Figure 5.19, A46					
			0.1	1	10	5	300	10	50	1.0E-09	1.28E+00	2.10E-01	1.67E-03	1.74E-03	1.48E-01	6.00E+01	5.00E+01	1.00E+00	1.00E+00	5.94E+01	8.58E-05	1.88E+01	2.72E-05
			0.1	1	10	5	300	50	50	1.0E-09	2.63E-01	1.21E+00	3.51E-04	3.34E-04	4.05E-02	1.60E+02	9.00E+01	1.00E+00	1.00E+00	1.22E+01	1.76E-05	9.60E+01	1.39E-04
			0.1	1	10	5	300	100	50	1.0E-09	4.04E-02	1.43E+00	5.36E-05	5.24E-05	1.51E-02	2.15E+02	1.20E+02	1.00E+00	1.00E+00	1.87E+00	2.71E-06	9.93E+01	1.43E-04
			0.1	1	10	5	300	500	50	1.0E-09	3.31E-04	1.49E+00	4.44E-07	4.65E-07	7.30E-04	3.35E+02	1.90E+02	1.00E+00	1.00E+00	1.54E-02	2.23E-08	5.18E+01	7.49E-05
			0.1	1	10	5	300	1000	50	1.0E-09	4.16E-05	1.49E+00	5.68E-08	6.01E-08	1.88E-04	4.65E+02	2.70E+02	1.00E+00	1.00E+00	1.93E-03	2.79E-09	3.19E+01	4.61E-05
			0.1	1	10	5	300	5000	50	1.0E-09	3.30E-07	1.46E+00	4.89E-10	5.78E-10	8.16E-06	1.61E+03	1.11E+03	1.00E+00	1.00E+00	1.53E-05	2.21E-11	7.64E+00	1.10E-05
			0.1	1	10	5	300	10000	50	1.0E-09	5.53E-08	1.35E+00	8.67E-11	1.14E-10	2.70E-06	3.23E+03	2.31E+03	1.00E+00	1.00E+00	2.56E-06	3.70E-12	3.64E+00	5.26E-06
		Inlet Flow Rate									Figure 5.10 A			Figure 5.10 C		Figure 5.15 A							
											Figure 5.19, A17			Figure 5.19, A27		Figure 5.19, A37		Figure 5.19, A47					
			0.1	1	10	5	300	300	0.1	1.0E-09	1.55E-03	1.49E+00	4.15E-09	4.20E-09	4.00E-06	3.70E+03	3.60E+03	1.00E+00	1.00E+00	1.43E-04	2.07E-10	1.38E-01	1.99E-07
			0.1	1	10	5	300	300	0.5	1.0E-09	1.55E-03	1.49E+00	2.07E-08	2.10E-08	2.00E-05	3.70E+03	3.60E+03	1.00E+00	1.00E+00	7.16E-04	1.03E-09	6.90E-01	9.97E-07
			0.1	1	10	5	300	300	1	1.0E-09	1.55E-03	1.49E+00	4.15E-08	4.20E-08	4.00E-05	3.70E+03	3.60E+03	1.00E+00	1.00E+00	1.43E-03	2.07E-09	1.38E+00	1.99E-06
			0.1	1	10	5	300	300	5	1.0E-09	1.55E-03	1.49E+00	2.07E-07	2.10E-07	2.00E-04	1.34E+03	1.27E+03	1.00E+00	1.00E+00	7.16E-03	1.03E-08	6.90E+00	9.97E-06
			0.1	1	10	5	300	300	10	1.0E-09	1.55E-03	1.49E+00	4.15E-07	4.20E-07	4.00E-04	7.35E+02	6.45E+02	1.00E+00	1.00E+00	1.43E-02	2.07E-08	1.38E+01	1.99E-05
			0.1	1	10	5	300	300	50	1.0E-09	1.55E-03	1.49E+00	2.07E-06	2.10E-06	2.00E-03	2.85E+02	1.55E+02	1.00E+00	1.00E+00	7.16E-02	1.03E-07	6.90E+01	9.97E-05
			0.1	1	10	5	300	300	100	1.0E-09	1.55E-03	1.49E+00	4.15E-06	4.20E-06	4.00E-03	2.25E+02	9.00E+01	1.00E+00	1.00E+00	1.43E-01	2.07E-07	1.38E+02	1.99E-04
			0.1	1	10	5	300	300	500	1.0E-09	1.55E-03	1.49E+00	2.07E-05	2.10E-05	2.00E-02	1.70E+02	1.50E+01	1.00E+00	1.00E+00	7.16E-01	1.03E-06	6.90E+02	9.97E-04
			0.1	1	10	5	300	300	1000	1.0E-09	1.55E-03	1.49E+00	4.15E-05	4.20E-05	4.00E-02	1.55E+02	1.00E+01	1.00E+00	1.00E+00	1.43E+00	2.07E-06	1.38E+03	1.99E-03
		Diffusion Coefficient Rate									Figure 5.10 B			Figure 5.10 D		Figure 5.15 B							
											Figure 5.19, A18			Figure 5.19, A28		Figure 5.19, A38		Figure 5.19, A48					
			0.1	1	10	5	300	300	50	1.0E-13	1.55E-03	1.49E+00	2.07E-06	2.10E-06	2.00E-03	3.70E+03	1.25E+02	1.00E+00	1.00E+00	7.16E+02	1.03E-07	6.90E+05	9.97E-05
			0.1	1	10	5	300	300	50	1.0E-12	1.55E-03	1.49E+00	2.07E-06	2.10E-06	2.00E-03	3.70E+03	1.15E+02	1.00E+00	1.00E+00	7.16E+01	1.03E-07	6.90E+04	9.97E-05
			0.1	1	10	5	300	300	50	1.0E-11	1.55E-03	1.49E+00	2.07E-06	2.10E-06	2.00E-03	3.70E+03	9.00E+01	1.00E+00	1.00E+00	7.16E+00	1.03E-07	6.90E+03	9.97E-05
			0.1	1	10	5	300	300	50	1.0E-10	1.55E-03	1.49E+00	2.07E-06	2.10E-06	2.00E-03	3.70E+03	7.00E+01	1.00E+00	1.00E+00	7.16E-01	1.03E-07	6.90E+02	9.97E-05
			0.1	1	10	5	300	300	50	1.0E-09	1.55E-03	1.49E+00	2.07E-06	2.10E-06	2.00E-03	6.45E+02	1.85E+02	1.00E+00	1.00E+00	7.16E-02	1.03E-07	6.90E+01	9.97E-05
			0.1	1	10	5	300	300	50	1.0E-08	1.55E-03	1.49E+00	2.07E-06	2.10E-06	2.00E-03	1.75E+02	1.35E+02	1.00E+00	1.00E+00	7.16E-03	1.03E-07	6.90E+00	9.97E-05
			0.1	1	10	5	300	300	50	1.0E-07	1.55E-03	1.49E+00	2.07E-06	2.10E-06	2.00E-03	1.50E+02	1.50E+02	1.00E+00	1.00E+00	7.16E-04	1.03E-07	6.90E-01	9.97E-05
		Porosity																					
											Figure 5.19, B11			Figure 5.19, B21		Figure 5.19, B31		Figure 5.19, B41					
			0.001	1	10	5	300	300	50	1.0E-09	7.92E-05	1.49E+00	1.08E-07	1.09E-07	2.00E-03	3.70E+03	5.00E+01	1.00E+00	1.00E+00	3.67E-03	5.30E-09	6.91E+01	9.98E-05
			0.01	1	10	5	300	300	50	1.0E-09	7.91E-04	1.49E+00	1.08E-06	1.09E-06	2.00E-03	2.02E+03	5.50E+01	1.00E+00	1.00E+00	3.66E-02	5.29E-08	6.90E+01	9.97E-05
			0.1	1	10	5	300	300	50	1.0E-09	7.81E-03	1.48E+00	1.06E-05	1.08E-05	1.99E-03	2.70E+02	1.55E+02	1.00E+00	1.00E+00	3.62E-01	5.22E-07	6.87E+01	9.92E-05
			0.2	1	10	5	300	300	50	1.0E-09	1.54E-02	1.48E+00	2.09E-05	2.13E-05	1.98E-03	2.05E+02	1.40E+02	1.00E+00	1.00E+00	7.13E-01	1.03E-06	6.83E+01	9.87E-05
			0.3	1	10	5	300	300	50	1.0E-09	2.28E-02	1.47E+00	3.10E-05	3.14E-05	1.97E-03	1.90E+02	1.35E+02	1.00E+00	1.00E+00	1.06E+00	1.53E-06	6.80E+01	9.82E-05
			0.4	1	10	5	300	300	50	1.0E-09	3.00E-02	1.46E+00	4.08E-05	4.14E-05	1.96E-03	1.80E+02	1.35E+02	1.00E+00	1.00E+00	1.39E+00	2.01E-06	6.76E+01	9.77E-05
			0.5	1	10	5	300	300	50	1.0E-09	3.70E-02	1.45E+00	5.03E-05	5.10E-05	1.95E-03	1.75E+02	1.30E+02	1.00E+00	1.00E+00	1.71E+00	2.47E-06	6.73E+01	9.72E-05
			0.6	1	10	5	300	300	50	1.0E-09	4.38E-02	1.45E+00	5.96E-05	6.05E-05	1.94E-03	1.70E+02	1.30E+02	1.00E+00	1.00E+00	2.01E+00	2.91E-06	6.70E+01	9.68E-05
			0.7	1	10	5	300	300	50	1.0E-09	5.05E-02	1.44E+00	6.86E-05	6.96E-05	1.93E-03	1.70E+02	1.30E+02	1.00E+00	1.00E+00	2.34E+00	3.38E-06	6.67E+01	9.63E-05
			0.8	1	10	5	300	300	50	1.0E-09	5.70E-02	1.43E+00	7.74E-05	7.86E-05	1.92E-03	1.65E+02	1.30E+02	1.00E+00	1.00E+00	2.64E+00	3.81E-06	6.64E+01	9.59E-05
			0.9	1	10	5	300	300	50	1.0E-09	6.33E-02	1.43E+00	8.60E-05	8.73E-05	1.91E-03	1.65E+02	1.30E+02	1.00E+00	1.00E+00	2.93E+00	4.23E-06	6.61E+01	9.54E-05
		Pore Radius																					
											Figure 5.19, B12			Figure 5.19, B22		Figure 5.19, B32		Figure 5.19, B42					
			0.1	0.001	10	5	300	300	50	1.0E-09	8.85E-09	1.49E+00	1.64E-11	1.65E-11	2.00E-03	2.85E+02	1.55E+02	1.00E+00	1.00E+00	4.10E-07	5.92E-13	6.91E+01	9.98E-05
			0.1	0.005	10	5	300	300	50	1.0E-09	2.21E-07	1.49E+00	3.01E-10	3.06E-10	2.00E-03	2.85E+02	1.55E+02	1.00E+00	1.00E+00	1.02E-05	1.48E-11	6.91E+01	9.98E-05
			0.1	0.01	10	5	300	300	50	1.0E-09	8.84E-07	1.49E+00	1.20E-09	1.22E-09	2.00E-03	2.85E+02	1.55E+02	1.00E+00	1.00E+00	4.09E-05	5.92E-11	6.91E+01	9.98E-05
			0.1	0.05	10	5	300	300	50	1.0E-09	2.20E-05	1.49E+00	2.99E-08	3.04E-08	2.00E-03	2.85E+02	1.55E+02	1.00E+00	1.00E+00	1.02E-03	1.47E-09	6.91E+01	9.98E-05
			0.1	0.1	10	5	300	300	50	1.0E-09	8.75E-05	1.49E+00	1.19E-07	1.21E-07	2.00E-03	2.85E+02	1.55E+02	1.00E+00	1.00E+00	4.05E-03	5.85E-09	6.91E+01	9.98E-05
			0.1	0.5	10	5	300	300	50	1.0E-09	2.08E

Outlet (SCPO)	Membrane Thi	0.1	1	5	5	300	300	50	1.0E-09	1.43E-02	1.48E+00	1.90E-05	1.90E-05	1.98E-03	2.15E+02	1.45E+02	1.00E+00	1.00E+00	6.60E-01	9.54E-07	6.83E+01	9.87E-05
		0.1	1	10	5	300	300	50	1.0E-09	7.81E-03	1.48E+00	1.06E-05	1.08E-05	1.99E-03	2.70E+02	1.55E+02	1.00E+00	1.00E+00	3.62E-01	5.22E-07	6.87E+01	9.92E-05
		0.1	1	50	5	300	300	50	1.0E-09	1.74E-03	1.49E+00	2.33E-06	2.27E-06	1.99E-03	6.60E+02	1.85E+02	1.00E+00	1.00E+00	8.08E-02	1.17E-07	6.89E+01	9.95E-05
		0.1	1	100	5	300	300	50	1.0E-09	8.82E-04	1.49E+00	1.17E-06	1.14E-06	1.98E-03	1.10E+03	1.50E+02	1.00E+00	1.00E+00	4.08E-02	5.90E-08	6.89E+01	9.95E-05
		0.1	1	500	5	300	300	50	1.0E-09	1.72E-04	1.45E+00	2.39E-07	2.19E-07	2.00E-03	3.70E+03	5.50E+01	1.00E+00	1.00E+00	7.94E-03	1.15E-08	6.74E+01	9.73E-05
		0.1	1	1000	5	300	300	50	1.0E-09	8.61E-05	1.45E+00	1.15E-07	9.95E-08	1.99E-03	3.70E+03	5.50E+01	1.00E+00	1.00E+00	3.98E-03	5.76E-09	6.73E+01	9.73E-05
	Membrane Length									*Figure 5.19, B14*		*Figure 5.19, B24*		*Figure 5.19, B34*		*Figure 5.19, B44*						
		0.1	1	10	0.1	300	300	50	1.0E-09	5.58E-05	1.49E+00	5.14E-08	4.11E-07	1.97E-03	1.95E+03	2.00E+01	1.00E+00	1.00E+00	2.59E-03	3.73E-09	6.92E+01	1.00E-04
		0.1	1	10	0.25	300	300	50	1.0E-09	1.32E-04	1.49E+00	1.48E-07	3.59E-07	1.98E-03	1.06E+03	2.00E+01	1.00E+00	1.00E+00	6.11E-03	8.82E-09	6.91E+01	9.99E-05
		0.1	1	10	0.5	300	300	50	1.0E-09	2.69E-04	1.49E+00	3.38E-07	4.52E-07	1.99E-03	7.15E+02	3.00E+01	1.00E+00	1.00E+00	1.25E-02	1.80E-08	6.91E+01	9.98E-05
		0.1	1	10	0.75	300	300	50	1.0E-09	4.39E-04	1.49E+00	5.68E-07	6.42E-07	1.99E-03	5.90E+02	5.00E+01	1.00E+00	1.00E+00	2.03E-02	2.94E-08	6.91E+01	9.98E-05
		0.1	1	10	1	300	300	50	1.0E-09	6.30E-04	1.49E+00	8.35E-07	9.01E-07	2.00E-03	5.15E+02	6.50E+01	1.00E+00	1.00E+00	2.92E-02	4.21E-08	6.91E+01	9.98E-05
		0.1	1	10	2.5	300	300	50	1.0E-09	2.47E-03	1.49E+00	3.30E-06	3.38E-06	2.00E-03	3.40E+02	1.10E+02	1.00E+00	1.00E+00	1.14E-01	1.65E-07	6.90E+01	9.97E-05
		0.1	1	10	5	300	300	50	1.0E-09	7.81E-03	1.48E+00	1.06E-05	1.08E-05	1.99E-03	2.70E+02	1.55E+02	1.00E+00	1.00E+00	3.62E-01	5.22E-07	6.87E+01	9.92E-05
		0.1	1	10	7.5	300	300	50	1.0E-09	1.62E-02	1.48E+00	2.17E-05	2.20E-05	1.98E-03	2.75E+02	1.90E+02	1.00E+00	1.00E+00	7.49E-01	1.08E-06	6.83E+01	9.87E-05
		0.1	1	10	10	300	300	50	1.0E-09	2.73E-02	1.46E+00	3.64E-05	3.68E-05	1.96E-03	2.90E+02	2.25E+02	1.00E+00	1.00E+00	1.27E+00	1.83E-06	6.78E+01	9.80E-05
		0.1	1	10	25	300	300	50	1.0E-09	1.29E-01	1.36E+00	1.73E-04	1.75E-04	1.83E-03	4.40E+02	4.05E+02	1.00E+00	1.00E+00	5.95E+00	8.61E-06	6.31E+01	9.11E-05
		0.1	1	10	50	300	300	50	1.0E-09	3.13E-01	1.17E+00	4.12E-04	4.23E-04	1.94E-03	7.10E+02	6.90E+02	1.00E+00	1.00E+00	1.45E+01	2.09E-05	5.40E+01	7.81E-05
		0.1	1	10	75	300	300	50	1.0E-09	4.31E-01	1.04E+00	5.89E-04	5.96E-04	1.42E-03	1.01E+03	9.95E+02	1.00E+00	1.00E+00	2.00E+01	2.88E-05	4.82E+01	6.96E-05
		0.1	1	10	100	300	300	50	1.0E-09	5.05E-01	9.72E-01	6.80E-04	6.94E-04	1.31E-03	1.31E+03	1.31E+03	1.00E+00	1.00E+00	2.34E+01	3.38E-05	4.50E+01	6.50E-05
	Cell Channel Height									*Figure 5.19, B15*		*Figure 5.19, B25*		*Figure 5.19, B35*		*Figure 5.19, B45*						
		0.1	1	10	5	10	300	50	1.0E-09	4.62E-05	1.50E+00	3.80E-05	5.92E-05	1.97E-03	5.00E+01	5.00E+01	1.00E+00	1.00E+00	4.14E-03	5.98E-09	6.93E+01	1.00E-04
		0.1	1	10	5	50	300	50	1.0E-09	3.19E-03	1.49E+00	9.36E-05	1.13E-04	1.97E-03	6.50E+01	5.50E+01	1.00E+00	1.00E+00	2.53E-01	3.65E-07	6.91E+01	9.98E-05
		0.1	1	10	5	100	300	50	1.0E-09	6.56E-03	1.49E+00	7.03E-05	7.40E-05	1.98E-03	9.50E+01	7.50E+01	1.00E+00	1.00E+00	4.56E-01	6.58E-07	6.89E+01	9.95E-05
		0.1	1	10	5	500	300	50	1.0E-09	8.01E-03	1.48E+00	3.91E-06	4.01E-06	1.99E-03	4.90E+02	2.55E+02	1.00E+00	1.00E+00	2.78E-01	4.02E-07	6.83E+01	9.87E-05
		0.1	1	10	5	1000	300	50	1.0E-09	8.09E-03	1.47E+00	1.00E-06	1.05E-06	1.96E-03	1.14E+03	5.35E+02	1.00E+00	1.00E+00	1.73E-01	2.50E-07	6.82E+01	9.85E-05
		0.1	1	10	5	5000	300	50	1.0E-09	9.14E-03	1.44E+00	3.72E-08	8.12E-08	1.94E-03	3.70E+03	2.39E+03	1.00E+00	1.00E+00	4.79E-02	6.92E-08	6.67E+01	9.63E-05
		0.1	1	10	5	10000	300	50	1.0E-09	9.81E-03	1.44E+00	4.32E-09	6.25E-08	1.93E-03	3.70E+03	2.56E+03	1.00E+00	1.00E+00	2.64E-02	3.82E-08	6.67E+01	9.63E-05
	Flow Channel Height									*Figure 5.19, B16*		*Figure 5.19, B26*		*Figure 5.19, B36*		*Figure 5.19, B46*						
		0.1	1	10	5	300	10	50	1.0E-09	1.35E+00	1.06E-01	1.78E-03	1.84E-03	7.14E-02	5.50E+01	5.50E+01	1.00E+00	1.00E+00	6.27E+01	9.06E-05	9.48E+00	1.37E-05
		0.1	1	10	5	300	50	50	1.0E-09	6.93E-01	7.82E-01	9.33E-04	9.25E-04	2.60E-02	1.10E+02	6.50E+01	1.00E+00	1.00E+00	3.21E+01	4.63E-05	6.21E+01	8.97E-05
		0.1	1	10	5	300	100	50	1.0E-09	1.82E-01	1.29E+00	2.41E-04	2.44E-04	1.37E-02	1.60E+02	1.05E+02	1.00E+00	1.00E+00	8.45E+00	1.22E-05	8.96E+01	1.29E-04
		0.1	1	10	5	300	500	50	1.0E-09	1.70E-03	1.49E+00	2.26E-06	2.35E-06	7.29E-04	3.30E+02	1.90E+02	1.00E+00	1.00E+00	7.89E-02	1.14E-07	5.18E+01	7.48E-05
		0.1	1	10	5	300	1000	50	1.0E-09	2.13E-04	1.49E+00	2.85E-07	2.95E-07	1.88E-04	4.60E+02	2.70E+02	1.00E+00	1.00E+00	9.84E-03	1.42E-08	3.19E+01	4.61E-05
		0.1	1	10	5	300	5000	50	1.0E-09	1.61E-06	1.46E+00	2.22E-09	2.34E-09	8.16E-06	1.61E+03	1.11E+03	1.00E+00	1.00E+00	7.44E-05	1.08E-10	7.64E+00	1.10E-05
		0.1	1	10	5	300	10000	50	1.0E-09	2.40E-07	1.35E+00	3.41E-10	3.67E-10	2.70E-06	3.23E+03	2.31E+03	1.00E+00	1.00E+00	1.11E-05	1.61E-11	3.64E+00	5.26E-06
	Inlet Flow Rate									*Figure 5.19, B17*		*Figure 5.19, B27*		*Figure 5.19, B37*		*Figure 5.19, B47*						
		0.1	1	10	5	300	300	0.1	1.0E-09	7.81E-03	1.48E+00	2.12E-08	2.15E-08	1.98E-06	3.70E+03	3.60E+03	1.00E+00	1.00E+00	7.23E-04	1.04E-09	1.37E-01	1.98E-07
		0.1	1	10	5	300	300	0.5	1.0E-09	7.81E-03	1.48E+00	1.06E-07	1.08E-07	1.99E-05	3.70E+03	3.60E+03	1.00E+00	1.00E+00	3.62E-03	5.22E-09	6.87E-01	9.92E-07
		0.1	1	10	5	300	300	1	1.0E-09	7.81E-03	1.48E+00	2.12E-07	2.15E-07	3.98E-05	3.70E+03	3.60E+03	1.00E+00	1.00E+00	7.23E-03	1.04E-08	1.37E+00	1.98E-06
		0.1	1	10	5	300	300	5	1.0E-09	7.81E-03	1.48E+00	1.06E-06	1.08E-06	1.99E-04	1.34E+03	1.27E+03	1.00E+00	1.00E+00	3.62E-02	5.22E-08	6.87E+00	9.92E-06
		0.1	1	10	5	300	300	10	1.0E-09	7.81E-03	1.48E+00	2.12E-06	2.15E-06	3.98E-04	7.30E+02	6.40E+02	1.00E+00	1.00E+00	7.23E-02	1.04E-07	1.37E+01	1.98E-05
		0.1	1	10	5	300	300	50	1.0E-09	7.81E-03	1.48E+00	1.06E-05	1.08E-05	1.99E-03	2.70E+02	1.55E+02	1.00E+00	1.00E+00	3.62E-01	5.22E-07	6.87E+01	9.92E-05
		0.1	1	10	5	300	300	100	1.0E-09	7.81E-03	1.48E+00	2.12E-05	2.15E-05	3.98E-03	2.05E+02	9.00E+01	1.00E+00	1.00E+00	7.23E-01	1.04E-06	1.37E+02	1.98E-04
		0.1	1	10	5	300	300	500	1.0E-09	7.81E-03	1.48E+00	1.06E-04	1.08E-04	1.99E-02	1.35E+02	1.50E+01	1.00E+00	1.00E+00	3.62E+00	5.22E-06	6.87E+02	9.92E-04
		0.1	1	10	5	300	300	1000	1.0E-09	7.81E-03	1.48E+00	2.12E-04	2.15E-04	3.98E-02	1.20E+02	1.00E+01	1.00E+00	1.00E+00	7.23E+00	1.04E-05	1.37E+03	1.99E-03
	Diffusion Coefficient Rate									*Figure 5.19, B18*		*Figure 5.19, B28*		*Figure 5.19, B38*		*Figure 5.19, B48*						
		0.1	1	10	5	300	300	50	1.0E-13	7.81E-03	1.48E+00	1.06E-05	1.08E-05	1.99E-03	3.70E+03	1.10E+02	1.00E+00	1.00E+00	3.62E-03	5.22E-07	6.87E-05	9.92E-05
		0.1	1	10	5	300	300	50	1.0E-12	7.81E-03	1.48E+00	1.06E-05	1.08E-05	1.99E-03	3.70E+03	1.05E+02	1.00E+00	1.00E+00	3.62E+02	5.22E-07	6.87E+04	9.92E-05
		0.1	1	10	5	300	300	50	1.0E-11	7.81E-03	1.48E+00	1.06E-05	1.08E-05	1.99E-03	3.70E+03	8.50E+01	1.00E+00	1.00E+00	3.62E+01	5.22E-07	6.87E+03	9.92E-05
		0.1	1	10	5	300	300	50	1.0E-10	7.81E-03	1.48E+00	1.06E-05	1.08E-05	1.99E-03	3.42E+03	6.50E+01	1.00E+00	1.00E+00	3.62E+00	5.22E-07	6.87E+02	9.92E-05
		0.1	1	10	5	300	300	50	1.0E-09	7.81E-03	1.48E+00	1.06E-05	1.08E-05	1.99E-03	3.70E+03	1.80E+02	1.00E+00	1.00E+00	3.62E-01	5.22E-07	6.87E+01	9.92E-05
		0.1	1	10	5	300	300	50	1.0E-08	7.81E-03	1.48E+00	1.06E-05	1.08E-05	1.99E-03	1.70E+02	1.35E+02	1.00E+00	1.00E+00	3.62E-02	5.22E-07	6.87E+00	9.92E-05
		0.1	1	10	5	300	300	50	1.0E-07	7.81E-03	1.48E+00	1.06E-05	1.08E-05	1.99E-03	1.50E+02	1.50E+02	1.00E+00	1.00E+00	3.62E-03	5.22E-07	6.87E-01	9.92E-05
Slime Direction Flow (PPSD)																	*Figure 5.13 D*					
	Porosity									*Figure 5.19, C11*		*Figure 5.19, C21*		*Figure 5.19, C31*		*Figure 5.19, C41*						
		0.001	1	10	5	300	300	50	1.0E-09	1.49E+00	1.49E+00	2.00E-03	2.03E-03	2.00E-03	5.50E+01	5.00E+01	1.89E-03	9.98E-01	6.91E+01	9.98E-05	6.91E+01	9.98E-05
		0.01	1	10	5	300	300	50	1.0E-09	1.49E+00	1.49E+00	2.00E-03	2.03E-03	2.00E-03	5.50E+01	5.00E+01	3.73E-02	9.63E-01	6.91E+01	9.98E-05	6.91E+01	9.98E-05
		0.1	1	10	5	300	300	50	1.0E-09	1.49E+00	1.49E+00	2.00E-03	2.03E-03	2.00E-03	5.00E+01	5.00E+01	2.67E-01	7.33E-01	6.91E+01	9.98E-05	6.91E+01	9.98E-05
		0.2	1	10	5	300	300	50	1.0E-09	1.49E+00	1.49E+00	2.00E-03	2.03E-03	2.00E-03	5.50E+01	5.00E+01	3.20E-01	6.80E-01	6.91E+01	9.98E-05	6.91E+01	9.98E-05
		0.3	1	10	5	300	300	50	1.0E-09	1.49E+00	1.49E+00	2.00E-03	2.03E-03	2.00E-03	5.50E+01	5.00E+01	3.38E-01	6.62E-01	6.91E+01	9.98E-05	6.91E+01	9.98E-05
		0.4	1	10	5	300	300	50	1.0E-09	1.49E+00	1.49E+00	2.00E-03	2.03E-03	2.00E-03	5.50E+01	5.00E+01	3.46E-01	6.54E-01	6.91E+01	9.98E-05	6.91E+01	9.98E-05
		0.5	1	10	5	300	300	50	1.0E-09	1.49E+00	1.49E+00	2.00E-03	2.03E-03	2.00E-03	5.50E+01	5.00E+01	3.51E-01	6.49E-01	6.91E+01	9.98E-05	6.91E+01	9.98E-05
		0.6	1	10	5	300	300	50	1.0E-09	1.49E+00	1.49E+00	2.00E-03	2.03E-03	2.00E-03	5.50E+01	5.00E+01	3.54E-01	6.46E-01	6.91E+01	9.98E-05	6.91E+01	9.98E-05
		0.7	1	10	5	300	300	50	1.0E-09	1.49E+00	1.49E+00	2.00E-03	2.03E-03	2.00E-03	5.50E+01	5.00E+01	3.56E-01	6.44E-01	6.91E+01	9.98E-05	6.91E+01	9.98E-05
		0.8	1	10	5	300	300	50	1.0E-09	1.49E+00	1.49E+00	2.00E-03	2.03E-03	2.00E-03	5.50E+01	5.00E+01	3.58E-01	6.42E-01	6.91E+01	9.98E-05	6.91E+01	9.98E-05
		0.9	1	10	5	300	300	50	1.0E-09	1.49E+00	1.49E+00	2.00E-03	2.03E-03	2.00E-03	5.50E+01	5.00E+01	3.59E-01	6.41E-01	6.91E+01	9.98E-05	6.91E+01	9.98E-05
	Pore Radius									*Figure 10 b)*							*Figure 5.13 E*					
										Figure 5.19, C12		*Figure 5.19, C22*		*Figure 5.19, C32*		*Figure 5.19, C42*						
		0.1	0.001	10	5	300	300	50	1.0E-09	1.49E+00	1.49E+00	2.00E-03	2.03E-03	2.00E-03	5.00E+01	4.50E+01	2.67E-01	7.33E-01	6.91E+01	9.98E-05	6.91E+01	9.98E-05
		0.1	0.005	10	5	300	300	50	1.0E-09	1.49E+00	1.49E+00	2.00E-03	2.03E-03	2.00E-03	5.00E+01	5.00E+01	2.67E-01	7.33E-01	6.91E+01	9.98E-05	6.91E+01	9.98E-05
		0.1	0.01	10	5	300	300	50	1.0E-09	1.49E+00	1.49E+00	2.00E-03	2.03E-03	2.00E-03	5.00E+01	5.00E+01	2.67E-01	7.33E-01	6.91E+01	9.98E-05	6.91E+01	9.98E-05
		0.1	0.05	10	5	300	300	50	1.0E-09	1.49E+00	1.49E+00	2.00E-03	2.03E-03	2.00E-03	5.00E+01	5.00E+01	2.67E-01	7.33E-01	6.91E+01	9.98E-05	6.91E+01	9.98E-05
		0.1	0.1	10	5	300	300	50	1.0E-09	1.49E+00	1.49E+00	2.00E-03	2.03E-03	2.00E-03	5.00E+01	5.00E+01	2.67E-01	7.33E-01	6.91E+01	9.98E-05	6.91E+01	9.98E-05
		0.1	0.5	10	5	300	300	50	1.0E-09	1.49E+00	1.49E+00	2.00E-03	2.03E-03	2.00E-03	5.00E+01	5.00E+01	2.67E-01	7.33E-01	6.91E+01	9.98E-05	6.91E+01	9.98E-05
		0.1	1	10	5	300	300	50	1.0E-09	1.49E+00	1.49E+00	2.00E-03	2.03E-03	2.00E-03	5.00E+01	5.00E+01	2.67E-01	7.33E-01	6.91E+01	9.98E-05	6.91E+01	9.98E-05
		0.1	5	10	5	300	300	50	1.0E-09	1.49E+00	1.49E+00	2.00E-03	2.03E-03	2.00E-03	5.50E+01	5.00E+01	2.67E-01	7.33E-01	6.91E+01	9.98E-05	6.91E+01	9.98E-05
		0.1	10	10	5	300	300	50	1.0E-09	1.49E+00	1.49E+00	2.00E-03	2.03E-03	2.00E-03	5.00E+01	5.00E+01	2.67E-01	7.33E-01	6.91E+01	9.98E-05	6.91E+01	9.98E-05
		0.1	50	10	5	300	300	50	1.0E-09	1.49E+00	1.49E+00	1.99E-03	2.01E-03	1.99E-03	5.00E+01	5.00E+01	2.67E-01	7.33E-01	6.89E+01	9.95E-05	6.89E+01	9.95E-05
		0.1	100	10	5	300	300	50	1.0E-09	1.48E+00	1.48E+00	1.97E-03	1.98E-03	1.98E-03	5.00E+01	5.00E+01	2.67E-01	7.33E-01	6.86E+01	9.91E-05	6.86E+01	9.91E-05
	Membrane Thickness																*Figure 5.13 F*					
										Figure 5.19, C13		*Figure 5.19, C23*		*Figure 5.19, C33*		*Figure 5.19, C43*						
		0.1	1	1	5	300	300	50	1.0E-09	1.49E+00	1.49E+00	2.00E-03	1.99E-03	2.00E-03	6.00E+01	5.50E+01	3.51E-01	6.47E-01	6.90E+01	9.97E-05	6.90E+01	9.97E-05
		0.1	1	5	5	300	300	50	1.0E-09	1.49E+00	1.49E+00	2.00E-03	1.99E-03	2.00E-03	5.50E+01	5.00E+01	3.10E-01	6.90E-01	6.90E+01	9.97E-05	6.90E+01	9.97E-05
		0.1	1	10	5	300	300	50	1.0E-09	1.49E+00	1.49E+00	2.00E-03	2.01E-03	2.00E-03	5.00E+01	5.00E+01	2.67E-01	7.33E-01	6.91E+01	9.98E-05	6.91E+01	9.98E-05
		0.1	1	50	5	300	300	50	1.0E-09	1.49E+00	1.49E+00	1.99E-03	1.97E-03	1.99E-03	5.50E+01	5.00E+01	1.23E-01	8.77E-01	6.89E+01	9.95E-05	6.90E+01	9.96E-05
		0.1	1	100	5	300	300	50	1.0E-09	1.49E+00	1.49E+00	1.98E-03	1.96E-03	1.98E-03	5.50E+01	5.00E+01	7.28E-02	9.27E-01	6.89E+01	9.95E-05	6.89E+01	9.96E-05
		0.1	1	500	5	300	300	50	1.0E-09	1.46E+00	1.45E+00	2.00E-03	1.88E-03	2.00E-03	1.05E+02	5.50E+01	1.72E-02	9.83E-01	6.74E+01	9.73E-05	6.74E+01	9.73E-05
		0.1	1	1000	5	300	300	50	1.0E-09	1.46E+00	1.45E+00	1.94E-03	1.74E-03	1.95E-03	2.75E+02	5.50E+01	8.95E-03	9.91E-01	6.76E+01	9.77E-05	6.73E+01	9.72E-05
	Membrane Length																*Figure 5.14 D*					
										Figure 5.19, C14		*Figure 5.19, C24*		*Figure 5.19, C34*		*Figure 5.19, C44*						
		0.1	1	10	0.1	300	300	50	1.0E-09	1.49E+00	1.49E+00	1.96E-03	1.99E-03	1.96E-03	2.50E+01	2.00E+01	2.51E-02	9.75E-01	6.92E+01	9.99E-05	6.92E+01	9.99E-05
		0.1	1	10	0.25	300	300	50	1.0E-09	1.49E+00	1.49E+00	1.98E-03	1.99E-03	1.98E-03	2.50E+01	2.00E+01	4.23E-02	9.58E-01	6.91E+01	9.99E-05	6.91E+01	9.99E-05
		0.1	1	10	0.5	300	300	50	1.0E-09	1.49E+00	1.49E+00	1.99E-03	2.00E-03	1.99E-03	2.50E+01	2.50E+01	6.33E-02	9.37E-01	6.91E+01	9.98E-05	6.91E+01	9.98E-05
		0.1	1	10	0.75	300	300	50	1.0E-09	1.49E+00	1.49E+00	2.00E-03	2.01E-03	2.00E-03	2.50E+01	2.50E+01	8.13E-02	9.19E-01	6.91E+01	9.98E-05	6.91E+01	9.98E-05
		0.1	1	10	1	300	300	50	1.0E-09	1.49E+00	1.49E+00	2.00E-03	2.02E-03	2.00E-03	2.50E+01	2.50E+01	9.77E-02	9.02E-01	6.91E+01	9.98E-05	6.91E+01	9.98E-05
		0.1	1	10	2.5	300	300	50	1.0E-09	1.49E+00	1.49E+00	2.00E-03	2.03E-03	2.00E-03	4.00E+01	3.50E+01	1.78E-01	8.22E-01	6.91E+01	9.98E-05	6.91E+01	9.98E-05
		0.1	1	10	5	300	300	50	1.0E-09	1.49E+00	1.49E+00	2.00E-03	2.03E-03	2.00E-03	5.00E+01	5.00E+01	2.67E-01	7.33E-01	6.91E+01	9.98E-05	6.91E+01	9.98E-05
		0.1	1	10	7.5	300	300	50	1.0E-09	1.49E+00	1.49E+00	2.00E-03	2.03E-03	2.00E-03	6.50E+01	6.50E+01	3.23E-01	6.77E-01	6.91E+01	9.98E-05	6.91E+01	9.98E-05
		0.1	1	10	10	300	300	50	1.0E-09	1.49E+00	1.49E+00	2.00E-03	2.03E-03	2.00E-03	8.00E+01	8.00E+01	3.60E-01	6.40E-01	6.91E+01	9.98E-05	6.91E+01	9.98E-05
		0.1	1	10	25	300	300	50	1.0E-09	1.49E+00	1.49E+00	2.00E-03	2.04E-03	2.00E-03	1.80E+02	1.75E+02	4.42E-01	5.58E-01	6.91E+01	9.98E-05	6.91E+01	9.98E-05
		0.1	1	10	50	300	300	50	1.0E-09	1.48E+00	1.48E+00	1.95E-03	2.03E-03	1.95E-03	3.40E+02	3.35E+02	4.71E-01	5.29E-01	6.85E+01	9.90E-05	6.85E+01	9.90E-05
		0.1	1	10	75	300	300	50	1.0E-09	1.47E+00	1.47E+00	2.01E-03	2.01E-03	1.95E-03	4.90E+02	4.80E+02	4.81E-01	5.19E-01	6.82E+01	9.85E-05	6.82E+01	9.85E-05
		0.1	1	10	100	300	300	50	1.0E-09	1.47E+00	1.48E+00	1.99E-03	2.03E-03	1.99E-03	6.55E+02	6.55E+02	4.86E-01	5.15E-01	6.82E+01	9.86E-05	6.83E+01	9.87E-05
	Cell Channel Height																*Figure 5.14 E*					
										Figure 5.19, C15		*Figure 5.19, C25*		*Figure 5.19, C35*		*Figure 5.19, C45*						
		0.1	1	10	5	10	300	50	1.0E-09	9.53E-02	2.84E+00	7.52E-02	1.26E-01	3.75E-03	4.00E+01	3.50E+01	4.00E-01	5.26E-01	8.54E+00	1.23E-05	1.32E+02	1.90E-04
		0.1	1	10	5	50	300	50	1.0E-09	7.86E-01	2.18E+00	2.61E-02	2.97E-02	2.93E-03	4.00E